UQAC
Université du Québec
à Chicoutimi

Superhydrophobic Silicone-based Nanocomposites for Application to High Voltage Insulator

by
Elham Vazirinasab
Under supervision of Prof. Gelareh Momen and co-supervision of Prof. Reza Jafari

Manuscript-Based Thesis Presented to Université du Québec à Chicoutimi in Partial fulfillment of the Requirements for the Degree of Doctor of Philosophy Ph.D.

Defended on 30 October 2020

BOARD OF EXAMINERS:

Professor Issouf Fofana, department of Applied Sciences at UQAC, President of the board of examiners

Professor Frej Mighri, department of Chemical Engineering at Laval university, External Member of examiners

Professor Yasar Kocaefe, department of Applied Sciences at UQAC, Internal Member of examiners

Professor Gelareh Momen, department of Applied Sciences at UQAC, Internal Member of examiners

Professor Reza Jafari, department of Applied Sciences at UQAC, Internal Member of examiners

Quebec, Canada

RÉSUMÉ

La mouillabilité est l'une des caractéristiques fondamentales de chaque surface solide qui peut affecter de différentes manières les propriétés finales de surface. À la lumière de divers chefs-d'œuvre de Mère Nature, particulièrement les feuilles de lotus, en tant que symbole de pureté, les surfaces superhydrophobes inspirées de la nature ont reçu une immense attention. Dans la présente thèse, deux approches distinctes sont choisies pour créer efficacement des surfaces autonettoyantes / superhydrophobes. Ces surfaces possèdent une excellente hydrofugation pour améliorer la durée de vie de différents matériaux d'ingénierie tels que le caoutchouc de silicone et le Teflon.

Dans un premier temps, le traitement au plasma à pression atmosphérique a été utilisé pour produire des surfaces autonettoyantes / superhydrophobes de caoutchouc de silicone vulcanisé à haute température (HTV-SR) via une technique de gravure. Cette approche est importante car l'utilisation d'un système plasma à pression atmosphérique est une technique simple, rapide et respectueuse de l'environnement. Ainsi utilisé l'air comprimé en tant que gaz écologique à plasma, cette technique offre un grand potentiel pour la production des surfaces superhydrophobes à grande échelle. Grâce au traitement au plasma, une amélioration substantielle de l'hydrofugation des surfaces HTV-SR (c'est-à-dire un angle de contact statique avec l'eau (WCA)> 160° et une hystérésis d'angle de contact (CAH) <3°) a été obtenue en raison de la formation de surfaces micro-nanostructurées semblables au corail. L'obtention des structures de surface appropriées dépend fortement de la composition du jet de plasma affectée par ses propres paramètres de fonctionnement. C'est pourquoi le rôle des paramètres opératoires de plasma sur la répulsion de l'eau de surface a été évalué à l'aide d'un plan d'expérience (DoE) pour déterminer les paramètres quasi optimaux.

Les propriétés glaciophobes sont divisées en deux catégories de propriétés d'antigivrage et de dégivrage. Les propriétés d'antigivrage correspondent au retard de la formation de glace, tandis que les propriétés de dégivrage se rapportent à la diminution de force d'adhérence de glace formée à la surface. Les techniques bien connues de mesure de l'adhérence de la glace, c'est-à-dire les tests d'adhérence par centrifugation et de poussée (push-off), ont fourni des comparaisons quantitatives de la force d'adhérence à la glace des surfaces produites. Le retard de la formation de glace et la force d'adhérence à la glace considérablement faible de la surface HTV-SR superhydrophobe traitée au plasma ont confirmé une amélioration de leur propriété glaciophobe. Cependant, la robustesse des surfaces superhydrophobes peut être considérée comme le talon d'Achille vers l'industrialisation et les applications dans la situation réelle. Pour garantir des propriétés superhydrophobes durables, la résistivité chimique ainsi que la durabilité mécanique de la surface superhydrophobe produite ont été rigoureusement évaluées. Bien que la surface produite ait conservé ses propriétés hydrofuges dans de nombreux tests, les surfaces ont perdu leurs propriétés superhydrophobes sous certains dommages mécaniques sévères.

Dans un second temps, en égard à la mauvaise durabilité mécanique et chimique des surfaces superhydrophobes qui sont susceptibles d'être endommagées, un nanocomposite superhydrophobe volumétrique et non fluoré a été produit. Il s'est fait par intégration de la terre de diatomée et des particules de silice pyrogénée dans la matrice HTV-SR. Le nanocomposite superhydrophobe volumétrique est un nouveau concept dans la fabrication de surfaces superhydrophobes tolérantes aux dommages où toutes leurs faces et couches sont superhydrophobes. Le rapport massique entre les terres de diatomées et la silice pyrogénée dans la structure de surface finale et la densité de réticulation du nanocomposite est très important. Fort de cela, une évaluation approfondie de l'hydrofugation, de la densité de réticulation et de la dureté des nanocomposites produits a été indiquée en fonction de ce rapport massique. En ce qui concerne la robustesse de la surface, plusieurs tests mécaniques et chimiques sévères ont été effectués. Il s'agit entre autres, de l'utilisation du papier abrasif, le grattage au couteau, le décollement au ruban, l'impact au jet d'eau et le sablage. Ces résultats montrent que la surface a conservé sa propriété de non-mouillabilité. De plus, même si lors de dommages mécaniques et / ou chimiques, la superhydrophobicité du nanocomposite était détériorée, l'hydrofugation pourrait être restaurée en enlevant la couche la plus externe. Cela est dû à la présence de micro-nanostructures intégrées à faible énergie de surface dans tout le corps du nanocomposite.

Enfin, pour examiner l'application potentielle de cette approche de traitement au plasma sur divers polymères, un matériau isolant thermoplastique, à savoir le polytétrafluoroéthylène (PTFE, Teflon), a été sélectionné pour fabriquer des surfaces superhydrophobes. Les surfaces en Téflon superhydrophobes produites possédaient des propriétés ultra-hydrofuges, glaciophobicités et auto-nettoyantes. Bien que le traitement au plasma n'ait pas modifié la composition chimique de surface du téflon, les micro-nanostructures hiérarchiques en forme de feuille de lotus créées sur la surface traitée au plasma étaient responsables de sa résistance à l'eau de surface. Le roulage des gouttelettes d'eau et le test d'impact ont permis de vérifier le rôle important des

micro-nanostructures hiérarchiques sur l'hydrophobicité et la stabilité du régime de Cassie-Baxter. En plus de ses capacités autonettoyantes, la surface de Teflon développée a montré la réduction de la force d'adhésion de la glace de sorte qu'elle soit qualifiée de surface passive antigivrante. Un retard du temps congélation des gouttelettes d'eau sur les surfaces superhydrophobes a également été observé en raison de la présence de poches d'air piégées dans les aspérités de surfaces.

Mots-clés: Superhydrophobicité; Hydrofuge; Plasma à la pression atmosphérique; Nanocomposite superhydrophobe volumétrique; Micro-nanostructures; Autonettoyant; glaciophobicité; Durabilité mécanique; Résistivité chimique; Caoutchouc de silicone; Teflon.

ABSTRACT

Wettability is one of the fundamental characterizations of each solid surface which might affect the final surface properties in different manners. In the light of various Mother Nature's masterpieces, specifically Lotus leaves, as a symbol of purity, the nature-inspired superhydrophobic surfaces have received immense attention. In the present thesis, two different approaches are opted to effectively create artificial self-cleaning/superhydrophobic surfaces to enhance the water-repellency of the engineered silicone rubber and Teflon materials.

Firstly, the atmospheric-pressure plasma treatment was used to produce self-cleaning/superhydrophobic high-temperature vulcanized silicone rubber (HTV-SR) surfaces via etching technique. This approach is significant since the use of an atmospheric-pressure plasma system as a simple, fast and environmentally friendly technique is combined with compressed air as an eco-friendly plasma gas which offers great potential for the mass production of superhydrophobic surfaces in an industrial scale. Using plasma treatment, a substantial enhancement in the water-repellency of HTV-SR surfaces, i.e., static water contact angle (WCA) >160° and a contact angle hysteresis (CAH) <3°, was attained due to the formation of coral-like micro-nanostructures on the surface. Possessing the appropriate surface structures depends highly on the composition of plasma jet affected by plasma operating parameters. Thus, the role of significant plasma operating parameters on the surface water-repellency was assessed with the help of a design of experiment (DoE) method to determine the near-optimal operating parameters.

The icephobic properties are divided into two categories of anti-icing and de-icing properties. Anti-icing properties correspond to the delay in the ice formation, while de-icing properties illustrate the reduction of the adhesion strength of the ice formed on the surface. The well-known ice adhesion measurement techniques, i.e., the centrifuge adhesion and push-off tests, were used to provide quantitative comparisons of the ice adhesion strength of the produced surfaces. The delayed ice formation and considerable low ice adhesion strength of the plasma-treated superhydrophobic HTV-SR surface confirmed their desirable icephobicity. However, the robustness of the superhydrophobic surfaces can be considered as the Achilles heel toward industrialization and real-life applications. To ensure long-lasting superhydrophobic properties, the mechanical durability and chemical stability of the produced superhydrophobic surface were rigorously evaluated. Although the produced surface preserved its water-repellent properties in multiple tests, under some harsh mechanical damages, the superhydrophobic properties were reduced.

Secondly, regarding the poor mechanochemical robustness of superhydrophobic surfaces susceptible to damage, a non-fluorinated volumetric superhydrophobic nanocomposite was produced through embedding diatomaceous earth and fumed silica particles into the HTV-SR matrix. The volumetric superhydrophobic nanocomposite is a new concept in fabrication of damage-tolerant superhydrophobic surfaces where each face and every layer of the nanocomposites is superhydrophobic. Given the importance of the diatomaceous earth/fumed silica mass ratio in final surface structure and crosslinking density of the nanocomposite, an in-depth assessment of the water-repellency, crosslinking density, and hardness of the produced nanocomposites was accomplished as a function of various diatomaceous earth to fumed silica mass ratios. Regarding the surface robustness, multiple severe mechanical and chemical tests were conducted including sandpaper and knife scratching, tape peeling, water jet impact, and sandblasting after which the surface retained its initial water-repellency. Moreover, even if during mechanical and/or chemical damages, the superhydrophobicity of the nanocomposite was deteriorated, the water-repellency could be restored by removing the outermost layer. It was due to the presence of embedded low surface energy micro-nanostructures within the entire body of the nanocomposite.

Thirdly, to scrutinize the potential application of plasma treatment approach to various polymers, a thermoplastic insulating material, i.e., polytetrafluoroethylene (PTFE) commercially known as Teflon, was selected to fabricate superhydrophobic surfaces. The produced superhydrophobic Teflon surfaces possessed ultra-water-repellency, icephobicity, and self-cleaning. Although the plasma treatment did not alter the chemical composition of the Teflon surface, the lotus leaf-like hierarchical micro-nanostructures created on the plasma-treated surface were responsible for its surface water-repellency. Both water droplet rolling off and impact test ascertained the significant role of the hierarchical micro-nanostructures on the surface water-repellency as well as the consistency of Cassie-Baxter regime. In addition to the self-cleaning properties, the micro-nanostructured Teflon surface substantially reduced the ice adhesion strength to a content that the produced surface could be categorized as a passive anti-icing surface. Moreover, the onset of freezing of a water droplet was reduced on the superhydrophobic surface due to the presence of air pockets trapped within its surface asperities.

The approaches introduced in this thesis can be implemented in different industries as they are cost-effective, quickly adaptable, and environmentally friendly methods.

Keywords: Superhydrophobicity; Water-repellency; Atmospheric-pressure plasma system; Plasma treatment; Volumetric superhydrophobic nanocomposite; Micro-nanostructures; Self-cleaning; Icephobicity; Mechanical durability; Chemical stability; Silicone rubber; Teflon.

TABLE OF CONTENTS

RÉSUMÉ ..... **ii**
ABSTRACT ..... **iv**
TABLE OF CONTENTS ..... **vi**
LIST OF TABLES ..... **x**
LIST OF FIGURES ..... **xi**
LIST OF ABBREVIATIONS ..... **xv**
LIST OF SYMBOLS ..... **xix**
DEDICATION ..... **xxi**
ACKNOWLEDGMENT ..... **xxii**
INTRODUCTION **1**
0-1 Definition of the problem 1
0-2 Overview 3
0-3 Objectives 4
0-4 Originality statement 5
0-5 Thesis outline 7
CHAPTER 1 - LITERATURE REVIEW **10**
1.1 Introduction 10
1.2 Fundamentals of superhydrophobicity 11
1.3 Fabrication of superhydrophobic surfaces 14
1.3.1 Chemical aspect 15
1.3.2 Physical aspect 18
1.4 Plasma treatment 22
1.4.1 The effect of plasma treatment on surface roughness 25
1.4.2 The effect of plasma treatment on surface chemical composition 28
1.4.3 Superhydrophobic surfaces using plasma treatment 30
1.5 Superhydrophobic nanocomposite 32
1.5.1 Mechanically self-healing superhydrophobic surfaces 35
1.5.2 Chemically self-healing superhydrophobic surfaces 36
1.5.3 Volumetric superhydrophobic nanocomposite 38
1.6 Application of superhydrophobic surfaces 41

1.6.1 Self-cleaning 42
1.6.2 Icephobicity 43
1.6.3 Corrosion resistance 45
1.7 Durability of superhydrophobic surfaces 45
CHAPTER 2 - ARTICLE 1: EVALUATION OF ATMOSPHERIC-PRESSURE PLASMA PARAMETERS TO ACHIEVE SUPERHYDROPHOBIC AND SELF-CLEANING HTV SILICONE RUBBER SURFACES VIA A SINGLE-STEP, ECO-FRIENDLY APPROACH 50
2.1 Abstract 50
2.2 Introduction 51
2.3 Experimental section 54
2.3.1 Materials 54
2.3.2 Atmospheric-pressure plasma treatment 54
2.3.3 Response surface method 55
2.3.4 Surface characterization 56
2.4 Results and discussion 57
2.4.1 Superhydrophobicity of the plasma-treated substrate based on DoE methods 57
2.4.2 Chemical characterization 62
2.4.3 Surface morphology 63
2.4.4 Wettability studies 67
2.4.5 Self-cleaning characteristics 69
2.5 Conclusion 72
CHAPTER 3 - ARTICLE 2: ICEPHOBICITY AND DURABILITY ASSESSMENT OF SUPERHYDROPHOBIC SURFACES: THE ROLE OF SURFACE ROUGHNESS AND THE ICE ADHESION MEASUREMENT TECHNIQUE 73
3.1 Abstract 73
3.2 Introduction 74
3.3 Materials and methods 77
3.3.1 Fabrication of superhydrophobic silicone rubber surfaces 77
3.3.2 Surface characterization 78
3.3.3 Icephobic properties 79
3.3.4 Durability properties 80

3.4 Results and discussion 81
3.4.1 Surface characterization 81
3.4.2 Icephobic properties 85
3.4.3 Anti-icing properties 86
3.4.4 De-icing properties 87
3.5 Durability property 91
3.5.1 Mechanical durability 91
3.5.2 Chemical durability 96
3.6 Conclusions 98
CHAPTER 4 - ARTICLE 3: A NON-FLUORINATED MECHANOCHEMICALLY-ROBUST VOLUMETRIC SUPERHYDROPHOBIC NANOCOMPOSITE 100
4.1 Abstract 100
4.2 Introduction 101
4.3 Materials and methods 103
4.3.1 Materials 103
4.3.2 Preparation of the nanocomposite 104
4.3.3 Characterization techniques 105
4.4 Results and discussion 107
4.4.1 Superhydrophobicity 107
4.4.2 Crosslinking density and hardness 110
4.4.3 Physical, chemical, and thermal characteristics 112
4.4.4 Mechanochemical robustness 117
4.4.5 Self-cleaning 125
4.5 Conclusion 126
CHAPTER 5 - ARTICLE 4: A COMPARATIVE STUDY OF THE ICEPHOBIC AND SELF-CLEANING PROPERTIES OF TEFLON MATERIALS HAVING DIFFERENT SURFACE MORPHOLOGIES 127
5.1 Abstract 127
5.2 Introduction 128
5.3 Materials and methods 129
5.3.1 Fabrication of superhydrophobic Teflon surfaces 129

5.3.2 Surface characterization and water-repellency properties 130
5.3.3 Icephobic and self-cleaning properties 131
5.4 Results and discussion 132
5.4.1 Surface morphology 132
5.4.2 Superhydrophobicity 135
5.4.3 Fourier transform infrared spectroscopy (FTIR) 136
5.4.4 Water-repellency properties 137
5.4.5 Water droplet impact 138
5.4.6 Icephobicity 140
5.4.7 Self-cleaning properties 143
5.5 Conclusion 145
CONCLUSIONS 147
RECOMMENDATIONS 153
APENDIX I 155
APENDIX II 160
REFERENCES 164
PUBLICATIONS 186

LIST OF TABLES

Table 1-1: Surface and wettability properties of PE before and after plasma treatment with air and nitrogen [155]..... 29

Table 2-1. The selected independent variables and their levels..... 56

Table 2-2. The three-level factorial experimental design, showing the factors and the corresponding levels for each experimental combination and the measured WCA and CAH values as the dependent responses. 57

Table 2-3. ANOVA results for water contact angle (WCA). 59

Table 2-4. ANOVA results for contact angle hysteresis (CAH). 59

Table 2-5. Roughness values (nm) based on AFM analysis..... 67

Table 3-1. Area and line roughness values obtained from profilometry analysis..... 82

Table 3-2. The ice adhesion reduction values for the μCM and APP-treated surfaces during the push-off and centrifuge tests..... 90

Table 4-1. Chemical composition and wettability properties of the HTV-SR nanocomposites..... 109

Table 4-2. Analysis of crosslinking measurements obtained from the swelling test as well as hardness values for pristine HTV-SR and each produced nanocomposite. 112

Table 5-1. The results of WCA and CAH for Teflon surfaces replicated on the produced aluminum templates at various etching times..... 129

Table 5-2. Area and line roughness values obtained from profilometry analysis..... 135

Table 5-3. Water contact angle (WCA) and contact angle hysteresis (CAH) of pristine, microstructured, and micro-nanostructured surfaces..... 136

Table 5-4. Freezing delay in seconds of the pristine, microstructured, and micro-nanostructured surfaces at various temperatures..... 143

Table AI-5. Ice adhesion reduction factor (ARF) of the μCM and APP-treated surfaces relative to the ice adhesion strength of an aluminum surface (A 6061) for push-off and centrifuge tests..... 156

Table AI-6. Water contact angle and contact angle hysteresis of the μCM and APP-treated surfaces before and after push-off and centrifuge tests. 156

LIST OF FIGURES

Figure 1-1. Water-repellency and self-cleaning behavior of Lotus leaf; a) spreading the clay as the contamination on the surface, followed by b) cleaning the surface by water. SEM images of the Lotus leaves showing the c) micro-sized roughness protrusions, and d) nano-sized roughness covered the protrusions [31]. *10*

Figure 1-2. A liquid droplet on different surfaces: (a) Young's model; (b) Wenzel's model; (c) the Cassie-Baxter model. *13*

Figure 1-3. Schematic of two essential criteria for fabrication of superhydrophobic surfaces. *14*

Figure 1-4. Schematic illustration of a) concept of top-down methods; and two common approaches including b) plasma etching, and c) templating. *20*

Figure 1-5. a) Schematic of concept of bottom-up approaches; b) schematic illustration of spray coating of a durable superhydrophobic epoxy/PDMS/SiO_2 composite coating, c1-c3) SEM images of pristine glass, copper foam, and filter paper, c4-c6) SEM images of the corresponding coated surfaces [112]. *21*

Figure 1-6. a1) An image of even distribution of glow discharge within low-pressure plasma treatment, a2) schematic of corresponding plasma system [127]; b1) an image of atmospheric-pressure plasma jet, b2) schematic of the corresponding plasma jet [21]. *24*

Figure 1-7. a) Dependence of etching rate of PDMS on plasma power and bias reference voltage [131]; b1 and b2) the changes in arithmetic mean surface roughness (R_a) , bumps width and height as a function of plasma power [132]; AFM scans of c1) untreated PET surface, plasma-treated surfaces for c2) 1 s, c3) 3 s and c4) 5 s [151]; AFM scans of d1) untreated PMMA films, d2) Ar plasma-treated after 90 s, and d3) He plasma-treated after 90 s [145]. *28*

Figure 1-8. Schematic illustration of three main categories of nanoparticles [175]. *32*

Figure 1-9. a1) the working principle of self-healing fluorinated silica and TiO_2 superhydrophobic coating, a2) changes of WCA against number of oleic acid adhesion followed by UV light irradiation [195]; b1-b4) schematic illustration of self-healing process of developed superhydrophobic surface where pressure-induced deformation was recovered by subsequent heating; 3D confocal microscopy images of the c1) original superhydrophobic surface, c2) after pressing the surface, and c3) after heating it at 85 °C for 120 s [198]. *36*

Figure 1-10. a1) Schematic illustration of working principle of self-healing superhydrophobic coating, a2) the reversible changes of WCA after plasma treatment, a3) the changes of WCA as a function of etching-healing cycles [202]; b1) schematic illustration of superhydrophobic coating, b2) changes of WCA and SA against UV irradiation time, b3) changes of SA as a function of UV irradiation and heat treatment cycles [205]. *38*

Figure 1-11. a1) Schematic illustration of a bulk material which can sustain its superhydrophobicity after mechanical abrasion, a2) superhydrophobicity of the broken material, a3) WCA and SA of water-repellent surface, a4) mirror-like phenomnon of the submerged sample in water [18]; sequential images of the removal process of b1-b3) hexadecane, and b4-b6) chloroform from water using porous polymer monolith [20]; c1) schematic image of fabrication process of ktejan black/carbon fiber/PP superhydrophobic material using abrasion method, c2) the changes of WCA and SA as a function of type of abrasive paper [210]. *41*

Figure 1-12. Schematic of main applications of superhydrophobic surfaces in different fields [215]. *42*

Figure 1-13. Schematic of durability of superhydrophobic surfaces based on three categories of mechanical, chemical and environmental durability. 47

Figure 2-1. (a) The atmospheric-pressure plasma jet and (b) a schematic of the plasma treatment jet..... 55

Figure 2-2. (a) Three-dimensional response surface and (b) contour plots for the effect of the reference voltage (%) and plasma jet speed (m min^{-1}) on the water contact angle of the plasma-treated silicone rubber. The red dots are the design points..... 60

Figure 2-3. (a) Three-dimensional response surface and (b) contour plots for the effect of the reference voltage (%) and plasma jet speed (m min^{-1}) on the contact angle hysteresis of the plasma-treated silicone rubber. The red dots are the design points..... 60

Figure 2-4. ATR-FTIR spectra of silicone rubber treated by atmospheric-pressure air plasma at various reference voltages, and plasma jet speed of 4 m min^{-1} and gas flow rate of 2500 L h^{-1}. 63

Figure 2-5. SEM images of (a-1, a-2) untreated silicone rubber at two different magnifications and (b–d) plasma-treated silicone rubber at different reference voltages; (b) 80%, (c) 90% and (d) 100% at magnifications of 1000× and 10000× (the plasma jet speed and gas flow rate were kept constant at 4 m min^{-1} and 2500 L h^{-1} respectively)..... 65

Figure 2-6. Surface profile of (a) untreated silicone rubber, (b) plasma-treated superhydrophobic silicone rubber at a reference voltage of 100%, a plasma jet speed of 4 m min^{-1} and a gas flow rate of 2000 L h^{-1} and (c) plasma-treated silicone rubber at a reference voltage of 80%, a plasma jet speed of 8 m min^{-1} and a gas flow rate of 2000 L h^{-1}. The inserted images are CAH..... 66

Figure 2-7. (a) The CAH of water droplets of various volumes on the superhydrophobic surface; (b) sequential images of a 4 µL water droplet before and after a severe contact with superhydrophobic surface; (c and d) sequential images of a water droplet impact on the untreated and the plasma-treated superhydrophobic surface, respectively. 69

Figure 2-8. Self-cleaning property of (b; d - left side) an untreated silicone rubber and (c; d – right side) plasma-treated superhydrophobic surface after the wet contaminant approach. 70

Figure 2-9. Self-cleaning property of the plasma-treated superhydrophobic surface and untreated silicone rubber subjected to the dry contaminant setup: (a) sequential photographs of the stiction of kaolin to the surface of a water droplet and the removal of kaolin from the superhydrophobic surface; (b) sweeping of a contaminated superhydrophobic surface by a single water droplet; (c) stiction of water droplets to the contaminated untreated silicone rubber surface. 71

Figure 3-1. Schematic of the (a) micro compression molding (µCM) and (b) atmospheric-pressure plasma (APP) techniques to create a micro-nanostructured silicone rubber surface. 78

Figure 3-2. The 3D surface profiles of the (a-1) pristine, (b-1) µCM, and (c-1) APP-treated silicone rubber surfaces. SEM images of the (a-2, a-3, and a-4) pristine, (b-2, b-3, and b-4) µCM, and (c-2, c-3, and c-4) APP-treated silicone rubber surfaces. Inset images represent the water contact angle and contact angle hysteresis of the corresponding surfaces. 82

Figure 3-3. FTIR spectra for (1) pristine, (2) µCM, and (3) APP-treated silicone rubber surfaces. 83

Figure 3-4. Images of droplet evaporation on (a) pristine, (b) µCM, and (c) APP-treated silicone rubber surfaces. (d) Changes to the water contact angle and contact line over time for each surface. 85

Figure 3-5. (a) Variation in water contact angle and (b) freezing delay at various temperatures for the pristine, µCM, and APP-treated surfaces (the dashed line in (a) shows the threshold of superhydrophobicity)..... 87

Figure 3-6. (a) De-icing pressure required for surfaces in the push-off test and (b) the corresponding de-icing energy of each surface. Ice adhesion strength for repetitive icing/de-icing cycles for the (c) push-off and (d) centrifuge tests. 89

Figure 3-7. Water contact angle and contact angle hysteresis as a function of abrasion cycles using various abrasion pressures for (a) μCM and (b) APP-treated surfaces. 92

Figure 3-8. SEM images at various magnifications of (a1-a3) μCM surface abraded at 3.2 kPa pressure, (b1-b3) μCM surface abraded at 6.4 kPa pressure, (c1-c3) APP-treated surface abraded at 3.2 kPa pressure, and (d1-d3) APP-treated surface abraded at 6.4 kPa pressure. 93

Figure 3-9. Water contact angle and contact angle hysteresis as a function of (a) finger-press cycle, (b) attach-detach cycle, (c) ultrasonication time, (d) continuous water droplet impact time, and (e) sandblasting time for μCM and APP-treated surfaces. 96

Figure 3-10. Water contact angle and contact angle hysteresis as a function of immersion time (days) in acidic, alkaline, and neutral solutions for (a) μCM and (b) APP-treated surfaces. (c) Water contact angle and contact angle hysteresis as a function of UV-light exposure time for μCM and APP-treated surfaces. 98

Figure 4-1. Schematic illustration of the fabrication of the volumetric superhydrophobic nanocomposite. 105

Figure 4-2. (a) The effect of DE concentration on the WCA and CAH of the surface and bulk portions of the HTV-SR nanocomposite; (b) a water droplet showing the WCA and CAH of a pristine HTV-SR and a nanocomposite D70F50; (c) SEM image of DE particles (×1000); (d) demonstration of the mirror-like phenomenon surrounding the bulk nanocomposite D70F50; (e) demonstration of the Moses effect around the intact and cut surfaces showing up to ~5 mm of water meniscus (red arrows were used to guide the eyes). The blue water droplets illustrate the superhydrophobicity of the surfaces. 110

Figure 4-3. Surface profiles and roughness values of (a) pristine HTV-SR and the nanocomposites (b) D60F60, (c) D70F50, and (d) D80F40; FESEM images of the surface of (e) the pristine HTV-SR and the nanocomposites (f) D60F60, (g) D70F50, and (h) D80F40; FESEM images of the cross section of (i) pristine HTV-SR and nanocomposites (j) D60F60, (k) D70F50, and (l) D80F40. All images (e–l) are at ×1000 magnification. 114

Figure 4-4. FESEM images of the surface of nanocomposites (a) D60F60, (b) D70F50, and (c) D80F40; FESEM images of the cross section of nanocomposites (d) D60F60, (e) D70F50, and (f) D80F40. All images (a–f) are at ×10000 magnification. 115

Figure 4-5. (a) FTIR spectra of the pristine HTV-SR and nanocomposite D70F50 (inset shows the FTIR spectra of FS and DE); (b) TGA curve of the pristine HTV-SR and nanocomposite D70F50. 117

Figure 4-6. (a)–(c) Sandpaper abrasion of the nanocomposite D70F50; (a) an image of the sandpaper abrasion apparatus; (b) WCA and CAH of the nanocomposite abraded by #160, #320, and #800 sandpaper after 250 abrasion cycles at a 5 kPa abrasion force; (c) WCA and CAH of the nanocomposite abraded by #160, #320, and #800 sandpaper after 250 abrasion cycles at a 25 kPa abrasion force; (d) knife scratching test; (e) tape peeling test; (f) WCA and CAH of the nanocomposite after multiple cycles of tape peeling; (g) water jet impact test; (h) sandblasting test; (i) WCA and CAH of the nanocomposite after several repeated cycles of ultrasonication and abrasion. Insets demonstrate the wettability of the nanocomposite after the associated tests. 120

Figure 4-7. Schematic illustration of the volumetric superhydrophobic nanocomposite containing DE and FS particles. 121

Figure 4-8. (a) Changes in WCA and CAH of the nanocomposite D70F50 over time during its immersion in deionized water and the acidic and alkaline solutions; (b) contact angle of droplets of deionized water and the acidic and alkaline solution during the droplet evaporation test (inset images show the WCA during evaporation of the water droplet); (c) WCA of the nanocomposite and pristine HTV-SR after heating for 2 h at different temperatures; (d) hydrophobic recovery of the nanocomposite following each cycle of plasma treatment; (e) WCA and CAH of the nanocomposite relative to the pristine HTV-SR as a function of the duration of UV irradiation; (f) water uptake of the pristine HTV-SR and superhydrophobic nanocomposite in relation to the duration of the sample immersion. 124

Figure 4-9. Self-cleaning ability of the volumetric superhydrophobic nanocomposite D70F50. (a) SiC particles having a size of 50 µm and (b) SiC particles having a size of 18 µm. A clean surface was observed in the final images of the rows. 126

Figure 5-1. Schema of the push-off test procedure. 131

Figure 5-2. SEM images of (a) pristine, (b) microstructured, and (c) micro-nanostructured surfaces. 132

Figure 5-3. SEM images of the microstructured surface at a (a) 1000×, (b) 2000×, and (c) 5000× magnification; SEM images of the micro-nanostructured surface at (d) 1000×, (e) 2000×, and (f) 5000× magnification. 133

Figure 5-4. 3D surface profiles of the (a) pristine, (b) microstructured, and (c) micro-nanostructured surfaces and (d) comparison of their 2D surface profiles. 135

Figure 5-5. FTIR spectra of the (1) pristine, (2) microstructured, and (3) micro-nanostructured surfaces. 137

Figure 5-6. Consecutive images of dyed water droplets leaving the (a) pristine, (b) microstructured, and (c) micro-nanostructured surfaces, demonstrating the water-repellency of each surface. 138

Figure 5-7. Time-lapse imagery of a water droplet impacting a (a) pristine, (b) microstructured, and (c) micro-nanostructured surface. 140

Figure 5-8. Ice adhesion strength and adhesion reduction factor (ARF) for pristine, microstructured, and micro-nanostructured surfaces. 141

Figure 5-9. Self-cleaning properties of the (a-c) pristine, (d-f) microstructured and (g-i) micro-nanostructured surfaces examined by water droplet sweeping. 144

Figure 5-10. Self-cleaning evaluation of (a–d) pristine, (e–h) microstructured, and (i–l) micro-nanostructured surfaces by observing of the cleaning of a dried contaminant solution using a water droplet. 145

LIST OF ABBREVIATIONS

2FI	Two-factor interaction
AC	Alternating current
AFM	Atomic force microscopy
Al_2O_3	Alumina
$Al_2O_3.3H_2O$	Alumina trihydrate
ANOVA	Analysis of variance
APP	Atmospheric-pressure plasma
Ar	Argon
ARF	Ice adhesion reduction factor
ATH	Alumina trihydrate
ATR	Attenuated total reflection
$CaCO_3$	Calcium carbonate
CAH	Contact angle hysteresis
CAT	Centrifuge adhesion test
CCA	Constant contact angle
CCL	Constant contact line
CF_4	Carbon tetrafluoride
CL	Contact line
CNT	Carbon nanotube

DC	Direct current
DE	Diatomaceous earth
DI	Deionized
DoE	Design of experiment
DVB	Divinylbenzene
EDM	Electrical-discharge machining
EPDM	Ethylene propylene diene monomer
FESEM	Field emission scanning electron microscopy
FS	Fumed silica
FTIR	Fourier-transform infrared spectroscopy
F-POSS	Fluorodecyl polyhedral oligomeric silsesquioxane
H_2	Hydrogen
HCl	Hydrochloric acid
HDPE	High density polyethylene
He	Helium
HMDSN	Hexamethyldisilazane
HTV-SR	High-temperature vulcanized silicone rubber
LIGA	Lithographie, Galvanoformung und Abformung
LIMA	Anti-icing materials international laboratory

LDPE	Low density polyethylene
LMWS	Low molecular weight siloxane
µCM	Micro compression molding
MVD	Median volumetric diameter
MWCNT	Multiwalled carbon nanotube
N_2	Nitrogen
NH_3	Ammonia
NH_4HCO_3	Ammonium bicarbonate
NSERC	Natural sciences and engineering research council of Canada
O_2	Oxygen
OH	Hydroxyl
PCL	Polycaprolactone
PDMS	Polydimethylsiloxane
PE	Polyethylene
PET	Polyethylene terephthalate
PLA	Poly(lactic acid)
PMC	Perfluoroalkyl methacrylic copolymer
PMMA	Polymethylmethacrylate
POSS	Polyhedral oligomeric silsesquioxane

PP	Poly(propylene)
PS	Polystyrene
PTFE	Polytetrafluoroethylene
PVC	Polyvinyl chloride
PVDF	Poly(vinylidene fluoride)
RMS	Root-mean-square
RTV-SR	Room-temperature vulcanized silicone rubber
SA	Sliding angle
SEM	Scanning electron microscopy
SF_6	Sulfur hexafluoride
SiC	Silicon carbide
SiO_2	Silicone oxide
TGA	Thermogravimetric analysis
TiO_2	Titanium oxide
TMS	Tetramethylsilane
UV	Ultraviolet
WCA	Water contact angle
XPS	X-ray photoelectron spectroscopy
ZnO	Zinc oxide

LIST OF SYMBOLS

A	Iced area
E	Modulus
F	Centrifugal force
k	Boltzmann constant
m	Detached ice mass
M_C	Crosslinking points
ν	Crosslinking density
ω	Centrifuge speed at which detachment occurred
Q	Swelling ratio
r	Beam radius
R_a	Arithmetic mean of line roughness
R_p	Maximum peak height of line roughness
R_q	Root-mean-square deviation of line roughness
R_t	Maximum peak to valley height of line roughness
S_a	Arithmetic mean height of area roughness
S_{ku}	Kurtosis coefficient of area roughness
S_q	Root-mean-square height of area roughness
S_{sk}	Skewness coefficient of area roughness

S_t	Maximum peak to valley height of area roughness
T	Absolute temperature
τ	Adhesion shear stress

DEDICATION

To my parents, *Mansour Vazirinasab* and *Masoumeh Sarhangnejad*, for their unconditional love, unwavering devotion and guidance which ceaselessly lighten my path.

To my beloved husband, *Khosrow Maghsoudi*, my endless source of passion, support, and encouragement, with whom I am literally living my dreams.

ACKNOWLEDGMENT

I would like to express my appreciation to my research supervisor, *Prof. Gelareh Momen*, for her continuous support, kindness and care during my PhD. Working with her made me not only a better researcher but a better person.

I would like to warmly thank my co-supervisor, *Prof. Reza Jafari*, for his support and guidance. I am also grateful for his continuous involvement in my project which helped me overcome the experimental challenges.

I am deeply grateful to the members of my committee, *Prof. Issouf Fofana, Prof. Yasar Kocaefe, Prof. Frej Mighri,* and *Prof. Duygu Kocaefe*, for their worthwhile guidance and support.

I would like to express my gratitude to *Mr. Tony Carreira*, the president of K-Line Insulators Ltd., for his valuable feedbacks and outstanding support during this academy-industry collaboration.

I would like to deeply thank *Mr. Pierre Camirand*, which his both technical and moral supports make my PhD life enjoyable and fulfilled.

I would like to take this opportunity to thank all the professionals and technicians for their assistance in this project, *Prof. Zhan Zhang* for carrying out the Scanning Electron Microscopy (SEM) tests at University Research Centre on Aluminum (CURAL), *Ms. Caroline Potvin*, the laboratory assistant of the chemistry department, and *Mr. Carl St-Louis*, the assistant of the materials characterization laboratory (University of Sherbrooke).

I would like to express my appreciation for the financial support of the *Natural Sciences and Engineering Research Council of Canada (NSERC)* and *K-Line Insulators Ltd.,* Toronto, Canada without which completion of this research would not have been possible.

Last but not least, I would like to sincerely thank my family and friends for all the love and support they provided me throughout my studies

INTRODUCTION

0-1 Definition of the problem

Among the most important parts of power transmission systems are electrical insulators by which the transmission lines are safely attached to the transmission tower. The high-voltage outdoor insulators act as the electrical supports to prevent the current to flow through the tower to the ground while simultaneously resisting the weight of the suspended wires. The functionality of the transmission systems extremely relies on the efficiency of high-voltage insulators influenced by the accumulation of ice and pollution on their surfaces [1, 2]. The ice and pollution accumulation caused serious problems mainly in cold climate regions and polluted areas, respectively. For instance, in 1998 in the north-eastern United States and south-eastern of Canada (from eastern Ontario to southern Quebec), the ice storm-related electrical blackouts left over 1 million people without power and an estimated damage cost exceeded US$4 billion. The same disaster happened in North America in 2013 and cost around US$200 million [3]. The frequency of sandstorm occurrences in desert areas as well as high density of pollutant in highly-polluted manufacturing cities increases the possibility of the sand and pollution accumulation on the high-voltage insulators [4]. When the surface of polluted insulator becomes wet or a thin film of thawed ice covers the surface, the conductive layer formed on the surface gives rise to the leakage current followed by partial evaporation. Subsequently, the presence of dry regions on the surface causes dry band arcing and partial electrical discharge which eventually may lead to the flashover and power system outage [5]. Therefore, the self-cleaning and anti-icing performance of the high-voltage insulators are of great importance and should be surveyed carefully.

Over the last few decades, conventional ceramic and glass insulators are getting replaced by polymeric insulators. The notable electrical parameters of polymeric materials such as low dielectric permittivity, low electrical conductivity and high breakdown voltage makes them promising candidates for insulator application. Due to their lighter weight, the transportation and installation procedure of polymeric insulators are easier than that of conventional ones. Moreover, compared to ceramic and glass insulators, they have higher flexibility, impact resistance and mechanical strength which makes them resistant to vandalism and damages [6, 7]. Polymeric insulators consist of two components, i.e., the core made of a composite of fiberglass with polyester

or epoxy, and the weather sheds made of insulating polymers like silicone rubber and ethylene propylene diene monomer (EPDM) rubber. During the last few decades, silicone rubber materials have found their way into the real-world applications such as automotive industry, aerospace, cookware, electronics industry, etc. The backbone of silicone rubber is consisted of siloxane (Si-O) groups responsible for its unique characteristics in terms of thermal stability, abrasion resistance, ultraviolet (UV) resistance and low electrical conductivity [8]. In addition to its superb properties, it also benefits greatly from its hydrophobic nature resulted from the presence of methyl side chains. Despite the hydrophobicity of silicone rubber, it cannot completely avert the detrimental accretion of ice and pollution on the shed of insulators.

Nowadays, it has been illustrated that there is a good correlation between self-cleaning/ ice-phobic properties and superhydrophobicity [9-12]. To reduce the chance of severe ice and pollution accumulation, nature-inspired water-repellent superhydrophobic surfaces characterized by water contact angle (WCA) higher than 150° and contact angle hysteresis (CAH) or sliding angle (SA) less than 10° are being studied. Having low surface energy (i.e. hydrophobic) materials along with desirable micro-nanostructured surface roughness can lead to the creation of superhydrophobic surfaces [13]. Considering the significant growing demand for prevention or reduction of ice and pollution accumulation on insulators, many efforts have been made chiefly concentrated on the fabrication of superhydrophobic coatings. Room-temperature vulcanized silicone rubber (RTV-SR) is one of the appealing candidates used in superhydrophobic coatings for insulators which suffer from the durability issues since they are less mechanically durable and wear out more simply than bulk materials. Moreover, significant amount of chemical solvents is needed to develop coatings which is detrimental to the environment.

In order to overcome the coatings disadvantages, two relatively novel approaches were elaborated to produce superhydrophobic high-temperature vulcanized silicone rubber (HTV-SR) out of bulk material. In this regard, the main objective of this Ph.D. project was to employ simple and effective methods for fabrication of self-cleaning and icephobic non-wettable HTV-SR-based materials to considerably diminish the probability of pollution and ice accumulation and subsequent prevention of flashover and electrical power outage. Moreover, to extend our understanding of the fabrication of self-cleaning and icephobic materials, we also selected a thermoplastic polymer. Teflon, as a widespread insulating material, was used to fabricate superhydrophobic

surfaces emerging self-cleaning and icephobic properties. This project is defined as an academic-industry collaboration between *Université du Québec à Chicoutimi (UQAC)* and *K-Line Insulators Company*.

0-2 Overview

Wettability is one of the basic characteristics of solid surfaces, and it reflects the affinity of a liquid to spread on or adhere to a solid surface. In the past decades, inspired by a vast number of natural phenomena such as the self-cleaning characteristics of the lotus leaf and the "anti-water" legs of a water strider, artificial superhydrophobic surfaces, as an extreme state of surface non-wettability, have received tremendous attention [14, 15]. Numerous applications have been reported for superhydrophobic surfaces including water-repellency, self-cleaning, icephobicity, anti-corrosion, anti-fouling, oil-water separation, and drag reduction [13].

Researchers have fabricated superhydrophobic surfaces mainly by (i) surface roughening of a low surface energy material or (ii) modifying a rough surface by deposition of low surface energy materials [14]. Multiple methods have been used to create roughness on low surface energy or inherently hydrophobic materials, such as silicones and fluorocarbons. Etching is one of the well-established approaches for generating micro-nanoroughnesses on diverse hydrophobic substrates. Etching refers to removing material from the substrate that can be divided into two main categories: (i) wet chemical etching where acidic or alkaline solutions etch dislocations or impurities on the substrates, and (ii) dry etching such as plasma etching, in which the generation of reactive atoms or ions in a gas discharge leads to the anisotropic etching of the surface [16, 17]. Plasma systems are extensively used for surface treatment which, in terms of applied pressure inside the plasma chamber, are divided into low-pressure and atmospheric-pressure plasma. Atmospheric-pressure plasma system is a simple, yet efficient, cost-effective and eco-friendly approach that enables the large-scale surface treatment and industrialization. In this project, the atmospheric-pressure air plasma system was employed as an etching technique to generate micro-nanostructures on the HTV-SR since it was more beneficial than a low-pressure system from a practical and industrial point of view and had been rarely studied.

However, the large-scale application of superhydrophobic surfaces is significantly hindered by their poor mechanical and chemical robustness which can be considered as their Achilles' heel. Since the majority of produced superhydrophobic surfaces have been concentrated on the formation of considerably thin micro-nanostructured coating layer on top of the base materials, these surfaces suffer from the loss of their functionality chiefly due to the mechanical damages. In order to overcome such an intrinsic weakness of

superhydrophobic surfaces, several strategies have been proposed among which a completely new generation of damage-tolerant superhydrophobic materials is the fabrication of volumetric superhydrophobic nanocomposites. The main concept of this approach is using particles themselves as the favorable roughness creators [18]. Considering the presence of particles throughout the whole bulk of the material, the superhydrophobic behavior lasts upon mechanical abrasion up to the point at which the materials are completely worn out which ensures the continual superhydrophobicity [19, 20]. In this regard, the second goal of this project was to produce an ultra-robust volumetric superhydrophobic HTV-SR nanocomposite. The extended superhydrophobicity throughout the whole bulk of the material was retained during the continuous mechanical abrasion.

0-3 Objectives

The general objective of this project is to develop water-repellent/self-cleaning materials based on two simple and non-expensive approaches including the use of atmospheric-pressure plasma system and the development of volumetric superhydrophobic nanocomposite. In this section, the specific objectives of each method sought to attain desirable water-repellency is defined in detail.

1) As the first approach to develop a water-repellent/self-cleaning surface via simple one-step atmospheric-pressure plasma treatment, some objectives should be met as follows:

- Studying the effect of various plasma operating parameters on the surface water-repellency.
- Optimization of the effective plasma operating parameters with the help of design of experiment (DoE) technique.
- Assessing the self-cleaning, icephobic, and durability properties of the produced superhydrophobic surfaces.

2) To enhance the robustness of the superhydrophobic surfaces, the development of a damage-tolerant volumetric superhydrophobic nanocomposite was specified as the second approach. The following objectives should be accomplished to gain the favorable nanocomposites:

- Determining the suitable micro and nanoparticles for creating the desired structures.

- Determining the best blending conditions to properly distribute micro and nanoparticles within matrix.
- Optimization of the particles concentration to enhance the non-wettability properties of the samples.
- Evaluating the self-cleaning properties.
- Rigorous assessment of durability properties of volumetric superhydrophobic nanocomposites.

0-4 Originality statement

In the present thesis, we focused on two different strategies for having water-repellent superhydrophobic surfaces. As the first approach, the atmospheric-pressure plasma treatment was opted to fabricate self-cleaning/superhydrophobic surfaces. According to the pressure applied inside the plasma chamber, there are two categories of plasma systems: low-pressure plasma and atmospheric-pressure plasma systems. In spite of its potential drawbacks such as high maintenance cost, being time-consuming and limited size of the treated object, low-pressure plasma system has been widely used for the creation of desirable roughness on various surfaces to achieve superhydrophobicity. However, the atmospheric-pressure plasma system utilized in this project can be a suitable alternative for industrial production of self-cleaning/superhydrophobic polymeric surfaces due to its continuous, rapid, timesaving, cost-effective, and environmentally friendly procedure. Another advantage of this approach relative to the use of low-pressure plasma is the simplicity for combining it with available production lines [14].

The atmospheric-pressure plasma system is chiefly used for plasma polymerization via a two-step process including the roughness formation followed by deposition of hydrophobic materials on the surface. However, only a handful of studies have reported the development of superhydrophobic surfaces via a one-step plasma etching technique. In the current project, the atmospheric pressure plasma system is used for making surface roughness on the inherent hydrophobic HTV-SR via a single-step procedure to attain superhydrophobic surfaces which, to our knowledge, has never been investigated.

Another significance of our approach is attributed to the combination of the atmospheric-pressure plasma system with compressed air as an eco-friendly plasma gas which enables the enhancement towards

industrialization of superhydrophobic surfaces for mass production. Air is an ideal candidate for plasma gas, as it is a natural, eco-friendly, inexpensive and abundant gas mixture. To the best of our knowledge, no published research papers have used air for fabrication of superhydrophobic/water-repellent surfaces via a plasma-etching technique. In addition to the superhydrophobicity, the icephobic properties of the produced surfaces were also thoroughly assessed which was hardly performed on the plasma-treated surfaces in the literature. Finally, yet importantly, the potential application of this approach goes well beyond the silicone rubber, as a thermoset material, and it can be utilized for the thermoplastic hydrophobic materials, e.g. polytetrafluoroethylene (PTFE), as well.

As the second approach, we concentrated on the development of volumetric superhydrophobic nanocomposites. Over the last few decades, non-wettable superhydrophobic coatings having self-cleaning and icephobic properties have been extensively developed through various methods such as spray coating, spin coating, electrodeposition, etc. However, there are several drawbacks related to the use of traditional coating technology such as being time consuming and labor-intensive, poor adhesion of coating to the substrate, less mechanical durability of coating compared to the bulk material, permanently losing the superhydrophobicity under mechanical damages, and constant needs for reapplying after wearing out. Thus, all of these issues restricted the commercialization of superhydrophobic surfaces. In the present work, unlike conventional methods for producing superhydrophobic materials essentially reliant on the surface manipulation techniques (e.g. coating, direct replication, etching, etc.), we developed a long-standing damage-tolerant volumetric superhydrophobic nanocomposite which had not been subjected to any surface treatment.

In this substance, the embedded micro and nanoparticles within the matrix are responsible for surface and bulk water-repellency called “volumetric superhydrophobicity”. In other words, the desirable micro-nanoroughnesses for volumetric superhydrophobicity is achieved via the distribution of specific-shaped particles throughout the bulk of the nanocomposite. To the best of our knowledge, this is the first time that the volumetric superhydrophobic HTV-SR nanocomposite has been fabricated.

Despite all the advantages of this concept, only a handful of studies have developed the mechanically robust volumetric superhydrophobic nanocomposites. Although the prepared nanocomposites in the literature can maintain the surface roughness after exposure to mechanical damages, still remains lack of some essential studies. For example, the physical stability of the prepared superhydrophobic nanocomposites was hardly

mentioned in the literature. Moreover, according to our literature review, the majority of the developed volumetric superhydrophobic nanocomposites contains high-priced rod-shaped particles or Teflon nanoparticles which are unfavorable in terms of cost-effectiveness or environmental friendliness. To the best of our knowledge, this is the first report on the fabrication of a physically stable, non-fluorinated, and inexpensive volumetric superhydrophobic nanocomposite via a simple method.

0-5 Thesis outline

In this section, a brief overview of 5 chapters composing this Ph.D. thesis is provided. For the readers to get familiar with the general idea behind this study, a literature review is presented in the subsequent chapter, Chapter 1. In this chapter, following the fundamentals of the superhydrophobic surfaces, their fabrication approaches based on both chemical and physical aspects are provided. Various intrinsic hydrophobic materials capable to be used for the development of superhydrophobic surfaces as well as different methods employed to create roughness on the surface referred as chemical and physical aspects are covered in the section entitled fabrication of superhydrophobic surfaces. Then, to have a better understanding of two approaches chosen in the present Ph.D. studies, the plasma treatment and superhydrophobic nanocomposite are discussed in depth. Moreover, a brief overview on the application of superhydrophobic surfaces including self-cleaning, icephobicity, and anti-corrosion, as well as their mechanical and chemical durability is presented. It is worth to mention that a small part of this chapter is stemmed from our review paper entitled “Application of superhydrophobic coatings as a corrosion barrier: A review” published in Journal of Surface and Coatings Technology [13]. The subsequent chapters correspond to each written article of the above-mentioned project.

In Chapter 2, superhydrophobic and self-cleaning properties of the plasma-treated silicone rubber surfaces are presented. In addition to the surface characterization, the influence of plasma operating parameters on the water-repellency of silicone rubber is assessed via a DoE method to determine the near-optimal operating parameters. The acquired results led to the journal article 1 “Evaluation of atmospheric-pressure plasma parameters to achieve superhydrophobic and self-cleaning HTV-SR surfaces via a single-step, eco-friendly approach” published in *Journal of Surface and Coatings Technology* [21].

In Chapter 3, the icephobicity and durability assessment of the developed superhydrophobic surfaces via two industrially applicable approaches of micro-compression molding and atmospheric-pressure plasma treatment are provided. All preparations (atmospheric-pressure air plasma treatment using optimized plasma

operating condition achieved from Chapter 2), analyses (including physicochemical characterization, superhydrophobicity, icephobicity and durability), and the associated interpretation of the properties of the developed plasma-treated surfaces are accomplished by the PhD candidate. Both anti-icing properties (delayed ice formation) and de-icing properties (reduced ice adhesion strength) of the produced surfaces subjected to two forms of icing conditions are examined. The well-known ice adhesion measurement techniques, i.e., the centrifuge adhesion and push-off tests, provide quantitative comparisons of the ice adhesion strength of the produced surfaces. Furthermore, a comprehensive series of experiments are carried out to vigorously evaluate the durability properties of the prepared surfaces is provided. These findings are reported in the paper entitled "Durability assessment of icephobic surfaces: the role of surface roughness and the ice adhesion measurement technique" submitted to *Journal of Materials Processing Technology* [22].

In chapter 4, the mechanochemically robust volumetric superhydrophobic nanocomposite is reported through the addition of diatomaceous earth and fumed silica particles to HTV-SR. The water-repellency of the produced nanocomposites—based on the WCA and CAH of the surface—in relation to various diatomaceous earth to fumed silica mass ratios of the nanocomposites is also presented. The mechanical robustness, chemical stability and UV resistance of the superhydrophobic nanocomposites is thoroughly surveyed in this chapter. The results of this study are presented in the paper entitled "A Non-Fluorinated Mechanochemically-Robust Volumetric Superhydrophobic Nanocomposite" accepted in the *Journal of Materials Science and Technology* [23].

In chapter 5, the conceivability of using thermoplastic fluorocarbon materials, as another appealing candidate for superhydrophobic surfaces, is investigated. The superhydrophobic, icephobic and self-cleaning characterization of the produced water-repellent surfaces through two simple and cost-effective approaches of micro-compression molding and atmospheric-pressure plasma treatment are provided. All preparations (atmospheric-pressure air plasma treatment), analyses (including physical and chemical characterization, water repellency, high-speed filming, icephobicity and self-cleaning), and the interpretation of the properties of produced plasma-treated surfaces are accomplished by the PhD candidate. Moreover, the water-repellency of the produced superhydrophobic surfaces is evaluated based on water droplet impact as well as rolling off water droplet. The freezing delay measurement and push-off analyses are performed to represent the icephobic properties. The findings achieved in this study led to the journal article entitled "A comparative study of the

icephobic and self-cleaning properties of Teflon materials having different surface morphologies" published in the *Journal of Materials Processing Technology* [24].

CHAPTER 1

LITERATURE REVIEW

1.1 Introduction

There are abundant examples of surfaces originated from nature on which water droplets cannot settle and move away instantly. Excellent capacities for water-repellency are demonstrated by many plants and animals including lotus leaves [25, 26], taro leaves [25], water strider legs [27], cicada wings [28, 29], butterfly wings [30], body feathers of penguins [31], and numerous other examples. Lotus (*Nelumbo nucifera*) leaves are one of the most prominent instances among naturally occurring superhydrophobic surfaces which, owing to their water-repellent and self-cleaning behavior, were considered as the symbol of purity [32]. A combination of hierarchical surface roughness and low surface energy wax-like materials are responsible for their superhydrophobicity. As shown in Figure 1-1, scanning electron microscopy (SEM) micrographs indicated that the rough surface is comprised of a hierarchical two-level roughness of the initial micro-sized (3–10 µm) roughness protrusions called cell papilla covered by a second epicuticular waxy layer of hydrophobic crystalloids having nano-sized (70–100 nm) roughness [33].

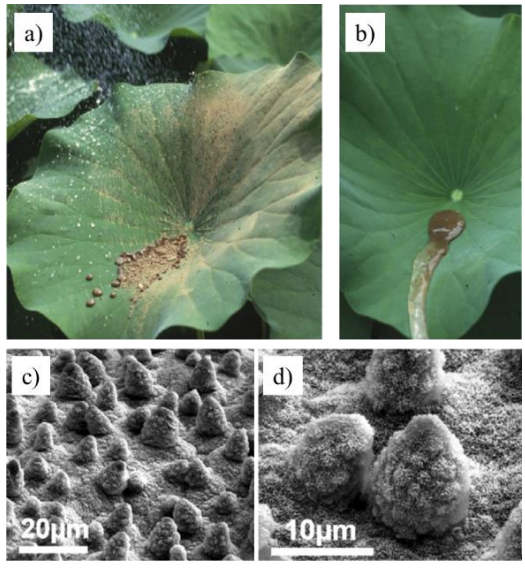

Figure 1-1. Water-repellency and self-cleaning behavior of Lotus leaf; a) spreading the clay as the contamination on the surface, followed by b) cleaning the surface by water. SEM images of the Lotus leaves showing the c) micro-sized roughness protrusions, and d) nano-sized roughness covered the protrusions [33].

Due to their wide range of applications, nature-inspired superhydrophobic water-repellent surfaces having WCA higher than 150° and CAH of less than 10° have received enormous attention in both academic and industrial fields. Self-cleaning [34, 35], icephobicity [24, 36], anti-corrosion [13, 37], oil-water separation [38, 39], and drag reduction [40] are some examples of the application of water-repellent superhydrophobic surfaces. Researchers have fabricated superhydrophobic surfaces mainly by (i) surface roughening of a low surface energy material or (ii) modifying a rough surface by depositing low surface energy materials [41].
In this chapter, firstly we provide a brief introduction on fundamental theories relevant to the wetting and non-wetting behavior of solid surfaces. Given that superhydrophobic surfaces must possess low-surface energy hydrophobic materials (chemical aspect) along with favorable surface roughness (physical aspect), we present their fabrication procedure regarding these two aspects. Then, as the used fabrication methods in the current thesis, plasma treatment and superhydrophobic nanocomposites are emphasized. This chapter proceeds with a short literature review on some applications of the superhydrophobic surfaces including self-cleaning and icephobicity as well as their durability challenges.

1.2 Fundamentals of superhydrophobicity

The non-wettability and self-cleaning behavior of lotus leaves are due to their high WCA and low CAH of around 161° and 2°, respectively. Consequently, superhydrophobic surfaces are defined based on two criteria; static WCA greater than 150° and dynamic contact angle (such as CAH) of less than 10° [32, 42].

Over the last few decades, the wettability of solid surfaces and solid-liquid physical interactions have been intensively studied. Young, Wenzel, and Cassie-Baxter are the principal equations for explaining surface wettability. Young's equation is the starting point for wetting models that results from the equilibrium of interaction forces along the triple line. It determines the static contact angle of a sessile drop on an ideal smooth, homogenous, rigid, and insoluble solid surface (Figure 1-2 (a)). As shown in Eq. 1-1, according to the Young's equation, the static contact angle depends only on the thermodynamic equilibrium of the interfacial tension of the solid-liquid-vapor interfaces [43, 44]:

$$\cos\theta = \frac{\gamma_{SV} - \gamma_{SL}}{\gamma_{LV}} \qquad 1-1$$

where θ is the contact angle, and γ_{SV}, γ_{SL}, and γ_{LV} are the interfacial tensions of the solid-vapor, solid-liquid, and liquid-vapor interfaces, respectively. It is clearly understood from Eq. 1-1 that forasmuch as the surface tensions of water and its surroundings (usually air) are fixed, a decrease in the surface tension of a solid

material leads to an increase in the static contact angle. Although the decreasing order of the surface energies of the chemical groups are known as $CH_2 > CH_3 > CF_2 > CH_2F > CF_3$, the highest reached static contact angle of a smooth surface using CF_3, as a chemical group with lowest surface energy, is about 120°, which does not fulfill the requirement for superhydrophobicity [45, 46].

Surface roughness is, therefore, the second critical factor for obtaining a superhydrophobic surface. Higher surface roughness combined with a lower surface energy are required to achieve a superior contact angle and superhydrophobicity [47]. The electron microscopy of the surface of lotus leaves confirmed that a combination of hierarchical surface micro-nanostructures and low surface energy wax-like materials are the principal reasons for its superhydrophobicity [32].

Many researchers, in particular Wenzel and Cassie-Baxter, endeavored to formulate a relationship between surface tension, roughness, and contact angle. Based on Wenzel's studies of the wettability of porous surfaces, the roughness of a surface dramatically affects the contact angle on the surface. As shown in Figure 1-2 (b), the liquid penetration into the rough grooves and the increase in the interfacial area for the spreading liquid are the main assumptions in Wenzel's theory [48]. At thermodynamic equilibrium, Wenzel's homogeneous wetting state proposed a linear relationship between the apparent contact angle and the roughness factor of the surface [41]:

$$\cos\theta_W = \frac{r(\gamma_{SV} - \gamma_{SL})}{\gamma_{LV}} = \mathrm{r}\cos\theta \qquad 1-2$$

where θ_w is the apparent contact angle on the rough surface, θ is Young's contact angle on a similar smooth surface, and r is the surface roughness factor. The surface roughness factor is defined as the ratio between the actual surface area and the geometrical projected surface area. Therefore, for a rough surface, r is >1. According to Wenzel's equation, creating roughness increases both the hydrophobicity and hydrophilicity, taking into consideration the prior nature of the surface. Thus, if the contact angle of the surface is >90°, hydrophobicity is improved by roughness whereas if the contact angle is <90°, hydrophilicity is enhanced [49].

Wenzel's theory, known as the homogeneous wetting state, occurs when a drop of liquid fills up the roughness grooves. A heterogeneous wetting state like Cassie-Baxter has air (or another fluids) trapped in the roughness grooves underneath the liquid and thus the latter is prevented from penetrating into the pores (Figure

1-2 (c)) [50]. In practical terms, the Cassie-Baxter equation applies only when the liquid is in contact with the solid surface at the top of the protrusions (Eq. 1-3) [51-53]:

$$\cos\theta_{CB} = f_s \cos\theta - (1 - f_s) = f_s \cos\theta + f_s - 1 \qquad 1-3$$

where θ_{CB}, θ, and f_s are the Cassie-Baxter contact angle, the Young's contact angle, and the ratio between the total area of solid-liquid interface and the total area of solid-liquid and liquid-air interface of the projected area, respectively. In addition, by the inclusion of the roughness factor of the wetted surface area, r_f, the Cassie-Baxter equation will be modified to this equation (Eq. 1-4) [53, 54]:

$$\cos\theta_{CB} = r_f f_s \cos\theta + f_s - 1 \qquad 1-4$$

where f_s=1 and r_f=r, the Cassie-Baxter equation converts to the Wenzel equation. The superhydrophobic surfaces have recently attracted great attention due to their unique water-repellency and anti-contamination properties. According to the Cassie-Baxter model, an increase in surface roughness leads to an increase in the amount of air trapped in the grooves. Consequently f_s decreases and the contact angle increases [14]. These theories explain the impact of surface roughness on the static contact angle and how the hydrophobicity and hydrophilicity may be enhanced. Due to the great mobility of droplets on surfaces having an ultra-high roughness, the dynamic of the droplet on the surface must be taken into consideration [41, 55].

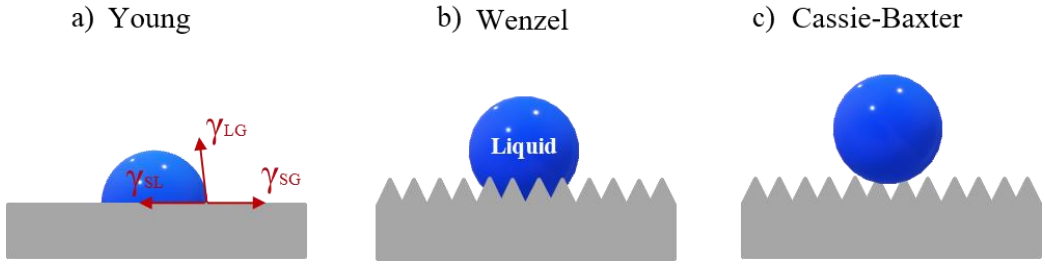

Figure 1-2. A liquid droplet on different surfaces: (a) Young's model; (b) Wenzel's model; (c) the Cassie-Baxter model.

The ability of a surface to shed water is defined as dynamic hydrophobicity. The molecular interactions between the liquid and the solid surface or irregularities, such as roughness or heterogeneities, can lead to hysteresis [14, 56-58]. The SA and CAH values are the representations of the dynamic contact angle. SA is defined as the critical angle at which a water droplet of a certain weight begins a downward slide. CAH can be measured based on different methods. According to the needle approach, CAH represents the difference between the contact angle at the front and rear of water droplet, known as advancing and receding WCA, just before the droplet starts moving on the surface. Surfaces of the Wenzel model demonstrate high static and

advancing contact angles but low receding contact angles. This leads to the high hysteresis and stiction of the water droplets to the surface. Highly mobile drops having a high contact angle and low hysteresis on superhydrophobic surfaces are in accordance with the Cassie-Baxter state [55, 59].

1.3 Fabrication of superhydrophobic surfaces

Geometric factor and surface chemistry are two principle requirements that should be satisfied to develop superhydrophobic surfaces. Creation of micro and/or nanostructured roughness on the intended surface could cause the surface wetting properties to become more pronounced, i.e., hydrophilic surface becomes superhydrophilic and hydrophobic one turns to superhydrophobic. As a result, having a low-surface energy hydrophobic material is another vital prerequisite to realize superhydrophobic surfaces. Given the inherent low surface energy of most polymeric materials as well as their decent workability, considerable number of studies have concentrated on using polymers such as silicones or fluorocarbons as the base materials for producing superhydrophobic surfaces [13, 60].

In addition to chemical aspects of superhydrophobic surfaces based on using either hydrophobic materials or coating the surface with low surface energy hydrophobic layer, there are various methods employed to generate roughness on the surfaces for developing superhydrophobic materials. According to the direction toward which the structures are formed, these methods mostly fall into three categories: top-down, bottom-up, and their combination. To have a better understanding of these two inseparable criteria, i.e., possessing hydrophobic materials and producing surface structures, for making water-repellent superhydrophobic surfaces, a brief overview is presented in the following sections concerning the chemical and physical aspects (Figure 1-3).

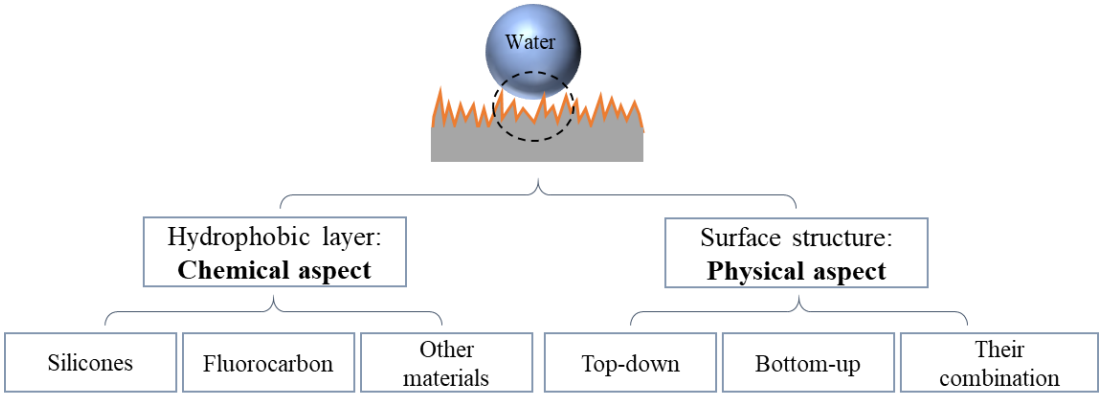

Figure 1-3. Schematic of two essential criteria for fabrication of superhydrophobic surfaces.

1.3.1 Chemical aspect

1.3.1.1 Silicones

Silicone rubber is one of the commonly used silicone materials in the preparation of superhydrophobic surfaces. During the last few decades, silicone rubber has found its way into the real-world applications such as automotive industry, aerospace, cookware, electronics industry, etc. They are mixed inorganic–organic polymers which comprise highly stable alternating silicon and oxygen atoms, called siloxane, that form the backbone of silicone rubber. The organic groups, including methyl, ethyl and phenyl, bound to the silicon atoms are the side chains [61]. The siloxane groups constituting the backbone are responsible for silicone rubber unique properties in terms of thermal stability, abrasion resistance, UV resistance and low electrical conductivity [8]. Owing to its ease of fabrication as well as excellent physical and chemical properties, good biocompatibility, and low cost, polydimethylsiloxane (PDMS) consisted of non-polar methyl groups as the side chains is the most common and commercially available silicone-based polymer [61, 62]. There are four structural characteristics related to the surface properties of PDMS including low intermolecular force between methyl groups, the specific flexibility and high strength of the siloxane backbone, and the partial ionic nature of the siloxane bond [63].

In order for the silicone rubber materials to vigorously resist mechanical stresses, they require vulcanization process to improve the mechanical, physical, and chemical properties. During vulcanization, chemical reactions among the unsaturated silicone rubber side chains lead to the creation of a three-dimensional network containing numerous inter-molecular chemical bonds so-called “crosslinks” [64]. The crosslinking density is defined as the number of crosslinked points per unit volume, expressed in $mol \cdot cm^{-3}$ [65]. Regarding the type of silicone rubber materials i.e. RTV-SR, HTV-SR, and liquid silicone rubber, there are three different crosslinking reactions including addition, peroxide, and condensation curing. Peroxide curing, used for HTV-SR materials, initiates with free-radical formation via heating or radiation. The resulting free radicals induce hydrogen abstraction of side chains of silicone rubber followed by creation of free radicals on it. The coupling reaction between two radicals allow the chains to form carbon-carbon crosslinks with one another [66, 67].

Apart from its outstanding physical and chemical properties, the “hydrophobic recovery” ability of silicone rubber makes it a promising alternative for superhydrophobic materials. When silicone-based materials are in service, their initial hydrophobicity can be lost over time due to some circumstances such as their

covering by hydrophilic contaminations, or partial electrical discharge. However, this induced surface hydrophilicity of silicone rubber is temporary. The process of repetitive repossession of hydrophobic properties which arises during time is called hydrophobic recovery. The storage conditions, whether in air or in liquid, temperature or subsequent adsorption of a surfactant may affect the hydrophobic recovery [68]. Considering the nature of the newly formed hydrophilic surface, different mechanisms can be responsible for hydrophobic recovery including, migration of uncrosslinked low molecular weight siloxane (LMWS) chains from the bulk to the surface, thermodynamically favorable reorientation of polar groups from the surface to the bulk phase or nonpolar groups from the bulk to the surface, and condensation of the surface hydroxyl groups [69, 70].

Various methods have been employed to create roughness on the silicone rubber materials. Gao et al. [71] developed a superhydrophobic silicone rubber using carbon tetrafluoride (CF_4) radio frequency capacitively coupled plasma. The hydrophobicity enhancement is resulted from simultaneous surface etching and fluorination. Artus et al. [72] fabricated flexible silicone nanofilaments having lengths of up to several micrometers and diameters of up to 150 nm by a chemical vapor deposition method. A dense and entangled arrangement of these nanofilaments on various substrate materials produced a transparent superhydrophobic coating. Ma et al. [73] produced block copolymer polystyrene (PS)-b-PDMS electrospun fibers with diameters in the range of 150-400 nm. A superhydrophobic membrane was achieved due to the presence of low surface energy PDMS materials and surface roughness of the electrospun fibers with submicron diameters. Using a subsequent procedure of UV-curing and solvent evaporation, Li et al. [74] produced a flexible bulk superhydrophobic PDMS/silica film. The robustness and regenerative characteristics of hierarchical structure of the produced superhydrophobic film are stemmed from the concurrent presence of silica particles and porous structure throughout the whole film.

1.3.1.2 Fluorocarbon

Fluorocarbons are another well-established materials used in a variety of applications specifically for superhydrophobic surfaces due to their many desirable properties including hydrophobicity, oil-repellency (oleophobicity), low surface energy, biofouling, and high resistance to chemical and oxidative degradation [75-77]. The superb properties of fluorocarbons arise from the unique characteristics of the fluorine atom. The high bonding energy along with the highly dispersive intermolecular force of the C-F bonds are responsible for the excellent properties of fluorocarbons [78]. Moreover, the excellent corrosion resistance and barrier properties

against organic solvents of the fluorocarbons make them a favorable alternative for gaskets, vessel liners, coated cookware and fabrics [79]. One of the well-known synthesized fluoropolymers is PTFE, commonly known as Teflon, which is widely used in the fabrication of superhydrophobic surfaces.

By extending a Teflon film to ~190%, the WCA increased from 118° to 165° due to the fibrous crystals and the large fraction of void spaces between them [80]. Toosi et al. [81] developed a superhydrophobic PTFE surface using femtosecond laser irradiation process. Among diverse micro-nanostructured morphologies including uniaxial and biaxial patterns, the biaxial scanned surfaces demonstrated a high WCA of 170° and a low CAH of 3°. Yong et al. [82] developed a superhydrophobic PTFE film with good chemical stability in various harsh environments, using femtosecond laser treatment.. A subsequent mechanical drilling process led to the formation of the penetrating microhole arrays so the produced sample could be used for oil/water separation application. A flexible superhydrophobic Teflon surface was obtained by a subsequent two-step procedure involving firstly, the formation of nanocone array using the oxygen plasma etching of the colloidal monolayer of PS beads, and secondly, modifying the nanocones by a gold nanoparticle film. The produced surface exhibited great water-repellent and self-cleaning properties [83]. However, the potential toxicity to humans of by-products from the breakdown of fluorinated compounds and environmental concerns have severely restricted the use of Teflon and other fluorocarbons [84, 85].

1.3.1.3 Other organic and inorganic materials

There are various organic and inorganic materials used for the fabrication of superhydrophobic surfaces. Hydrocarbons, polyvinyl chloride (PVC), polymethylmethacrylate (PMMA), poly(lactic acid) (PLA), and PS are some examples of organic polymer matrixes used as coatings or substrates to create superhydrophobic surfaces [86-89]. Liu et al. [90] developed a mechanochemically robust superhydrophobic low density polyethylene (LDPE) film by coating silicone nanofilaments on a plasma activated LDPE surface. The self-cleaning and water-repellent properties of the film were retained even after oil contamination. By the addition of 33 wt.% surface modified silica nanoparticles to various matrixes, i.e., polyethylene (PE), PVC and PMMA, Gao et al. [91] developed a facile approach to fabricate superhydrophobic coatings applicable to coat diverse substrates. Through a 3D printing, a superhydrophobic PLA packing was produced to be used as an oil/water separator. Superhydrophobicity was attained via a low-cost and bioinspired modification techniques of selective solvent etching and nanoparticle decoration. By adjusting the internal geometry of packing, a

separation efficiency of 95% was obtained at a relatively high but persistent flux of oil/water emulsion [92]. Lv et al. [89] produced a superhydrophobic nanofibrous membrane out of polycaprolactone (PCL)/PS composite for oil/water separation. The hydrophobicity and oil absorption capacity of the composite membrane were higher than PCL and PS solely.

Numerous studies have been conducted on the significant role of inorganic particles such as silicone oxide (SiO_2), titanium oxide (TiO_2), zinc oxide (ZnO), calcium carbonate ($CaCO_3$) and alumina (Al_2O_3) on superhydrophobic surfaces [93-97]. The presence of these particles can not only impart multiple characteristics to the coatings but induce roughness on the surface. For instance, in the light of photocatalytic activity of TiO_2 and ZnO particles, some superhydrophobic coatings were produced which showed reversible switchable wettability. In other words, under UV illumination, a sharp wettability conversion of TiO_2- or ZnO-based coatings from superhydrophobicity to superhydrophilicity was observed [97, 98]. Moreover, the antibacterial activity of both of these particles makes them the promising alternatives for medical applications [99, 100]. The Al_2O_3, SiO_2 and TiO_2 particles can enhance the electrical conductivity of the superhydrophobic polymer coatings [101].

1.3.2 Physical aspect

1.3.2.1 Top-down approaches

As a basic term in microelectronics, top-down methods are related to the removing materials from the surface by carving, molding, or machining bulk materials with tools and lasers. Based on top-down methods, many studies have been devoted to produce favorable roughness directly on the intended materials including etching, templating, micromachining, and lithographic approaches (Figure 1-4 (a)) [41]. Thus, since the final surface roughness is created out of bulk material, they have less interfacial adhesion issues than bottom-up approaches [102]. Etching and templating are two most common top-down approaches (Figure 1-4 (b and c)). Etching processes refer to removing materials from the surface following a reaction mechanism [21]. Templating mainly involves three consecutive steps of template making, a molding step where replication occurs, and a demolding step [103]. In micromachining technique, both ordered and non-ordered structures can be produced on the substrate using various sources such as laser, electrical-discharge machining (EDM) and LIGA (German acronym for Lithographie, Galvanoformung und Abformung) [104]. Lithography as a common

method used for making regular and well-defined structures involves using various source of lights to irradiate via a mask onto the photoresist-coated substrates [105].

Etching is one of the well-established conventional top-down methods in terms of simplicity, cost-effectiveness, ease of operation as well as scalability. The two major types of etching are wet chemical etching and dry etching (e.g., plasma treatment). In wet chemical etching process, various liquid chemicals or etchants are utilized to selectively remove some part of the immersed material [106]. For instance, dislocations or impurities on metal substrates can be etched by acidic or alkaline solutions to induce roughness on the surface. Although, wet chemical etching process has some advantages, e.g., simple equipment, high etching rate and good selectivity, there are many drawbacks including tends to be isotropic etching, non-environmentally friendly, needs for large amounts of chemical etchant to completely cover the substrate material, as well as continual replacement of chemical etchants to keep the same initial etching rate [107]. However, in dry etching, reactive plasma radicals or etchant gasses selectively remove the substrate material. Plasma based dry etching, has a broad range of application in the medical, food and industrial field due to its simplicity, environmentally friendly process, and good process control. It usually gives an anisotropic etch profiles as well. Furthermore, plasma treatment is a decent way to create roughness on the surface without affecting the desired bulk properties of materials [108]. Since the plasma treatment is of special interest in the present Ph.D. thesis, a detailed literature review is given in the subsequent sections.

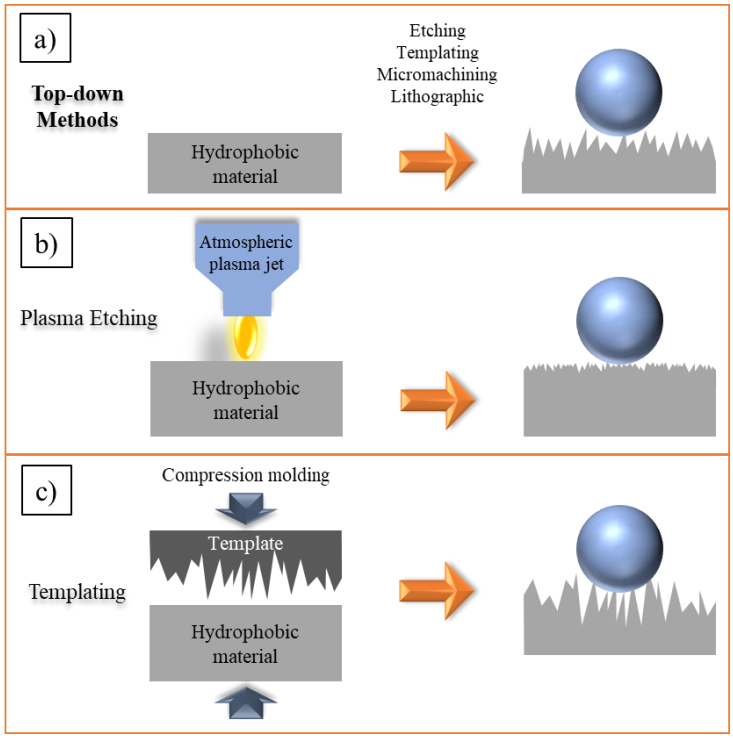

Figure 1-4. Schematic illustration of a) concept of top-down methods; and two common approaches including b) plasma etching, and c) templating.

1.3.2.2 Bottom-up approaches

On the contrary, bottom-up methods are based on developing greater and more complicated objects by integration of smaller pieces [41, 109]. Chemical deposition, sol-gel, spray coating and spin coating are some examples of bottom-up approaches by which superhydrophobic layer containing multiple components are deposited on the substrate (Figure 1-5 (a)) [110-112]. Chemical deposition is a general term for spontaneous self-assembling and deposition of components on a substrate via chemical reaction which divided into three categories of chemical bath deposition, chemical vapor deposition and electrochemical deposition [41, 113]. Sol-gel method involves the preparation of sol using hydrolysis of the corresponding oxide within a solvent followed by network formation process called gel formation. A solvent-rich, three-dimensional gel network arises from condensation and inorganic polymerization process [114]. Spray, spin, and dip coating can be considered as the physical deposition methods where multiscale structures are created on the surface through simple yet scalable approach [105]. For instance, Li et al. [115] developed a durable epoxy/PDMS/SiO_2 superhydrophobic coatings (Figure 1-5 (b)). They developed superhydrophobic coatings on various substrates including glass, copper foam and filter paper possessing relatively good mechanical durability. As shown in

Figure 1-5 (c1-c6)), regardless of the type of surface, the microstructures formed on the surface led to WCA>150° and superhydrophobicity.

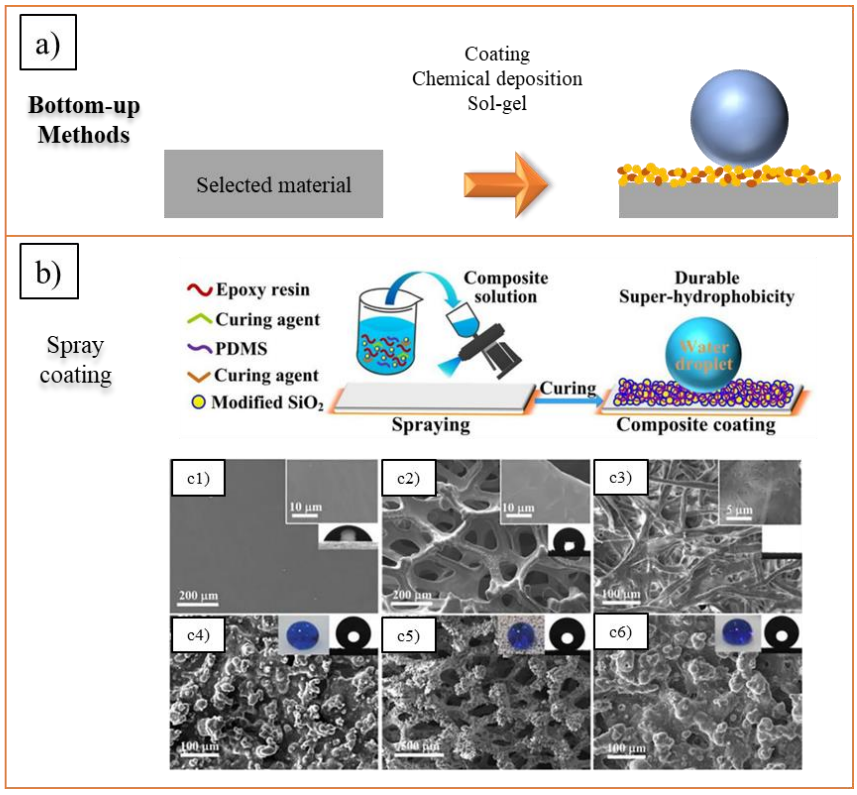

Figure 1-5. a) Schematic of concept of bottom-up approaches; b) schematic illustration of spray coating of a durable superhydrophobic epoxy/PDMS/SiO_2 composite coating, c1-c3) SEM images of pristine glass, copper foam, and filter paper, c4-c6) SEM images of the corresponding coated surfaces [115].

Since bottom-up methods are generally substrate independent, they are more applicable in the fabrication of superhydrophobic surfaces yet might suffer from low mechanical durability and interfacial adhesion of upper layer to the substrate [116, 117]. Some studies, addressing the weak interfacial adhesion, delamination or wearing out of the superhydrophobic coatings, developed some strategies to enhance their mechanical stability such as grafting, crosslinking, and self-healing methods [118-120].

All these methods are concentrated on the fabrication of superhydrophobic coatings on the substrate materials where robustness especially mechanical durability as well as limited thickness of the coatings are still a concern. One of the new concepts in the development of superhydrophobic materials having permanent superhydrophobic properties is the creation of low-surface-energy micro-nanostructures extending through the whole volume of the hydrophobic material. The superhydrophobic materials named volumetric superhydrophobic nanocomposite can be considered as a novel bottom-up approach in which the incorporation

of micro and nanoparticles within hydrophobic matrixes offers a three-dimensional continuous superhydrophobicity. Later, a brief discussion of this approach is presented.

1.3.2.3 Combination of top-down and bottom-up approaches

There are some methods by which the hierarchical multiscale surface roughness was created with the combination of both top-down and bottom-up approaches. Generally, these methods comprise a two-step procedure of producing rough structures on the surface using top-down methods with subsequent formation of soft structures based on bottom-up approaches. For example, there is a hybrid plasma system consisting of an etching step (top-down approach) and a polymer deposition step (bottom-up approach) consecutively [121].

1.4 Plasma treatment

From the physical point of view, plasma is a partially ionized gas consisting of a mixture of ions (positive and negative), free electrons, and neutral species. It is mainly considered as the fourth state of matter, the other three are gas, liquid and solid. By applying a considerable amount of electrical energy to a gas stream, the atoms and molecules of gas are ionized and transformed into the high-speed stream of glow discharge, so-called plasma, which is being shot at a sample in pulses. In order to generate plasma, the gas breakdown voltage must be surmounted by applied electrical energy which relies on the electrode spacing and the pressure [122]. Plasma systems can be categorized in diverse ways presented as follows [123].

- Based on applied pressure inside the plasma chamber: low-pressure and atmospheric-pressure plasma.
- Based on the temperature of plasma gas (including electrons and ions) and degree of ionization: hot and cold plasma.
- Based on the excitation frequency: direct current (DC) and alternating current (AC), radio frequency, and microwave plasma.
- Based on the electron affinity of plasma gases: electropositive and electronegative plasma gas.

In the following, we elucidated the first category. Low-pressure plasmas have wide range of applications in fabrication of superhydrophobic surfaces, materials processing, manufacturing semiconductor devices as well as surface finishing of medical implants, sterilization and production of antibacterial surfaces [124, 125]. Due to the low plasma gas temperature (below 150 °C) during this procedure, this is a beneficial method for the thermally sensitive substrates [122]. On the other hand, the existing ions in the plasma stream can be

accelerated toward a substrate in an intended direction. This accelerated plasma stream leads to directional etching of submicron features. In addition, an even glow discharge distribution can be created over large substrate areas causing the uniform surface treatment at the same etching rate (Figure 1-6 (a1 and a2)) [126]. However, operating the plasma at reduced pressure has several drawbacks. Vacuum systems are expensive and have high maintenance cost, and some unforeseen accidents in these systems may lead to an economical and safety issues as well. Furthermore, as it is a batch process, the size of the object that need to be treated is confined by the size of the vacuum chamber [122]. The atmospheric-pressure plasma overcomes the disadvantages of vacuum operation due to its continuous treatment, lower energy consumption, shorter processing times, lack of need for vacuum equipment, as well as cost-effectiveness. Moreover, the simplicity of incorporating the atmospheric-pressure plasma system with the available production lines can be considered as an essential advantage of this approach compared to the low-pressure plasma treatment [127, 128].

Transferred arcs, plasma torches, corona discharges, and dielectric barrier discharges are the common sources of atmospheric-pressure plasma systems. The temperature of electron and reactive neutrals higher than 3000 °C, as well as density of charge species in the range of 10^{16}–10^{19} cm^{-3} is obtained in arcs and torches [122]. These plasmas are mainly applied in metallurgy because of the high plasma gas temperature. Lower temperature (50–400 °C) of weakly ionized gas along with less density of charged species is the main characteristic of corona and dielectric barrier discharges. Due to the non-uniformity of these discharges, their use in materials processing is limited. An atmospheric-pressure plasma jet is an effective process which exhibits many characteristics of a conventional low-pressure plasma including, approximately low plasma gas temperature, charged species density between 10^{11}–10^{12} cm^{-3}, and high concentration of reactive species (10-100 ppm) (Figure 1-6 (b1 and b2)) [122, 129].

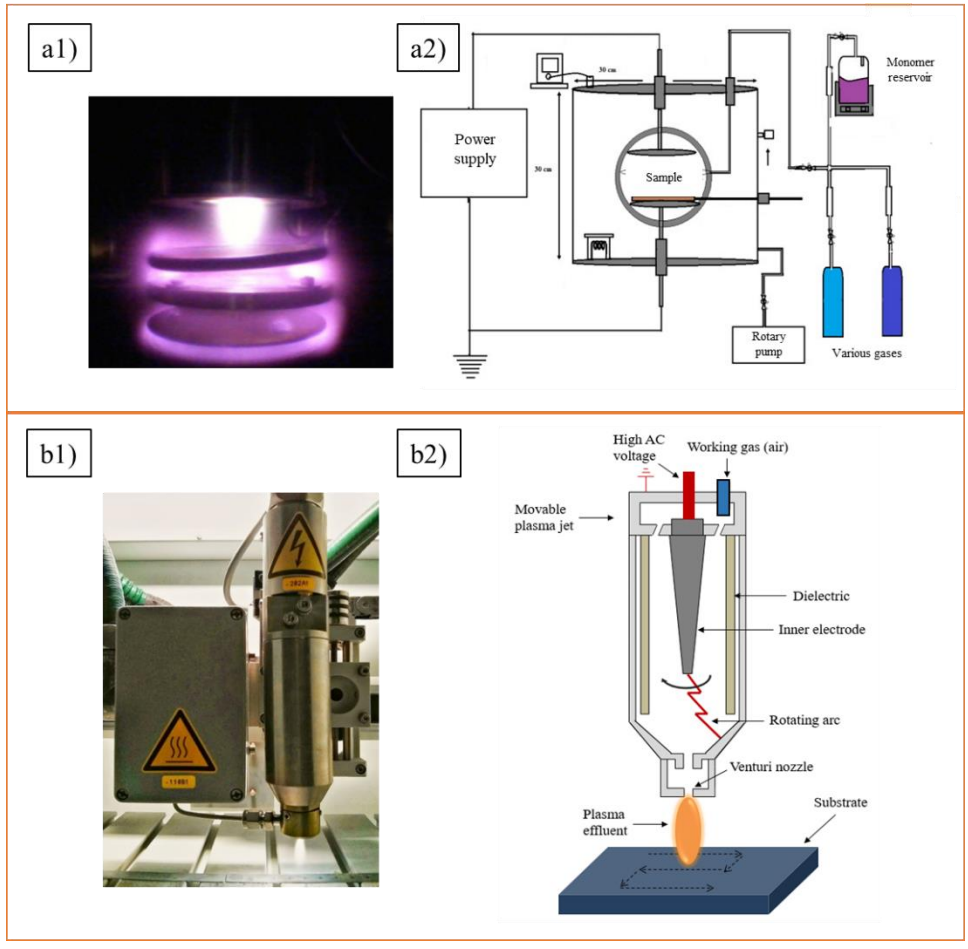

Figure 1-6. a1) An image of even distribution of glow discharge within low-pressure plasma treatment, a2) schematic of corresponding plasma system [130]; b1) an image of atmospheric-pressure plasma jet, b2) schematic of the corresponding plasma jet [21].

In addition to the surface roughness, plasma treatment may influence the surface chemical composition which can be controlled by various plasma parameters. Several studies have investigated the effect of plasma parameters on surface properties; however, it should be noted that these variables are sometimes specific to the system characteristics, and therefore they cannot be generally applied to all plasma systems. In the current Ph.D. study, atmospheric-pressure plasma treatment is of specific interest because of its relative simplicity, low cost, high speed, easy implementation and industrial applicability. Plasma generation power, treatment time, distance from nuzzle to the substrate, cycle time, gas flow rate as well as the type of plasma gas are the effective parameters in atmospheric-pressure plasma jet. Throughout the following sections, the effect of some of these factors on surface roughness and chemical composition of the plasma-treated surfaces is presented.

1.4.1 The effect of plasma treatment on surface roughness

One of the common applications of plasma system is to generate micro-nanostructures on the surface. This approach is called plasma etching. Surface treatment by plasma system always involves plasma etching alterable by the plasma parameters and substrate materials. In plasma etching, the generated reactive atoms or ions (such as oxygen, chlorine, fluorine) in the gas discharge are responsible for the dry etching. The anisotropic etching of the materials can be a result of plasma treatment [41].

Numerous studies have assessed the impact of atmospheric-pressure plasma treatment on surface roughness of polymers some of which have worked on surface roughness considering plasma parameters [14, 129, 131]. It has been shown that by controlling diverse plasma parameters, surface topography can be adjusted to a significant degree. In addition to the direct effect of these parameters, there is an indirect effect which arises from interaction among the parameters that influences the results. Therefore, in order to control the final surface roughness affecting the wetting properties, these parameters and their interactions should be carefully monitored and adjusted. In this section, we concentrated on correlation between different parameters of atmospheric-pressure plasma system and surface roughness.

One of the most important factors in plasma treatment is plasma power. Low plasma power merely activates the surface, and therefore becomes ineffective in plasma etching [14]. Increasing the plasma power directly enhances the ionization of etching gases, excitation and the degree of dissociation of gas molecules [61, 132]. Consequently, high power usually enhances the amounts of erosion which will subsequently lead to the higher roughness [131, 133]. The great etching rate of PDMS under sulfur hexafluoride (SF_6) plasma gas was achieved at high plasma power and caused the formation of PDMS microstructures possessing good anisotropy (Figure 1-7 (a)) [134]. During air plasma treatment, the width and height of the bumps formed on the surface of polypropylene (PP) increased by increasing the plasma power due to the local modifications of the surface crystalline level (Figure 1-7 (b1 and b2)). The high discharge heating led to the formation of hot spot on the surface and melting the polymer at the point. Subsequently, the polymer became more amorphous and local surface crystalline level would get modified [135]. It was shown that the root-mean-square (RMS) roughness values of LDPE treated by argon plasma gas slightly increased as a function of applied power ranging from 3 to 11 W. The higher the plasma power, the broader the peaks and depths will be [136]. Indeed, increasing the plasma power should be controlled in order to have appropriate surface roughness and uniformity

at the same time. Uncontrolled increase of plasma power could lead to adverse results. Yasuda et al. [137] showed that the surface would be over-etched by oxygen radicals at highest plasma power and surface uniformity would be deteriorated by area of non-active particles. Moreover, exceed plasma gas temperature damaged the surface during treatment.

Treatment time can also significantly affect the etching of the substrate. In the system used in the present study, treatment time is expressed as the plasma jet speed and number of passes [21]. Faster jet speed and smaller number of passes illustrates shorter treatment time, and vice versa. Since the etching of the polymer surface depends on the degree of crystallinity of the polymer, the PMMA substrate etched homogeneously through a short time air plasma treatment and led to smoother surface roughness. However, in longer treatment time, the RMS roughness was up to two times higher than that of untreated surfaces which could be elucidated by thermal damage caused by overheating of the sample during treatment [138, 139]. In another research, the gradual increase of surface roughness was observed corresponding to higher plasma treatment time. After 32 s plasma treatment, the RMS roughness became more than 6 times greater than untreated substrate which was related to the appearance of bumps on the treated surface [140]. It was demonstrated that the roughness increased at low jet speed. As shown in Figure 1-7 (c1-c4), increasing the treatment time resulted in higher RMS roughness of poly(ethylene terephthalate) (PET) related to crystalline character of biaxially oriented chains. As the etching rate of crystalline parts is lower than that of amorphous parts, the roughness differed with respect to the plasma treatment time [138]. On the other hand, at considerably increased treatment time, the plasma-formed features became smaller, more pronounced, more contorted and closer together, and no change in roughness was observed [141, 142]. It can be concluded that there is an optimum plasma treatment time to get higher surface roughness.

The type of plasma gas and its flow rate are also of great importance in plasma treatment. Specific plasma particles can react with certain atoms or phases on the substrate and produced reaction gaseous compounds are ejected off the surface. Atmospheric-pressure plasma treatment has good selectivity. For example, O_2/He plasma gas etches Kapton and organic materials, where oxygen reacts with carbon and hydrogen and produces gaseous carbon dioxide, carbon monoxide and water [143-145]. However, a CF_4/He plasma gas can etch inorganic materials like SiO_2 and Tungsten [143].

There are different gases used for plasma etching, such as air, O_2, N_2, Ar, He, CF_4, SF_6, etc. Ion-surface collisions are the predominant factor of N_2 plasma etching of PMMA surfaces which is due to non-reactivity of nitrogen gas in plasma etching. Higher surface roughness with lower etching rate was achieved after N_2 plasma treatment [138]. Due to the high reactivity of O_2, higher etching rate and lower surface roughness was achieved in comparison to plasma generated in other gases as N_2, air, Ar, H_2 and ammonia (NH_3) [138, 146]. However, a conflicting result was attained by Rezaei et al [131]. They stated that the surface roughness of He/O_2 plasma treatment resulted in higher topographical changes of PET films in comparison to He/N_2 plasma. The morphology of the air-plasma treated PET surface displayed peaky structures with up to two times higher surface roughness compared to Ar/O_2 plasma-treated PET [138].

Carbone et al. [147] investigated the surface modification of PTFE by an Ar and Ar/O_2 plasma created with an atmospheric-pressure radio frequency system. It was claimed that by the addition of oxygen to the Ar plasma gas, the formation of volatile species was increased leading to the roughening of the surface and increasing the hydrophobicity of the PTFE up to 130°. Wang et al. [148] compared the surface treatment of PMMA using Ar and He. In comparison to Ar, using He as a plasma gas resulted in the formation of smaller spikes and consequently higher surface roughness was achieved (Figure 1-7 (d1-d3)). In terms of argon plasma-treated PDMS surface, the bond breaking, reorganization of the chemical groups and possibly chain scission of the PDMS backbones on the surface could be responsible for enhancing the surface roughness [149]. In another research, the argon bombardment during treatment induced augmentation of the crosslinking characteristic of poly(ether)sulfone. As a consequence, the number of high and deep points on the surface decreased and a smoother surface with lower surface roughness was attained [150]. The surface roughness of the Ar/CF_4 plasma treated PMMA substrate was improved from 4.63 nm to 11.8 nm because of the formation of hill-like granules on the surface [151].

In order to enhance the hydrophobic property of the material, the fluorine-based gases such as CF_4 and SF_6 are mainly used. Furthermore, as the constituent C-F bond of the fluorinated gases can be easily activated in the plasma, the high concentration of reactive radicals is simply attained leads to the creation of hydrophobic particulates in the gas phase. The arrangement of these particulates on the intended surface can enhance the final hydrophobicity. While it is worth mentioning that the plasma-generated fluorine radicals and ions are highly toxic and corrosive, and the adhesion of fluorinated particulates to the substrate is weak [152].

The other essential factor is the distance from the nuzzle to the substrate. Temperature or composition of plasma stream as the representatives of its physical and chemical characteristics can vary significantly with the distance between plasma nuzzle and the substrate. Therefore changing the distance will subsequently alter the surface properties [127]. Kewitz et al. [153] reported that the energy influx decreased with the square of the distance. The energy flux of the plasma streams varied more at shorter distances for different gas flows.

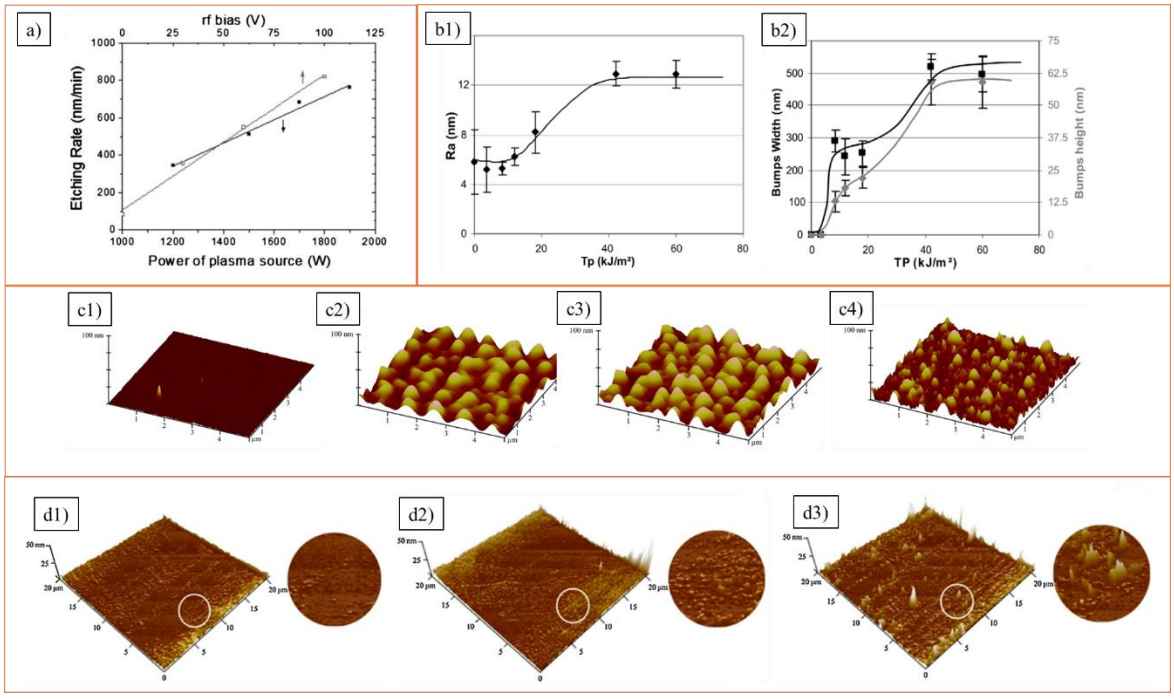

Figure 1-7. a) Dependence of etching rate of PDMS on plasma power and bias reference voltage [134]; b1 and b2) the changes in arithmetic mean surface roughness (R_a) , bumps width and height as a function of plasma power [135]; AFM scans of c1) untreated PET surface, plasma-treated surfaces for c2) 1 s, c3) 3 s and c4) 5 s [154]; AFM scans of d1) untreated PMMA films, d2) Ar plasma-treated after 90 s, and d3) He plasma-treated after 90 s [148].

1.4.2 The effect of plasma treatment on surface chemical composition

As it was mentioned that during plasma treatment, the surface modification and etching of the substrate are inevitable and parallel, and both of which may have an impact on the final surface wettability. The collision of high-energy particles of the plasma discharge with the substrate surface may lead to the breakage of some chemical bonds and formation of new ones all of which could alter the chemical composition of the substrate compared to untreated sample. Little et al. [155] claimed that higher wettability of PCL after treatment by an atmospheric-pressure glow discharge plasma is proportional to the formation of surface roughness (55-60%) and surface functionalization (40-45%). During air-plasma treatment, surface oxidation of PP was confirmed

using x-ray photoelectron spectroscopy (XPS) analysis. The addition of oxygen to the surface during treatment as well as post-treatment reaction of the formed active radicals on the surface with oxygen from air could oxidize the PP surface. Small amounts of nitrogen were also detected on the treated surfaces [156]. Given the plasma gas used for treatment of PET surfaces, the wettability and free energy of the treated surfaces were in the following order: N_2 > air > Ar gases [157]. The same overall trend of strong oxidation without any evidence of nitrogen was found on the air or N_2 plasma-treated PMMA. The scission of C-C and/or C-H bonds with further reaction with oxygen present in the surrounding air led to the higher concentration of oxygen containing bonds (C-O and C=O) [138]. The surface tension of PE was improved after air and nitrogen plasma treatment due to the incorporation of hydrophilic functional groups containing oxygen and nitrogen onto the PE surface (Table 1-1) [158].

Table 1-1: Surface and wettability properties of PE before and after plasma treatment with air and nitrogen [158].

Treatment	**RMS roughness (nm)**	**XPS**		**Surface tension ($mN.m^{-1}$)**	**Water contact angle (°)**
		O (at.%)	N (at.%)		
Reference	9.1	3.0	<0.1	30.2	93.3
Air plasma	14.3	21.4	3.3	67.5	21.6
Nitrogen plasma	11	16.9	5.4	55.3	41.0

Juárez-Moreno et al. [149] investigated the surface chemical composition of PDMS using O_2, Ar and N_2 plasmas. By increasing power and treatment time, hydroxyl groups appeared on the surface of O_2 plasma-treated surfaces. On the other hand, instead of amine group, some silynitrile groups were found on the PDMS surface after N_2 plasma treatment. During plasma treatment with inert gases like Ar, an etching process and hydrogen abstraction are expected yielding free radicals at or near the surface. However, it is not expected to add new chemical functionalities from the gas phase yet two free radicals can either recombine or produce unsaturations, branches or crosslinks [159]. The higher O/C atomic ratio of surface treated LDPE by Ar plasma jet than pristine surface can be attributed to the operation in ambient air and admixture of air in the plasma effluent. It can be the main reason of higher surface wettability of plasma-modified LDPE [160].

1.4.3 Superhydrophobic surfaces using plasma treatment

As mentioned before, the generation of surface roughness along with chemical modification can enhance the hydrophobic characteristics of treated surfaces. It is worth to mention that plasma system can be used not only as an etching system but also to apply low surface energy materials on the surface. The majority of plasma-based superhydrophobic surfaces can be divided into three main approaches: (1) roughening hydrophobic materials, (2) surface etching with subsequent deposition of hydrophobic coatings, and (3) making decent hydrophobic structural features in one-step of the deposition or growing coating layers [152].

In order to generate superhydrophobic surfaces based on the first category, plasma etching as a stand-alone treatment can be applied to develop roughness on various low-surface energy materials, especially PTFE. Barshilia et al. [161] created superhydrophobic PTFE surfaces with leaf-like micro-protrusions by means of Ar/O_2 low-pressure plasma treatment. After 4 h treatment, the highest value of the WCA ~158° was achieved at the maximum average surface roughness value. The superhydrophobic PTFE surfaces were generated by almost the same plasma procedure exhibited the maximum WCA of 178.9°, with a SA less than 1°. The aging resistance of the plasma-treated surfaces in ambient condition was confirmed after prolonged exposure to air for 80 days. Good water-repellency with stable WCA was observed even after the repetitive water droplet impact experiments [162].

In addition to the plasma etching technique on low surface energy materials, there is a surface chemical modification method, called functionalization, by which surface etching and modification is accomplished simultaneously [163]. CF_4 is the most common gas used for etching and fluorination of the surface. In this case, fluorinated groups deposited on the substrate are covalently bonded to the surface which can further decrease the surface energy. Samples etched with CF_4 plasma gas exhibit a significant amount of fluorocarbon groups along with high roughness [164, 165]. Yang et al. [166] fabricated a superhydrophobic polyvinylidene fluoride (PVDF) flat sheet membrane via CF_4 plasma surface modification. It was observed that 30% water flux enhancement on the superhydrophobic membranes (WCA of 162.41°) compared to the pristine PVDF membrane. Gao et al. [167] investigated the surface treatment of silicone rubber samples using CF_4 low-pressure plasma treatment. Concurrent increment of surface roughness by the ablation reaction of CF_4 plasma and formation of $[–SiF_x(CH_3)_{2-x}–O–]_n$ (x=1, 2) structure produced by the direct attachment of F atoms to Si are the main reasons of fabrication of superhydrophobic surfaces. CF_x nano-particulates-based superhydrophobic

coating was created using CF_4, H_2 and He plasma treatment. A superhydrophobic coating with aspect ratio lower than 0.2 and average roughness of 10 nm was attained [168].

Under atmospheric-pressure condition, plasma polymerization process has been widely used by which superhydrophobic surfaces are made using deposition of hydrophobic coatings on micro-nanostructured substrates by precursor in gas phase. Technically, it is different from functionalization according to the fact that it involves coating the surface instead of covalently binding plasma species to the surface [169]. Most of these studies are composed of two separate steps, plasma etching and deposition of a hydrophobic layer [170-172]. However, single-step plasma deposition and polymerization processes are more appealing in practical application point of view which are placed in the third category. To apply a superhydrophobic coating, e.g. fluorocarbons and organosilicons, on a flat substrate, the hydrophobic micro and/or nano-scale surface roughness should be generated during one-step plasma treatment [173]. Due to the corrosivity and high toxicity of created fluorine radicals and ions during plasma treatment, the benign hydrocarbon precursor gases are a safer alternative for atmospheric-pressure plasma conditions. The superhydrophobic silicone substrate covered with nano-roughened hydrocarbon coating was achieved using benzene as the main precursor along with C6 hydrocarbons as a reactive gas in helium plasma. It was stated that no pre-roughening of the substrate was accomplished [152]. However, the benzene-based coatings were very powdery and the particle adhesion to the substrate was weak. Marchand et al. [173] developed a more durable superhydrophobic film using an organosilane precursor. The organic-inorganic hybrid precursor of tetramethylsilane (TMS) was chosen due to its stability, volatility and relatively low health hazardous. The dissociation of TMS in the atmospheric plasma led to the formation of the mild fusing/agglomeration of particulates through gas-phase condensation reactions. Fused particles behave more as a continuous layer compared to a powder coating and resulted in a more durable coating. In another research, the atmospheric-pressure plasma jet was used to form the hexamethyldisilazane (HMDSN) plasma polymerized nano-film on a silicon wafer. The superhydrophobic surface exhibited the organosilicon sphere stacking structure [174].

Forasmuch as coatings have low durability and wear out more readily, creation of roughness on the hydrophobic silicone rubber using one-step plasma treatment is the main purpose of this project. To the best of our knowledge, most of the research that has been surveyed the roughening hydrophobic materials, has been performed using low-pressure plasma system. Air atmospheric-pressure plasma treatment is considered as the

basic system of this project which is more useful than low-pressure system from practical and industrial point of view.

1.5 Superhydrophobic nanocomposite

As it was mentioned earlier, various types of micro and nanoparticles are utilized in fabrication of superhydrophobic nanocomposite coatings to not only induce sufficient roughness on the substrate but improve specific properties regarding the final application of the coating. There are various factors used to describe the particle shape including aspect ratio, Stokes's shape factor, and radial shape factor [175]. According to the aspect ratio as a common factor to characterize the particle shape (i.e. the ratio between length and thickness of the particles), four categories are defined for particles known as spherical, disc-shaped, bladed and rod-like [176]. Owing to their exceedingly small size as well as their high surface area, the incorporation of nanoparticles into the polymer matrix can significantly enhance various physical and chemical properties of nanocomposites. There are three main categories to characterize the nanoparticles having one or more dimensions in the nanoscale: one-dimensional nanoparticles as the sheets, laminas and plates; two-dimensional nanoparticles as the nanotubes and nanofibers, three-dimensional nanoparticles as spherical ones (Figure 1-8) [177].

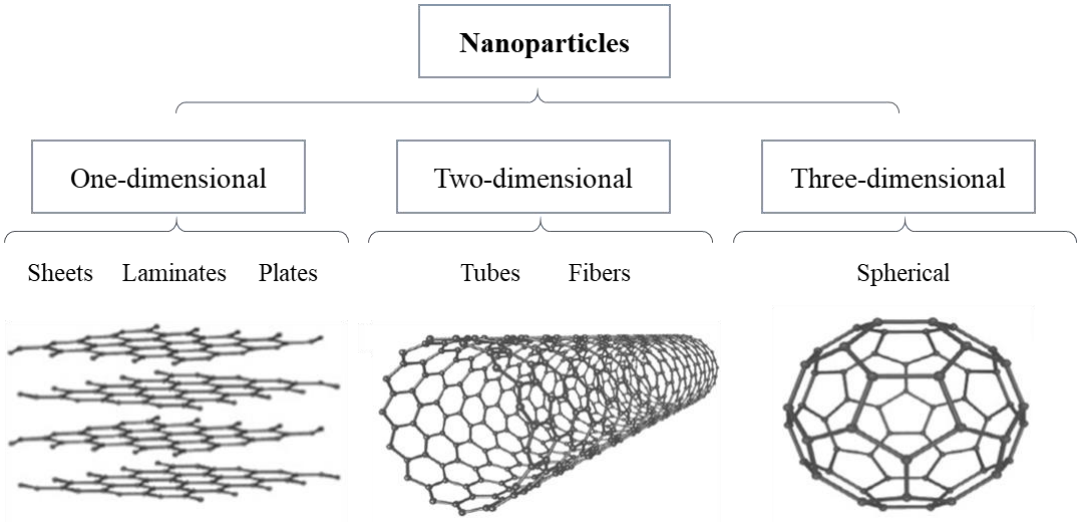

Figure 1-8. Schematic illustration of three main categories of nanoparticles [178].

Metal oxides including SiO_2, ZnO and TiO_2 are some examples of existing spherical particles [179]. It was demonstrated that particles synthesized from amorphous compounds are spherical, while particles of crystalline solid phases show characteristic of crystal habits [180]. There are also spherical polymer particles

which can be converted into non-spherical particles using specific methods [181]. The disc-shaped particles exist in microscale, e.g., diatomaceous earth, and nanoscale, e.g., nanosheets of graphene and nano clay. In such particles, the nanoscale thickness of particles leads to their great aspect ratio [182]. Carbon nanotube (CNT), nanofiber of peptide and nanocellulose are some examples of rod-like particles [183].

According to the literature, in addition to the surface superhydrophobicity, other properties of the nanocomposite coatings can also be enhanced by addition of particles such as electrical conductivity, thermal conductivity, mechanical strength, anti-bacterial properties and photocatalytic wettability. CNTs and graphene have been widely used in development of conductive superhydrophobic nanocomposite coatings. Zhang et al. [184] fabricated superhydrophobic multiwalled carbon nanotubes (MWCNTs)/epoxy nanocomposite coating with high electrical conductivity. Owing to the hierarchically porous three-dimensional nanostructure of MWCNTs, WCA of 154° and sliding angle of ~6° was achieved. Asthana et al. [185] reported that the combination of carbon black and graphene nanosheets illustrated both excellent water impalement resistance and electrical conductivity as well as superhydrophobic and oleophilic behavior. Feng et al. [186] developed a superhydrophobic nanocomposite coating using two-dimensional graphene nanosheets led to the self-wrinkling surface morphology. Ribeiro et al. [187] verified the efficiency of alumina trihydrate (ATH) on thermal conductivity, flame retardancy, as well as tracking and erosion resistance of a superhydrophobic RTV-SR coating containing ATH and silica particles. The superior water-repellency and anticorrosion performance along with good thermal conductivity were obtained by the addition of TiO_2 to polyaniline [188]. Cully et al. [189] demonstrated that the presence of silica particles at a volume fraction of 25 vol.% significantly improved the Young's modulus and hardness properties of superhydrophobic coating. Copper oxide nanoparticles with hydrophobic silica were used to produce a superhydrophobic coatings with extremely low bacterial adhesion via spray-coating [190]. Due to the excellent simultaneously photocatalytic and photostimulated superhydrophoilic properties of TiO_2 nanoparticles, a superhydrophobic high density polyethylene (HDPE)/TiO_2 nanocomposite film was fabricated exhibiting self-cleaning properties and UV-induced reversible wettability [191].

Albeit tremendous efforts have been devoted to design non-wettable superhydrophobic surfaces, robustness is still one of the bottlenecks hindering their practical applications. Unlike the living biological surfaces, the water-repellent behavior of biomimetic surfaces is hardly recoverable once destroyed [192]. Loss

of designed surface roughness due to mechanical damages, and/or diminution of the intrinsic surface hydrophobicity as a result of chemical reaction or formation of hydrophilic contamination are responsible for the lost water-repellency of superhydrophobic materials. As a consequence, the Cassie-Baxter state may become unstable where the transition from Cassie-Baxter to Wenzel regime may occur and eventually results in a higher CAH [19].

Nowadays, several strategies are proposed to delay or prevent the Cassie-Wenzel transition. The most important factor for stability of Cassie-Baxter state is the maintenance of surface textures. Some studies [193, 194] employed dual-scale or multiple-scales of geometric features to ensure the stability of Cassie-Baxter state even after elimination of upper portion of the surface features. Such morphology composed robust microscale protrusions which protected fragile nanoscale features superimposed on them against mechanical forces. In this situation, unlike surfaces without nanostructures, the microscale features do not need to have large aspect ratio to maintain the Cassie-Baxter state. Nevertheless, during mechanical damages, if the height of the microscale features became lower than threshold value required to sustain the droplet on top of the asperities, the droplet would sink into the grooves. Eventually, a transition to the Wenzel regime and increase in CAH would be observed [195].

The second most important factor for robustness of superhydrophobic surface is retaining the surface chemistry. Loss of hydrophobicity due to mechanical or chemical damages is closely related to the degree of coating homogeneity in the bulk. During mechanical damages, the chemical homogeneity of the coating throughout bulk can have a positive effect on the preserving the surface hydrophobicity. Otherwise, if the top-coat or surface functionalization strategy is utilized to create a superhydrophobic surface, the elimination of the thin upper layer by mechanical forces can lead to the loss of surface hydrophobicity [196]. Moreover, due to chemical damages, the chemical composition of the exact upper layer of superhydrophobic surfaces can alter and results in damaged surface hydrophobicity. According to the literature, there are various methods proposed to tackle the robustness issues and prolong the lifespan of superhydrophobic surfaces. Based on the source of regeneration of water-repellent behavior, these approaches can fall into three main categories: mechanically self-healing superhydrophobic surfaces, chemically self-healing superhydrophobic surfaces, and volumetric superhydrophobic nanocomposite. Each category is briefly explained in the following sections.

1.5.1 Mechanically self-healing superhydrophobic surfaces

Generally, the micro-nanostructures are susceptible to be damaged or destroyed after mechanical wear and abrasion. Thus, regenerating the surface topographies is an effective strategy to develop durable self-healing superhydrophobic surfaces. Reorganization of the micro and nanoparticles on the surface is a way to restore the initial structure of the damaged surfaces. To do so, Puretskiy et al. [197] developed a self-repairable superhydrophobic surface based on highly fluorinated crystalline fusible wax included with colloidal particles. The particles spontaneously segregated at the interface with air and formed hierarchical surfaces with self-cleaning properties. The scratched surface recovered its superhydrophobic properties after melting due to the migration of particles to the newly formed surface. Chen et al. [198] developed a self-repairing superhydrophobic nanocomposite coating containing fluorinated silica and TiO_2 nanoparticles embedded within the polystyrene matrix. During UV irradiation of abraded surface, the top layer of polystyrene was decomposed due to the photocatalysis of TiO_2 nanoparticles. Consequently, fluorinated silica and TiO_2 nanoparticles were exposed creating the appropriate surface morphology. Thereafter, migration of low surface energy agents to the surface restored the superhydrophobicity (Figure 1-9 (a1 and a2)). Lewin et al. [199] claimed that the concentration of polyhedral oligomeric silsesquioxanes (POSS) nanoparticles was increased due to the migration of particles to the surface of nanocomposite. The concentration gradient was produced by intermittent heating and cooling.

Huang et al. [200] worked on roughness regeneration of a superhydrophobic surface due to the cross-scale structural deformations from microscale to nanoscale. As a result, the damaged roughness could be repaired by itself immediately. It was observed that such hierarchical structural response was highly relevant to the abrasion intensity. Based on the shape memory polymer, Lv et al. [201] developed a self-healing superhydrophobic surfaces where the pressed surface microstructure, the damaged surface chemistry, and the surface superhydrophobicity can be recovered through a heating process (Figure 1-9 (b1-b4)). As shown in Figure 1-9 (c1-c3), the microscopy images confirmed that the shape memory effect of the epoxy used in this study had a particular ability to memorize the temporary shape after deformation and restore the permanent morphology upon heating treatment. Although there are several studies concentrated on the regeneration or recovery of surface structures, it still demands significant efforts to prolong the lifespan of water-repellent surfaces.

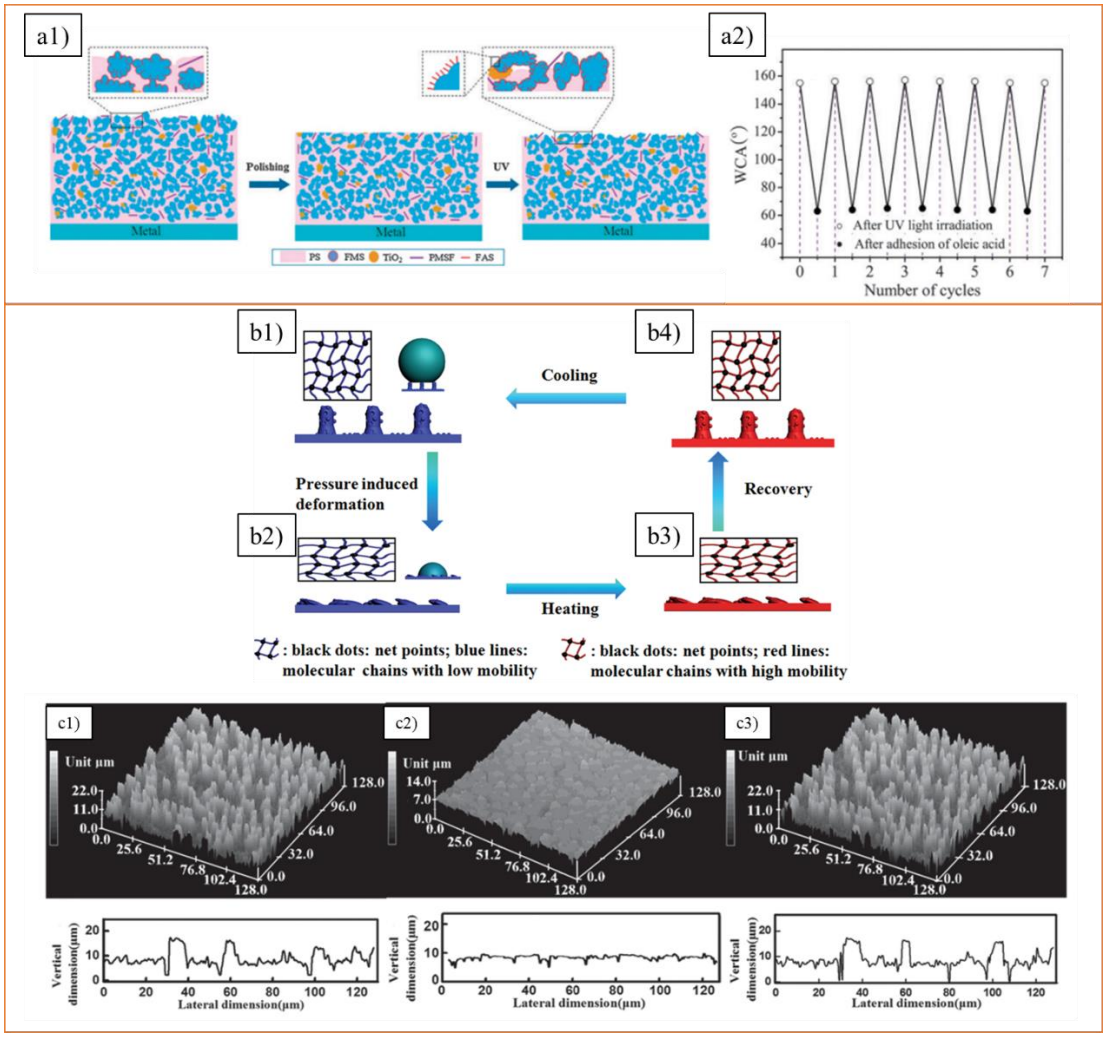

Figure 1-9. a1) the working principle of self-healing fluorinated silica and TiO_2 superhydrophobic coating, a2) changes of WCA against number of oleic acid adhesion followed by UV light irradiation [198]; b1-b4) schematic illustration of self-healing process of developed superhydrophobic surface where pressure-induced deformation was recovered by subsequent heating; 3D confocal microscopy images of the c1) original superhydrophobic surface, c2) after pressing the surface, and c3) after heating it at 85 °C for 120 s [201].

1.5.2 Chemically self-healing superhydrophobic surfaces

Regarding diverse applications of self-cleaning water-repellent surfaces, there is a need to create superhydrophobic surfaces on the hydrophilic materials by the development of patterned surface topographies with special hydrophobic coating. This approach has a main drawback which is stated in the study of Xiu et al. [202]. They illustrated that after rubbing the superhydrophobic surface against sandpaper, the hydrophilic silicon oxide beneath the coating would be exposed due to the wearing off the superhydrophobic coating from the tops of the micropyramids. Despite the high WCA of the rubbed surface, the CAH increased because of the adhesion of water to the tops of the abraded micropyramids. Inspired by the regeneration of the hydrophobic

wax layer on top of the natural leaves, the chemically self-healing approach was proposed to recover the superhydrophobic properties using hydrophobic low-molecular weight compound embedded in cavities or pores of the superhydrophobic materials. Li. et al [203] developed a superhydrophobic film with a self-healing hydrophobic surfactant coating that relies on the tendency of the film to minimize its surface energy. During deposition of a hydrophobic silane surfactant layer, an excess of surfactant was used so that a large amount of silane was absorbed within the bulk film. The diffusion of silane to the hydrophilic surface induced by mechanical damage or chemical modification can minimize its surface energy and effectively recover the damaged hydrophobic layer. The surfactant reservoir enabled the hydrophobic layer to be restored many times. The self-healing behavior of low surface energy perfluorooctyl acid stored within the nanopores of anodized aluminum was surveyed by damaging the upper layer of superhydrophobic surface using O_2 plasma treatment. After treatment, the surface became superhydrophilic. As the short time exposure to plasma wouldn't have significant impact on the underlying perfluorooctyl acid, WCA of the treated surface increased along with the time to restore its superhydrophobicity after 48 h [204]. Li et al. [205] fabricated a self-healing superhydrophobic coating using encapsulated healing agents of reacted fluoroalkylsilane within layered polymeric coating. After decomposition of the top hydrophobic layer or scratching the coating, the superhydrophobicity was regained under ambient condition with a relative humidity of 40% for 4 h (Figure 1-10 (a1-a3)). It was observed that at higher relative humidity, the self-healing process was faster. Golovin et al. [206] developed numerous self-healing superhydrophobic surfaces using different hydrophobic fillers including fluorodecyl polyhedral oligomeric silsesquioxane (F-POSS). Although the coating subjected to the O_2 plasma treatment became hydrophilic due to the hydrolyzation of F-POSS, the surface regained its superhydrophobicity by heating treatment. The heating process was a driving force induced the remained F-POSS to migrate to the surface.

Silicone rubber can serve as a reservoir for hydrophobic LMWS which migrate from the bulk to the surface to recover the water-repellency. Yan et al. [207] investigated the hydrophobic recovery of the corona-aged silicone rubber surface. Migration of low molecular weight components from bulk to the damaged surface led to the full recovery of superhydrophobic characteristic through a self-healing process. It was claimed that the corona aging propagated some surface cracks which could accelerate the recovery process of low surface energy, and it is beneficial to the self-healing properties of superhydrophobic silicone rubber. Tu et al. [208]

developed a self-healing superhydrophobic nanocomposite coating on hydrophilic wood surface through two subsequent steps of precoating the surface with PDMS followed by spray coating with perfluoroalkyl methacrylic copolymer (PMC)/TiO_2 nanocomposite. The samples subjected to 10 h of UV irradiation showed WCA of >150°, while CAH increased up to 25°. The superhydrophobicity was deteriorated due to the demolition of the PMC layer and the exposition of TiO_2 particles to water. The water-repellency, however, was restored by the migration of LMWS during heat treatment (Figure 1-10 (b1-b3)).

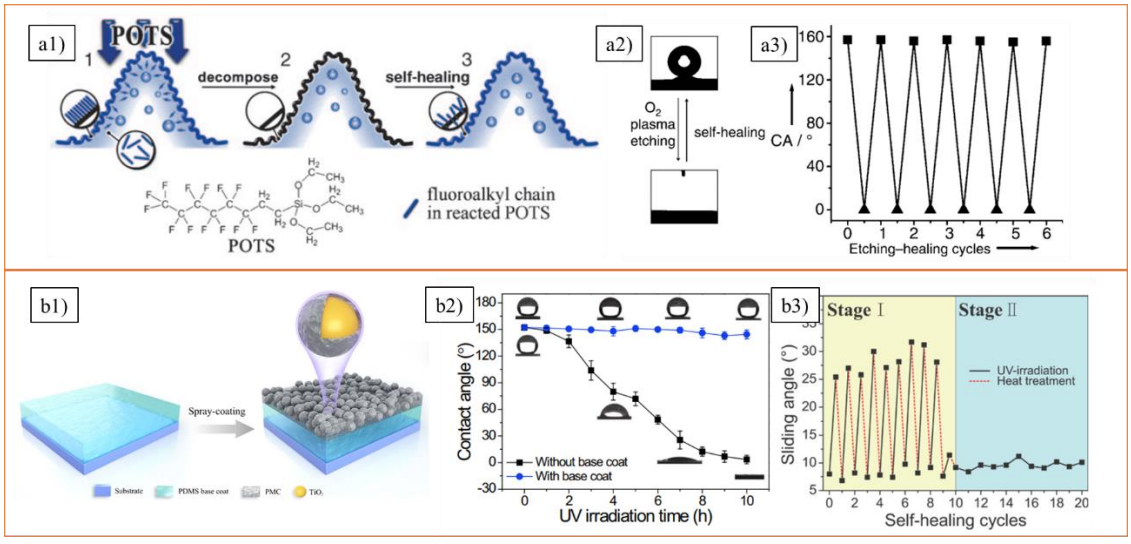

Figure 1-10. a1) Schematic illustration of working principle of self-healing superhydrophobic coating, a2) the reversible changes of WCA after plasma treatment, a3) the changes of WCA as a function of etching-healing cycles [205]; b1) schematic illustration of superhydrophobic coating, b2) changes of WCA and SA against UV irradiation time, b3) changes of SA as a function of UV irradiation and heat treatment cycles [208].

1.5.3 Volumetric superhydrophobic nanocomposite

One of the new concepts in designing damage-tolerant superhydrophobic materials is the development of volumetric superhydrophobic nanocomposites which possess low surface-energy micro and/or nanostructures embedded within its whole volume. Based on this concept, the bulk material regains the rough surface textures by taking abrasion itself as the trigger. It ensured continued superhydrophobicity due to the presence of hydrophobic microstructures extended throughout the whole volume [83]. Unlike self-healing superhydrophobic surfaces, no external stimulus is needed to regenerate the favorable surface roughness after mechanical abrasion.

The literature review revealed that only a handful of studies have been conducted on fabrication of volumetric superhydrophobic nanocomposites which is called in the literature as superhydrophobic bulk

material. Zhu et al. [209] reported a superhydrophobic CNT–PTFE bulk material to solve the lack of mechanical durability and oil fouling problems of superhydrophobic surfaces. There was no loss of superhydrophobicity after abrasion of the bulk material for 20 cycles and even cutting deep into it. The oil contaminated bulk material could regain its superhydrophobicity by directly burning off the oil in air. Furthermore, the CNT–PTFE bulk material can be manipulated by a magnet bar when some iron oxide particles were added to the material [210]. Aktas et al. [211] deposited a PTFE layer on the 3D assembled TiO_2 via chemical vapor deposition approach to fabricate a robust superhydrophobic 3D TiO_2/PTFE material. A compression molded silica/PTFE nanocomposite at the mass ratio of 1:4 showed rather stable superhydrophobicity toward corrosive mediums, particularly under acidic conditions. In addition to the proper chemical stability, the produced superhydrophobic materials were capable to absorb different types of oil or organic solvents [192]. The presence of fluorine-containing compound at high mass ratio is the key point of the mentioned superhydrophobic bulk materials.

Despite their lowest surface energy and water aversion, the environmental and health issues raised for fluorinated materials restricted their application in various materials including superhydrophobic surfaces. Zhang et al. [18] prepared a non-fluorinated bulk material of inorganic/PP composite with excellent surface and bulk superhydrophobic properties through dispersion of inorganic TiO_2 and hydrophobic SiO_2 particle fillers. Due to the presence of photocatalytic TiO_2 nanorods, the WCA of the superhydrophobic surfaces reduced gradually under UV irradiation which eventually led to the transition from non-wettable to wettable surfaces. The mechanical abrasion of the outermost UV irradiated layer revealed a fresh underlying superhydrophobic layer (Figure 1-11 (a1-a4)). In another research, a class of superhydrophobic bulk material possessing melt-coatability was fabricated by compression molding of the octadecyl chain grafted silica nanoparticles at 150 °C for 8 h. The WCA on the broken portions of the sample was as high as 160°. The self-cleaning properties of both fresh and cut surfaces were similar. Since it was a meltable material, the broken or cut pieces could be joined together by heating treatment without disturbing superhydrophobic properties [212].

For oil–water separation, the damage-tolerant porous superhydrophobic materials with bulk level water-repellency were reported. Li et al. [20] fabricated a porous divinylbenzene (DVB)/fumed silica polymer monolith with a WCA of 161.3° and sliding angle (SA) smaller than 4.0°. The tunable hierarchical porous structure featuring relatively high oil absorbency was achieved through solvothermal method in which ethyl

acetate was considered as both solvent and template (Figure 1-11 (b1-b6)). In another study, it was shown that a porous superhydrophobic bulk material with high corrosion resistivity and oil absorbency was created by the addition of ammonium bicarbonate (NH_4HCO_3) as a pore-forming agent to the PVDF/CNT/SiO_2 nanocomposite. The hierarchical strawberry-like structure was achieved due to the randomly orientated and entangled nano-scaled CNTs and SiO_2 exposed on the microscale protrusions surface of PVDF [19].

There are some studies where the appropriate roughness needed for superhydrophobicity is created via mechanical abrasion. Cai et al. [213] developed a bulk superhydrophobic conductive material with a range of roughnesses induced by abrasive paper. The high WCA and low SA was achieved by the addition of 33.3 wt.% of the fillers with the ratio of 4:1 for Ketjen black to vapor grown carbon fibre particles. Increasing the abrasive paper grit led to the enhancement of WCA. However, by increasing beyond a certain grit, the WCA started to decrease (Figure 1-11 (c1 and c2)). Via compression molding of the hydrophobic silica/polymer nanocomposites with subsequent mechanical abrasion, Zhang et al. [214] reported robust and non-fluorinated superhydrophobic free-standing items. Various mechanical and chemical strengths were enhanced by increasing the compression up to 40 MPa. The materials retained water-repellency after various damages such as sandpaper abrasion, knife/file scratch, liquid nitrogen, severe sand/water impact, as well as acidic/alkali corrosion tests.

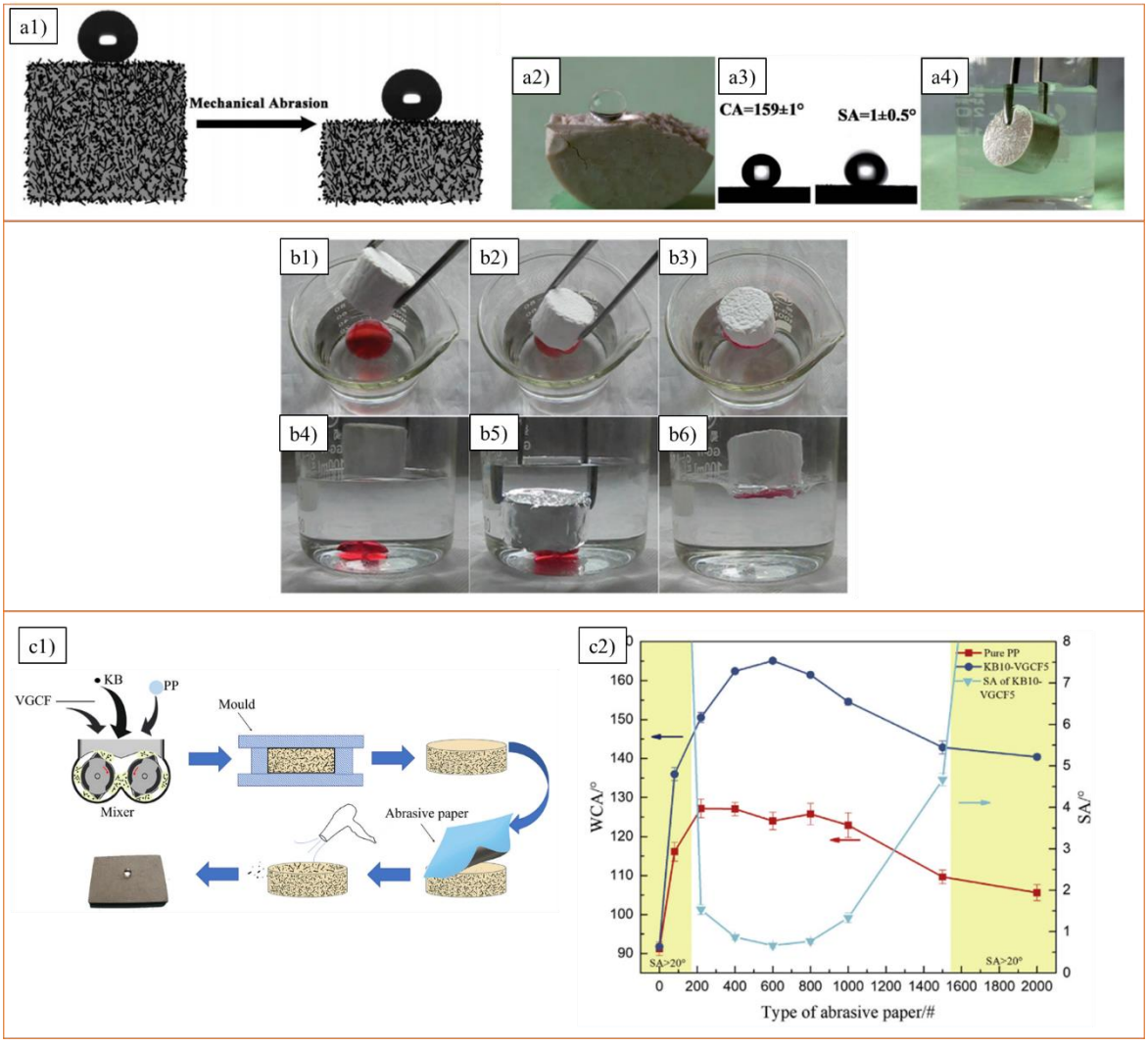

Figure 1-11. a1) Schematic illustration of a bulk material which can sustain its superhydrophobicity after mechanical abrasion, a2) superhydrophobicity of the broken material, a3) WCA and SA of water-repellent surface, a4) mirror-like phenomnon of the submerged sample in water [18]; sequential images of the removal process of b1-b3) hexadecane, and b4-b6) chloroform from water using porous polymer monolith [20]; c1) schematic image of fabrication process of ktejan black/carbon fiber/PP superhydrophobic material using abrasion method, c2) the changes of WCA and SA as a function of type of abrasive paper [213].

1.6 Application of superhydrophobic surfaces

The superhydrophobic surfaces have recently attracted great attention due to their unique water-repellency and anti-contamination properties. As shown in Figure 1-12, these surfaces are used across a wide range of application areas, including self-cleaning, icephobicity, corrosion resistance, anti-fouling, oil/water separation, drag reduction of flowing fluids, anti-bacterial adhesion, windshields and architecture coatings, etc. [13, 24, 32, 87, 215, 216]. In addition to their different applications, there are various other advantages offered

by this method such as reduction in maintenance costs, elimination of monotonous manual effort, and also a reduction in the time spent in cleaning the final product [217]. A brief description of some of these important applications are presented in the following subsections.

Figure 1-12. Schematic of main applications of superhydrophobic surfaces in different fields [218].

1.6.1 Self-cleaning

There are numerous phenomena originated from nature. Self-cleaning is one amongst them inspired from anti-contamination and self-cleaning characteristic of various plant species specifically lotus leaves. This property has attracted immense commercial and academic interest, due to its extensive range of applications from cleaning the window glasses and solar panels to textiles [217]. Artificial self-cleaning surfaces are mainly divided into four categories: 1) water-repellent superhydrophobic self-cleaning, 2) TiO_2-based self-cleaning, 3) gecko setae-inspired dry self-cleaning, 4) marine organisms inspired anti-fouling self-cleaning such as shark skin [218]. The most well-known one is superhydrophobic self-cleaning surfaces which stems from the high water-repellency and rolling of water droplets over the superhydrophobic substrate. Due to the usual hydrophilic nature of contaminants, the adhesion of contaminant particles to the water droplet is greater than the adhesion of contamination to the superhydrophobic surface [215]. Consequently, the contamination can

easily adhere to the round-shaped water droplets rolling off the surface and be removed from the material surface [24, 219].

A series of parameters affect the self-cleaning ability of superhydrophobic surfaces. Although the possibility of self-cleaning from hydrophilic surface was mentioned in various studies, Hechentaler et al. [220] reported that presence of nanotexture and hydrophobicity of the material increased the rate of particle removal. Yu et al. [221] illustrated that high WCA, low CAH, low adhesion force between solid surface and the particle, and an adequate particle size are the necessary preconditions for having a self-cleaning surface. As expected, the macroscopic contamination can easily be removed with the help of water droplets during rain or artificial showers [222]. Bhushan et al. [42] studied the effect of different surface structures on self-cleaning characterization by water droplets. Unlike flat, nanostructured, and microstructured surfaces, the water droplets with nearly zero kinetic energy were capable of removing almost entire contaminant particles from hierarchical surfaces. The same observations were reported in various studies showing that only hierarchical surface roughness can repel both macroscopic and microscopic particles [215] [32, 223, 224]. Moreover, the resistance of superhydrophobic surfaces to particulate matter and nanosized contamination is inevitable for the use of these surfaces for a variety of real-world applications. Geyer et al. [225] illustrated that creation of the pores having the lowest possible size was a vital requirement for attaining a high contamination resistance. They observed that water-repellent superhydrophobic surfaces with nanoscale pore size could resist to long-term contamination tests. The importance of nanoscale roughness features on self-cleaning ability was emphasized in other studies as well [220, 226].

1.6.2 Icephobicity

Among the appealing characterizations of superhydrophobic surfaces is icephobicity. A spread spectrum of industries such as transportation systems, transmission systems, and infrastructures are impacted by the fascinating life-giving yet potentially destructive icing phenomenon. For instance, ice accretion on the aircrafts may result in higher drag force followed by loss of lift force. Eventually, they can lead to some catastrophic irreparable occurrences [227]. The reliability of transmission systems is highly dependent on the performance of insulators affected notably by the ice accumulation on their surfaces [2, 228]. For instance, in 1998 in the northeastern United States, the ice storm-related electrical blackouts left over 1 million people

without power and an estimated damage cost exceeded US$1 billion. The same disaster happened in China in 2008 and 100 km of 500 kV transmission lines were severely damaged [3].

The main strategies have been taken to overcome the icing issue are known as “de-icing” and “anti-icing” methods. De-icing approaches are comprised of active methods where some mechanical, thermal and chemical forces are used to eliminate the accumulated ice from the surface. Vapor heating, electro-thermally melting, mechanical vibration and using some chemical de-icer like ethylene glycol are some examples of de-icing methods which mainly rely on continuous heating, intermittent vibration and unceasing usage of chemical de-icer of the frozen parts. Consequently, these methods are highly time- and energy-consuming, expensive, laborious, and environmentally unfriendly [229].

The anti-icing represents a passive approach where no external energy is required. There are several definitions corresponding to different yet interrelated properties of icephobic surfaces which can be mainly divided into two categories: they should prevent or delay ice formation on the surfaces, and if ice accumulated on them, they should show poor normal and/or shear ice adhesion strength [230]. In pursuit of materials having icephobic properties, superhydrophobic surfaces have enticed numerous researchers since recent decades [231-233]. Given that the presence of insulating air pockets among the surface asperities can hinder the heat transfer between water droplet and the superhydrophobic surface, the water droplet demonstrates a delayed freezing time on the superhydrophobic surfaces. Moreover, the reduced contact area between water droplet and the superhydrophobic surface provides small number of potential sites as the homogenous ice nucleation pointes. As the next reason, the extreme mobility of the water droplet on the superhydrophobic surface leads to the rebounding or shedding time less than needed time for ice nucleation [234].

Although it is reported that surfaces having lower surface energy lead to the lower ice adhesion and icing probability, surface roughness is the key parameter affecting the icephobic behavior of the superhydrophobic surfaces [235, 236]. Shen et al. [237] illustrated that there was lower ice accumulation on the single nanostructured surface than that of micro-nanostructured superhydrophobic surface. He et al. [238] studied the effect of surface roughness on ice adhesion strength. The hierarchical micro-nanostructured surfaces demonstrated lower ice adhesion strength compared to microstructured and nanostructured superhydrophobic surfaces. Consequently, development of a favorable superhydrophobic and icephobic surface is one of the attractive but challenging studies.

1.6.3 Corrosion resistance

As another vital application of superhydrophobic surfaces, a brief description of corrosion resistance is provided in this section. Corrosion is defined as "the physico-chemical interaction between a metal and its environment, which results in changes in the properties of the metal and which may often lead to impairment of the function of the metal, the environment, or the technical system of which these form a part" [239]. Under normal environmental conditions, corrosive reactions progressively deteriorate surfaces, particularly the surfaces of reactive metals, surfaces that are used extensively in industrial applications. Globally, annual costs related to infrastructure corrosion are at least $1.8 trillion US. This represents 3–4% of the gross domestic product of industrialized countries [240]. In addition to pollution, humidity, salt, acids, and bases are the main corrosive environments that severely corrode metal and/or alloy surfaces [241]. Corrosion involves two different processes. At active areas (anodes), the movement of metal ions into solution produces an ionic current in the solution. At less active areas (cathodes), the passage of electrons from a metal to an acceptor such as oxygen, another oxidizing agent, or hydrogen ions creates an electronic current in the metal [242].

Superhydrophobic surfaces are being investigated as a solution to reduce the corrosion of the metal substrates like aluminum, copper, magnesium, and steel alloys. The anti-corrosivity of superhydrophobic surfaces when in contact with a corrosive solution depends on the air trapped in the surface grooves that hinders direct contact between the corrosive media and the material. In fact, this air trapped acts as an inherent isolator [243, 244]. Regarding different types of applications, there are numerous options for evaluating corrosivity such as deionized water, hydrochloric acid (HCl), potassium chloride, disodium phosphate, sodium bicarbonate, etc. Moreover, corrosion is assessed using resistance, weight loss measurements, neutron reflectivity, potentiodynamic curves, and electrochemical impedance spectroscopy. The latter two methods are the most practical means recently being used [245].

1.7 Durability of superhydrophobic surfaces

To date, poor durability of superhydrophobic surfaces hindered their usage for various applications. The superhydrophobic surfaces prone to lose their water-repellency due to the damaged surface topography, elimination of low-surface-energy materials or failure of both [246]. Following the mechanical and/or chemical failures, the penetration of the water droplet into the surface asperities leads to the transition from Cassie-

Baxter to energetically more favorable Wenzel regime. The result is a strong adhesion of water droplet to the surface and loss of water-repellency [247].

There are numerous parameters affecting the durability of superhydrophobic surfaces. Mechanical abrasion, adhesion, dynamic impact, pH, time, temperature, humidity, and UV irradiation are among the significant parameters influenced the water-repellent performance of superhydrophobic surfaces [248]. Based on the nature of these parameters, they can chiefly fall into three categories of mechanical, chemical, and environmental durability (Figure 1-13). Sandpaper abrasion, knife scratching, file scratching, pencil hardness, finger-press, tape peeling, solid particle impact, droplet impact, laundry wear and ultrasonication tests are some examples of the mechanical durability analyses [213, 214, 249-251]. Rubbing one surface with another solid surface is one of the frequently encountered situations in daily use of superhydrophobic surfaces which might be endangering water-repellent performance of these materials. For the mechanical abrasion tests, the most effective parameters are surface roughness of the abrasive paper, its chemical composition and Young's modulus. Due to the lack of a standardized method for mechanical durability measurement using hand-applied abrasion test, there are numerous other factors presented in the literature influencing final wettability such as applied pressure on the abrasive paper, type of movement, amount of surface in contact with abrasive paper, etc. [252]. Zhang et al. [214] investigated the effect of grit number on the surface water-repellency. Due to the fine roughness of 1200Cw sandpaper, the WCA decreased from 155° to 120°. However, low grit numbers (grits 320, 600, and 800Cw) had lower effect on the superhydrophobicity due to the formation of significant structure on the abraded surface. Milionis et al. [250] studied the durability of the produced biodegradable superhydrophobic coating against sandpaper abrasion. The WCA and SA of the abraded surfaces as a function of applied downward pressure showed that the water-repellency deteriorated by increasing the pressure where a transition from non-wetting "Lotus" state to "Rose petal" state was observed. Cai et al. [213] demonstrated that orthogonal and random abrasion motions were resulted in higher WCA than unidirectional method due to the formation of "gullies" and great number of microscale protrusions on the surface.

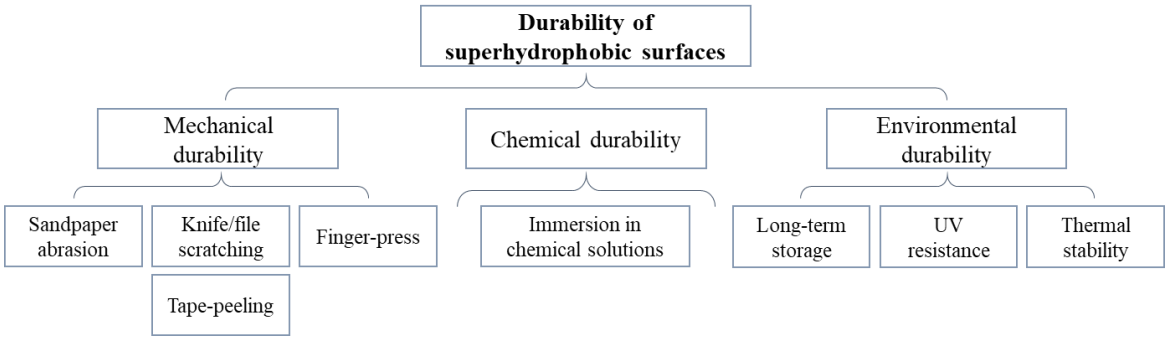

Figure 1-13. Schematic of durability of superhydrophobic surfaces based on three categories of mechanical, chemical and environmental durability.

Knife, blade or file scratching is another applicable approach to evaluate the robustness and consistency of the superhydrophobic surfaces. Long et al. [251] illustrated that the superhydrophobicity of the developed PDMS coating was not affected by some horizontal or vertical scratches on the surface. The file abrasion was performed on SiO_2/polymer nanocomposites in both air and water. The results showed the retained superhydrophobicity of the superhydrophobic free-standing materials [214]. The bare finger-press test as a qualitative test can mimic human handling of a material to test whether a superhydrophobic surface can be suitable for commercial use. In addition to mechanical damage, a bare finger-press also adds salt and oil contaminants to the surface. Therefore, the finger-press test can both physically and chemically affect a superhydrophobic surface [253]. Tape-peeling is one of the simplest and most common testing methods used in coating technology. This test demonstrates the adhesion strength of coatings to the substrate by removing the coating materials with the help of a tape [196]. Tape-peeling can easily remove particles attached to the surface solely with Van der Waals interactions. However, tape-peeling has no cinsiderable effect on particles if they are chemically binded to the surface by silica bridges [254]. Moreover, increasing the tape adhesion strength has a detrimental effect on the particles' detachment and surface non-wettability [255].

Prevention of the liquid penetration and corrosion resistance are among the primary applications of the superhydrophobic surfaces. Therefore, stability against chemical solutions plays a vital role in the successful execution of superhydrophobic surfaces. Immersion in chemical solutions is one of the most important tests used to assess the chemical stability of water-repellent surfaces. Boinovich et al. [256] studied the effect of fluoro- and hydrocarbon surfactants on the final chemical stability of the produced superhydrophobic surfaces through long-term contact with diverse chemical media. During short-term contact, all physically and chemically absorbed surfactants demonstrated high stability, while under prolonged contact, the chemically

absorbed surfactants were more stable than physical ones. Moreover, the behavior of contact angle and surface tension of fluoro-surfactants as a function of time of exposure to both acidic and alkaline solutions confirmed their better stability compared to hydrocarbon surfactants. Wang et al. [257] fabricated a stearic acid modified ZnO superhydrophobic filter paper. The maximum contact angle of 157° was obtained in pH 8 solution. The contact angle of acidic and alkaline solutions of pH 2 and 14 was considerably decreased. Xu et al. [258] developed a green self-cleaning and anti-fouling superhydrophobic coating on the copper mesh. It was observed that by increasing the pH value from 1 to 13, the contact angle increased then decreased. The maximum contact angle was reached at pH value of 7. The same trend was observed by Pandit et al. [259] where the chemical stability of a superhydrophobically coated wood surfaces was assessed via immersion technique. The superhydrophobicity was considerably diminished within less than an hour for samples immersed in acidic and alkaline solutions having pH value of 2 and 13. Whilst the contact angle of the superhydrophobic surface remained nearly intact even after 300 h immersion in pH 8 solution. A coating containing silane-treated SiO_2 nanoparticles was applied on the wooden samples by an alkali-driven method to generate alkaline-containing water-repellent surfaces. Although the alkaline had almost no effect on the chemical stability in acidic media (pH = 1), the higher amount of alkaline relatively improved the chemical stability of samples immersed in alkaline solutions (pH = 13) [260]. To determine the behavior of superhydrophobic surfaces against chemical solutions in a less aggressive test compared to immersion, there is an analysis called droplet contact test where the alteration of a droplet contact angle as a function of time is evaluated. Zhang et al. [214] placed droplets of acidic (pH = 1) and alkaline (pH = 14) solutions on the surface for 30 min. During time, the contact angle of the acidic/alkaline droplets decreased from ~165° to ~152° yet remained higher than 150°.

Since one of the main applications of superhydrophobic surfaces is for outdoor usage, several other experiments should be conducted in order to evaluate their environmental durability such as long-term storage, UV resistance, thermal stability, etc. Wang et al. [257] assessed the WCA and SA of superhydrophobic paper stored for 1-6 months in an ambient condition. After 6 months, the WCA decreased to 153° and SA reached 3° still the paper was superhydrophobic. During UV light exposure, the oxidation of organic components in the coatings can deteriorate the water-repellent performance of superhydrophobic surfaces [18]. Between hydrocarbon and fluorocarbon materials, the latter is more resistant to UV. It was observed that the stability of

the surface modified SiO_2 particles against UV irradiation was in the order of perfluorosilane> isobutylsilane> polybutadiene surface treatment [102]. Li at al. [115] illustrated that after 48 h exposure of superhydrophobic epoxy/PDMS/SiO_2 composite coating to UV light, the WCA showed negligible changes. Li et al. [20] developed a superhydrophobic coating showing switchable wettability under UV irradiation. When the sample was irradiated with UV light, a conversion of superhydrophobicity into superhydrophilicity was observed. However, the water-repellency could be restored by abrasion or cutting the upper layer. Under some circumstances, the superhydrophobic surfaces might be exposed to high temperature. Thus, thermal stability of the produced surfaces is important. Due to the considerable thermal stability of polyimide, the produced superhydrophobic film showed great stability even after thermal treatment at 400 °C for 30 min [261]. Deng et al. [254] produced a superhydrophobic coating made of porous SiO_2 particles. The coating was thermally stable at temperature below 350 °C for 10 h.

CHAPTER 2

ARTICLE 1: EVALUATION OF ATMOSPHERIC-PRESSURE PLASMA PARAMETERS TO ACHIEVE SUPERHYDROPHOBIC AND SELF-CLEANING HTV SILICONE RUBBER SURFACES VIA A SINGLE-STEP, ECO-FRIENDLY APPROACH

E. Vazirinasab*, R. Jafari, G. Momen
Department of Applied Sciences, University of Québec in Chicoutimi (UQAC)
555, boul. de l'université, Chicoutimi, Québec, G7H 2B1 Canada
* E-mail: elham.vazirinasab1@uqac.ca

2.1 Abstract

Effective self-cleaning and superhydrophobic surfaces having superb water-repellency are among the most widespread alternatives for eliminating surface contamination, corrosion resistance, reducing ice accumulation, etc. to enhance the lifespan of various engineered materials. In this study, we developed a simple methodology, based on an atmospheric-pressure air plasma system, as a simple, environmentally friendly and industry applicable approach for fabricating superhydrophobic surfaces. Our approach is significant as the use of an atmospheric-pressure plasma system combined with compressed air as an eco-friendly plasma gas offers great potential for the industrialization of superhydrophobic surfaces for mass production. The creation of micro-nanostructured surface roughness on a low surface energy high temperature vulcanized silicone rubber (HTV-SR) substrate resulted in a static water contact angle (WCA) >160° and a contact angle hysteresis (CAH) <3°. Scanning electron microscopy (SEM) revealed the presence of the plasma-induced coral-like micro-nanostructures responsible for the superhydrophobicity of the surfaces. We assessed the influence of plasma operating parameters on the water-repellency of silicone rubber via a design of experiment (DoE) method to determine the near-optimal operating parameters; once established, we could assess the characteristics of the surfaces. In addition to the superhydrophobic surfaces, we also fabricated another surface, named a slippery hydrophobic surface, under specific plasma operating conditions. Superhydrophobic surfaces prepared at these optimal plasma operating conditions showed favorable water-repellency and self-cleaning properties under both wet and dry conditions.

Keywords: Superhydrophobic, plasma operating parameters, response surface method, atmospheric-pressure plasma, silicone rubber, self-cleaning.

2.2 Introduction

Wettability is one of the basic characteristics of solid surfaces, and it reflects the affinity of a solid surface to absorb water or other liquids. In the past decades, superhydrophobic surfaces, as an extreme state of surface non-wettability, have attracted tremendous attention in terms of science and technology due to their potential applications in various fields where self-cleaning, antifouling, anti-corrosion, anti-icing and drag reduction [13, 262-268] properties are sought. Lotus leaves [25], the penguin feathers [269] and butterfly wings [30] are natural examples of plants and animals having excellent surface water-repellency.

For a superhydrophobic surface to be produced, two main criteria must be respected: low surface energy materials and hierarchical surface roughness. Young, who began to explore the relationship between surface tension and static contact angle, developed an equation to determine the contact angle of a sessile drop on an ideal smooth surface [270]. However, in the case of a rough surface, the Wenzel (homogeneous wetting) regime and the Cassie-Baxter (heterogenous wetting) regime are the main theories under which the relationship between surface tension, surface roughness (or topography) and contact angle can be described [47, 51]. To fabricate a desirable superhydrophobic surface having water-repellent properties, surfaces having a high WCA coupled with a low CAH fall into the Cassie-Baxter state. However, the Wenzel regime is usually characterized by strong pinning of a water droplet to the surface having a high WCA, resulting in a higher CAH. As such, the water-repellency of a surface depends much more on a lower CAH than a higher WCA [271].

Researchers have fabricated superhydrophobic surfaces mainly by (i) surface roughening of a low surface energy material or (ii) modifying a rough surface by depositing low surface energy materials [41]. Multiple methods have been used to fabricate roughness on low surface energy or inherently hydrophobic materials, such as silicones and fluorocarbons. One of the common hydrophobic materials is silicone, a material that is used in diverse fields, including medical, industrial and household applications [103, 272]. Silicone rubber has the characteristics of both organic and inorganic components where the binding of the organic groups—which includes methyl, ethyl and phenyl—directly to the silicon atoms leads to the inherent hydrophobicity of the silicone rubber [61].

In relation to superhydrophobicity, etching is one of the well-established approaches for generating micro-nanostructures on diverse hydrophobic substrates. Etching refers to removing material from the substrate, and this process can be divided into two main categories: (i) wet chemical etching [103, 273-275],

where acid or base solutions etch dislocations or impurities on the substrates, and (ii) dry etching, such as plasma etching [75, 276-278], in which the generation of reactive atoms or ions in a gas discharge leads to the anisotropic etching of the surface [13]. Although chemical etching is an inexpensive and relatively simple approach that can be easily scaled up, it is not an environmentally friendly procedure due to the use of various corrosive bases or acids; in addition this method is limited to metallic materials [279, 280]. Furthermore, the etching rate is sensitive to time and chemical concentration. So dry etching can be a better alternative for reducing the environmental impact in the fabrication of superhydrophobic surfaces in terms of elimination the usage of the corrosive bases or acids.

Plasma treatment, as a subcategory of dry etching, can produce superhydrophobic surfaces on a variety of metallic and non-metallic materials. There are two categories of plasma systems based on the pressure applied in the plasma chamber: low-pressure plasma and atmospheric-pressure plasma systems. Low-pressure plasmas have a wide range of applications in the fabrication of superhydrophobic surfaces, such as material processing, the manufacture of semiconductor devices as well as surface finishing of medical implants, sterilization and production of antibacterial surfaces [124, 125, 281]. However, operating the plasma at reduced pressure has several drawbacks. Vacuum systems are expensive and have high maintenance costs, and some unforeseen accidents in these systems can lead to economic and safety issues. Furthermore, as it is a batch process, the size of the object requiring treatment is confined by the size of the vacuum chamber [122, 282]. However, continuous treatment with atmospheric-pressure plasma eliminated the disadvantages of a vacuum operation as there was no need for vacuum equipment. It resulted in a rapid and cost-effective procedure. Another advantage of this approach relative to the use of low-pressure plasma is the simplicity for combining it with available production lines [34, 283].

In addition to the pressure applied in the plasma chamber, plasma gas also plays an important role in relation to surface roughness and the final water-repellency of the substrate. Various gases are used for plasma etching including oxygen, nitrogen, argon, helium, CF_4, SF_6 and their combination. For example, a superhydrophobic poly(tetrafluoroethylene) (PTFE) surface was created via high-energy oxygen plasma-etching treatment. The increase in surface roughness was responsible for the water-repellency of the surface [284]. Barshilia et al. [161] fabricated superhydrophobic PTFE surfaces using Ar/O_2 plasma gas in a vacuum chamber. After 4 h of treatment, the leaf-like micro-protrusions with the WCA of 158° was achieved showing

the maximum average surface roughness of 1.96 μm. The same procedure was performed by Ryo et al. [162] to produce a superhydrophobic PTFE substrate having an extremely high WCA of 178.9° and a very low sliding angle of 1°. One of the gases commonly used in plasma treatment is CF_4 through which surface etching and fluorination can occur simultaneously. With CF_4, fluorinated groups are covalently bonded to the surface to decrease the energy of the treated substrate further. As a result, samples etched with CF_4 exhibit a significant number of fluorocarbon groups along with a high surface roughness [164]. Yang et al. [166] fabricated a superhydrophobic polyvinylidene fluoride (PVDF) flat sheet membrane via CF_4 plasma surface modification. The fabrication of the superhydrophobic surfaces was primarily due to the concurrent increases of surface roughness due to the ablation reaction of CF_4 plasma and the formation of $[–SiF_x(CH_3)_{2-x}–O–]_n$ (x=1, 2) structures produced by the direct attachment of F atoms to Si [167]. Superhydrophobic surfaces having oleophilic properties have been created by PTFE samples being irradiated with CF_4 plasma [277]. Superhydrophobic silicone rubber surfaces were obtained using CF_4 radio frequency plasma with the objective of extending the life-span of the surface as an outdoor insulator [285]. Although many studies have focused on CF_4 as a plasma gas, using it has some serious disadvantages including its high cost and CF_4 being a potent greenhouse gas. Air is an ideal candidate for plasma gas as it is a natural, eco-friendly, inexpensive and abundant gas mixture. To the best of our knowledge, no published research papers have used air as a plasma gas for fabrication of superhydrophobic surfaces via a plasma-etching technique.

Plasma generation in an atmospheric-pressure air plasma system depends highly on several operation parameters, including the reference voltage, plasma frequency, cycle time, distance between nozzle outlet and substrate, speed of the plasma jet, gas flow rate and the number of passes. Changes in these parameters affect the etched shape profile, surface roughness and chemical composition of the substrate and thereby alter surface hydrophobicity. To develop a desirable superhydrophobic surface, the relationships between these decisive factors and surface morphology and wettability must be controlled precisely as there are a considerable number of interactions among these parameters. In a traditional trial and error approach, one of the operation parameters is altered while the others remain constant. This approach is quite time-consuming, costly, laborious and does not consider the interaction among factors or their relative importance [286]. DoE, using a response surface method, enables simultaneous alteration in the operation parameters by which the correlation between several independent factors and the desired responses can be specified. Response surface methodology is a set of

mathematical methods and is preferred in cases where one requires a particular optimal condition or a multiple response optimization related to diverse factors [287].

Here, we present an eco-friendly one-step procedure that uses a plasma-etching treatment to create micro-nanostructures on silicone rubber. We apply an atmospheric-pressure air plasma system as this approach is more beneficial than a low-pressure system from a practical and industrial point of view that has been rarely studied. We use a DoE method to determine the optimal plasma operating conditions under which further analyses of the prepared superhydrophobic surfaces can be performed. Of note, at specific operating conditions we achieved a hydrophobic surface having a low WCA and low CAH; this surface is named a slippery hydrophobic surface and demonstrates an interesting characteristic in terms of slippage of water over the surface. We use SEM to verify the created coral-like roughness of the plasma-treated surfaces responsible for ultra-water-repellency and Fourier-transform infrared spectroscopy (FTIR) to assess the chemical characterization of the substrate. We also examined the water-repellency of the prepared surfaces using severe water contact and water droplet impact analysis. The self-cleaning properties of the surfaces were then analyzed under both wet and dry conditions to simulate the self-cleaning of prepared surfaces under ambient conditions.

2.3 Experimental section

2.3.1 Materials

High temperature vulcanized silicone rubber (HTV-SR) hybrid composites were supplied by K-Line Insulators Limited, Canada. The material consists of a matrix of long-chain silicone rubber and fillers, such as alumina trihydrate ($Al_2O_3.3H_2O$) and silicon oxide (SiO_2). All HTV-SR samples were cleaned in ultrasonic baths of acetone and deionized water for 30 min. The plasma was applied to samples having dimensions of 15 mm × 15 mm × 2 mm. We used compressed air, as a green, non-expensive and abundant gas, for the plasma treatment of the silicone rubber samples.

2.3.2 Atmospheric-pressure plasma treatment

To create surface roughness, we used the “Plasma Jet AS400” (Plasmatreat GmbH, Germany) atmospheric-pressure plasma system. The plasma was generated in the movable jet by inducing the electric arc to the injected gas inside the jet. Then, the plasma was ejected from the nozzle outlet at the bottom of the jet and interacted with the surrounding atmosphere and substrate. The plasma jet, positioned perpendicular to the

sample's surface, moved across the surface in a 2-D manner (Figure 2-1). The diverse plasma parameters, i.e., reference voltage, plasma frequency, cycle time, distance between nozzle outlet and substrate, speed of the plasma jet, gas flow rate and the number of passes can be adjusted via a software interface designed to control the different aspects of plasma generation. Based on some preliminary trials, it was revealed that the plasma frequency, cycle time, distance between nozzle and substrate and the number of passes were less important and were maintained at 21 kHz, 100%, 8 mm and four, respectively. We assessed the effect of the three remaining factors—reference voltage, plasma jet speed and gas flow rate—on the wetting characteristics of the plasma-treated surfaces with the help of Design-Expert® software, version 11, Stat-Ease, Inc., Minneapolis, MN, USA, via a response surface methodology.

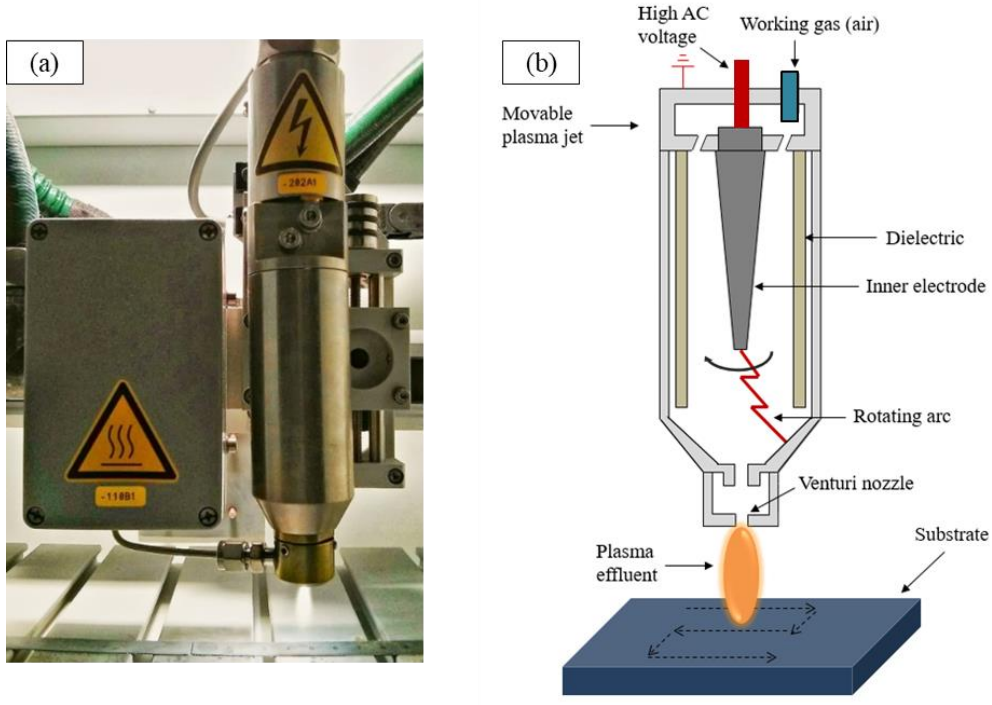

Figure 2-1. (a) The atmospheric-pressure plasma jet and (b) a schematic of the plasma treatment jet.

2.3.3 Response surface method

The response surface method is one of the well-known approximations and experimental design approaches. We applied a three-level factorial design based on the response surface method to investigate the influence of the experimental parameters and the interaction among these factors on the non-wetting properties of the plasma-treated silicone rubber surfaces. Three numerical factors at three levels were the inputs for the design, while WCA and CAH were defined as the responses. The values and levels of the three experimental

factors are reported in Table 2-1. The three different levels of each factor are coded as -1 (low level), 0 (mid-level) and +1 (high level). Based on this three-level factorial design, we performed 28 experimental runs.

Table 2-1. The selected independent variables and their levels.

Experimental parameters	*Unit*	*Symbol*	*Low level (-1)*	*Mid-level (0)*	*High level (+1)*
Reference voltage	%	A	80	90	100
Plasma jet speed	m min^{-1}	B	4	6	8
Gas flow rate	L h^{-1}	C	2000	2500	3000

2.3.4 Surface characterization

We measured the static WCA to investigate the wettability of samples. The WCA was assessed via the sessile drop method in air at 25 °C using a Kruss™ DSA100 goniometer equipped with a video camera. Double distilled water drops (4 µL each) were placed on the surface, and the WCA was determined by the Young–Laplace approximation method. To ensure a complete hydrophobic recovery, we characterized precisely all the samples 48 h after treatment. CAH was determined by computation of the difference between the advancing and receding WCAs of the moving water droplet on the surface. The average WCA and CAH values were determined by measuring the same sample at five different points. To determine the variation of the chemical functional groups of the silicone rubber samples, we measured the Attenuated Total Reflection FTIR (ATR-FTIR) via a Cary 630 FTIR spectrometer (Agilent, USA) in ATR mode. We used a JSM-6480 LV scanning electron microscope to view and evaluate the produced micro-nanostructures of the samples. Before analysis, the HTV-SR samples were coated with a thin layer of gold-palladium alloy to enhance the imaging. The surface roughness of the samples was evaluated using an Atomic Force Microscopy (AFM) (Bruker, Multimode8). The water droplet impact process was recorded by a high-speed camera (FASTCAM SA1.1 by Photron) at a constant framing rate of 5400 fps and room temperature of 22 °C. In all measurements, 20-µL DI water droplets were released with zero initial velocity from a height of 3 cm. We assessed the self-cleaning nature of the prepared superhydrophobic surfaces by contaminating the samples under both wet and dry conditions. For the wet conditions, we first placed the samples in the container holding a 24 g L^{-1} dirty solution that contained equal amounts of kaolin, carbon black and salt in water. The samples were first left for 90 min for the particles to settle onto the surface. Then we removed the samples from the dirty solution to survey its self-cleaning characteristic. For the next step, we left the samples in the dirty solution to become completely dry at room

temperature for 48 h. The samples were then tested by applying water droplets to the surface. For the dry condition, kaolin contaminants were sieved through a #60 mesh and applied to the substrate. The sample was left for 30 minutes. We then dropped a 20-µL water droplet onto the substrate to wash the pollution layer.

2.4 Results and discussion

2.4.1 Superhydrophobicity of the plasma-treated substrate based on DoE methods

The response surface method determined the relationship between the wettability of HTV-SR and the selected plasma operation parameters, and also optimized these parameters. WCA and CAH measurements, selected as responses, provided an assessment of the wetting characteristic of silicone rubber surfaces (Table 2-2).

Table 2-2. The three-level factorial experimental design, showing the factors and the corresponding levels for each experimental combination and the measured WCA and CAH values as the dependent responses.

		Independent factors			*Responses*	
Std	*Run*	A: Reference voltage (%)	B: Plasma jet speed (m min^{-1})	C: Gas flow rate (L h^{-1})	Water contact angle (°)	Contact angle hysteresis (°)
1	10	80	4	2000	139	54.7
2	12	90	4	2000	163	2.2
3	21	100	4	2000	161	1.6
4	17	80	6	2000	116	27.3
5	16	90	6	2000	136	7.8
6	28	100	6	2000	124	18.6
7	20	80	8	2000	104	5.7
8	23	90	8	2000	115	18.8
9	19	100	8	2000	104	13.2
10	3	80	4	2500	130	34.9
11	15	90	4	2500	160	2.6
12	26	100	4	2500	163	2.2
13	8	80	6	2500	103	11.9
14	1	90	6	2500	139	24.8
15	6	90	6	2500	143	22.4
16	24	100	6	2500	158	4.5
17	5	80	8	2500	103	8.8
18	27	90	8	2500	113	18.1
19	14	100	8	2500	133	52.4
20	4	80	4	3000	122	20.3
21	25	90	4	3000	137	22.3
22	22	100	4	3000	154	0.8
23	13	80	6	3000	99	18.1
24	18	90	6	3000	122	17
25	9	100	6	3000	113	19.9
26	11	80	8	3000	108	21.1
27	2	90	8	3000	130	39.5
28	7	100	8	3000	109	31.7

According to the WCA data, all 28 plasma-treated surfaces were hydrophobic, i.e. WCA was greater than 90°. Based on DoE design, we developed quadratic and two-factor interaction (2FI) models to characterize the effects of different plasma parameters and their interactions on WCA and CAH. The resulting regression equations, in terms of coded factors, were:

$$WCA = +137.24 + 10.83 \times A - 17.22 \times B - 3.78 \times C - 4.67 \times AB + 1.42 \times AC + 6.17 \times BC - 11.03 \times A^2 + 6.47 \times B^2 - 8.86 \times C^2 \quad 2\text{- }1$$

$$\ln(CAH) = +2.51 - 0.4311 \times A + 0.5565 \times B + 0.2219 \times C + 1.05 \times AB + 0.0287 \times AC + 0.1913 \times BC \quad 2\text{-}2$$

in which A, B and C are reference voltage, plasma jet speed and gas flow rate, respectively. Analysis of variance (ANOVA) evaluated the significance of the effect of each variable (and their interactions with each other) on the responses and the adequacy of the developed models. Table 2-3 and Table 2-4 present the ANOVA results obtained for WCA and CAH, respectively. As the *p*-value of models was less than 0.05, both regression models were significant ($p < 0.0001$) which means there is only a 0.01% chance that the F-value could occur due to the noises. Adjusted R^2 values for WCA and ln(CAH) (0.7873 and 0.6278, respectively) agreed reasonably well with the predicted R^2 values (0.6737 and 0.4455 for WCA and CAH, respectively). As the difference between the adjusted R^2 and predicted R^2 of the developed models were less than 0.2, the good predictive ability of the model was confirmed [288]. Adequate precision measures the signal to noise ratio and a value >4 indicates adequate model discrimination. Adequate precision values for WCA and ln(CAH) were 11.5288 and 11.0052, respectively. Thus, regression models were statistically significant and adequate for predicting and optimizing the plasma treatment process.

Given their lower *p*-values, plasma jet speed (B) and the interaction of the reference voltage and plasma jet speed (AB) were deemed the most significant factors affecting WCA and CAH results, respectively. The reference voltage (A), the second-order effect of the reference voltage (A^2), the second-order effect of the gas flow rate (C^2) and the interaction of plasma jet speed and gas flow rate (BC) also had a significant effect ($p < 0.05$) on WCA. In addition to AB, changes in the CAH of the plasma-treated samples were also attributed to the plasma jet speed (B) and the reference voltage (A) ($p < 0.05$). Other factors, where $p > 0.05$, had less effect on WCA and CAH over the studied range.

Table 2-3. ANOVA results for water contact angle (WCA).

Source	*Sum of squares*	*df*	*Mean square*	F-*value*	p-*value*
Model	9979.62	9	1108.85	12.10	<0.0001
A-Reference voltage	2112.50	1	2112.50	23.06	0.0001
B-Plasma jet speed	5338.89	1	5338.89	58.28	<0.0001
C-Gas flow rate	256.89	1	256.89	2.80	0.1113
AB	261.33	1	261.33	2.85	0.1085
AC	24.08	1	24.08	0.26	0.6144
BC	456.33	1	456.33	4.98	0.0386
A^2	775.51	1	775.51	8.46	0.0094
B^2	266.91	1	266.91	2.91	0.1050
C^2	500.75	1	500.75	5.47	0.0311
Residual	1649.06	18	91.61		
Lack of fit	1641.06	17	96.53	12.07	0.2231
Pure error	8.00	1	8.00		
Cor. total	11628.68	27			

Table 2-4. ANOVA results for contact angle hysteresis (CAH).

Source	*Sum of squares*	*df*	*Mean square*	F-*value*	p-*value*
Model	23.40	6	3.90	8.59	<0.0001
A-Reference voltage	3.35	1	3.35	7.37	0.0130
B-Plasma jet speed	5.57	1	5.57	12.28	0.0021
C-Gas flow rate	0.89	1	0.89	1.95	0.1769
AB	13.15	1	13.15	28.96	<0.0001
AC	0.01	1	0.01	0.02	0.8843
BC	0.44	1	0.44	0.96	0.3366
Residual	9.53	21	0.45		
Lack of fit	9.53	20	0.48	91.98	0.0820
Pure error	0.01	1	0.01		
Cor. total	32.94	27			

Figure 2-2 and Figure 2-3 illustrate the three-dimensional (3-D) response surface and contour plots derived from these equations. The two significant factors, i.e., reference voltage and plasma jet speed, are plotted together, while the remaining factor (gas flow rate) is set at its center-point value. Where there are weak (or no) interactions between two process parameters, the fitted response surface will be a plane (i.e., contour lines will be straight); interactions between the parameters produce curved contour lines and a contour produced by a second-order model will be elliptical. The curve lines of the illustrated contour plots highlight the strong interaction between the reference voltage and plasma jet speed [289].

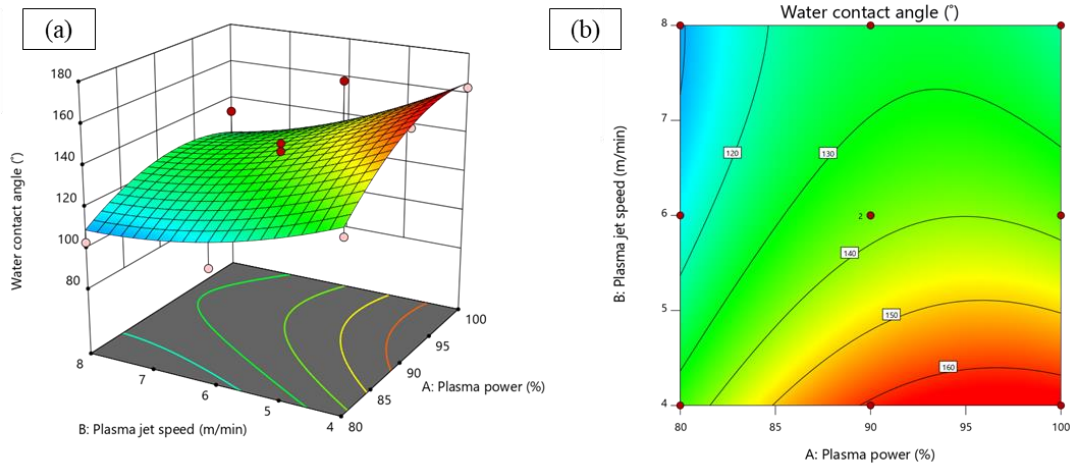

Figure 2-2. (a) Three-dimensional response surface and (b) contour plots for the effect of the reference voltage (%) and plasma jet speed (m min^{-1}) on the water contact angle of the plasma-treated silicone rubber. The red dots are the design points.

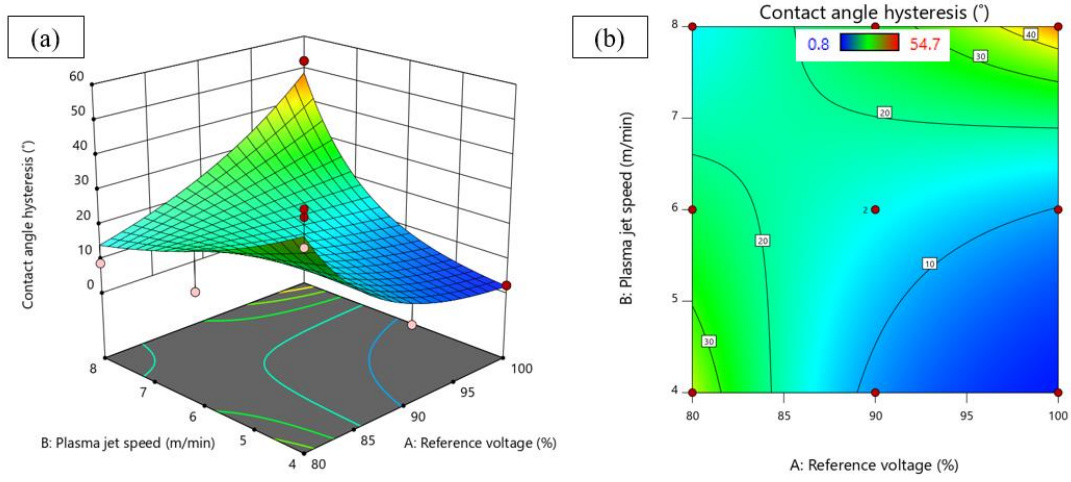

Figure 2-3. (a) Three-dimensional response surface and (b) contour plots for the effect of the reference voltage (%) and plasma jet speed (m min^{-1}) on the contact angle hysteresis of the plasma-treated silicone rubber. The red dots are the design points.

The WCA and CAH of the untreated silicone rubber were 116° ± 2° and 47° ± 3°, respectively. The highest WCA values were coupled with the lowest CAH values toward the highest reference voltage and lowest plasma jet speed. At a constant reference voltage, an increase in the plasma jet speed decreased the WCA (Figure 2-2). Plasma jet speed can be considered as the inverse of treatment time; a faster plasma jet speed results in a shorter treatment time and a lower WCA. On the other hand, increased reference voltage leads to a higher WCA. High power usually enhances the ionization of the etching gas and increases both the amount of surface erosion and roughness [61]. Consequently, the recommended optimal plasma operating conditions for

creating favorable superhydrophobicity and water-repellency are a reference voltage of 95%, a plasma jet speed of 4 m min^{-1} and a gas flow rate of 2500 L h^{-1}.

Our results for CAH were more ambiguous (Figure 2-3). We observed an inverse relationship between CAH values and reference voltage when the plasma jet speed was fixed at 4 m min^{-1}, as samples produced at a higher reference voltage had a lower CAH stemming from increased surface roughness. Superhydrophobic surfaces having the desired water-repellency were produced at a high reference voltage and low plasma jet speed. Although we obtained a surface having a low WCA at a high jet speed of 8 m min^{-1}, a decrease in reference voltage led to a CAH <10°. Therefore, we obtained a surface having both a low WCA and low CAH at ~103° and ~9° using a plasma jet speed of 8 m min^{-1}.

It should be noted that low CAH occurs due to a variety of reasons. Physical homogeneity, originating from the insignificant and homogeneous roughness of the surface, can prevent the physical pinning of the three-phase contact line and lead to a low CAH. Chemical homogeneity, related to the homogeneous chemical composition of the substrate, also leads to a low CAH. Adsorption and desorption between the liquid and the surface molecules should be eliminated to avoid energy dissipation during droplet motion that results in a higher hysteresis [271]. Once advancing and receding WCAs were >90°, the CAH increased as roughness increased (and the physical heterogeneity of the substrate increased [290, 291]) from 1.5 nm to 158.3 nm. However, superhydrophobic surfaces having an ultra-low CAH were also created on surfaces having a higher roughness. Thus, the relationship between CAH and roughness can be described with a bell curve, i.e., a maximum point can be defined for the surface roughness resulting in the highest CAH. At lower or higher values of roughness, a lower CAH is produced due to the physical homogeneity of the surface (lower roughness) or enhanced physical heterogeneity and the presence of air pockets within the surface roughness (higher roughness).

In this study, we observed that a low reference voltage, low gas flow rate, and high plasma jet speed led to a reduced CAH. As illustrated in the surface morphology section, these plasma conditions decreased initial surface roughness. Regarding the effect of these conditions on the reduced surface roughness, it can be said that at a low gas flow rate and reference voltage, there were few numbers of low-energy ions and neutral particles (called as plasma particles) in the plasma stream. Moreover, at a high plasma jet speed, there is a great chance of collision of plasma particles with one another and a low possibility for vertical diffusion of these

particles in concave structures. Altogether, these specific conditions produce the etching of the greater number of convex structures than concave structures on the surface. Consequently, the plasma acted as a polishing tool and swept over the surface to produce a smoother surface [292, 293]. This decrease in roughness led to a reduction in CAH due to the physical homogeneity of the silicone rubber substrate following plasma treatment.

2.4.2 Chemical characterization

During plasma treatment, the surface undergoes both physical and chemical modification, and both changes impact the final surface wettability. The collision of high-energy particles of the plasma discharged with the substrate can cause the breakage of some of the chemical bonds and form new bonds, thereby altering the chemical composition of the treated substrate.

The ATR-FTIR spectra highlighted differences in the chemical composition of untreated and plasma-treated silicone rubber samples via changes in peak positions and shapes that varied depending on the applied reference voltage (Figure 2-4). The absorption spectra observed ca. 2960 and 1410 cm^{-1} is related to the different stretching and bending modes of an aliphatic C–H in CH_3. The absorption peak visible at 1260 cm^{-1} relates to a symmetric CH_3 deformation of Si–CH_3. The absorption peak at 790 cm^{-1} characterizes Si–$(CH_3)_2$. The most intense absorption peak, at ca. 850–870 cm^{-1}, corresponds to the Si–$(CH_3)_3$ chemical groups. The characteristic peak of Si–O–Si is visible ca. 1000–1110 cm^{-1} in which the presence of the most intense absorption peak at 1015 cm^{-1} is due to an asymmetric Si–O–Si stretching vibration [294]. The intensity reduction of the absorption peak of Si–CH_3 is greater than that of Si–O–Si and C–H as reference voltage increased from 80 to 100%. In addition, the intensity of the Si–$(CH_3)_2$ spectrum decreased less than the Si–CH_3 chemical bond. This latter observation can be attributed to the two main reasons: (1) a weaker-binding energy of the Si–CH_3 chemical bond relative to that of Si–O and C–H, and (2) reorientation of the methyl groups from the bulk to the surface of the material. The Si–CH_3 chemical bond is more exposed to breakage by which the replacement reaction of CH_3 in Si–CH_3 is dominant over the replacement reactions of H in C–H or O in Si–O–Si [167, 295]. The reorientation of these groups to the bulk of the material is explained by hydrophobic recovery, encouraging Si-CH_3 to remain on the surface and for oxidized species to reorient themselves [167, 295]. Furthermore, the gradual elimination of peaks centered at 3450 cm^{-1} —assigned to hydroxyl groups (OH) in the fillers like the alumina trihydrate (ATH) ($Al_2O_3.3H_2O$) and the end groups in the polymer backbone—is the most visible difference between the plasma-treated silicone rubber and the untreated substrate. This can

occur via endothermic decomposition of ATH at high temperatures during plasma treatment. At the reference voltages of 90 and 100 %, the presence of a broad absorption peak at ~3100–3700 cm^{-1} can be ascribed to the oxidation reaction between oxygen molecules and silicone rubber by which the $–CH_3$ deforms to $–CH_2$ and produces hydroxyl ($Si-CH_2OH$) and peroxides ($Si-CH_2OOH$) [296]. Although the wettability of the silicone rubber surface was enhanced immediately after plasma treatment due to the presence of hydroxyl groups on top of the substrate, hydrophobicity is restored as surface hydrophilic groups and untreated low molecular weight silicone (LMWS) species respectively reorient and migrate to the surface.

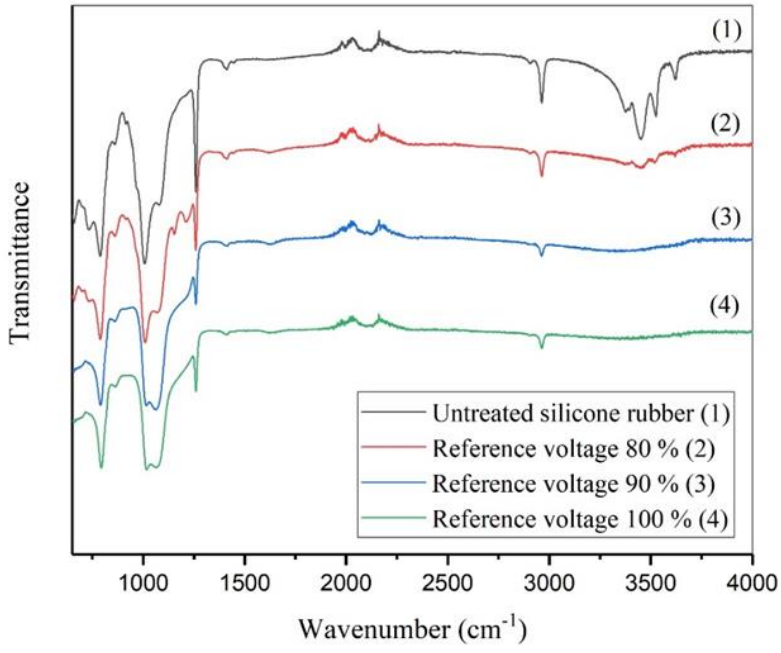

Figure 2-4. ATR-FTIR spectra of silicone rubber treated by atmospheric-pressure air plasma at various reference voltages, and plasma jet speed of 4 m min^{-1} and gas flow rate of 2500 L h^{-1}.

2.4.3 Surface morphology

Water contact angle and the wettability of a plasma-treated surface depends on surface roughness combined with the chemical composition of the substrate. We used an SEM to view the formation of roughness and surface micro-nanostructure on the plasma-treated silicone rubber surfaces produced at various reference voltages. Before atmospheric-pressure air plasma treatment, the silicone rubber surface appeared to be relatively smooth (Figure 2-5 (a)). The morphology of the plasma-treated sample at 80% reference voltage demonstrated some nano-sized protrusions (Figure 2-5 (b)). These protrusions became more pronounced at higher reference voltages, and the coral-like structures became the dominant morphology (Figure 2-5 (c–d)). As the reference voltage increased from 80 to 100 %, the size of the granular nanostructures increased, and the

surface had more clustered coral-like structures. At 100% reference voltage, the space between roughness features was minimal, and the aggregated coral-like clusters created some micro-sized structures on the surface. In general, two main changes occur in the polymer substrate during plasma treatment: (1) chemical modification via reaction of the surface with plasma species to generate new functional groups, and (2) physical etching through chemical reaction and surface etching leading to roughening of the substrate [161]. Since silicone rubber chains contain organic groups (like methyl) attached on an inorganic siloxane backbone, the organic groups are more likely to etch during air plasma treatment due to the reaction of oxygen with carbon and hydrogen. This process led to the creation of coral-like protrusions on the surface [138].

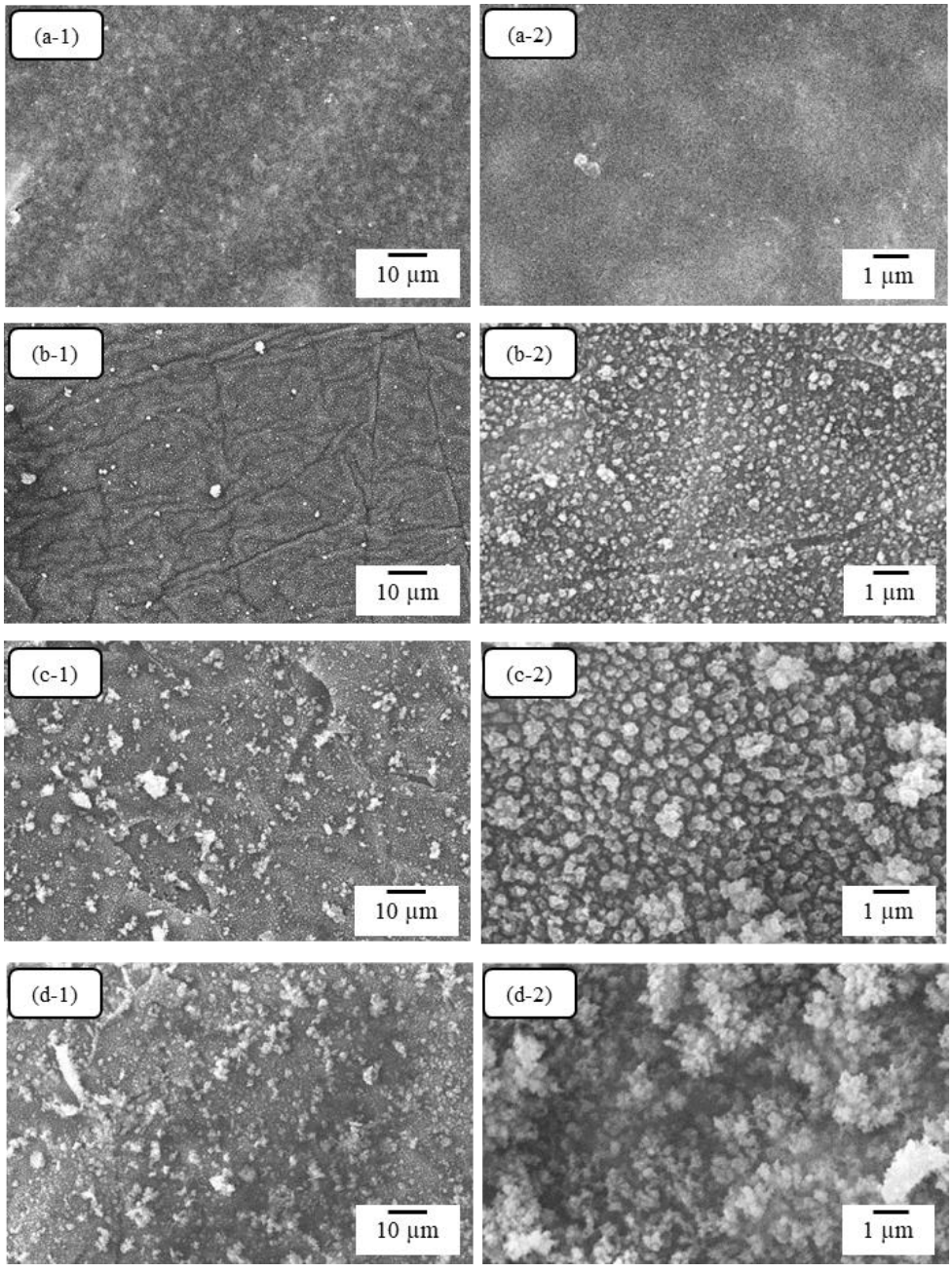

Figure 2-5. SEM images of (a-1, a-2) untreated silicone rubber at two different magnifications and (b–d) plasma-treated silicone rubber at different reference voltages; (b) 80%, (c) 90% and (d) 100% at magnifications of 1000× and 10000× (the plasma jet speed and gas flow rate were kept constant at 4 m min^{-1} and 2500 L h^{-1} respectively).

AFM analysis confirmed the presence of plasma-induced micro-nanostructures on the superhydrophobic surfaces (Figure 2-6); enhanced roughness was apparent for the superhydrophobic sample. Both the arithmetic mean (R_a) and maximum structure height (R_p) were five times higher for the treated surface than the untreated substrate, while the root mean square (RMS) roughness of the silicone rubber surface before

and after plasma treatment increased from 45 to 277 nm. Increased roughness on the substrate surface favors the presence of air pockets within the more complex structures (Table 2-5).

As mentioned earlier, at specific plasma conditions, some samples demonstrated a simultaneous low WCA and low CAH, i.e., slippery hydrophobicity, a pattern that can be expected as the reduction in CAH can be associated with the physical homogeneity of the silicone rubber substrate due to the plasma treatment. To confirm plasma treatment–related physical homogeneity, we compared the roughness of untreated, superhydrophobic and slippery hydrophobic plasma-treated silicone rubber surfaces (Figure 2-6). We observed that the physical homogeneity of a smooth surface having sporadic nano-scale bumps was responsible for the low CAH of the slippery hydrophobic surface (Figure 2-6 (c)).

Thus, the results from the analysis of surface morphology and FTIR confirm that the combination of low surface energy materials and surface roughness are the main causes for the increased water-repellency of the plasma-treated surfaces. It also reveals the relationship between physical homogeneity and the low CAH of the slippery hydrophobic surfaces.

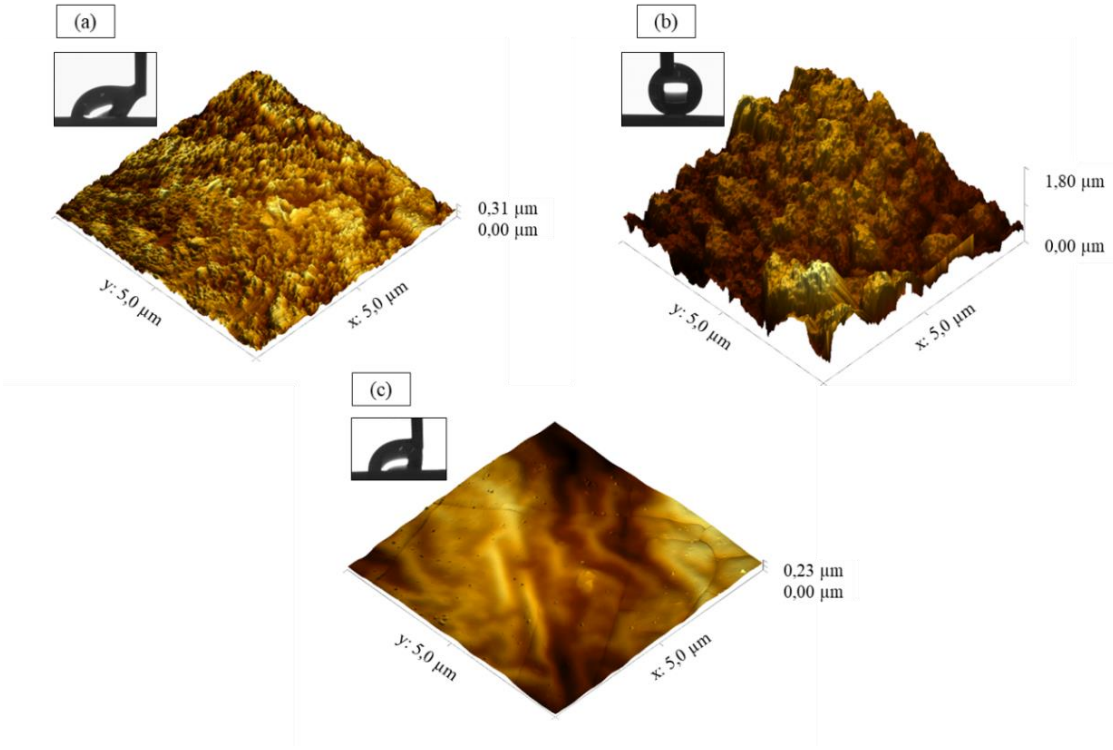

Figure 2-6. Surface profile of (a) untreated silicone rubber, (b) plasma-treated superhydrophobic silicone rubber at a reference voltage of 100%, a plasma jet speed of 4 m min^{-1} and a gas flow rate of 2000 L h^{-1} and (c) plasma-treated silicone rubber at a reference voltage of 80%, a plasma jet speed of 8 m min^{-1} and a gas flow rate of 2000 L h^{-1}. The inserted images are CAH.

Table 2-5. Roughness values (nm) based on AFM analysis.

	Root mean square (RMS)	*Arithmetic mean (R_a)*	*Maximum peak height (R_p)*
Untreated silicone rubber	45.4	37.4	308.9
Plasma-treated superhydrophobic silicone rubber	276.7	218.7	1843.4
Plasma-treated slippery hydrophobic silicone rubber	40.0	32.5	234.8

2.4.4 Wettability studies

The superhydrophobic surfaces having low CAH exhibit water-repellency, a key element to prevent water droplets from sticking to the substrate. The superhydrophobic surface produced at optimal plasma operating conditions—reference voltage of 95%, plasma jet speed of 4 m min^{-1} and gas flow rate of 2500 L h^{-1}—had a WCA > 160° and CAH <3° even when the volume of the water droplet increased to 20 µL (Figure 2-7 (a)). Due to the excellent water-repellency of the plasma-treated surface, the water droplet maintained a spherical shape at high volume. The illustrated water-repellency arises from air trapped in the cavities between the coral-like asperities. This leads to a composite solid-air-liquid interface contrary to a homogeneous solid-liquid interface. The presence of the composite solid-liquid-air interface is responsible for the reduced adhesion between the water droplet and the substrate and produces a favorable water-repellency [13, 297]. This result points out that these surfaces are well suited for exterior applications exposed to rain of variable droplet size.

The extremely water-repellency and low adhesion properties of the prepared superhydrophobic surface were also examined by exerting pressure on the water droplet with the help of a needle tip. The severe contact process of a water droplet with the substrate can be divided into four states illustrated in Figure 2-7 (b): initial contact, tight contact, severe contact and detachment [298, 299]. In the first moment of initial contact, the droplet shape did not alter, compared to its initial spherical form. As the droplet was pushed down, during tight and severe contact, its shape showed negligible change. Even at severe contact, the water droplet maintained its spherical shape and WCA remained higher than 160°. During the detachment step, the water droplet was easily removed from the surface as if there was no adhesion between water droplet and substrate, and no trace of water remained on the surface. These observations asserted the extremely weak adhesion between water droplet and substrate by which the great water-repellency of the superhydrophobic surface was obtained. It

also indicated the consistency of the Cassie-Baxter regime in which the water droplet was not pinned to the rough surface.

To survey the dynamic behavior of a water droplet on the superhydrophobic surfaces, we performed a water droplet impact test. We used a high-speed camera to record the impingement process and bouncing behavior of a 20 µL water droplet when released from a height of 3 cm above the surface (Figure 2-7 (c, d)). On the untreated silicone rubber, the free-falling water droplet spread on the surface then retracted without leaving the substrate, confirming the full energy dissipation and adhesion of the water droplet to the untreated silicone rubber surface.

The behavior of impacting water droplets on the superhydrophobic surface consisted of three stages: spreading, retraction and rebounding (Figure 2-7 (d)). After the initial collision, the droplet spread along the radial direction until the spreading diameter reached a maximum value at $t = 4$ ms. During the spreading process, the kinetic energy of the droplet was transformed into surface energy [300, 301]. A portion of the kinetic energy was dissipated during the spreading stage, induced mainly by the surface properties, which is caused by impact and overcoming of the sliding frictional force and adhesion force on the surface [302]. Due to the low energy dissipation of the plasma-treated silicone rubber substrate, the surface energy of the droplet was much higher than the droplet in the static state. This led to the retraction process and conversion of part of the surface energy into kinetic energy. During retraction, which lasted for 12 ms, the droplet reshaped itself into a vertical liquid column to reduce its interfacial energy, and a secondary droplet was generated at the top of the droplet and separated from the main droplet at high speed. Subsequently, as the inertia force in the vertical direction overcame the sum of droplet gravity and adhesion force on the superhydrophobic surface, the droplet rebounded from the surface [302, 303]. Contact time, at which point the droplet is in contact with the surface before bouncing off, was almost 16 ms. Furthermore, the surface was so water-repellent that nine full bounces were observed. The droplet finally came to rest on the surface after almost 454 ms with the dissipation of all its kinetic energy. The number of bounces of a water droplet dropped onto a superhydrophobic surface depends on the surface microstructure, surface energy and static WCA [304].

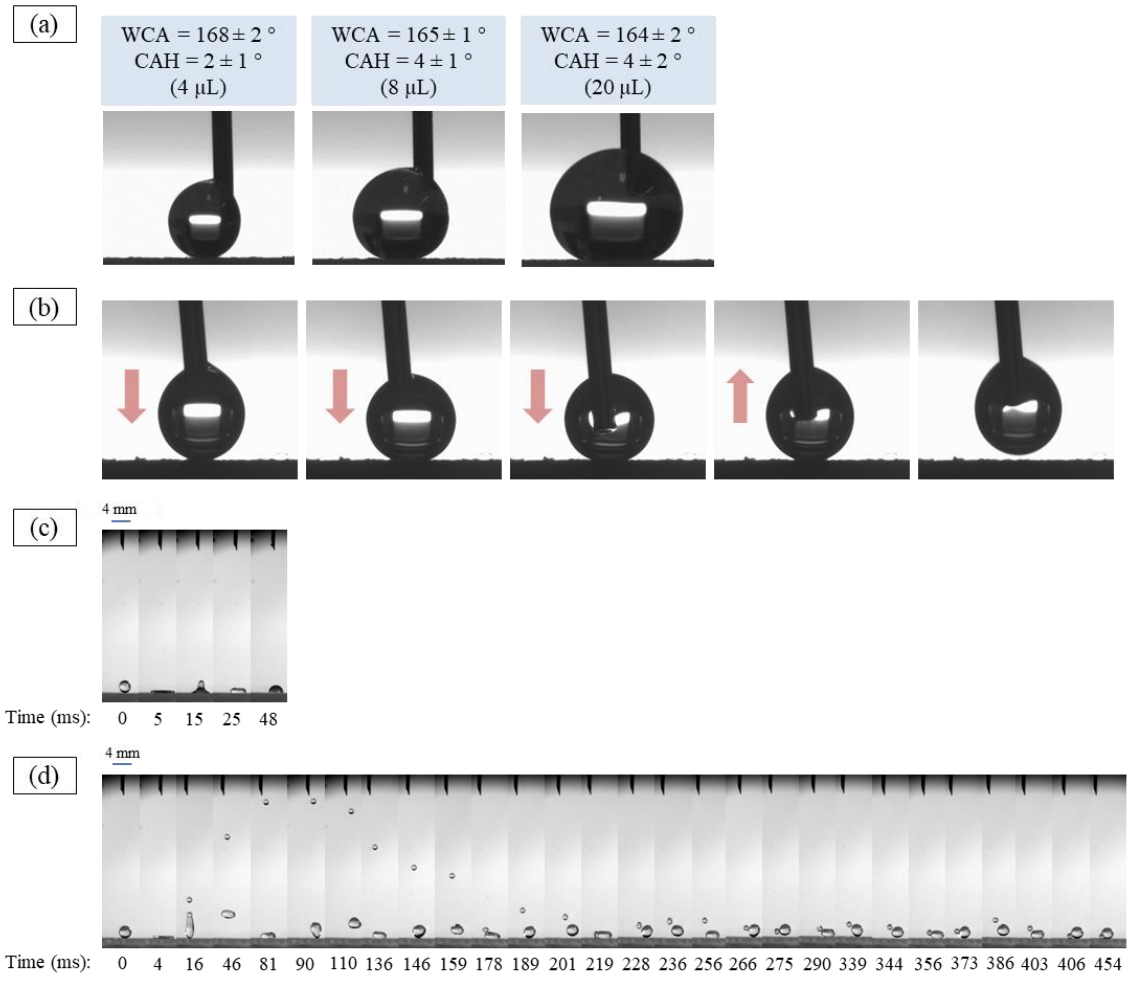

Figure 2-7. (a) The CAH of water droplets of various volumes on the superhydrophobic surface; (b) sequential images of a 4 µL water droplet before and after a severe contact with superhydrophobic surface; (c and d) sequential images of a water droplet impact on the untreated and the plasma-treated superhydrophobic surface, respectively.

2.4.5 Self-cleaning characteristics

Self-cleaning refers to the ability of a surface to remain contaminant-free by the action of water. This property is sought-after as it allows the removal of contaminants without cost, additional effort or the use of detergents [305]. Generally, the presence of suspended particles in air leads to the deposition of either dry pollution due to the wind and gravity forces or by contaminated particles dissolved in the rain falling onto the surfaces. To survey the self-cleaning property of the prepared superhydrophobic surfaces, we assessed two different scenarios: a wet condition where the surface was exposed to a contaminant solution and a dry condition where only the solid contamination applied on the surface. We examined the self-cleaning property of the prepared superhydrophobic surface at optimal plasma operating conditions (i.e., reference voltage of

95%, plasma jet speed of 4 m min^{-1} and gas flow rate of 2500 L h^{-1}). In the first stage of the wet experiment, the samples remained in the dirty solution for 90 min to allow the contaminants to settle onto the surfaces (Figure 2-8). Upon the superhydrophobic sample being removed from the dirty solution, the dirty layer slipped off the surface, returning the superhydrophobic sample to its original state (Figure 2-8 (c, d)). On the untreated substrate, however, the contaminants remained and formed a dirty layer (Figure 2-8 (b, d)).

As sedimentation and drying of the dirty solution would be expected to occur on outdoor surfaces due to warm temperatures, solar radiation and the movement of air, during the second stage of the wet experiment, the samples were left for 48 h in the dirty solution. Thus, the water evaporated allowing us to assess the self-cleaning property of these surfaces after drying. After drying, the untreated sample retained a homogeneous accumulation of contaminants across its surface. The contaminants remained fixed on the untreated surface after it had been rinsed with water for 5 s using a syringe. While the superhydrophobic surface remained clean as if it had not been submerged at all in the dirty solution. As such, it did not require cleaning with water. Videos of the self-cleaning nature of samples, based on the wet method, can be viewed in the accompanying Supplementary Video.

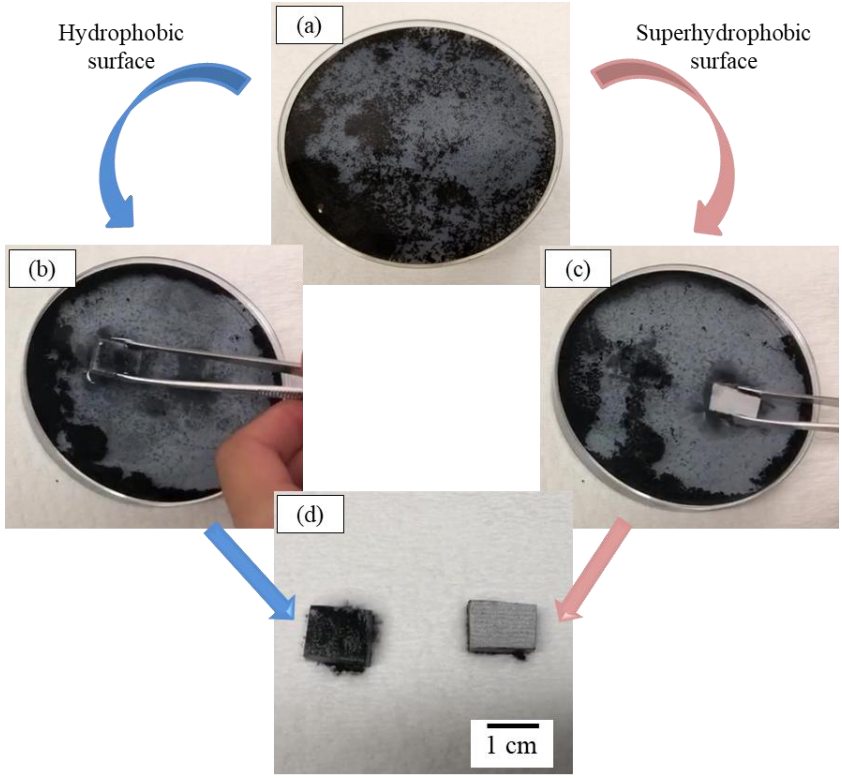

Figure 2-8. Self-cleaning property of (b; d - left side) an untreated silicone rubber and (c; d – right side) plasma-treated superhydrophobic surface after the wet contaminant approach.

Under the dry contaminant scenario, the kaolin powder that was spread over the superhydrophobic surface was absorbed instantly to the water droplet (Figure 2-9). When displacing the droplet over the surface with the help of needle tip, the dry contaminant adhered to the droplet and was removed, leaving behind a clear surface for which superhydrophobicity was restored. The water droplet did not stick to the roughened superhydrophobic surface despite the relatively high volume of water in the droplet (20 µL) that may be expected normally to favor penetration of the water into empty spaces driven by the high gravity applied to the droplet (Figure 2-9 (b)). The water droplet maintained its spherical shape upon collecting the contaminants. The great adhesion between water droplets and contaminant particles coupled with the presence of air pockets among the coral-like micro-nanostructures on the superhydrophobic surfaces leads to the adhesion of the contaminant onto the water droplet and its removal when the superhydrophobic surface is tilted at a small angle [41]. It is worth noting that a single water droplet was sufficient to clean up a considerable amount of contaminant. However, the water droplets adhered to the untreated silicone rubber surface and could not clean the kaolin contamination spread over the surface. Both the wet and dry experiments confirm the self-cleaning property of the prepared superhydrophobic surface.

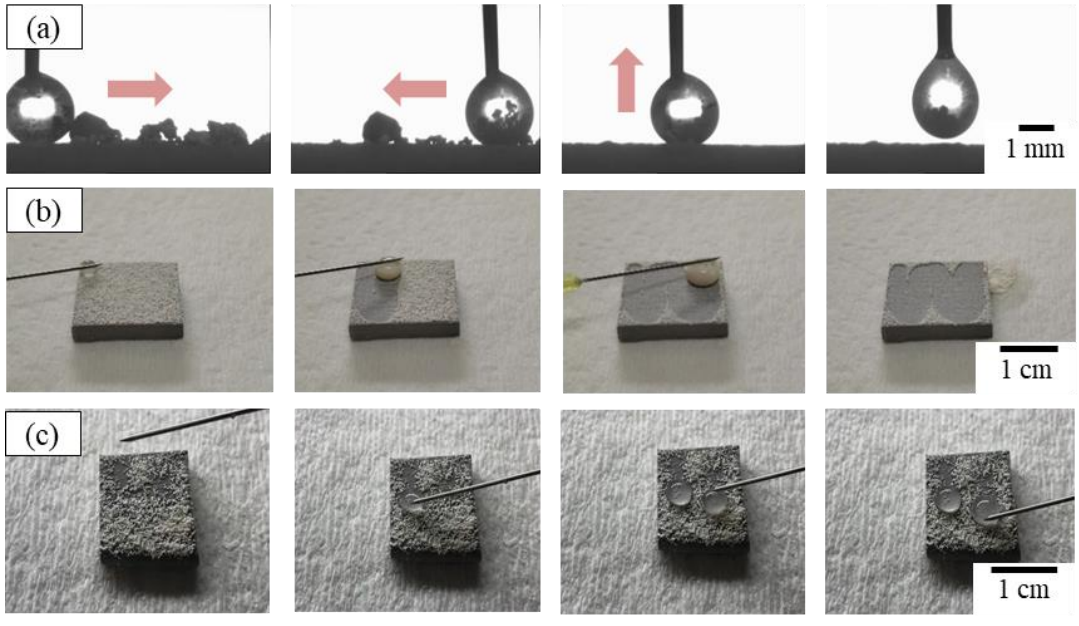

Figure 2-9. Self-cleaning property of the plasma-treated superhydrophobic surface and untreated silicone rubber subjected to the dry contaminant setup: (a) sequential photographs of the stiction of kaolin to the surface of a water droplet and the removal of kaolin from the superhydrophobic surface; (b) sweeping of a contaminated superhydrophobic surface by a single water droplet; (c) stiction of water droplets to the contaminated untreated silicone rubber surface.

2.5 Conclusion

We have presented a simple and eco-friendly approach for fabricating superhydrophobic surfaces on low surface energy materials. We developed a superhydrophobic HTV-SR surface using atmospheric-pressure plasma system that did not require a vacuum chamber. Furthermore, our approach relies on ambient air as the plasma formation gas and therefore represents an economically attractive option for industrial applications. To survey the effect of various plasma parameters on the non-wettability of the fabricated silicone rubber surfaces, we applied a DoE method based on the three independent factors of reference voltage, plasma jet speed and gas flow rate, each at three levels. At a constant gas flow rate, the increase in reference voltage and/or a decrease in plasma jet speed had a similar effect of increasing the WCA. We obtained superhydrophobic surfaces having a WCA >160° and a CAH <3° at a plasma jet speed of 4 m min^{-1} and a reference voltage of 90–100%. Furthermore, under particular plasma conditions, i.e., low reference voltage and high plasma jet speed, slippery hydrophobic surfaces having a simultaneous low CA and low CAH were achieved. FTIR analysis confirmed the gradual elimination of hydroxyl groups as reference voltage increased due to the decomposition of ATH fillers under the high temperatures of plasma treatment. SEM images illustrated the micro-nanostructures of coral-like clusters after plasma treatment. By increasing the reference voltage, the size and coalescence of clusters increased and resulted in a reduction of space between clusters and the creation of micro-roughness on the substrate. AFM confirmed this pattern of increased roughness and was consistent with our SEM observations. The entrapped air pockets within the micro-nanostructures favored the lower adhesion of water droplets onto the surface and the increased water-repellency of the substrate. The comparatively smooth surface of slippery hydrophobic samples responsible for low CAH was also confirmed by AFM analysis. The prepared superhydrophobic surfaces showed impressive water-repellency in addition to their self-cleaning property under both wet and dry contamination scenarios.

Acknowledgments

The authors gratefully acknowledge the Natural Sciences and Engineering Research Council of Canada (NSERC) for financial support.

CHAPTER 3

ARTICLE 2: ICEPHOBICITY AND DURABILITY ASSESSMENT OF SUPERHYDROPHOBIC SURFACES: THE ROLE OF SURFACE ROUGHNESS AND THE ICE ADHESION MEASUREMENT TECHNIQUE

K. Maghsoudi*, E. Vazirinasab, G. Momen, R. Jafari
Department of Applied Sciences, University of Quebec in Chicoutimi (UQAC)
555, boul. de l'Université, Chicoutimi, Québec, G7H 2B1, Canada
* E-mail: *Khosrow.maghsoudi1@uqac.ca*

3.1 Abstract

The durability of anti-wetting properties is of great importance for ensuring long-lasting superhydrophobic and icephobic surfaces that require minimal maintenance and resurfacing. Herein, we fabricated superhydrophobic silicone rubber surfaces having ultra-water repellency and icephobic properties via two industrially applicable methods: micro compression molding (μCM) and atmospheric pressure plasma (APP) treatment. We produced surfaces covered by micro-nanostructures of differing sizes. We evaluated the anti-icing properties (delayed ice formation) and de-icing properties (reduced ice adhesion strength) of the produced surfaces that were subjected to two forms of icing conditions. The well-known ice adhesion measurement techniques, i.e., the centrifuge adhesion and push-off tests, provided quantitative comparisons of the ice adhesion strength of the produced surfaces. We observed two different mechanical deformations during the ice detachment from the surfaces. Although both superhydrophobic surfaces reduced ice adhesion strength, the smaller surface micro-nanostructures produced a greater reduction in ice adhesion by favoring less ice interlocking with the surface asperities. To rigorously assess the durability of the produced surfaces, we carried out a comprehensive series of experiments that covered a wide range of real-life conditions. Under harsh environmental conditions, the surfaces maintained a water contact angle and contact angle hysteresis of >150° and <10°, respectively, thereby confirming the resistance of the superhydrophobic silicone surfaces to severe chemical and mechanical damage. In some cases where water repellency was lost, the silicone rubber surfaces demonstrated a satisfactory recovery of their anti-wetting properties.

Keywords: Superhydrophobicity; Icephobicity; Anti-icing; Ice adhesion measurement; Durability; Recovery.

3.2 Introduction

Water-repellent superhydrophobic surfaces are determined by a water contact angle (WCA) >150° and a contact angle hysteresis (CAH) or sliding angle (SA) <10°. Maghsoudi et al. [306] declared that for a material to demonstrate superhydrophobic properties, it usually fulfills two prerequisites: 1) having the non-polar groups on the surface as the hydrophobic characteristics and 2) the presence of micro-nanofeatures that roughen the surface. Among multiple approaches for fabrication of superhydrophobic surfaces, Maghsoudi et al. [307] reviewed that direct replication method including micro injection molding, micro compression molding, and hot embossing is advantageous for mass production. In addition, Vazirinasab et al. [308] demonstrated that surface treatment by atmospheric pressure plasma is an industrially conceivable facile approach. Superhydrophobic surfaces have been the focus of multiple recent studies due to their wide range of applications. Vazirinasab et al. [309] expressed that these applications include anti-wetting, anti-icing, low-adhesion, low-drag, corrosion resistant, buoyancy enhancement, and self-cleaning applications. Recently, potential applications of superhydrophobic surfaces have been studied by many researchers. Huang et al. [310] developed superhydrophobic filtrating materials for application to oil/water separation. Yuan et al. [311] showed how hierarchical superhydrophobic structures exhibited excellent adsorption capacity for fast and selective oil/water separation. Li et al. [312] studied the droplet dynamics on well-defined structured superhydrophobic surfaces which is highly important in self-transportation of droplets.

Superhydrophobic surfaces are among the best candidate surfaces for exhibiting icephobic properties. Alizadeh et al. [313] showed that such water-repelling surfaces can delay ice formation, known as the anti-icing property, and Momen et al. [314] observed reduced ice adhesion strength for superhydrophobic surfaces, known as the de-icing property. Ice formation on a superhydrophobic surface having micro-nanostructures is affected by (1) the reduced area in contact between the substrate and water droplets due to the high WCA. Yancheshme et al. [315] stated that this scenario leads to a reduced heat transfer via conduction, (2) Shen et al. [316] found that the trapped air between the surface micro-nanostructures acting as an insulating layer reduces the heat transfer, (3) Eberle et al. [317] considered the limited number of sites at the solid-liquid interface available for the heterogeneous nucleation of ice, and (4) Yao et al. [318] took the shorter rebounding time—

shorter rest time—of water droplets compared to the nucleation time into account. Moreover, Ling et al. [319] showed that the reduced ice adhesion strength was due to the formation of microcracks caused by surface roughness causing interfacial stress concentrations, and the reduced contact area between the formed ice and the surface due to the limited solid–liquid contact area. However, Ling et al. [319] also stated that surface roughness may negatively affect icephobicity due to the interlocked ice within the surface structures. This mechanical interlocking is governed by the stability of the Cassie-Baxter regime. Although there is, on one hand, a fully Cassie-Baxter state and, on the other, a Wenzel state, Cansoy et al. [320] showed that an intermediate state can exist where a water droplet penetrates partially into the surface structures. Li et al. [321] declared that the degree of this penetration can affect the mechanical interlocking of ice producing either a "Cassie ice" or "Wenzel ice". Consequently, the surface geometry has a decisive effect on the icephobic behavior of the produced surfaces. Among the various surface geometries, including microstructures, nanostructures, and hierarchical micro-nanostructures, He et al. [322] determined that hierarchical micro-nanostructures have demonstrated the lowest ice adhesion strength. Moreover, the effect of ice type on the icephobic properties of a certain surface is worth studying. According to Ryerson [323], atmospheric icing phenomena are divided into glaze ice, hard rime, and frost having a density of 0.7-0.9, 0.3-0.7, and <0.1 g/cm^3, respectively. Rime ice and frost are formed from the fogs and in-clouds containing supercooled droplets, while glaze ice can be produced by both the precipitation (freezing rain or drizzle) and in-cloud icing. Stenroos [324] reported that the droplet sizes vary between few μm to 50 μm for the in-cloud icing and from 100 μm to several mm for the precipitation icing. Fortin et al. and Liu et al. [325, 326] reported that the greatest ice adhesion strength belongs to glaze ice. Work et al. [327] reviewed that in many studies, the ice adhesion strength of a surface is evaluated against bulk ice rather than atmospheric icing. Consequently, to rigorously assess the icephobic properties of a micro-nanostructured surface, the influence of various ice types should be studied. The ice adhesion measurement technique should also be added to this list. These techniques include centrifugal adhesion test (CAT), shear strength tests (e.g. push-off and zero-degree cone tests), and tensile strength test. For a certain surface, the ice adhesion results obtained from the different techniques are not necessarily identical. Rønneberg et al. [328] claimed that this difference can stem from either the nature and conditions of the employed adhesion test or the behavior of the ice-solid interface subjected to the ice detachment.

Although multiple applications benefit from superhydrophobic surfaces, the durability of these surfaces against mechanical forces and chemical media remains questionable. Golovin et al. [329] described that in general, superhydrophobic surfaces prone to mechanical or chemical damage either lose surface roughness or the low surface energy chemical bonds. This fragility can lead to a transition from the Cassie-Baxter state to the Wenzel state, a state that is energetically more favorable for the water droplet. Milionis et al. [330] showed that the transition to the Wenzel state induces a strong pinning that increases the adhesion between the water droplet and the substrate; the result is a loss of water repellency or anti-wetting performance of the surface. The lack of a defined standard procedure for evaluating the durability of different types of superhydrophobic surfaces has led to a myriad of set-ups and procedures to measure surface durability. These durability measurements are divided into tests of mechanical durability and chemical resistivity. Mechanical durability analyses include abrasion resistance under a specific force, wear resistance by rubbing the surface, the tape-peel tests, scratch tests, and fatigue testing. The chemical durability analyses include immersion in aqueous solutions of varying pH, and exposure to UV light, as investigated. Some analyses, such as water droplet impacts and the ultrasonic treatment of surfaces in water involve both mechanical and chemical testing. Therefore, a comprehensive set of tests is required to assess the durability properties of a superhydrophobic and icephobic surface.

Although many investigations have reported changes to ice adhesion strength when surfaces are subjected to various mechanical tests as reviewed by Work et al. [327], only few studies [331-334] have reported changes of the WCA and CAH after several cycles of icing/de-icing. Of the published results, the WCA generally decreases and the CAH increases after multiple cycles. The adhesive strength and the mechanical bonding between the fabricated micro-nanostructures and the substrate are critical in explaining the wettability of the surfaces following the icing/de-icing cycles. Lazauskas et al. [335] demonstrated that these cycles can transform a spiky surface morphology into a bumpy surface when the nanostructured protrusions become damaged.

Silicone rubber material has exhibited hydrophobic-recovery properties where low molecular weight silicone (LMWS) chains diffused from the bulk material to the surface. Yan et al. [336] showed that this self-healing has also been occurred via the reorientation of methyl groups from the bulk material to the surface and the reorientation of hydroxyl groups from the surface into the bulk material by the partial segmental movement

of silicone rubber chains. Hillborg et al. [337] also considered the condensation of silanol groups for such behavior. While Maghsoudi et al. [306] observed that the migration of LMWS to the surface dominates the hydrophobic recovery of polluted silicone rubber surfaces, Liu et al. [338] considered the conformational reorientation of groups as the main responsible for the hydrophobic recovery of surfaces when silicone rubber chains become aged or oxidized. Thus, the ability of a surface to recover its anti-wetting properties is as important as the evaluation of the durability of superhydrophobic surfaces.

In the present study, we produce superhydrophobic silicone rubber surfaces using two industrially applicable approaches, i.e., micro compression molding (μCM) and atmospheric pressure plasma (APP) treatment. The produced surfaces showed having a high WCA and very low CAH. The low CAH of both produced surfaces was created by micro-nanostructures that established a Cassie-Baxter regime. Owing to this low CAH, these produced surfaces demonstrated icephobic properties. We assessed the anti-icing and de-icing properties by measuring freezing delay times and ice adhesion strength, respectively. We applied two common methods to measure ice adhesion strength, the centrifuge adhesion (CAT) and push-off tests under various icing conditions. This is, to our knowledge, the first study to investigate the ice adhesion strength by two methods and two icing conditions to provide a comprehensive comparison. In addition to applying repetitive icing/de-icing cycles to study the durability of the produced surfaces, we also studied the durability of the surfaces under mechanical and chemical forces. We also rigorously examined the recovery of surface hydrophobicity/superhydrophobicity of the silicone surfaces in cases where the superhydrophobicity of a surface was lost.

3.3 Materials and methods

3.3.1 Fabrication of superhydrophobic silicone rubber surfaces

We fabricated the superhydrophobic silicone rubber surfaces using a direct replication method (via a μCM, Carver Inc., USA) and an atmospheric-pressure plasma machine (Plasmatreat GmbH, Germany) (Figure 3-1). A chemical-etching method—15 wt.% HCl solution for 2 h—created micro-nanostructures on an A6061 aluminum template. The curing time of 4.7 min, mold temperature of 149 °C, and molding pressure of 49.7 MPa were selected as process conditions. The selected optimal plasma parameters were a reference voltage of 100%, plasma jet speed of 4 $m \cdot min^{-1}$, gas flow rate of 2500 $L \cdot h^{-1}$, plasma frequency of 21 kHz, a cycle time of

100%, as well as a distance between nuzzle and substrate of 8 mm. The plasma jet passed along the surface four times.

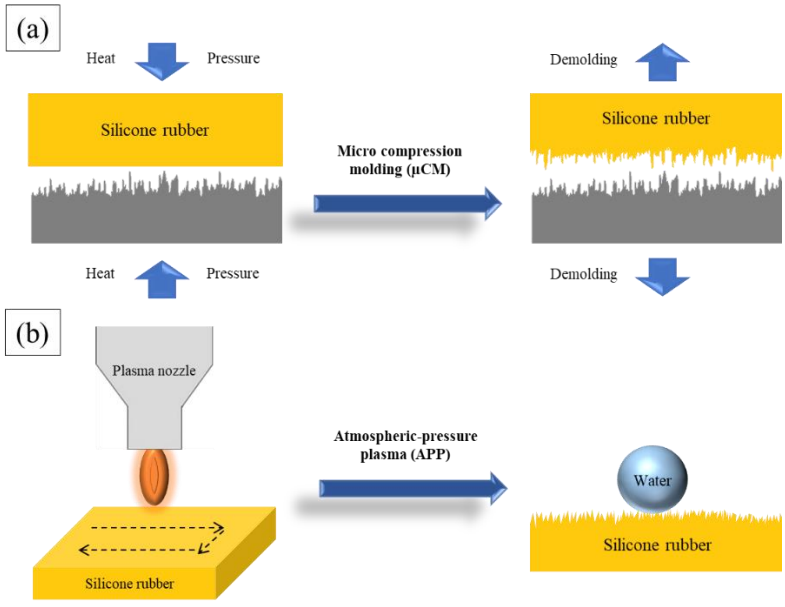

Figure 3-1. Schematic of the (a) micro compression molding (μCM) and (b) atmospheric-pressure plasma (APP) techniques to create a micro-nanostructured silicone rubber surface.

3.3.2 Surface characterization

A Kruss™ DSA100 goniometer determined the WCA and CAH at 25 ± 0.5 °C. We deposited a 4-μL water droplet onto the sample surface to determine the WCA using the Young-Laplace approximation. The CAH equaled the difference between the advancing and receding contact angles when the water droplet moved across the surface. To ensure accuracy and reproducibility, we measured the angles at five points on each sample; the average and standard deviation of the measurements are reported. We relied on scanning electron microscopy (SEM) (JSM-6480 LV SEM manufactured by JEOL Japan) to observe the produced surfaces, and we applied a thin layer of gold-palladium alloy coated on the silicone surfaces to enhance imaging quality. An optical profiler (Profil3D Filmetrics, USA) measured surface roughness. The line and area roughness values were calculated based on the ASME B46.1 2D and ASME B46.1 3D standards, respectively. To analyze the chemical functions on the surface based on an evaluation of the surface chemical composition, we ran Fourier transform infrared spectroscopy (FTIR) using a Cary 630 FTIR Spectrometer (Agilent, USA) in ATR (attenuated total reflection) mode to acquire the highest quality spectra in the infrared range of 400–4000 cm^{-1}. A 4-μL water droplet was observed during the evaporation process, and the images were captured by a digital camera placed on a Kruss goniometer machine. The camera images were set at 8× magnification. The software

(DSA1 v 1.9, Drop Shape Analysis for DSA100) calculated the contact line length and the contact area with the substrate as a function of time. We therefore monitored changes in the contact line length between the droplet and the surfaces. The temperature of all experiments was identical to that used during the WCA tests.

3.3.3 Icephobic properties

The WCA of surfaces at below-zero temperatures as well as the freezing delay times were determined in the cold chamber of the Kruss machine. The Peltier cooling stage can reach -30 °C with a control precision of 0.1 °C. The delay in the initiation of water droplet freezing was reported as the freezing delay time. The humidity variation is limited in the closed chamber of the Kruss machine. Moreover, to avoid the influence of condensation on the measurements we used anhydrous calcium sulfate desiccants (Indicating DRIERITE impregnated with cobalt chloride). We determined the ice adhesion strength of the produced samples via two separate methods to obtain a comprehensive comparison of the icephobic properties under various conditions.

For the centrifuge test, samples were iced under freezing drizzle conditions in a climatic chamber at -8.0 ± 0.2 °C by spraying supercooled water microdroplets onto the surfaces. Such conditions resulted in the deposition of glaze ice from the water droplets, having a median volumetric diameter (MVD) of 324 µm on an 1100 ± 70 mm^2 surface and a thickness of around 7 ± 1 mm. Droplet speed corresponded to their free-fall values in the vertical airflow. The samples were iced for about 35 minutes to obtain around 5.5 ± 0.5 g of ice. All samples were iced simultaneously. The iced samples were tested individually in a centrifuge placed in a climatic chamber at -10.0 ± 0.2 °C. The centrifugal force (F) was calculated as $F = mr\omega^2$, using the detached ice mass (m), the speed at which the detachment occurred (ω), and the beam radius (r). The ice adhesion shear stress was then calculated as $\tau = F/A$, where A is the iced area. The reduction in ice adhesion was defined as [τ (pristine silicone rubber) - τ (superhydrophobic silicone rubber)]/ τ (pristine silicone rubber).

In the push-off test, a thin 1-cm diameter cylindrical plastic mold was placed onto the substrate. We then filled the mold with deionized water and placed the mold and substrate into a cold chamber at -10.0 ± 0.2 °C for 24 h to form an ice cylinder. After removing the sample from the cold chamber, we placed the test sample onto the holder and fixed the sample using two screws. A remote computer-controlled interface then controlled the turning of the screws at a fixed rate of 0.05 $mm \cdot s^{-1}$ so that the sample holder was pushed gradually toward the force gage. The force gage measured the shear force ten times per second until the ice detached. The adhesion stress was therefore calculated knowing the maximum force and the icing area. We

calculated the corresponding de-icing energy for each surface using the area under the developed force-displacement curves.

3.3.4 Durability properties

We used an Elcometer 3000 Clemen Unit (Elcometer, USA) with 4000-grit silicon carbide sandpaper to evaluate the durability of the superhydrophobic surfaces against abrasion. The applied pressures on the samples' surfaces during abrasion were 1.6 kPa, 3.2 kPa, and 6.4 kPa. We ran the process repeatedly over 2.5 cm of the surface. We measured the WCA and CAH after each block of 50 abrasion cycles.

We also evaluated the durability of the produced silicone rubber surfaces via a finger-press test where a vertical pressure of 80 ± 8.8 kPa was applied to the surface by a bare thumb. We measured the average force applied by a bare thumb using a digital force gauge. To reduce the measurement error, we did these measurements while the hand was stationary. We also carried out a tape-peeling test by applying and removing a pressure-sensitive Scotch-600 tape at approximately 30 kPa pressure to the surface. To test surface durability when subjected to ultrasonication, the surfaces were placed into 100 mL of deionized water in a Branson 2510 ultrasonication bath. After each 60-min interval, we removed the sample, dried the sample for 15 min at 70 °C, then measured the CA. In the continuous water droplet impact durability test, water droplets produced at a rate of 1 mL·min-1 from a distance of ~10 cm above the surface fell onto the surface that was placed at a slope of ~5°. The impact point was marked for WCA measurements. Each cycle required 1000 s, during which time ~17 mL water dropped onto the surface. The test ran for 7000 s, i.e., ~120 mL of water in total.We used buffer solutions having a pH of 2 and 12 as the acidic and alkaline media and used also deionized water (pH 7) to study the durability of the produced surfaces over 15 days. After a 3-day interval, we removed each sample from the solution, rinsed the sample ultrasonically for 15 min, dried the sample at 70 °C for 15 min, and we then measured the WCA and CAH. We used a QUV accelerated weathering tester for the accelerated UV-weathering test to evaluate the destruction of the surface anti-wetting properties when subjected to simulated outdoor conditions within a controlled laboratory setting. The tests were conducted according to ASTM G154 using UVA-340 fluorescent lamps and a test cycle of 8 h, a temperature of 60 °C, and an irradiance of 0.89 $W \cdot m^{-2}$.

Given the extensive use of HTV-SR in high-voltage insulators, it is relevant to assess the durability of our produced surfaces against harsh weather conditions, e.g., sandstorms. We sandblasted our samples in a

sandblasting cabinet under conditions of air blow pressure at 20 psi, an air blower velocity of 10 m/s, a sand feed of 0.07 g/s—thus 4.2 g of sand blown onto the surface after 1 min of air blowing. This amount corresponds to a single sandstorm in Borg-El-Arab, Egypt. Given that approximately 20 sandstorms occur per year at this location, a 20-min test simulates one year of exposure to sandstorm conditions [339]. The distance between the gun and the sample surface was 25 cm, and the impact angle was set at 90°. We used silicon carbide (SiC) particles to conduct the tests. During a sandstorm, the height to which sands and dust can reach depends on wind strength and the amplitude of wind velocity fluctuations. This height thus varies from 1 m above the ground to 15.24 m. However under similar conditions, dust or finer sediments (<63 µm) are lifted higher than coarse sand (>63 µm) [340]. On the other hand, a typical height of an electrical transmission tower is 15–50 m; we therefore used a particle size of 18 µm for the test.

3.4 Results and discussion

3.4.1 Surface characterization

The WCA and CAH of the pristine silicone rubber surface were 115 ± 1.8° and 43.4 ± 1.9°, respectively. A WCA of 166.6 ± 1.9° and 165.8 ± 1.3° and CAH of 0.6 ± 0.3° and 1.1 ± 0.6° for the µCM and APP-treated silicone rubber surfaces, respectively, testified to the superhydrophobic property of the produced samples. The presence of micro-nanostructures on the silicone surfaces satisfied the required condition of "low surface energy material and surface roughness" to achieve superhydrophobicity. The surface profiles and SEM images of the surfaces at various magnifications are presented in Figure 3-2. Surface morphologies differed for each surface. Both 1D roughness (line roughness) and 2D roughness (area roughness) values were reported for comparative purposes (Table 3-1). The skewness coefficient (S_{sk}), representing the symmetry level of the surface height relative to the mean plane, and the kurtosis coefficient (S_{ku}), which describes the sharpness of the probability density of the profile, are also provided. Compared to a pristine surface, the micro compression molding process significantly increased surface roughness. The root-mean-square height (S_q) of the µCM surface increased ~5 times. Although the APP-treated surface possessed almost the same S_q as the pristine surface, the skewness and kurtosis values showed jagged surface structures with considerably higher peaks and lower valleys than those on the pristine surface. This observation was similar to that observed in case of a plasma treated Teflon surface compared to a non-treated Teflon surface [341].

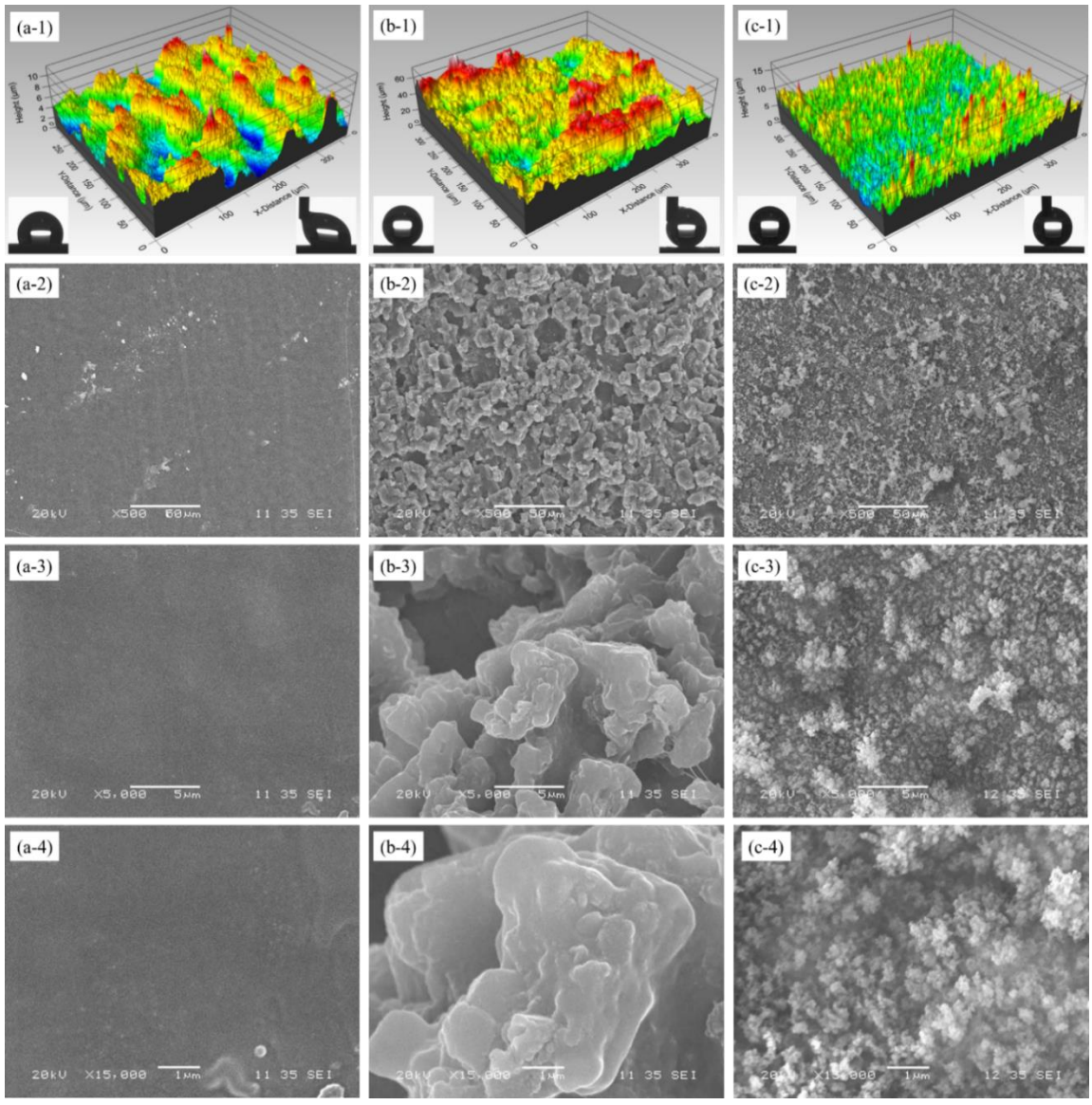

Figure 3-2. The 3D surface profiles of the (a-1) pristine, (b-1) µCM, and (c-1) APP-treated silicone rubber surfaces. SEM images of the (a-2, a-3, and a-4) pristine, (b-2, b-3, and b-4) µCM, and (c-2, c-3, and c-4) APP-treated silicone rubber surfaces. Inset images represent the water contact angle and contact angle hysteresis of the corresponding surfaces.

Table 3-1. Area and line roughness values obtained from profilometry analysis.

	Pristine	**µCM**	**APP**
Area roughness (µm)			
Maximum peak to valley height (S_t)	11.68	71.54	16.38
Arithmetic mean height (S_a)	1.46	7.43	1.19

Root mean square height (S_q)	1.76	9.40	1.53
Skewness (S_{sk})	0.07	0.09	0.33
Kurtosis (S_{ku})	2.38	3.008	3.99
Line roughness (µm)			
Maximum peak to valley height (R_t)	5.196	15.16	5.79
Arithmetic mean deviation (R_a)	0.70	2.54	0.70
Root mean square deviation (R_q)	0.89	3.17	0.91

FTIR analysis assessed the presence of chemical bonds on the produced silicone rubber surfaces (Figure 3-3). The pristine and µCM surfaces showed identical absorption spectra of Si–$(CH_3)_2$, Si–O–Si, Si(CH_3), and –OH at the approximate positions of 805–855 cm^{-1}, 1000–1110 cm^{-1}, 1245–1275 cm^{-1}, and 3200–3550 cm^{-1}, respectively [21, 103]. For the APP-treated surface, the Si-containing bonds, in particular for Si–$(CH_3)_2$, were modified. Under plasma treatment, the Si–CH_3 bonds are prone to breakage due to their relatively low binding energy [342]. Moreover, the –OH spectrum almost vanished. The disappearance of hydroxyl groups (–OH) is attributed to the endothermic decomposition of alumina trihydrate (ATH) particles at high temperatures during the plasma treatment [21].

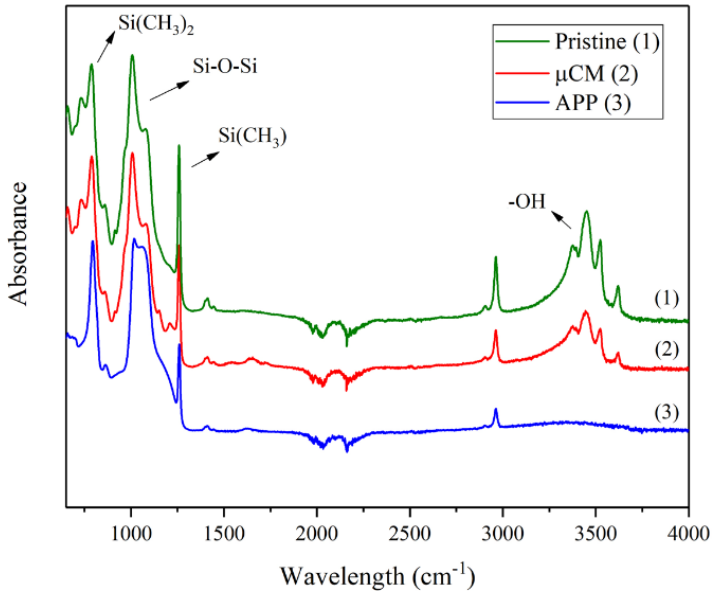

Figure 3-3. FTIR spectra for (1) pristine, (2) µCM, and (3) APP-treated silicone rubber surfaces.

The CAH values of the produced superhydrophobic surfaces demonstrated that the created roughness led the surfaces to fall into a Cassie-Baxter state. However, we then carried out the droplet evaporation test to

obtain more information about the kinetics of the interfacial interactions. Evaporation occurs due to the diffusion and/or convection of water molecules into the environment. Three modes of evaporation explain the changes in the WCA and contact line (CL) of a water droplet on a solid surface in calm air. Depending on the WCA or CL being constant or decreased, the modes are the constant contact line (CCL), the constant contact angle (CCA), and mixed modes. The emergence of each mode depends highly on surface geometry and chemistry, which directly influences the wetting regimes [343].

Figure 3-4 presents the evolution of WCA and CL due to the evaporation of small water droplets placed on hydrophobic and superhydrophobic surfaces. On the superhydrophobic surfaces, the water droplets underwent a linear decrease in CL and a gradual reduction of WCA. These observations showed the mobility of the CL due to the low CAH of the superhydrophobic surfaces. Over time, the water droplet preserved its initial marble-like shape by which a consistent Cassie-Baxter regime could be confirmed [344]. On the pristine surface, however, the steep slope of WCA reduction, with the increase in CL during the first stages of evaporation, and followed by a sharp drop at later stages, indicated the high adhesion of the water droplet to the solid surface. The greater adhesion of the droplet to the pristine surface relative to its adhesion to the superhydrophobic surfaces caused greater evaporation from the upper portion of the droplet on the pristine surface rather than along the triple liquid/solid/air line. This causes the droplet to be flattened on the surface, thereby leading to a decreased WCA for the pristine surface. Moreover, the pinned CL of the pristine surface over the mobile behavior of the CL on the superhydrophobic surfaces led to a different water droplet duration. The longer duration of a water droplet on a superhydrophobic surface, relative to that on a pristine surface, resulted from the high aspect ratio of the droplet, which led to a longer thermal resistance path, and the low effective thermal conductivity of the surface due to the presence of air pockets [345]. Moreover, three possibilities exist for water droplet evaporation on superhydrophobic surfaces. Evaporation can occur from the upper portion of the droplet, from the triple line, and from the contact line. The latter causes the presence of a water gas phase within the structures of the superhydrophobic surfaces. Comparing the behavior of the water droplet on the µCM and APP-treated superhydrophobic surfaces over time revealed that the presence of larger structures on the µCM surface facilitated a greater contact between the water liquid phase and water gas phase trapped within the surface structures. Consequently, the WCA of the µCM surface experienced a greater reduction than that of the APP-treated surface over time.

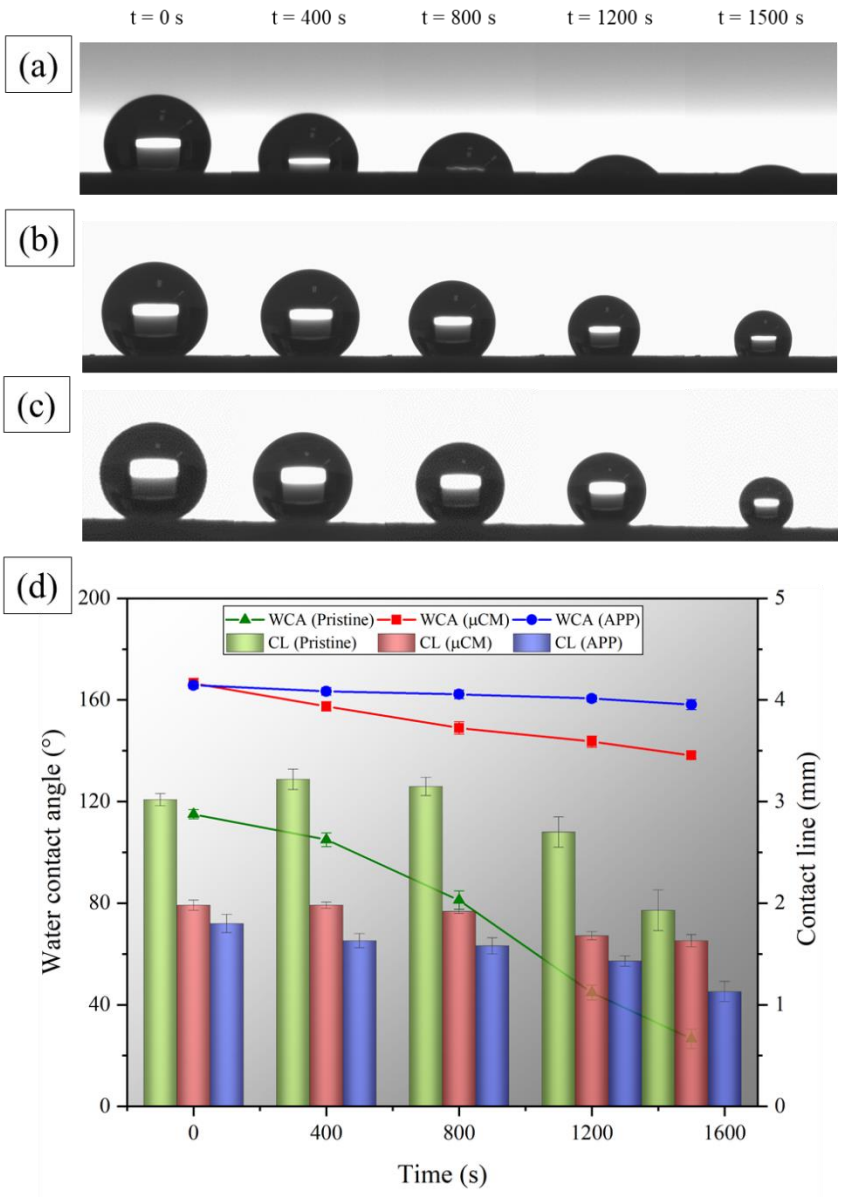

Figure 3-4. Images of droplet evaporation on (a) pristine, (b) μCM, and (c) APP-treated silicone rubber surfaces. (d) Changes to the water contact angle and contact line over time for each surface.

3.4.2 Icephobic properties

In the development of icephobic surfaces, two main properties are usually considered: anti-icing and de-icing. Anti-icing refers to a property of surface to delay or reduce ice accretion, whereas the de-icing approach is attributed to the removal of formed ice on the surface [346]. The anti-icing property of the produced surfaces was examined through the measurement of the WCA at below-zero temperatures and the freezing

delay. The de-icing property, however, was examined using measurements of the ice adhesion strength based on the centrifuge and push-off tests.

3.4.3 Anti-icing properties

To assess the behavior of the produced surfaces at supercooled temperatures, we measured the variation of WCA at various temperatures (Figure 3-5 (a)). The WCA decreased for all surfaces at below-zero temperatures. This decrease was expected and can be attributed to water surface tension at low temperatures [347]. At low temperatures, the surface tension of the water droplets strengthens, thus leading to an increase in the internal pressure of a droplet and may provoke a transition from a Cassie-Baxter to a Wenzel regime [348]. The APP-treated surface displayed a relatively higher WCA than that of the µCM surface at freezing temperatures. This difference can be attributed to the better functionality of the lower surface roughness on the APP-treated surface compared to µCM surface roughness in the Cassie-to-Wenzel transition at freezing temperatures. A close inspection of the curve slope of each surface revealed that the WCA of the APP-treated surface decreased slower than that of the WCA for the µCM surface at temperatures between 15 and -10 °C. However, below -10 °C, the WCA of both surfaces decreased monotonically due to the increased internal pressure of the droplet and a possible wetting regime transition.

We also present the results of freezing delay for three temperatures: -15 °C, -20 °C, and -25 °C (Figure 3-5 (b)). We did not consider the freezing delays at -5 °C and -10 °C given that they were too long for this experiment. We observed a marked delay in freezing on the superhydrophobic surfaces due to the presence of micro-nanostructures when compared to the pristine surfaces, which lack these structures. As an initial explanation of such behavior is the reduced contact area between the water droplet and the surfaces when WCA is high. As such, the thermal conductivity decreased dramatically for superhydrophobic surfaces compared to the pristine surface. In addition, the delay in freezing time stemmed from the micro air pockets trapped between the surface asperities to therefore act as a thermal barrier. Consequently, the formation of micro-nanostructures on the superhydrophobic surfaces led to less heat dissipation than observed from the smooth pristine surface [349]. Therefore, the greater the volume of a trapped air pocket, the longer the freezing delay. Using the profilometry technique, we determined that, compared to the pristine surface, the µCM and APP-treated surfaces entrapped 14.2× and 4.7× more air, respectively, within their surface structures. At -15 °C, the µCM surface showed a ~40% greater delay in freezing time compared to the APP-treated surface that had a relatively

greater abundance of nanostructures. This difference was most significant at -25 °C. As for the µCM surface, the freezing delay time was ~2.5× greater than that of the APP-treated surface. This illustrates that surface roughness has a more considerable contribution to the freezing process at lower temperatures.

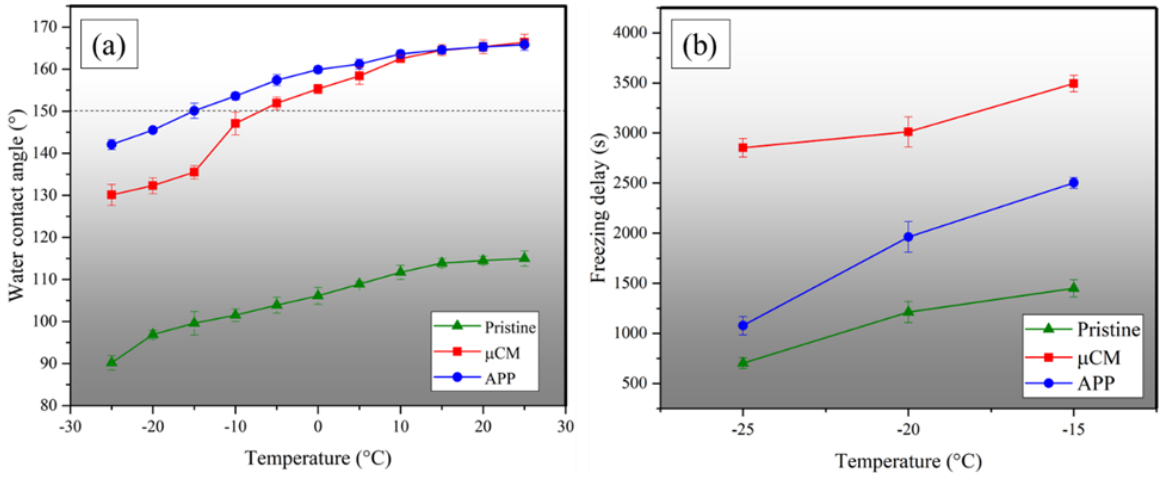

Figure 3-5. (a) Variation in water contact angle and (b) freezing delay at various temperatures for the pristine, µCM, and APP-treated surfaces (the dashed line in (a) shows the threshold of superhydrophobicity).

3.4.4 De-icing properties

Through the push-off test, it was observed that both superhydrophobic surfaces reduced ice adhesion strength. While de-icing of the pristine surface required a pressure of 132.8 kPa, the µCM and APP-treated surfaces required only 90.1 kPa and 32.9 kPa, respectively, to become de-iced during the first icing/de-icing cycle (Figure 3-6 (a)). The energy required for de-icing the pristine surface was ~30 mJ, whereas the µCM and APP-treated surfaces required only 8.75 mJ and 0.51 mJ, respectively (Figure 3-6 (b)). Regarding the shape of the produced curves (Figure 3-6 (b)), it can be concluded that the pristine and µCM surfaces showed the same behavior when de-icing, the plastic deformation of ice [350]. In this case, the applied force to the ice pillar increases gradually until the force overcomes the adhesion force between the ice and top of the surface structures and detaches the interlocked ice from the surface asperities. The lower force required for the µCM surface, relative to the pristine surface, relates to the lower ice-surface contact area due to the higher WCA of the µCM surface and less interlocked ice between the surface asperities. However, the APP-treated curve showed a very different behavior, i.e., elastic deformation. A sudden jump in the curve was observed at the de-icing point showing that the amount of interlocked ice was negligible, and the applied force was only required to overcome the adhesion of ice to the top of the features [350]. Thus, there is a similarity between the de-icing

behavior of the pristine and μCM surfaces, a behavior that is in sharp contrast with that of the APP-treated surface.

The push-off test was repeated seven times on each surface to assess the durability of the surfaces under repetitive icing/de-icing cycles. The ice adhesion strength of the μCM surface did not necessarily increase (Figure 3-6 (c)), and in some cases, ice adhesion strength was even lower after the first cycle of the test, e.g., cycles 2 and 5. This testifies to the durability of the μCM surface micro-nanostructures during the de-icing process. The ice adhesion strength of the APP-treated surface, on the other hand, increased gradually after the 4^{th} cycle, related to the removal of nanostructures during ice detachment (discussed in detail below).

We observed almost identical trends when the centrifuge tests assessed ice-covered surfaces under conditions of freezing drizzle (Figure 3-6 (d)). The pristine silicone rubber surface showed an ice adhesion strength of about 120 ± 3.6 kPa; both superhydrophobic surfaces reduced the ice adhesion strength. The adhesion strength of the μCM surface did not significantly increase (even at the 6^{th} cycle, the ice adhesion strength remained low), while that of the APP-treated surface increased significantly through the seven icing/de-icing cycles. Thus, ice adhesion to the μCM surface depended highly on the probability that ice interlocked into the surface structures, while the increased ice adhesion strength of the APP-treated surface stemmed from the gradual deterioration of nanostructures. The SEM images of the surfaces after the 7^{th} icing/de-icing cycle are shown in Figure AI-1.

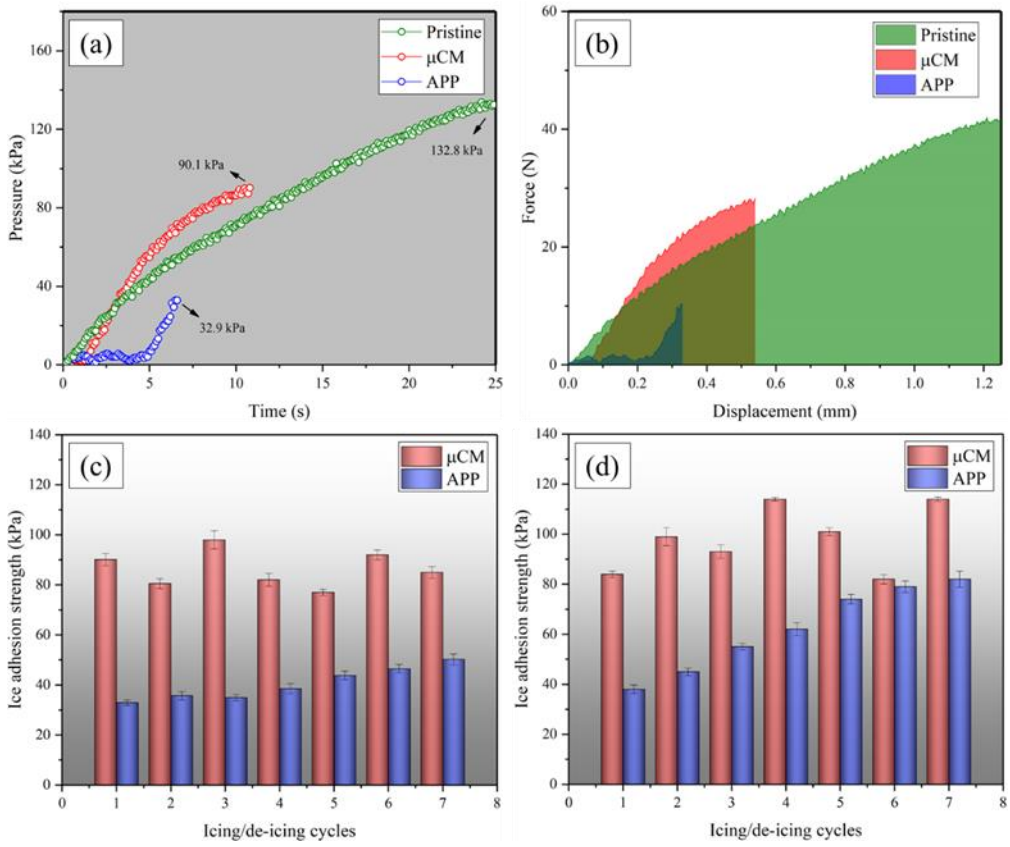

Figure 3-6. (a) De-icing pressure required for surfaces in the push-off test and (b) the corresponding de-icing energy of each surface. Ice adhesion strength for repetitive icing/de-icing cycles for the (c) push-off and (d) centrifuge tests.

Compared to the untreated silicone rubber surface, ice adhesion reduction varied between ~26% and ~42% for the µCM surface and decreased ~75% to ~62% for the APP-treated surface over seven icing/de-icing cycles in the push-off test (Table 3-2). In the centrifuge test, the ice adhesion strength decreased ~30% for the µCM surface and ~68% for the APP-treated surface after the first cycle (Table 3-2Table 3-2). The APP-treated surface showed a better de-icing property at each cycle although also showed a significant loss of its de-icing properties, whereas the µCM surface exhibited a lower reduction in ice adhesion but showed a greater durability against repetitive icing/de-icing cycles. The ice adhesion reduction factor (ARF) values—usually reported according to the ice adhesion strength of bare aluminum—offer a better understanding of the de-icing properties of the produced surfaces (Table AI-5).

In terms of the de-icing properties of surfaces having hierarchical micro-nanostructures, surfaces having a lower surface roughness produced a lower ice adhesion. This relates to the interlocking of ice into the surface structures, which can result in enhanced adhesion strength. Davis et al. [351] observed that among three

surfaces having arithmetic mean surface roughness values of 8.7 µm, 2.7 µm, and 1.6 µm, the lowest ice adhesion strength was obtained for the surface having the lowest surface roughness. A comparison of the root mean square height (S_q) of the µCM and APP-treated surfaces (9.40 and 1.53, respectively) confirms this observation. However, higher surface roughness can improve surface durability against repetitive icing/de-icing cycles.

Table 3-2. The ice adhesion reduction values for the µCM and APP-treated surfaces during the push-off and centrifuge tests.

Ice adhesion reduction (%)	Icing/de-icing cycles		1	2	3	4	5	6	7
	push-off	µCM	32.3 ± 1.9	39.5 ± 2.3	26.3 ± 2.9	38.3 ± 1.9	42.1 ± 2.3	30.8 ± 1.9	36.1 ± 1.7
		APP	75.3 ± 1.7	73.2 ± 1.9	73.8 ± 2.6	71.0 ± 1.9	67.1 ± 1.3	65.0 ± 2.3	62.2 ± 1.7
	centrifuge	µCM	30.0 ± 1.3	17.5 ± 3.6	22.5 ± 2.7	15.0 ± 0.7	15.8 ± 1.6	31.7 ± 1.9	15.0 ± 0.7
		APP	68.3 ± 1.7	62.5 ± 1.5	54.2 ± 1.3	48.3 ± 2.6	38.3 ± 1.9	34.2 ± 2.3	30.8 ± 3.3

The differing results of the two measurement methods for ice adhesion (push-off test and centrifuge test) may stem from a difference between the type of ice formed in each test. In the push-off test, a non-impact bulk ice forms on the surface by placing a water pillar on the surface, and the icephobic behavior of the surfaces depends highly on the Cassie-Baxter consistency during the icing process. If the micro-nanostructures resist the penetration of water into the surface asperities before icing, a non-interlocked ice (Cassie ice) can form on the surface and produce a low ice adhesion strength. However, in the centrifuge test, the surfaces were covered with glaze ice produced by freezing drizzle; freezing drizzle represents one of the most severe icing conditions where the supercooled microdroplets can penetrate the surface structures. Therefore, the ice adhesion strength in the centrifuge test depended highly on the icing condition parameters, particularly the MVD [234]. The APP-treated surface, with reduced surface roughness, resisted the penetration of water microdroplets (size of 324 µm), whereas the water microdroplets could penetrate partially into the µCM surface structures producing a higher ice adhesion strength. The WCA and CAH of the produced surfaces were measured after the 7th cycle of icing/de-icing in both the push-off and centrifuge tests (Table AI-6). Both surfaces presented a high WCA and low CAH to demonstrate the stability of water-repellency after multiple icing/de-icing cycles. The photographs of each surface at the 1st and 7th icing/de-icing cycles after ice accumulation and ice removal in

the centrifuge test are presented in Figure AI-2. In the 1st cycle, the spherical shape of supercooled water droplets freezing on the superhydrophobic surfaces highlighted the water-repellent property at a freezing temperature. This was not observed for the pristine surface. The rounded shape of the formed ice on the APP-treated surface at the 7th cycle illustrated its most favorable water-repellent property.

3.5 Durability property

We investigated the durability of the produced superhydrophobic surfaces through various mechanical and chemical tests that represent the real-life applications, including abrasion using sandpaper, a finger-press test, a tape-peeling test, sandstorm simulation, ultrasonication treatment, continuous water droplet impacts, immersion in chemical solutions, and exposure to UV-light radiation. We closely monitored and recorded the WCA and CAH of the samples to study the capacity of a surface to recover its superhydrophobicity, where applicable.

3.5.1 Mechanical durability

The sandpaper abrasion test of superhydrophobic surfaces is effective for evaluating mechanical durability; however, studies often stop abrasion cycles before any deterioration of superhydrophobicity [352-354]. Here, we maintained the cycles once the superhydrophobic properties began to deteriorate to provide a thorough understanding of mechanical stability. The superhydrophobic properties of the µCM surface were not lost (WCA >150°) even after 300 abrasion cycles for abrasion pressures of 1.6 kPa and 3.2 kPa (Figure 3-7). However, the CAH increased to >10° after 250 cycles. Under these same conditions, i.e., abrasion pressures of 1.6 kPa and 3.2 kPa, the WCA of the APP-treated surfaces fell below 150° after 200 and 150 cycles, respectively. The CAH became >10° after 100 cycles. Increasing the abrasion pressure to 6.4 kPa, which is a relatively high pressure for any abrasion test, the µCM surface maintained its WCA >150° after 200 cycles, whereas the APP-treated surface showed a WCA <150° after 100 cycles. The CAH of the µCM surface increased to >10° after 100 cycles, whereas that of the APP-treated surface showed a CAH of ca. 20° after 50 cycles. This observation relates to the fast deterioration of surface micro-nanostructures under such high abrasion pressure.

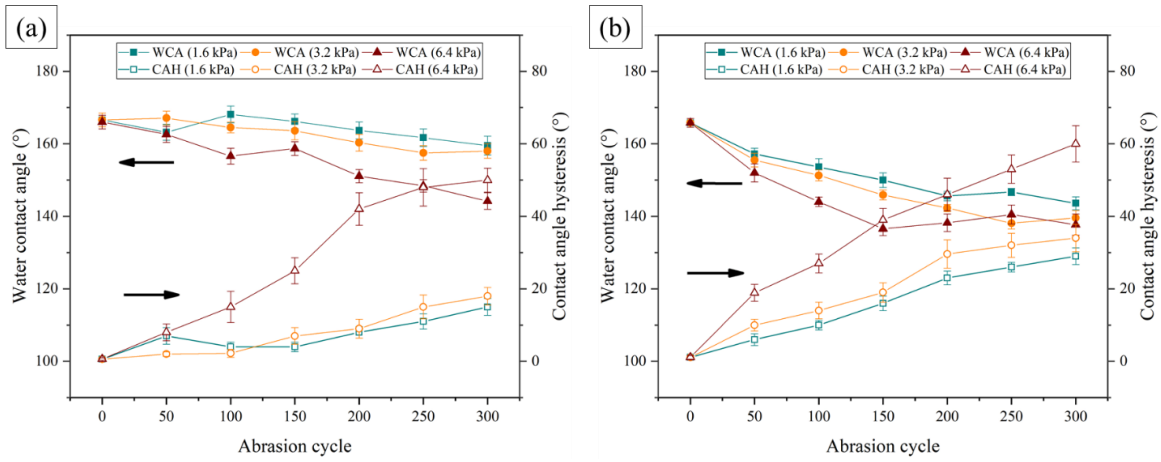

Figure 3-7. Water contact angle and contact angle hysteresis as a function of abrasion cycles using various abrasion pressures for (a) µCM and (b) APP-treated surfaces.

SEM images of the surfaces after being abraded for 300 cycles using sandpaper (Figure 3-8) illustrate the decreased micro-nanostructures on the surface after the abrasion process. When comparing surfaces abraded using pressures of 3.2 kPa and 6.4 kPa, we observed that the greater the abrasion pressure, the more the surface asperities wore out. Higher abrasion pressures produced flatter surfaces and removed the microstructures. The red outlines in Figure 3-8 illustrate areas where structures were lost due to abrasion, while the yellow outlines denote areas where the structures remained intact or less severely damaged. A greater number of yellow areas are present in samples subjected to 3.2 kPa abrasion pressures, explaining the relatively high WCA, whereas the greater number of red shapes in the sample abraded at 6.4 kPa indicates the flattened structures and, therefore, explains the reduced WCA and increased CAH.

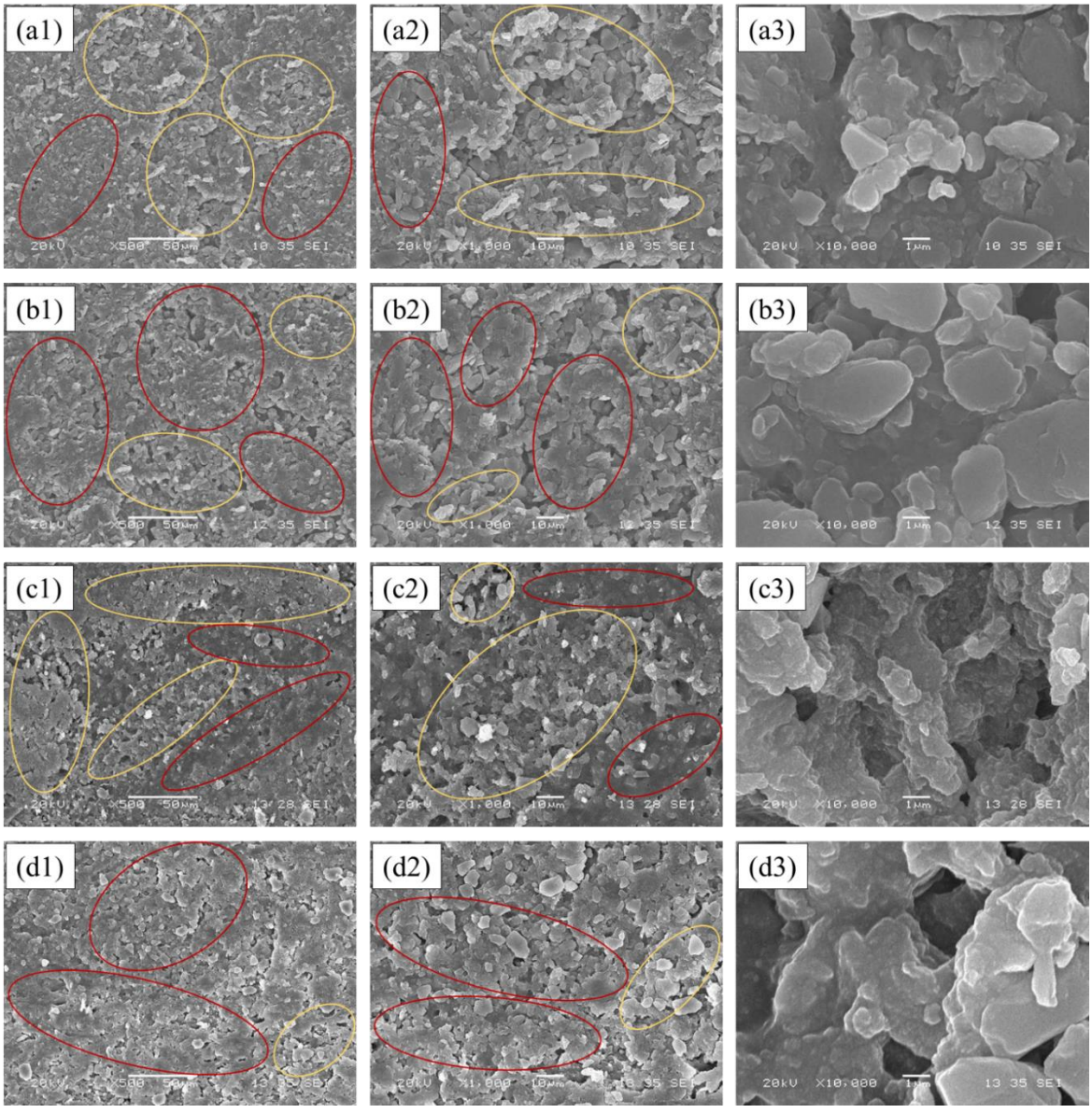

Figure 3-8. SEM images at various magnifications of (a1-a3) µCM surface abraded at 3.2 kPa pressure, (b1-b3) µCM surface abraded at 6.4 kPa pressure, (c1-c3) APP-treated surface abraded at 3.2 kPa pressure, and (d1-d3) APP-treated surface abraded at 6.4 kPa pressure.

We measured the WCA of both surfaces abraded at 6.4 kPa at regular intervals to determine the recovery of surface superhydrophobicity (Figure AI-3 (a)). The WCA of the µCM surface increased constantly up to 20 days after the tests, and it thereafter remained unchanged at the value of ~157°. For the µCM surface (an initial WCA of 166.6°), the recovery capability of the silicone surface was significant. The WCA of the APP-treated surface (an initial WCA of 165.8°), however, showed a slight increase after the first 10 days post-test and then remained at an almost constant value of ~143°, showing non-superhydrophobic behavior. During the abrasion test, the asperities may undergo two changes. First, the microstructures and nanostructures are worn out as they

are vulnerable to abrasion. This type of deformation is not reversible, which explains the permanent deterioration of CAH—CAH did not change considerably after the tests and remained >10° even after 50 days of rest for both prepared surfaces. Second, as the complete wearing of microstructures is less possible than the full loss of nanostructures, the microstructures are bent and stretched under pressure and drag forces. Therefore, there is a possibility of recovery due to the elastic properties of silicone rubber asperities, where microstructures can return upright and recover their initial position with time.

We also examined the durability of the produced silicone rubber surfaces via a finger-press test where we applied a pressure of 80 ± 8.8 kPa to the surfaces using a bare thumb (Figure 3-9 (a)). This test can mimic human handling of a material to test whether a superhydrophobic surface can be suitable for commercial use. In addition to mechanical damage, a bare finger-press also adds salt and oil contaminants to the surface. Therefore, the finger-press test can both physically and chemically affect a superhydrophobic surface [253]. In our finger-press tests, the µCM surfaces degraded more than the APP-treated surfaces. Although the WCA of both surfaces decreased almost similarly and remained at >150° after 50 cycles (APP-treated showed a slightly more durable behavior), the CAH of the µCM surfaces increased markedly after 10 cycles, whereas the CAH of the APP-treated surface remained <10° even after 50 finger-press cycles.

The increase in WCA after a single day of recovery following the finger-press test was an important result (Figure AI-3 (b)). The WCA of the finger-pressed µCM surface increased from 148.5° to 164.2°, while the WCA of the APP-treated surface increased from 152.8° to 155.9°. The micro-nanostructured silicone asperities could therefore return to their initial position after the finger force was released due to the rubber elasticity. These post-pressure behaviors are explained by the different micro-nanostructures on the surfaces. A portion of the WCA loss can also be attributed to the added salt and oil contaminant from thumb to the surface. As such, some of the observed WCA recovery can be related to the migration of LMWS to the surface and covering the contamination molecules transferred to the surface by the thumb. Finally, after 10 days of recovery, the CAH of the µCM surface attained 9° (while the graph plateaued after Day 8). The CAH of the APP-treated surface did not show any significant change.

The tape-peeling test involved applying and removing a pressure-sensitive Scotch-600 tape with approximately 30 kPa pressure to the surface. According to Wang et al. [355], this pressure is much larger than the pressure described in the standard test method for measuring adhesion by the tape test. In terms of the

pressure placed onto the surface, this test combines the effects of the finger-press test and the adhesion test, as though the sample underwent 50 cycles of the finger-press test and tape-peeling test simultaneously. After 50 attach-detach cycles, both surfaces remained superhydrophobic with a WCA >160° and a CAH < 6° (Figure 3-9 (b)).

In ultrasonication, the energy is applied by waves at an ultrasonic frequency (>20 kHz) within a liquid media. This energy can damage a surface lacking a strong physical morphology or a strong chemical bonding with the substrate.[253] The μCM surface was durable against long-term ultrasonication. After 4 h of continuous ultrasonication, the WCA of the μCM surface remained at ~160° and the CAH was at ~10° (Figure 3-9 (c)), confirming the strong physical micro-nanostructured morphology of the prepared superhydrophobic surface. The APP-treated surface, however, was significantly vulnerable to ultrasonication. The WCA of the APP surface dropped below 150° after 60 min and was ~124° after 4 h. The CAH increased to >20° after 60 min and to ~60° after 4 h. This marked change occurs as nanostructures are removed from the APP-treated surface by the high levels of applied ultrasonic energy (Figure AI-4).

We investigated the dynamic impact durability of the superhydrophobic surfaces under a liquid phase. This evaluation is very important in terms of the application of produced superhydrophobic surfaces under rain precipitation. We conducted this test using the parameters of ~1 $mL \cdot min^{-1}$ and we ran the test for 7000 seconds, i.e., ~120 mL water impacting a single point of the surface at a speed of 1.4 m/s, a speed equivalent to that of 3.0-mm diameter raindrops.[356] The WCA and CAH remained >150° and <10° after being exposed to a water jet impact, i.e., ~6000 droplet impact events, after 7000 s (Figure 3-9 (d)). A reduction of the surficial anti-wetting properties can be attributed to the partial penetration of water into the surficial hierarchical structures due to the instantaneous pressure exerted on the surface [253].

The dynamic impact durability of the produced superhydrophobic surfaces under a solid phase was also examined. We simulated sandstorm conditions (average particle size of 18 μm) in a sandblasting machine. Each individual surface was exposed to the sand stream at a pressure of 20 psi for 20 min, and we recorded the WCA and CAH every 5 min (Figure 3-9 (e)). Both surfaces showed a WCA >150° and a CAH <10° after 20 min of sandblasting (corresponding to a full year of real-life sandstorm events). The SEM images of the sandblasted surfaces are shown in Figure AI-5.

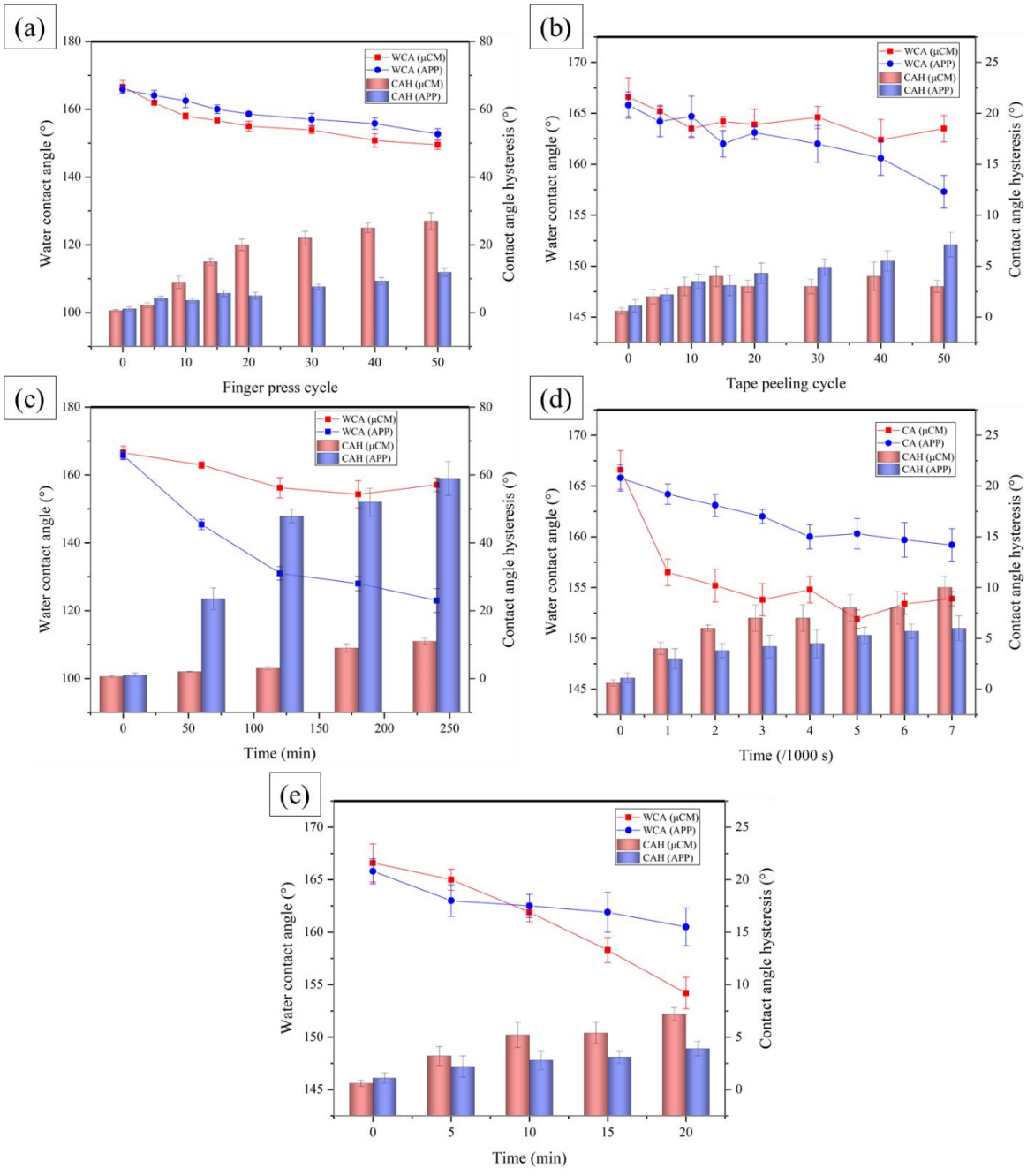

Figure 3-9. Water contact angle and contact angle hysteresis as a function of (a) finger-press cycle, (b) attach-detach cycle, (c) ultrasonication time, (d) continuous water droplet impact time, and (e) sandblasting time for μCM and APP-treated surfaces.

3.5.2 Chemical durability

We then tested the durability of the produced superhydrophobic surfaces against buffer solutions of pH 2, pH 12, and deionized water of pH 7. When superhydrophobic surfaces are immersed in aqueous solutions, there are two possibilities for deterioration of superhydrophobic behavior. One possibility is related to the

penetration of liquid into the surface structures (Cassie-to-Wenzel transition) which is mainly dominated by capillary forces. [357] showed that the morphology of the surface structures determines the capillary forces dominating the penetration of the droplet into the surface structures. The other possibility, however, is related to the formed chemical bonds due to the presence of aqueous medium.

After 15 days of immersion in the acidic solution, the WCA of the µCM surface remained >155°, while the CAH increased to 12°; thus, the surface was superhydrophobic with a weak roll-off property (Figure 3-10 (a)). The µCM surface in the alkaline solution had a WCA remaining at >160° and a CAH remaining at <5°. The WCA of the µCM surface was >150° and the CAH increased to 30° after 15 days of water immersion. These observations can be attributed to the presence of oxide/hydroxide groups in the vicinity of the solutions for an extended period of time. On the µCM surface, the silicone rubber chains, as well as the ATH particles, react with the acid, base, and water to produce these oxide/hydroxide groups.

The APP-treated surface demonstrated extraordinary durability against the three aqueous media. A WCA >160° and CAH <5° testified to a desirable chemical durability of the APP-treated surface (Figure 3-10 (b)). The APP process at elevated temperatures breaks the chemical bonds of the silicone rubber chains, and therefore the surface is mainly covered by silicon oxide [358]. These SiO_2 do not react with the acidic, alkaline, and neutral water media. As such, the SiO_2 acts as a shield to prevent chemical reactions on the APP-treated surface. Moreover, according to [359] the capillary pressure, corresponding to the pressure that resists water penetration, is inversely related to the structure gap ($P_c = 2\sigma.cos\theta/r$, where σ is liquid surface tension, θ is the intrinsic contact angle of the surface, and r is the distance between the surface structures). Therefore, on the immersed surfaces, the smaller micro-nanostructures having greater capillary force can hinder the Cassie-to-Wenzel transition. This is witnessed by lower reduction of WCA on the APP-treated surface.

Due to the migration of LMWS molecules from the bulk material to the surface and the reorientation of methyl and hydroxyl groups by conformational changes, the optimal WCA and CAH conditions were recovered (Figure AI-3 (c)). This restoration was due to the rotation and movement of the LMWS chains that are thermodynamically driven to the surface to minimize free energy at the surface.

Finally, sunlight radiation is a major cause of damage to materials used outdoors. Hence, the durability of silicone surfaces used for outdoor applications, e.g., electrical insulation, is of great importance. The sun emits ultraviolet, visible light, and infrared waves, ultraviolet waves being the most destructive. The WCA and

CAH of the superhydrophobic surface remained >150° and <10° respectively after being exposed to 1200 h of UV light, representing about six years under natural conditions (Figure 3-10 (c)). The produced surfaces thus demonstrated resistance against accelerated UV-light exposure. The better performance of the APP-treated surface over that of the µCM surface is due to the silicon oxide layer formed on the surface acting as a shield against UV-light exposure.

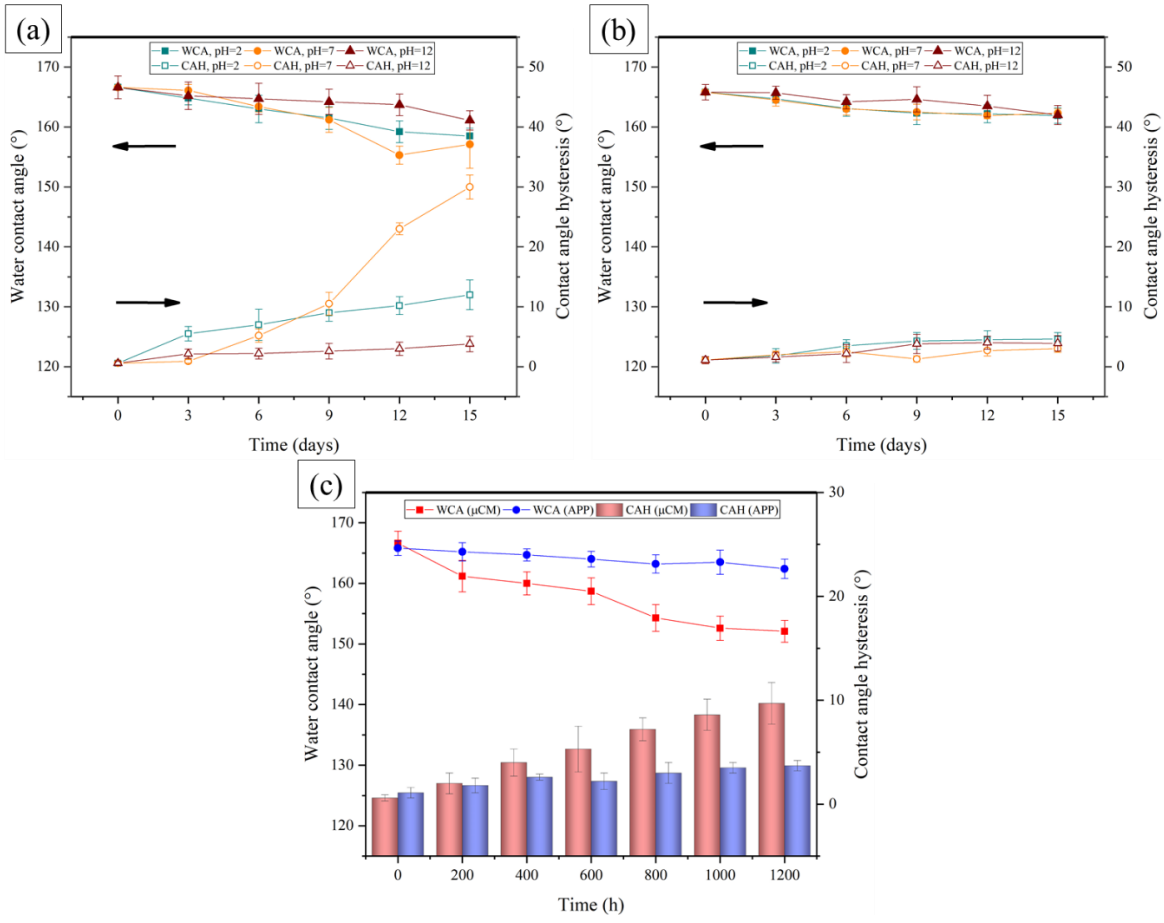

Figure 3-10. Water contact angle and contact angle hysteresis as a function of immersion time (days) in acidic, alkaline, and neutral solutions for (a) µCM and (b) APP-treated surfaces. (c) Water contact angle and contact angle hysteresis as a function of UV-light exposure time for µCM and APP-treated surfaces.

3.6 Conclusions

We produced superhydrophobic silicone rubber surfaces having a WCA >150° and a CAH <10° via straightforward direct replication method using a micro compression molding (µCM) system and a simple treatment by atmospheric-pressure plasma (APP). The observed delay in the freezing time of droplets on the produced superhydrophobic surfaces stemmed from the creation of air pockets on their surfaces. The larger micro-nanostructures showed better anti-icing properties as they could trap more air within their micro air

pockets. As for the µCM surface, the freezing delay time was ~2.5× more than that of APP-treated surface at –25 °C. Using centrifuge and push-off tests—with corresponding icing conditions of hard rime and bulk ice, respectively—we demonstrated that the produced superhydrophobic surfaces also decreased ice adhesion strength. The mechanism of ice removal for the µCM and the pristine surface was the plastic deformation of ice, while elastic deformation controlled ice removal from the APP-treated surface. Compared to a pristine silicone rubber, the APP-treated surface (S_q = 1.53 µm) decreased the ice adhesion strength up to 75% in a push-off test and 68% in a centrifuge test, whereas the µCM surface (S_q = 9.40 µm) reduced ice adhesion strength up to 42% in a push-off test and 32% in a centrifuge test. Therefore, for surfaces having hierarchical micro-nanostructures, those surfaces with a lower surface roughness are characterized by a lower ice adhesion strength. The stronger physical bonding between the micro-nanostructures and the bulk material in the µCM surface, however, led to a relatively constant ice adhesion strength throughout repetitive icing/de-icing cycles. The durability of the produced silicone rubber superhydrophobic surfaces were tested through mechanical and chemical experiments. The samples showed desirable durability properties maintaining a WCA of >150° and a CAH of <10° in several tests. Silicone rubber materials also showed a self-repair capacity stemming from the elasticity of the rubber and migration of LMWS to the surface. This recovery compensated for the loss of anti-wetting properties in some destructive tests, and the WCA recovered after a couple of days.

Acknowledgments

The authors acknowledge the financial support from the Natural Sciences and Engineering Research Council of Canada (NSERC) and K-Line Insulators Limited, Toronto, Canada. We also thank the Anti-icing Materials International Laboratory (LIMA) for carrying out the centrifuge adhesion tests.

CHAPTER 4

ARTICLE 3: A NON-FLUORINATED MECHANOCHEMICALLY-ROBUST VOLUMETRIC SUPERHYDROPHOBIC NANOCOMPOSITE

E. Vazirinasab*, G. Momen, R. Jafari
Department of Applied Sciences, University of Québec in Chicoutimi (UQAC)
555, boul. de l'université, Chicoutimi, Québec, G7H 2B1 Canada
* E-mail: elham.vazirinasab1@uqac.ca

4.1 Abstract

The widespread use of water-repellent superhydrophobic surfaces is limited by the inherent fragility of their micro- and nanoscale roughness, which is prone to damage and degradation. Here, we report on a non-fluorinated volumetric superhydrophobic nanocomposites that demonstrate mechanochemical robustness. The nanocomposites are produced through the addition of microscale diatomaceous earth and nanoscale fumed silica particles to high-temperature vulcanized silicone rubber. The water-repellency of the surface and bulk of nanocomposites having 120 phr of filler was determined based on the water contact angle and contact angle hysteresis. We compared the water-repellency of nanocomposites of differing diatomaceous earth to fumed silica mass ratios. Increasing the amount of diatomaceous earth enhanced the water-repellency of the nanocomposite surface, whereas an increased amount of fumed silica improved the water-repellency of the bulk material. Moreover, increasing the diatomaceous earth/fumed silica mass ratio improved the cross-linking density and hardness values of the nanocomposite. Despite being subjected to a range of mechanical durability tests, including sandpaper abrasion, knife scratching, tape peeling, water jet impact, and sandblasting, the nanocomposite maintained a water contact angle of 163° and contact angle hysteresis of 2°. When the water-repellency of the prepared nanocomposites eventually deteriorated, we restored their superhydrophobicity by removing the upper surface of the nanocomposite. This extraordinary robustness stems from the embedded low surface energy micro/nanostructures distributed throughout the nanocomposite. We also demonstrated the chemical stability, UV resistance, and self-cleaning abilities of the nanocomposite to illustrate the potential for real-life applications of this material.

Keywords*:* Volumetric superhydrophobic, nanocomposite, diatomaceous earth, hierarchical micro-nanostructure, mechanical robustness, chemical stability, self-cleaning.

4.2 Introduction

Over the last few decades, silicone rubber materials have found their way into applications within the automotive and electronics industries, aerospace applications, cookware, etc. The backbone of silicone rubber consists of siloxane (Si-O) groups, which provide its unique characteristics in terms of thermal stability, abrasion resistance, UV resistance, and low electrical conductivity [64]. In addition to these superb properties, the hydrophobic nature of silicone rubber also makes it an attractive material for use in superhydrophobic (SH) applications. Low surface energy (i.e., hydrophobic) materials coupled with desirable micro/nanostructured surface roughness are required to create SH surfaces. Fluorocarbons have been widely used for creating SH surfaces due to their very low surface energy and water repellency; however, their application has been limited because of environmental concerns related to their use and their potential toxicity to humans from by-products related to the breakdown of fluorinated compounds [84, 85]. Thus, alternative means of achieving SH surfaces are required.

Artificial SH surfaces, having a water contact angle (WCA) >150° and a contact angle hysteresis (CAH) <10°, have attracted tremendous amount of attention because of their range of potential use in self-cleaning [34, 360], icephobicity [24, 361], anti-corrosion [37, 362], oil-water separation [38, 363], and drag reduction [364] applications. Such surfaces have been produced using various methods, such as anodization, electrodeposition, direct replication, plasma treatment, dip coating, spray coating, and 3D printing [275, 365-370]. Maghsoudi et al. [103] fabricated SH high-temperature vulcanized silicone rubber (HTV-SR) surfaces through a direct replication method where chemically etched aluminum substrates were used as templates. Zhou et al. [371] prepared a durable SH fabric using a silicone rubber coating that contained fluorinated alkyl silane (FAS) modified silica. The particular morphology induced by the silica nanoparticles was observed on the inherent microscale roughness of the fabric weave, which led to the hierarchical micro/nanostructures on the surface. In another study, multimodal surface roughness was achieved by laser treatment of the silicone rubber surface [372]. Studies of these artificial SH surfaces have concentrated on applying a very thin SH layer (micro- or nanoscale) onto the base materials. These SH layers, however, suffer from the loss of functionality,

chiefly through mechanical damage; their inherent fragility is the main factor leading to their short-term durability.

Proposed strategies to enhance the durability of SH surfaces include the self-healing ability of surfaces inspired by the renewable superhydrophobicity of some natural surfaces, such as those of some plant leaves [195, 373]. Li et al. [205] produced a self-healing SH surface using a porous polymer coating by preserving excess amounts of reacted low surface tension fluoroalkylsilane as a healing agent. Once the surface is scratched or decomposed, the healing agent migrates to the surface and relies on humidity as the external stimulus for regenerating superhydrophobicity. As another approach, colloidal particles can spontaneously self-organize on the surface to produce self-healing SH surfaces. When induced by intermittent heating and cooling, colloidal particles can also migrate to the surface of perfluorinated wax and recover the initial surface roughness [197]. Application of such external stimuli for self-healing surfaces is nonetheless essential for these approaches.

One of the novel concepts in the fabrication of ultra-durable SH materials is the use of the particles themselves to create a favorable roughness on the surface. Within these SH materials, the presence of particles throughout the entire bulk material ensures a continual superhydrophobicity. Once water-repellency has deteriorated, a high WCA and low CAH can be regained by mechanical abrasion or by cutting the damaged upper layer. Importantly, this mechanical abrasion permits the SH behavior to be maintained until the point when the whole materials are completely worn out [18, 374]. SH bulk materials having a tunable hierarchical porosity—fabricated by divinylbenzene and silica composites—have shown good mechanical, chemical, and environmental resistance [20]. This prepared polymer monolith can also be applied as a painting material to obtain superhydrophobicity on various surfaces. Zhang et al. [18] fabricated a UV-responsive, reversible wettability polypropylene/titanium oxide (TiO_2)/silica nanocomposite. Due to the presence of TiO_2 nanorods, the SH surface became superhydrophilic after UV irradiation. Once the initial superhydrophobicity is reduced, conditions are restored by eliminating the worn uppermost layer via mechanical abrasion. Porous SH and superoleophilic bulk materials have also been created using NH_4HCO_3 as a pore-forming reagent. The fabricated strawberry-like morphologies had randomly oriented carbon nanotubes and silica formed on poly(vinylidene fluoride) protuberances containing numerous pores throughout the structures [19]. Zhu et al. [209] used a SH CNT-PTFE bulk material for oil-water separation applications; they relied on the relatively

large pore volume of the bulk material for separating the two liquids. After fouling by oil, the superhydrophobicity was restored by either directly burning the diffused oil or by abrading the polluted layers. Although these examples of SH bulk materials can maintain surface roughness after exposure to mechanical damage, they lack either physical stability, cost-effectiveness, a minor environmental impact, or a combination of these.

In a nutshell, the mechanical robustness of SH surfaces is a complex yet attractive feature in commercialization of these surfaces. To address the aforementioned concerns, we used a simple approach to develop an inexpensive and non-fluorinated damage-tolerant volumetric SH nanocomposite using HTV-SR containing diatomaceous earth (DE) and fumed silica (FS) fillers. DE particles are a low-cost, environmentally benign, and globally abundant mineral, which range in size from μm to several mm. These particles also have nanoscale pores [375]. Their chemical composition is mostly silica (86%–96%) with less than 5% alumina (Al_2O_3) and ferric acid (Fe_2O_3) [376]. Due to their unique hierarchical porous structures, DE particles have been used in SH coatings despite their hydrophilic nature [377]. Several methods have modified DE to produce SH coatings in which the DE particles were functionalized mainly using fluorosilanes [378, 379].

Here, we produce an ultra-robust volumetric SH HTV-SR nanocomposite using DE and FS particles in which the extended superhydrophobicity within the entire bulk material is retained despite continuous mechanical abrasion. Unlike conventional methods for producing SH materials that depend mainly on surface manipulation techniques, e.g., coating, direct replication, surface etching methods [275, 365-367], we develop a long-lasting volumetric SH nanocomposite that requires no surface treatment or external stimuli which means its superhydrophobicity is self-maintained.

4.3 Materials and methods

4.3.1 Materials

HTV-SR (ELASTOSIL® R 401/60) was kindly obtained from Wacker Chemie AG (Germany) to use as the matrix. DE particles, also known as Kieselguhr and dicumyl peroxide, were provided by Alfa Aesar. Hydrophobic FS, treated with hexamethyldisilazane (AEROSIL® R 812 S) and having a specific surface area of 195–245 m2·g-1, was kindly supplied by Evonik Corporation (USA). All chemicals were used as received.

4.3.2 Preparation of the nanocomposite

Our approach for fabricating the volumetric superhydrophobic nanocomposites relied on two complementary steps: (1) incorporating the particles into the HTV-SR via the solution-mixing method to produce the rubber compound; and (2) vulcanizing the prepared rubber compound using compression molding. Each of these steps are explained in detail as follows:

To achieve an appropriate dispersion of particles into the HTV-SR, we employed a solution-mixing method (Figure 4-1). We dissolved 12 g of HTV-SR in 100 mL of toluene using an overhead stirrer. Meanwhile, DE particles were dispersed into the toluene via sonication for 60 min. DE suspensions of various weight fractions—ranging from 30 to 90 wt.%—were added to the HTV-SR solution and blended for 100 min at 70 °C. Thereafter, we added the sonicated-FS-in-toluene solution (the weight fraction varied between 30 and 90 wt.%) to the HTV-SR/ DE compound. The mixture was stirred continuously using an overhead stirrer at 70 °C for 200 min to obtain a nanocomposite with homogeneously dispersed particles. Then, 0.09 g of dicumyl peroxide as a curing agent was dissolved in the aforementioned solution by mixing them at room temperature for 20 min. We left the prepared solution for 24 h under a vacuum to remove residual toluene and obtain the final rubber compound.

To vulcanize the prepared rubber compound, we used an automatic hydraulic press machine (Carver Inc., USA). The compound was placed into a three-piece square mold having a 3-mm thickness and compressed under desired conditions, i.e. 10 MPa of pressure for 10 min at 175 °C.

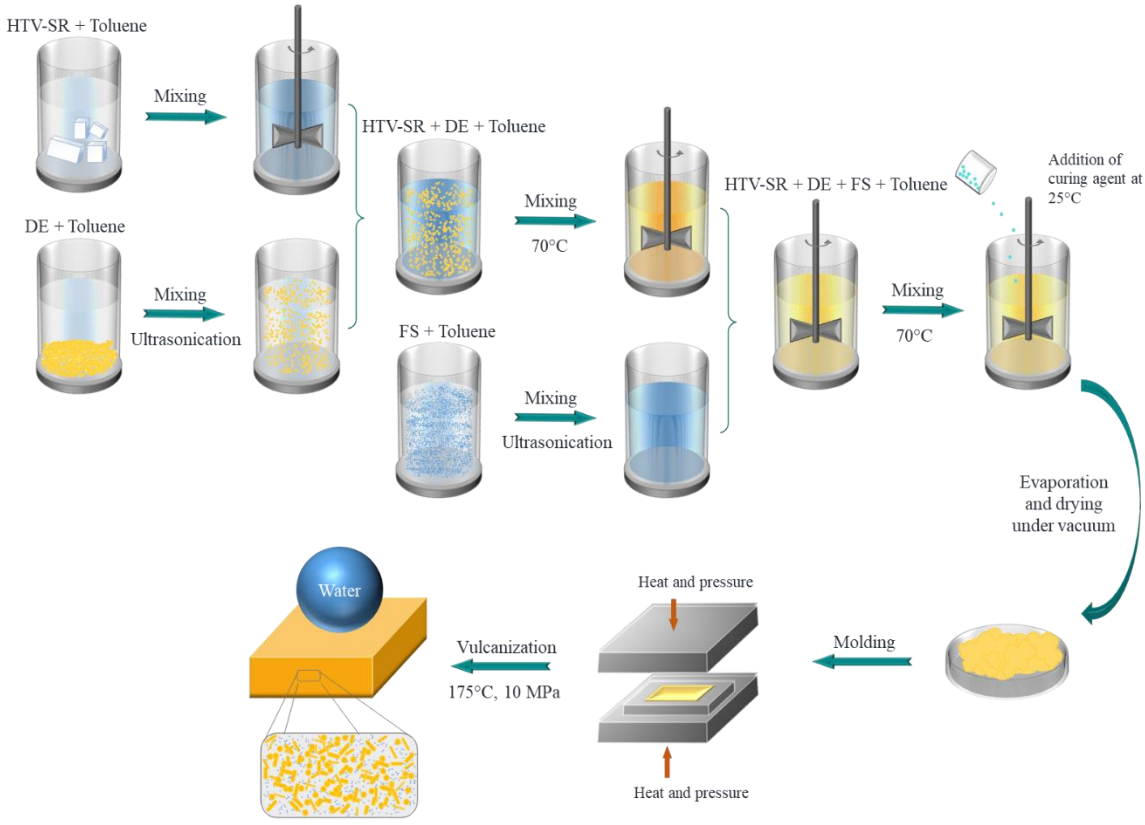

Figure 4-1. Schematic illustration of the fabrication of the volumetric superhydrophobic nanocomposite.

4.3.3 Characterization techniques

We used the sessile drop method to measure the contact angle using a Kruss™ DSA100 goniometer at room temperature. According to the Young-Laplace approximation method, the static WCA of a 4-µL distilled water droplet deposited onto the sample surface was measured by drop shape analysis software. To measure the CAH, we moved a 4-µL water droplet in a single direction across the surface using a needle tip. CAH was determined by measuring the difference between the advancing and receding contact angles. We reported the WCA and CAH results as the average of five measurements at various spots on each sample, and we included the associated standard deviation.

Scanning electron microscopy (SEM), field emission scanning electron microscopy (FESEM), and profilometry analyses were conducted to evaluate the morphology of the surface and bulk of the nanocomposite. The selected samples were submerged in liquid nitrogen for several minutes and immediately broken apart for bulk imaging. To enhance the imaging quality, all samples were sputter-coated with a nano layer of gold-palladium coating prior to SEM and FESEM analyses performed using JSM-6480 LV and Hitachi

S-4700 microscopes, respectively. The quantification of surface roughness was accomplished using an optical profiler (Profil3D, Filmetrics, USA).

The chemical functionality of the silicone rubber samples was assessed by Fourier transform infrared spectroscopy (FTIR) in the mode of attenuated total reflection (ATR). An Agilent FTIR spectrometer (Cary 630, USA) characterized the surface chemical functional groups of the silicone rubber both with and without particles. The thermal stability of the nanocomposites was measured by the thermogravimetric analysis (TGA) using a Setaram Setsys 24 with a 1600C TG/DTA rod configuration.

In regard to adding particles to the HTV-SR, we ran swelling experiments to analyze the effect of particles on the swelling ratio, crosslinking density, and average mass between the crosslinking points (M_C) as representatives of the structural parameters of the nanocomposites. The samples, weighing 200–300 mg, were immersed in toluene for 72 h at ambient temperature to come to an equilibrium swollen state. Then, we removed the samples and immediately weighed them. We then placed the samples in an oven to dry at 60 °C for 24 h, after which time we again recorded their weights. The swelling ratio was calculated by $Q = (m_1 - m_2)/m_2$, where m_1 and m_2 are the weights of swollen samples before and after drying respectively. The volume fraction of the HTV-SR in the swollen specimen can be computed by [380]:

$$\varphi = \frac{\left(\frac{m_2 \times b}{\rho_r}\right)}{\left(\frac{m_2 \times b}{\rho_r}\right) + \left(\frac{m_1 - m_2}{\rho_s}\right)} \quad 4\text{-}1$$

where b, ρ_r, and ρ_s are the weight fractions of rubber, density of rubber (1.15 g/cm^3), and density of toluene (0.866 g/cm^3), respectively. According to Flory-Rehner theory, the crosslinking density (ν) and M_C can be calculated as follows [381]:

$$\nu = \frac{-(\ln(1-\varphi) + \varphi + \chi\varphi^2)}{V(\varphi^{\frac{1}{3}} - \frac{\varphi}{2})} \quad 4\text{-}2$$

$$M_C = \frac{\rho_r}{\nu} \quad 4\text{-}3$$

where V is molar volume of the toluene (106.7 cm^3/mol), and χ is the Flory-Huggins polymer-solvent interaction parameter, calculated as $\chi = 0.459 + 0.134\varphi + 0.59\varphi^2$. Moreover, hardness values were obtained using a Shore A durometer (2000 max-hand durometer, Rex Gauge, USA). The test was repeated six times for each nanocomposite.

To assess the mechanical robustness of the prepared nanocomposites, a series of experiments were carried out that included abrasion, knife scratching, tape peeling, water jet impact, sandblasting, and ultrasonication. Abrasion tests were conducted using an abrasion apparatus (manual clemen unit, Elcometer 3000, USA) equipped with an adjustable loaded force. One abrasion cycle consisted of dragging the sample along sandpaper for 20 cm with an abrasion force of 5.0 kPa and 25.0 kPa applied to the samples. To survey the effect of sandpaper grit numbers on the superhydrophobicity of the nanocomposite, a broad range of sandpapers, i.e., from #160 to #800 grit was used. Another mechanical test was a tape-peeling analysis during which the transparent tape was attached to the material surface with a constant force. We then peeled the tape from the surface. The procedure was repeated for 200 times. The WCA and CAH of the substrate were determined after every 40 cycles. For water jet test, a water jet was injected to the surface for 15 min at an angle of 30° from a syringe equipped with a needle (diameter = 0.9 mm). The durability of the nanocomposite against sandblasting was assessed using SiC particles having an average size of ~18.3 µm, that were projected at 0.13 MPa pressure for 1 min. Then, the surface was cleaned with the help of compressed air. The robustness of the nanocomposite under ultrasonication was examined using a Branson 2510 ultrasonication bath.

To evaluate chemical stability, two methods of immersion and droplet evaporation were performed. The immersion test involved prepared samples being submerged in corrosive acidic (pH = 2) and alkaline (pH = 12) solutions, as well as deionized water (pH = 7) as a reference, for five days at room temperature. We recorded the WCA and CAH daily. For the droplet evaporation technique, a droplet of deionized water, acidic (pH = 2) and alkaline (pH = 12) solutions was placed on the sample, and changes in the WCA were measured over 25 min. The ultraviolet (UV) resistance of the prepared nanocomposites was surveyed by a QUV-accelerated weathering tester. Based on ASTM G154, UVA-340 fluorescent lamps were used to irradiate samples with the radiation energy of 0.89 W m^{-2} at 60 °C.

4.4 Results and discussion

4.4.1 Superhydrophobicity

Here, we fabricated hierarchical micro-nanostructured superhydrophobic nanocomposites by dispersing two different fillers, i.e., micro-sized DE and nano-sized FS in the HTV-SR. No further surface treatment was required. As the specific particle concentration had a considerable effect on surface morphology, the wettability of the surface varied. We examined the influence of the amount of filler on the final WCA and CAH of the

surface and bulk of the nanocomposites. Wettability properties of seven mass ratios of micro-sized DE and nano-sized FS are presented in Table 4-1 and Figure 4-2 (a). The nomenclature of the samples is attributed to the type of the incorporated particle followed by its associated phr. For example, D70F50 represents a nanocomposite containing 70 phr of DE and 50 phr of FS. As shown in Figure 4-2 (b), the WCA and CAH of pristine HTV-SR were 110° and 46.6°, respectively. In terms of surface water-repellency, although the nanocomposites D30F90 and D40F80 had a WCA >150°, implying superhydrophobicity, a >10° CAH demonstrated an undesirable level of water-repellency. A DE/FS mass ratio above 50:70 gave rise to the water-repellency—WCA >160° and CAH <5°—for the surface of prepared nanocomposites. This emphasizes the pivotal role of DE particles in achieving surface water-repellent properties due to their particular morphology. The specific structure of the DE particles is visible in Figure 4-2 (c). The DE particles used in this study possess various shapes, including tubular, annular, and planar forms; majority of DE particles contain numerous nanoscale holes on their structures.

It should be noted, however, that the presence of FS particles is essential for creating the volumetric superhydrophobic nanocomposite. To measure the superhydrophobicity of the bulk material, the nanocomposites cut in half with a cutter blade, and the WCA and CAH of the bulk material were also measured. Unlike the surface of the material, a reduced DE/FS mass ratio enhanced the water-repellency of the bulk material; however, at a DE/FS mass ratio less than 50/70, the WCA and CAH gradually deteriorated. Thus, at a high FS concentration, not only was there a low amount of DE particles available, but there was also a certain amount of overlap between the FS nanoparticles, causing roughness to decrease and the water-repellent properties of the bulk material to be reduced. Based on the WCA and CAH of the surface and bulk portions of the nanocomposites, relatively equal amounts of DE and FS are required to prepare a consistent volumetric superhydrophobic nanocomposite. Consequently, the special morphology of the DE particles as well as aggregated FS, together formed the micro-nanostructures vital for developing a volumetric superhydrophobic and water-repellent nanocomposite.

We selected the nanocomposite D70F50, having a DE/FS mass ratio of 70:50, to demonstrate superhydrophobic properties. When the nanocomposite submerged in water using an external force, each one of the six surfaces glittered underneath the water, acting much like a silver mirror (Figure 4-2 (d)). The reflection of the light within the air layer trapped within the roughness features is responsible for the brightness

of the superhydrophobic surfaces. This observation verified the presence of solid-liquid-air composite interfaces forming the Cassie-Baxter wetting regime [20]. The 20-µL water droplets appeared to sustain the quasi-spherical shape on the top layer and cut surface of the superhydrophobic nanocomposite. It can be said that by cutting deep into the nanocomposite, not only did the superhydrophobicity not decrease, but a fresh superhydrophobic layer emerges. Moreover, the superb water-repellency behavior of the volumetric superhydrophobic nanocomposite can also be observed in Figure 4-2 (e) where the nanocomposite is surrounded by up to 5 mm of water meniscus (shown by red line arrows), a phenomenon known as the Moses effect. This is due to the remarkable superhydrophobicity of the substrate acting as a barrier and hindering the wetting of the nanocomposite under water.

Table 4-1. Chemical composition and wettability properties of the HTV-SR nanocomposites.

Type	*HTV-SR (phr)*	*DE (phr)*	*FS (phr)*	*WCA of the surface (°)*	*CAH of the surface (°)*	*WCA of the bulk (°)*	*CAH of the bulk (°)*
HTV-SR	100	0	0	110.0 ± 1.7	46.6 ± 2.4	112.5 ± 2.1	47.2 ± 2.5
D30F90	100	30	90	152.1 ± 1.2	17.3 ± 1.5	155.8 ± 0.9	9.6 ± 1.3
D40F80	100	40	80	156.6 ± 1.0	11.6 ± 1.2	158.4 ± 1.0	5.7 ± 0.5
D50F70	100	50	70	159.8 ± 0.8	5.8 ± 1.0	159.2 ± 1.2	3.9 ± 1.0
D60F60	100	60	60	162.7 ± 0.6	3.1 ± 0.8	161.3 ± 0.6	4.5 ± 0.8
D70F50	100	70	50	163.1 ± 0.5	2.5 ± 0.9	157.3 ± 0.8	10.9 ± 0.6
D80F40	100	80	40	164.2 ± 0.7	2.2 ± 0.6	155.9 ± 1.0	20.5 ± 0.7
D90F30	100	90	30	163.1 ± 0.8	4.2 ± 0.5	152.0 ± 0.8	25.8 ± 0.9

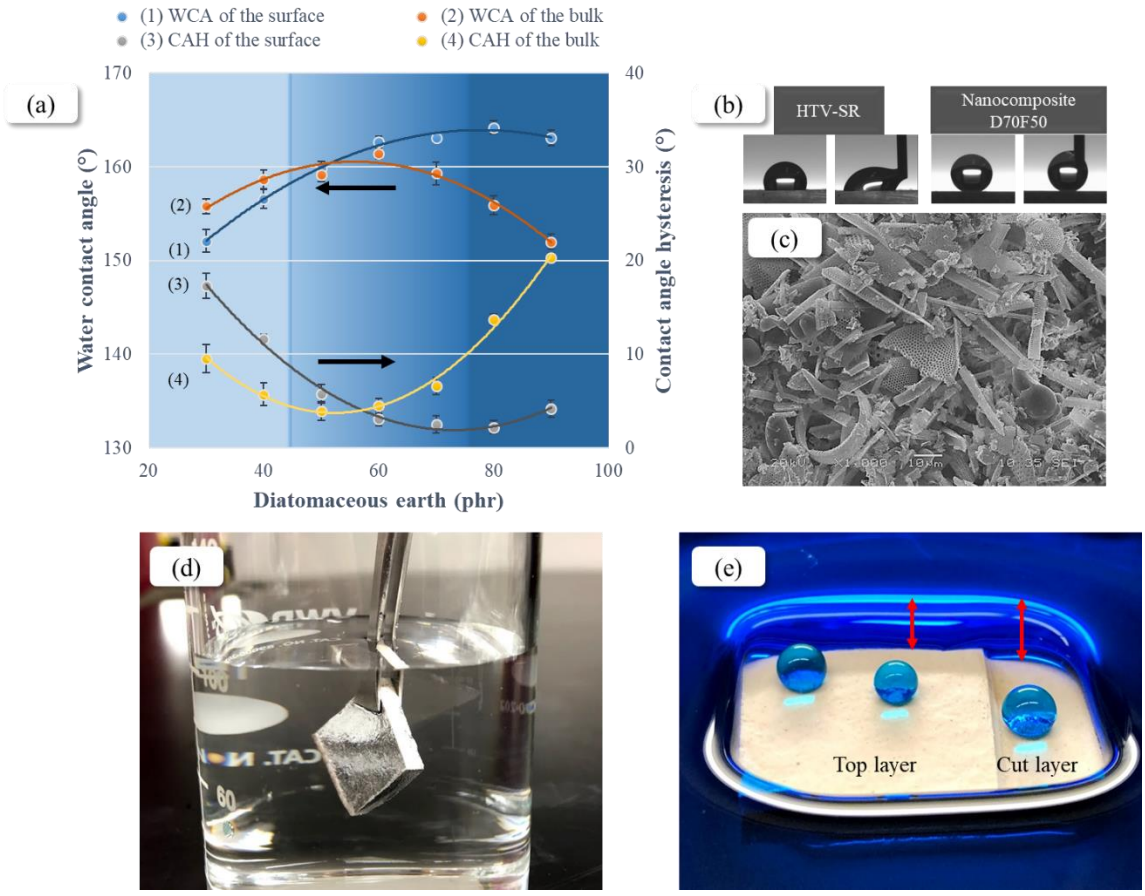

Figure 4-2. (a) The effect of DE concentration on the WCA and CAH of the surface and bulk portions of the HTV-SR nanocomposite; (b) a water droplet showing the WCA and CAH of a pristine HTV-SR and a nanocomposite D70F50; (c) SEM image of DE particles (×1000); (d) demonstration of the mirror-like phenomenon surrounding the bulk nanocomposite D70F50; (e) demonstration of the Moses effect around the intact and cut surfaces showing up to ~5 mm of water meniscus (red arrows were used to guide the eyes). The blue water droplets illustrate the superhydrophobicity of the surfaces.

4.4.2 Crosslinking density and hardness

One of the basic measurements to describe the structural and physical properties of rubber materials is the swelling of the material in solvents such as toluene. The average molecular weight between two M_C and crosslinking density are two main parameters determined by the swelling approach. The equilibrium of the osmotic pressure of the solvent and the elasticity of the polymer network specifies the swelling ratio, which represents the degree of elongated conformation of the polymeric chains. Thus, a high swelling ratio is related to an elevated M_C, which leads to a low crosslinking density [382]. The swelling ratio, crosslinking density, and M_C values of the fabricated nanocomposites are presented in Table 4-2. The crosslinking density of the nanocomposites, except for nanocomposites D30F90 and D40F80, was higher than that of the pristine HTV-SR (1.63×10^{-4} mol cm^{-3}). Three main chemical and physical interactions affected crosslinking density: the

chemical interactions among particles, the number of crosslinking points between silicone rubber chains, as well as the interfacial interaction between silicone rubber chains and particles [383]. The increased crosslinking density of superhydrophobic nanocomposites relative to that of pristine HTV-SR can be ascribed to the interfacial interactions between siloxane groups of DE particles and silicone rubber chains as well as the interaction among aggregated FS particles. The positive effect of adding particles on the enhancement of crosslinking density has been previously observed. Zabihi et al [384] reported an increase in the crosslinking density of epoxy by adding 10 wt.% iron nanoparticles, and Olad et al. [385] increased silica content to produce a higher crosslinking density. The crosslinking density of butadiene rubber filled with 45 phr silica enhanced from 2.25×10^{-4} to 4.28×10^{-4} mol cm^{-3} [386].

The increased amount of bound rubber can be related indirectly to the potential reinforcement and modulus of HTV-SR [387]. The correlation between the modulus of rubber materials at a low strain and the crosslinking density can be stated by $E = 3vkT$ where v, E, k, and T are the crosslinking density, modulus, Boltzmann constant, and temperature, respectively [388]. As such, it was the modulus of these prepared nanocomposites that was enhanced relative to the pristine HTV-SR.

Although the crosslinking density of most produced nanocomposites was higher than that of pristine HTV-SR, the crosslinking density was reduced by gradually replacing DE particles with FS to the point where the crosslinking density of nanocomposites D30F90 and D40F80 was respectively 29% and 17% less than that of pristine HTV-SR. Regarding the nanoscale size of the FS, it could allow them to be located among the rubber chains and possibly restrict crosslinking reactions. This would lead to a reduced crosslinking density and an increase in M_C.

Hardness is another parameter required to be assessed when designing hybrid composites. To the best of our knowledge, such a criterion has not been assessed in previous investigations of superhydrophobic bulk materials [20, 209, 210]. The hardness test confirms whether the produced superhydrophobic bulk materials are physically stable enough to be used in real-life applications. The addition of particles into the HTV-SR enhanced hardness (Table 4-2). The hardness of sample D70F50 was 53% higher than that of pristine HTV-SR. Increasing the mass ratio of DE/FS enhanced hardness values, following along the same trend as crosslinking density. For filled-rubber composites, the greater the crosslinking density, the greater the hardness. In other words, compared to an unfilled rubber, the addition of reinforcing fillers increases crosslinking density

followed by enhancement of hardness [389, 390]. In the highly filled-rubber composites produced in this study, three main factors favored higher hardness values for the nanocomposites: the greater amount of micro-sized DE as elastic solid particles, a high crosslinking density, and a restricted movement of HTV-SR chains by nano-sized FS fillers.

Table 4-2. Analysis of crosslinking measurements obtained from the swelling test as well as hardness values for pristine HTV-SR and each produced nanocomposite.

Type	*Swelling ratio*	*Crosslinking density (mol cm^{-3}) × 10^{-4}*	*M_C (g/mol)*	*Hardness (Shore A)*
HTV-SR	1.485 ± 0.002	1.63 ± 0.02	7076 ± 109	62.8 ± 0.7
D30F90	0.848 ± 0.006	1.16 ± 0.06	9943 ± 452	92.0 ± 0.6
D40F80	0.765 ± 0.005	1.35 ± 0.05	8519 ± 360	91.2 ± 0.9
D50F70	0.668 ± 0.004	1.65 ± 0.04	6974 ± 278	92.1 ± 0.5
D60F60	0.639 ± 0.003	1.76 ± 0.03	6540 ± 163	94.8 ± 0.6
D70F50	0.595 ± 0.004	1.95 ± 0.04	5896 ± 271	96.1 ± 0.4
D80F40	0.550 ± 0.002	2.18 ± 0.02	5263 ± 102	97.0 ± 0.4
D90F30	0.562 ± 0.004	2.12 ± 0.04	5427 ± 265	97.2 ± 0.9

4.4.3 Physical, chemical, and thermal characteristics

The formation of roughness on the surface is one of two requirements for having superhydrophobic surfaces. With the help of profilometry and SEM analyses, we observed the presence of particles on the surface of the HTV-SR. The specific structure of the micro-sized DE particles along with the aggregated nano-sized FS were responsible for the non-wettability of the prepared nanocomposites. Given the favorable results for wettability, crosslinking density, and hardness, we also studied the surface morphology of the pristine HTV-SR and nanocomposites D60F60, D70F50, and D80F40 (Figure 4-3 (a–h)). The root mean square (RMS) roughness value represents the standard deviation of the distribution of surface roughness height within the scanned area. Pristine HTV-SR had a relatively smooth surface roughness with the RMS and arithmetic average (R_a) roughness values of 1.761 and 1.461 µm, respectively. After the incorporation of particles, hierarchical micro-nanostructures were created on the substrate. Due to the shape and variable size of the micro-sized DE particles, the increased mass ratio of DE/FS increased the roughness values. Sample D80F40—having 80 phr micro-sized DE and 40 phr nano-sized FS—produced 70% and 62% higher RMS and mean roughness values, respectively, than those of the pristine HTV-SR.

As for the other parameters, Skewness (R_{sq}) and kurtosis (R_{ku}) coefficients were also compared. R_{sq} describes the symmetry level of the surface heights distribution relative to the mean. A R_{sq} of zero represents a flawless, symmetric surface roughness having an equal presence of protrusions and depressions. A positive R_{sq} value testifies to high protrusions dominating the surface, while a negative R_{sq} represents a surface dominated by deep depressions [391]. R_{sq} gradually increased as particles were added. When the mass ratio of DE/FS was enhanced, the R_{sq} increased until a maximum value of -0.413, indicating the dominance of deep depressions. This surface pattern originated from the agglomeration of DE particles of various shapes and sizes in the matrix.

R_{ku} reflects the distribution of protrusions and depressions as well as the sharpness of the surface roughness features. A value of R_{ku} >3 illustrates a surface having spiky protrusions and/or sharp depressions, while a value of <3 reflects a more compressed distribution of roughness features compared to a Gaussian distribution [392]. A R_{ku} = 3.190 for a high mass ratio illustrated a relatively high number of spiky surface features with the presence of a high amount of DE particles. We directly observed the enhanced surface roughness at a high mass ratio using FESEM analysis (Figure 4-3 (e–h)). As shown in Figure 4-3 (h), the abundance of DE particles on the surface is responsible for the high surface roughness. As well, we also observed submicron-scale fiber-like morphologies that had fiber diameters <200 nm in the higher magnification images. These fiber-like morphologies are caused by the orientation and filamentation of long polymer chain structures of SR molecules produced at specific pressures and temperatures near the mold surface. The higher roughness and the specific shape of DE particles were responsible for the superhydrophobicity of the nanocomposites.

The cryogenically fractured surfaces of the pristine HTV-SR and nanocomposites are displayed in Figure 4-3 (i–l). Compared to the pristine HTV-SR, the fractured surface of nanocomposites demonstrated rougher and more irregular surfaces having a great number of micro-sized depressions. This pattern is produced by the interfacial debonding of the fillers and HTV-SR. Stress concentrations at the interface of fillers and matrix initiated numerous cracks along the nanocomposite that can propagate and result in fracturing. Moreover, the numerous nano-sized FS particles within nanocomposite D60F60 produced a rougher fracture surface having more wave-like structures in comparison to the other nanocomposites. This stemmed from the higher number of nano-sized FS particles that created greater concentrations of stress to produce a greater

debonding effect. All these depressions and roughness features create the superhydrophobicity of the bulk material.

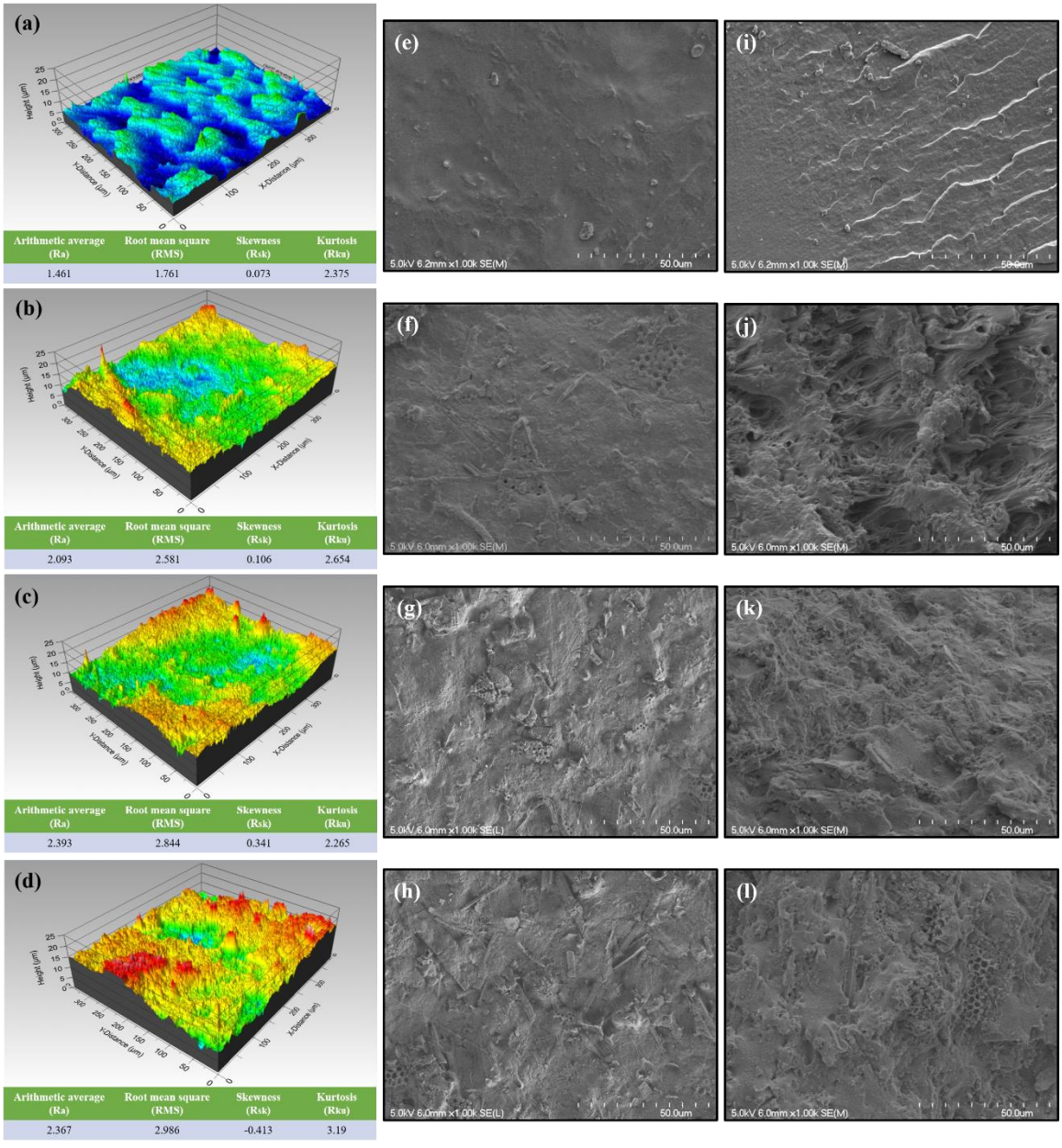

Figure 4-3. Surface profiles and roughness values of (a) pristine HTV-SR and the nanocomposites (b) D60F60, (c) D70F50, and (d) D80F40; FESEM images of the surface of (e) the pristine HTV-SR and the nanocomposites (f) D60F60, (g) D70F50, and (h) D80F40; FESEM images of the cross section of (i) pristine HTV-SR and nanocomposites (j) D60F60, (k) D70F50, and (l) D80F40. All images (e–l) are at ×1000 magnification.

Moreover, the FESEM images of nanocomposites at ×10000 magnification reveal the dispersion of nano-sized FS on the surface and within the bulk material (Figure 4-4). It can be seen that the prime particles as well as agglomerates <200 nm are distributed uniformly within the matrix and are located on the DE

structures. The presence of nano-holes on both the surface and cross-sections of the nanocomposites stems from the specific yet diverse structural features of the DE particles (see Figure 4-4(c)). Clusters of holes on each surface correspond to a single DE particle of a specific structure. Although we expected an incompatibility of the hydrophobic HTV-SR matrix and the hydrophilic DE particles, we observed no clear gaps or interfaces between the HTV-SR and DE; the lack of the features reflects their compatibility and interfacial adhesion. When the HTV-SR and DE were solution-blended together at a high temperature (70 °C), the reaction between the methyl groups of silicone rubber and the siloxane groups of DE likely improved the matrix-particle compatibility.

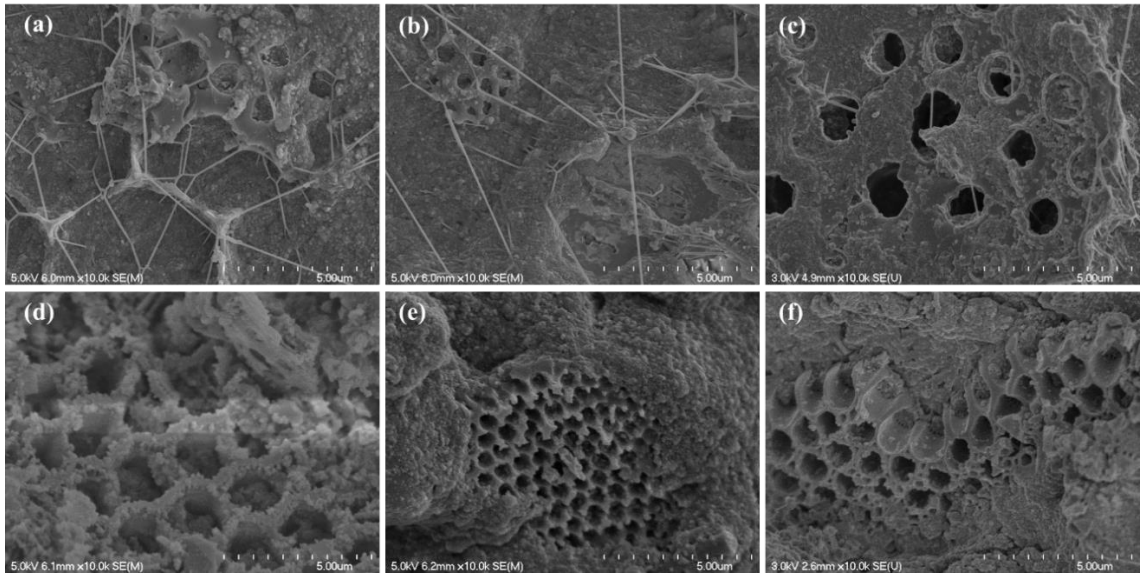

Figure 4-4. FESEM images of the surface of nanocomposites (a) D60F60, (b) D70F50, and (c) D80F40; FESEM images of the cross section of nanocomposites (d) D60F60, (e) D70F50, and (f) D80F40. All images (a–f) are at ×10000 magnification.

The addition of diverse particles affects the chemical characterization of the composites. As expected, we observed that all five nanocomposites showed similar FTIR spectra. For brevity, we only present the FTIR spectra of the pristine HTV-SR, the nanocomposite D70F50, and the fillers alone (Figure 4-5 (a)). As most of the DE is amorphous silica, its FTIR spectra is identical to FS and indicates two absorption bands at 799 and 1062 cm^{-1} that correspond to siloxane groups. We did not observe any hydroxyl absorption bands in the FTIR spectra of DE, as we had placed DE particles in an oven for 24 h prior to conducting the FTIR test. The volumetric superhydrophobic nanocomposite showed virtually identical FTIR spectra to the reference matrix. There are two broad absorption spectra at around 790–840 and 1000–1110 cm^{-1} that are assigned to the symmetric and asymmetric stretching vibrations of Si–O–Si. The remaining spectra common between HTV-

SR and nanocomposites are related to the stretching and bending modes of C–H in CH_3 (approximately 2961 and 1410 cm^{-1}), symmetric CH_3 deformation in Si–CH_3 (1258 cm^{-1}), and Si–O bonds in Si–$(CH_3)_2$ (785 cm^{-1}) [21, 296, 393]. Adding fillers reduced the intensity of the absorption peaks compared to the pristine HTV-SR, with the absorption peaks reducing in intensity to become more similar to the absorption peaks of the fillers themselves. Given the high-volume percentage of FS, the fillers had a dominant effect on the chemical composition of the nanocomposite. On the other hand, comparing the percentage of absorption peaks of the HTV-SR and nanocomposite, we detected the greatest reduction in the relative intensity of absorption peaks at 1258 cm^{-1} and 2961 cm^{-1}. This observation can be attributed to the reaction between the methyl groups of the HTV-SR and the siloxane groups of DE particles.

TGA to evaluate the thermal stability of the pristine HTV-SR and nanocomposite D70F50. As expected, the nanocomposite demonstrated substantially enhanced thermal stability with the addition of inorganic particles. The $T_{10\%}$ and $T_{50\%}$ temperatures of pristine HTV-SR and nanocomposite D70F50—corresponding to respective 10% and 50% weight loss—are demonstrated in Figure 4-5 (b). After adding the particles, $T_{10\%}$ was significantly enhanced from 447 °C to 553 °C; a pattern that can be related to the enhanced interfacial interaction between the fillers and HTV-SR. Given the good thermal stability of both the DE and FS fillers, the ~33% weight loss of the nanocomposite should result from the decomposition of the HTV-SR matrix that is much less than that of the pristine HTV-SR (~69% weight loss). Finally, the TGA results confirm the stability of nanocomposite up to 500 °C, a temperature that fulfills most of the indoor and outdoor requirements for materials. The TGA curves of nanocomposite D60F60 and D80F40 are presented in the supplementary materials (Figure AII-3).

Given its marked water-repellency and hardness, the volumetric superhydrophobic HTV-SR/DE/FS nanocomposite having a DE/FS mass ratio of 70/50 was preferentially chosen for the subsequent analyses of mechanochemical robustness.

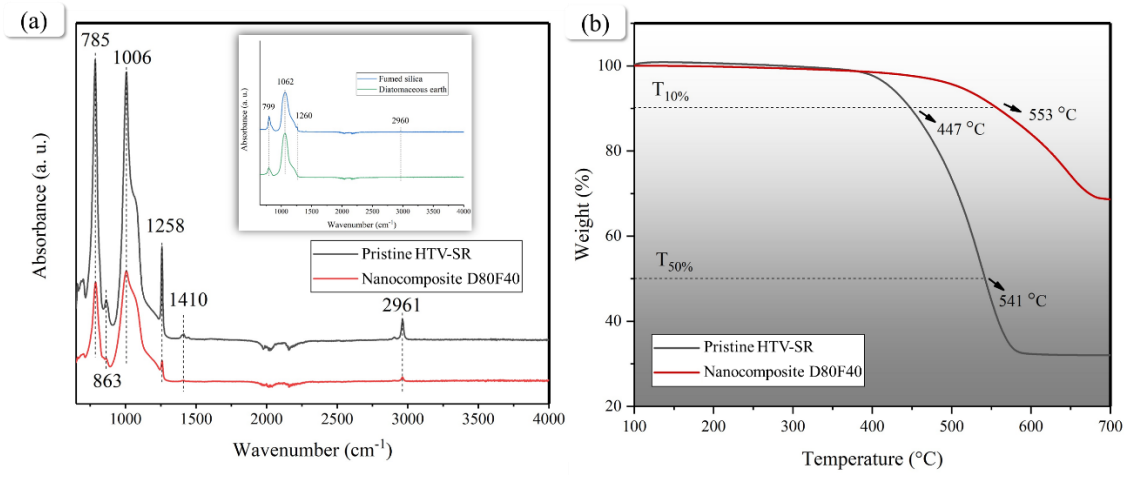

Figure 4-5. (a) FTIR spectra of the pristine HTV-SR and nanocomposite D70F50 (inset shows the FTIR spectra of FS and DE); (b) TGA curve of the pristine HTV-SR and nanocomposite D70F50.

4.4.4 Mechanochemical robustness

As one of the aims of this study is to fabricate super-durable volumetric superhydrophobic nanocomposites, we undertook a comprehensive study of the long-term mechanochemical robustness of the prepared robust volumetric superhydrophobic nanocomposite. These tests included mechanical durability as well as chemical and UV resistance. The mechanical robustness of the prepared nanocomposites was assessed by a series of tests: sandpaper abrasion, knife scratching, tape peeling, water jet impact, sandblasting, and ultrasonication.

In the sandpaper test, an abrasion cycle consisted of dragging the sample along the sandpaper for 20 cm under a specific abrasion force applied on sample. Regardless of the abrasion force, i.e. 5 kPa or 25 kPa, or sandpaper grit, i.e. #160, #320 and #800, after 250 abrasion cycles the WCA of superhydrophobic nanocomposite remained almost >160° and CAH <5° (Figure 4-6 (b and c)). This resistance to abrasion outperformed many other existing superhydrophobic surfaces. Chen et al. [394] reported a WCA of ~150° and sliding angle of ~25° after 40 abrasion cycles for a superhydrophobic multilayer coating. Wang et al. [395] fabricated a mechanically robust superhydrophobic steel surface where the WCA reduced to 152° and CAH increased to 8° after a 110-cm abrasion distance. Another mechanically robust superhydrophobic coating lost superhydrophobicity after a 200-cm abrasion distance using #180 sandpaper [396].

The abrasion procedure could have been continued to a point that all nanocomposites had worn out, yet where the nanocomposite remained superhydrophobic. Thus, we can name this material as an abrasion-insensitive superhydrophobic nanocomposite. The restored superhydrophobicity signified the emergence of a

fresh superhydrophobic layer on the surface after each abrasion cycle. The freshly exposed surface morphology of the nanocomposite after 250 abrasion cycles with #320 sandpaper is shown in Figure AII-5 in ESI. The morphology of the abraded surface differed from the intact surface, yet the abraded surface remained covered by numerous depressions and protrusions. These features were responsible for the continued water-repellency properties.

The volumetric superhydrophobic nanocomposite also a retained favorable water-repellency after being subjected to knife scratching, tape peeling, water jet impact, and sandblasting tests. In knife scratching test, the surface was scratched in multiple directiones by a brand-new cutter blade. Water droplets continued to roll off the surface after the scratching (Figure 4-6 (d)). We also performed a multiple mechanical approach—knife scratching, finger pressing, and tape peeling. Nevertheless, we observed no visible changes to water-repellency. We subjected the nanocomposite to cycles of adhesion/peeling of adhesive tape. After 200 cycles, as shown in Figure 4-6 (e and f), the WCA and CAH of the nanocomposite was not altered.

Two impact tests also failed to eliminate the water-repellency of the nanosurface. A red-colored water jet arriving at the superhydrophobic surface at an angle of about 30° impacted the superhydrophobic nanocomposite and was fully repelled at about 16° (Figure 4-6 (g). After 15 min of testing, the surface remained intact and dry, confirming the stability of the air trapped among the micro-nanostructures on the surface of the volumetric superhydrophobic nanocomposite. During sandblasting, the superhydrophobic nanocomposite was also blasted vigorously by SiC particles for 1 min (at a pressure of 20 psi from ~25 cm distance) followed by the application of compressed air to remove all particles. The sandblasted nanocomposite retained a high WCA and its superhydrophobic characteristics (Figure 4-6 (h)).

We also performed ultrasonication of the volumetric superhydrophobic nanocomposites in water. In ultrasonication, the ultrasonic frequency (>20 kHz) is transformed into energy and applied to the immersed nanocomposite. This procedure can be highly destructive to surface micro-nanostructures. We subjected the submerged samples to ultrasonication for various lengths of time, after which we withdrew the samples from the water bath and dried them in an oven at 80 °C for 1 hr. After 1 h of ultrasonication, we observed a slight change in WCA and CAH; however, the nanocomposite maintained its superhydrophobic characteristics, i.e., WCA >150° and CAH <10°. By lengthening the ultrasonication to 2 h, the WCA reached 150° and the CAH increased to about 20°. This deterioration in water-repellency may relate to the formation of hydrogen bonds

due to the reaction between the water molecules and the DE particles on the sample surface, as well as the damage sustained to the surface micro/nanostructures due to the high-frequency energy of ultrasonication. The lost superhydrophobicity of the ultrasonicated nanocomposite was partly restored after being heated at 80 °C for 24 h—we observed a WCA of 154.6° and a CAH of 9.4 °—due to the hydrophobic recovery ability of silicone rubber. Through hydrophobic recovery, the migrated low molecular weight siloxane (LMWS) covered the hydrogen bonds that were produced on the surface after ultrasonication. To reinstate instantly the micro/nanostructures of the nanocomposite lost due to the high-frequency energy, we removed the upper layer through sanding or cutting. We achieved a WCA of 163.7° and a CAH of 2.8°. We repeated this two-step procedure, i.e., 2-h ultrasonication followed by surface abrasion, five times. As shown in Figure 4-6 (i), we obtained a WCA >160° and a CAH <5° after each ultrasonication–abrasion cycle.

All these tests confirm the mechanical robustness of the produced volumetric SH nanocomposite under various harsh conditions and its restoring ability. The presence of embedded DE and FS particles within the bulk material provides a source of regenerative surface micro/nanostructures (Figure 4-7). The regeneration of favorable micro/nanostructure roughnesses, corresponding to the exposed DE and FS particles on the surface, ensures a continuous superhydrophobicity. Once water-repellency and roughness features have deteriorated, they can be regenerated endlessly by abrading the surface. The entire process can be repeated until the nanocomposite is completely worn out. This feature provides a range of possibilities for the real-life application of these fabricated volumetric SH nanocomposite.

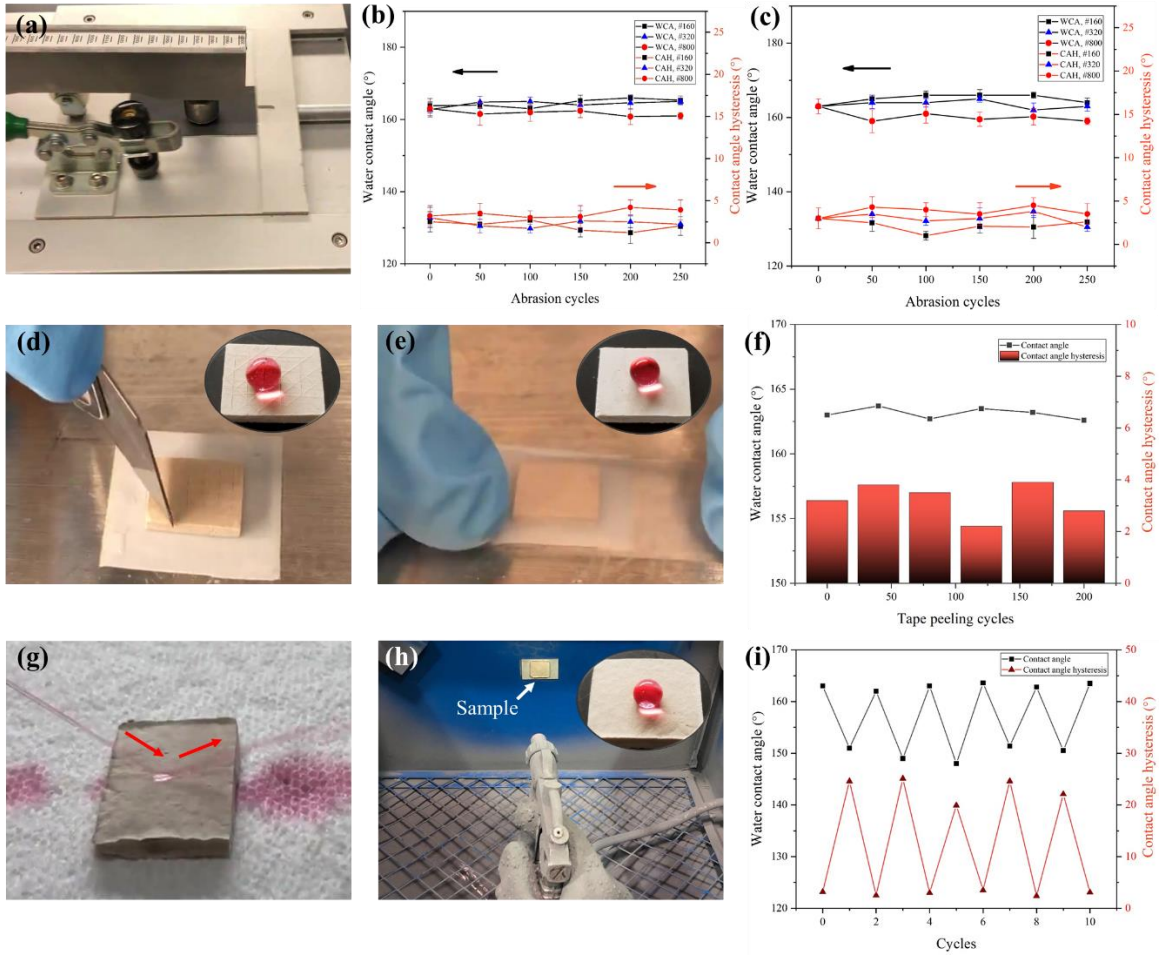

Figure 4-6. (a)–(c) Sandpaper abrasion of the nanocomposite D70F50; (a) an image of the sandpaper abrasion apparatus; (b) WCA and CAH of the nanocomposite abraded by #160, #320, and #800 sandpaper after 250 abrasion cycles at a 5 kPa abrasion force; (c) WCA and CAH of the nanocomposite abraded by #160, #320, and #800 sandpaper after 250 abrasion cycles at a 25 kPa abrasion force; (d) knife scratching test; (e) tape peeling test; (f) WCA and CAH of the nanocomposite after multiple cycles of tape peeling; (g) water jet impact test; (h) sandblasting test; (i) WCA and CAH of the nanocomposite after several repeated cycles of ultrasonication and abrasion. Insets demonstrate the wettability of the nanocomposite after the associated tests.

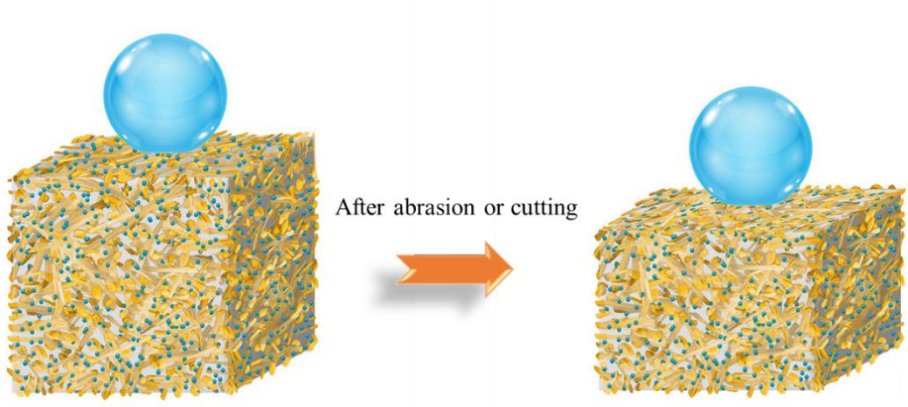

Figure 4-7. Schematic illustration of the volumetric superhydrophobic nanocomposite containing DE and FS particles.

In addition to the mechanical robustness, the chemical, thermal, and UV resistance of the prepared volumetric superhydrophobic nanocomposites are also important for use of these materials in real-life conditions. To assess chemical stability, we studied two methods of immersion and droplet evaporation (Figure 4-8 (a and b)). As an aggressive experiment, an immersion test was conducted. After five days of continuous contact with deionized water, the WCA and CAH of the sample remained almost constant, i.e., >160° and <4°, respectively. In acidic and alkaline solutions, the same results were observed so the WCA was >155° and the CAH was <6° after five days. During the immersion process, we observed neither the formation of adsorption/wetting film on the surface of the samples nor any chemical interactions with the deionized water or the acidic and alkaline solutions that altered the non-wetting properties of the samples.

In the droplet evaporation technique, although the size of the droplets gradually decreased due to evaporation, the WCA remained >154°. These observations demonstrated the consistency of the Cassie-Baxter regime on the surfaces, but they also testified to the remarkable chemical stability of the nanocomposite when subjected to these three different wetting media. In the Cassie-Baxter wetting regime, the presence of air pockets among the roughness asperities severely limits the contact area between the substrate and solution; thus, the deterioration of the WCA and CAH values is effectively delayed for an extended period.

To ensure the persistent superhydrophobicity of the nanocomposite at high temperatures, we assessed the thermal stability of pristine and superhydrophobic nanocomposites by heating the samples at different temperatures in a furnace for 2 hr followed by their cooling to room temperature (Figure 4-8 (c)). The WCA of pristine HTV-SR decreased gradually from 116° to 105° as the temperature increased to 300 °C. At 400 °C, the WCA decreased rapidly to 81°, while the nanocomposite retained its superhydrophobicity with the WCA

and CAH of the superhydrophobic nanocomposite remaining almost unchanged even after thermal annealing at 400 °C for 2 h. Thus, the presence of micro- and nanoparticles enhanced the thermal stability of the nanocomposite and produced a long-lasting superhydrophobic nanocomposite.

Given the ability of silicone rubber to recover its hydrophobicity, we applied air plasma to the superhydrophobic nanocomposite using an atmospheric-pressure plasma system. Immediately after treatment, the non-wettable superhydrophobic characteristic became superhydrophilic and fully wetted during contact with a single water droplet (Figure 4-8 (d)). This observation is caused by the oxidation of methyl groups with O_2 in the plasma stream and the formation of hydrophilic hydroxyl groups on the surface. Interestingly, however, thanks to the migration of low molecular weight siloxane oligomers from the bulk to the surface as well as reorientation of hydroxyl groups from the surface into the bulk material [397], the superhydrophobicity of the nanocomposite was restored after four days. We performed five cycles of plasma treatment and four days of recovery, and the WCA remained >160°.

To evaluate the performance of volumetric superhydrophobic nanocomposites in outdoor applications, we then exposed our sample to UV irradiation at 70 °C for 300 h. These conditions correspond to about two years of exposure to UV-light radiation under natural conditions in Toronto, Ontario [398]. The WCA and CAH of the samples remained constant (Figure 4-8 (e)), confirming the excellent UV stability of both the pristine HTV-SR and nanocomposite due to the high binding energy of the $(SiO)_x$ functional groups of silicone rubber that hinder exceeding chain scission [399].

Moreover, the presence of some voids and free volumes on the surface and within the bulk material may produce several paths for the diffusion of water into the nanocomposite and thereby accelerate aging, while also deteriorating the chemical and mechanical properties of nanocomposites [400]. To ascertain the water absorption of the prepared superhydrophobic nanocomposite compared to that of the pristine SR, we left the samples submerged in deionized water for 10 days. Every two days, we withdrew the samples from the water, wiped off each side of the immersed sample with tissue, and then weighed the samples. Water absorption was calculated as follows:

$$M = \frac{m_2 - m_1}{m_1} \times 100 \qquad 4\text{-}4$$

where M is the water absorption capacity, and m_1 and m_2 are the weights of the sample before and after water absorption, respectively. The pristine HTV-SR showed up to 14% water absorption, a value indicating

the diffusion of water into the free volumes among the polymeric chains (Figure 4-8 (f)). Due to the volumetric superhydrophobicity, water absorption into the nanocomposite after 10 days was almost zero. In typical superhydrophobic surfaces, water is absorbed through the non-water-repellent side of the samples. However, in this study, due to the great water-repellency of the whole bulk of the sample material, the water uptake of the prepared nanocomposite was nil.

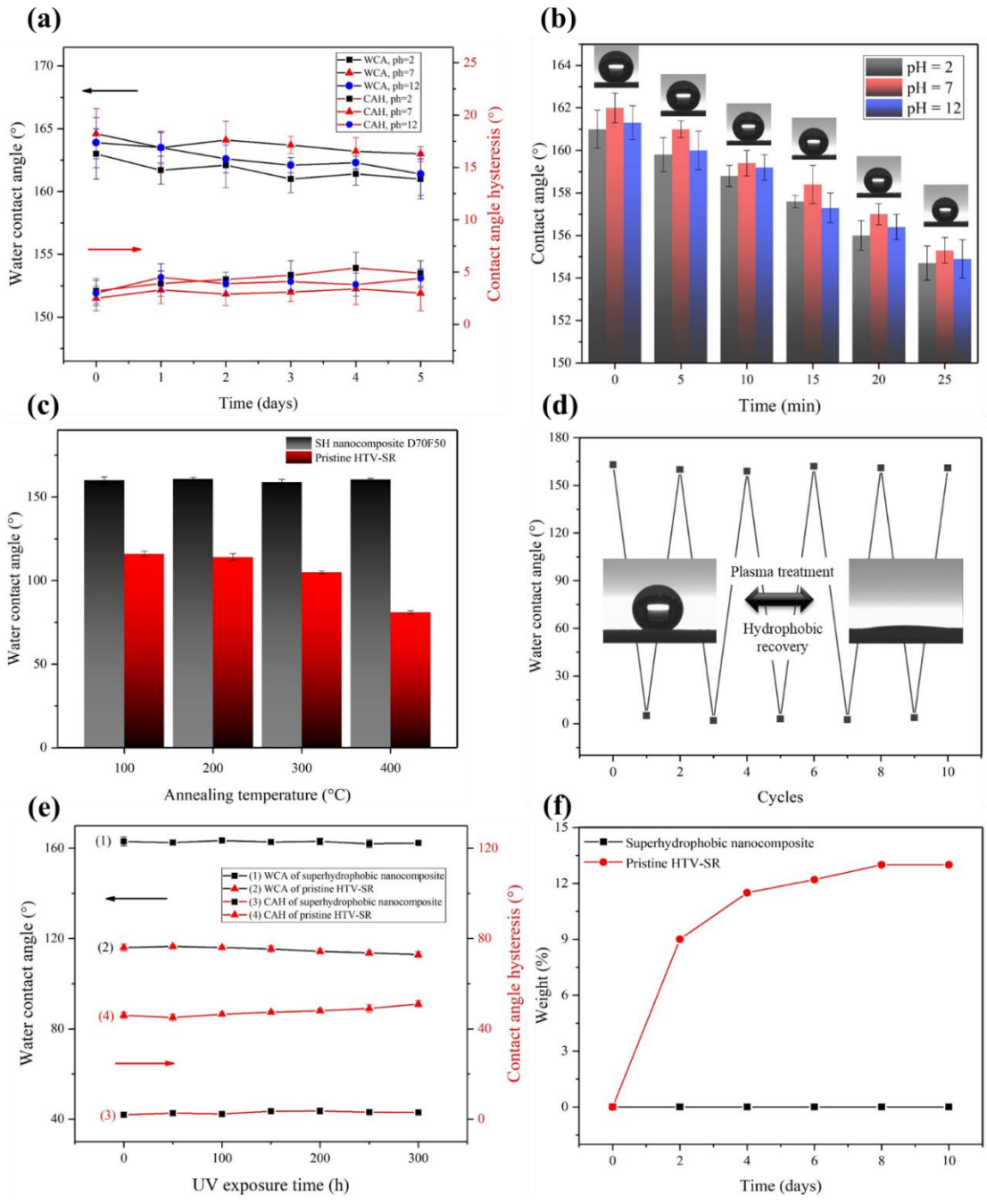

Figure 4-8. (a) Changes in WCA and CAH of the nanocomposite D70F50 over time during its immersion in deionized water and the acidic and alkaline solutions; (b) contact angle of droplets of deionized water and the acidic and alkaline solution during the droplet evaporation test (inset images show the WCA during evaporation of the water droplet); (c) WCA of the nanocomposite and pristine HTV-SR after heating for 2 h at different temperatures; (d) hydrophobic recovery of the nanocomposite following each cycle of plasma treatment; (e) WCA and CAH of the nanocomposite relative to the pristine HTV-SR as a function of the duration of UV irradiation; (f) water uptake of the pristine HTV-SR and superhydrophobic *nanocomposite in relation to the duration of the sample immersion.*

4.4.5 Self-cleaning

Self-cleaning is a characteristic of superhydrophobic surfaces that stems from the high water-repellency and rolling of water droplets over the superhydrophobic substrate. Due to the usual hydrophilic nature of contaminants, the adhesion between water droplets and contamination particles is greater than that between the superhydrophobic surface and the contamination [24, 215]. Consequently, the contamination can easily adhere to the round-shaped water droplets rolling off the surface and be removed from the material surface [219].

High WCA, low CAH, low adhesion force, and an adequate particle size are necessary for creating a self-cleaning surface [221]. As we are using superhydrophobic substrates, three of these conditions are already attained. To assess the effect of particle size of the contaminant on the self-cleaning characteristic of the volumetric superhydrophobic nanocomposite, we tested the self-cleaning properties of the superhydrophobic nanocomposite using hydrophilic SiC particles having diameters of 50 µm and 18 µm. The particles were spread uniformly over the surface of the nanocomposites that were placed with a 10° tilt angle. As shown in Figure 4-9, we used a syringe needle to place 20-µL water droplets onto the contaminated surface. Regardless of particle size, all particles adhered easily to the water droplets and resulted in a completely clean superhydrophobic surface.

To assess the self-cleaning property of volumetric superhydrophobic nanocomposites under wet conditions, we prepared a 30 g L^{-1} dirty solution, containing water and silicon carbide particles that had an average diameter of 18 µm mixed in water. We submerged the samples in the dirty solution and vigorously shook the sample in the dirty solution for several seconds before removing the samples. As shown in Videos 4 and 5 in the ESI, dirty layers formed on the pristine HTV-SR and covered all sides of the sample, whereas the entire volumetric superhydrophobic nanocomposite remained clean. This observation emphasized the self-cleaning and dirt-repelling ability of the prepared nanocomposites on all exposed surfaces.

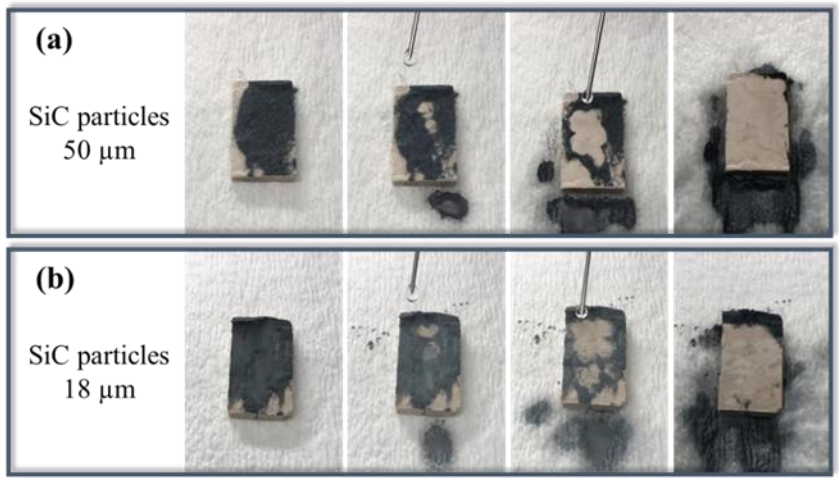

Figure 4-9. Self-cleaning ability of the volumetric superhydrophobic nanocomposite D70F50. (a) SiC particles having a size of 50 µm and (b) SiC particles having a size of 18 µm. A clean surface was observed in the final images of the rows.

4.5 Conclusion

Durable superhydrophobic materials are in high demand for applications in real-life situations. Here, we fabricated an ultra-robust, non-fluorinated, volumetric superhydrophobic and self-cleaning HTV-SR/ micro-sized-DE/ nano-sized-FS nanocomposite. In addition to superhydrophobicity, hardness and crosslinking density of the SR were enhanced by the adding of nano/microparticles to the HTV-SR, confirming the physical stability of the nanocomposite. The superhydrophobicity of the prepared nanocomposite was retained despite multiple aggressive mechanical, chemical, and UV analyses. After 250 cycles of sandpaper abrasion under the 5.0 kPa and 25.0 kPa abrasion forces with various sandpaper grits, WCA and CAH remained at ~160° and <5°. Following abrasion, the surface micro-nanostructures were replaced by fresh micro-nanostructures consisting of DE and agglomerated FS particles as well as channel-like structures induced by the sandpaper. Moreover, knife scratching, tape peeling, water jet impact and sandblasting experiments did not affect the water-repellent properties of the prepared microcomposite. The superhydrophobic nanocomposite also demonstrated outstanding chemical and UV resistance. Water uptake by superhydrophobic nanocomposite remained almost nil even after 10 days of submersion.

Acknowledgments

The authors gratefully acknowledge the Natural Sciences and Engineering Research Council of Canada (NSERC) and K-Line Insulators Limited (Toronto, Canada) for financial support.

CHAPTER 5

ARTICLE 4: A COMPARATIVE STUDY OF THE ICEPHOBIC AND SELF-CLEANING PROPERTIES OF TEFLON MATERIALS HAVING DIFFERENT SURFACE MORPHOLOGIES

E. Vazirinasab, K. Maghsoudi*, R. Jafari, G. Momen
Department of Applied Sciences, University of Quebec in Chicoutimi (UQAC)
555, boul. de l'Université, Chicoutimi, Québec, G7H 2B1, Canada
* E-mail: Khosrow.maghsoudi1@uqac.ca

5.1 Abstract

Materials having fluorocarbon bonds are among the best candidates for the fabrication of superhydrophobic surfaces. Here, two facile, non-expensive, and industrialized approaches were described to produce superhydrophobic Teflon materials having ultra-water-repellency, icephobic, and self-cleaning properties. Direct replication and plasma-treatment approaches produced Teflon sheets having very different surface patterns, i.e. microstructures and micro-nanostructures. Neither approach altered the chemical composition of the original Teflon surfaces. Rice leaf–like microstructures were produced on the replicated surface, whereas lotus leaf–like hierarchical micro-nanostructures characterized the plasma-treated surface. Water droplets rolled off the micro-nanostructured surfaces ~10% faster than off the microstructured surfaces. The micro-nanostructured surface also produced more rebounds for a water droplet during the impact test. Although both surfaces possessed similar self-cleaning properties, the micro-nanostructured surface reduced ice adhesion to a greater degree than the microstructured surface. The more effective ice repellency of the micro-nanostructured surface was due to its surface morphology that reduced the interlocking of ice inside the surface asperities. However, the microstructured surface delayed considerably the onset of freezing of a water droplet due to the larger micro-air pockets trapped within its surface asperities.

Keywords: Teflon surface; icephobic; self-cleaning; surface morphology; freezing delay; ice adhesion reduction.

5.2 Introduction

Icing phenomena on outdoor equipment such as transmission cables, aircraft, wind turbines, and telecommunication towers can lead to their mechanical failure and their becoming safety hazards. To reduce this damage to vulnerable outdoor infrastructure, attempts have been made to create anti-icing/icephobic surfaces [234, 265, 276, 401-405]. Icephobic surfaces are normally defined by an ice adhesion strength of <100 kPa [406]. In reality, two main categories of de-icing and anti-icing techniques exist and differ in their ice adhesion requirements. The first is composed of active methods where thermal or mechanical energy is used to de-ice. The second represents passive methods where no external energy is applied [407]. For the passive removal of ice, a much lower ice adhesion strength (<20 kPa) is required [406].

Superhydrophobic surfaces having a water contact angle (WCA) >150° and a contact angle hysteresis (CAH) <10° can be created through a combination of low surface energy materials and micro- and/or nanostructured surface topography [408]. This combination leads to the trapping of air pockets in the depressions on the surface and produces a composite air-liquid-solid interface. This interface increases WCA and decreases CAH to produce a Cassie-Baxter state [51]. Such non-wetting surfaces are among the best candidates for delaying ice formation and reducing the energy needed for de-icing. Superhydrophobic surfaces having various surface roughness—microstructures, nanostructures, hierarchical structures—demonstrate different icing behaviors during both ice formation and de-icing [238, 313, 317, 350, 409-413]. These various icing behaviors are due to (a) the amount of heat transfer through the trapped air in between the surface asperities [313, 410], (b) the effect of surface roughness on the heterogeneous nucleation rate of ice at the water-solid interface [313, 317], and (c) the interlocking of created ice within the surface asperities [238, 350, 412].

Over the last decade, multiple approaches have been used to create superhydrophobic surfaces [13, 35, 110, 414-423]. The direct replication and plasma-treatment methods are compatible with industrial applications. They do not require complex engineering procedures or a long fabrication time [103, 262]. Moreover, these approaches can fabricate superhydrophobic surfaces on a wide range of materials [34, 424]. Polytetrafluoroethylene (PTFE) is a polymer that has extremely low surface energy (18.6 mN/m at 20 °C) making PTFE a promising candidate for fabricating superhydrophobic surfaces [425]. Previous studies have described creating superhydrophobic surfaces using a PTFE coating generated by sputtering [14, 426, 427].

Here, however, fabrication of superhydrophobic PTFE materials, e.g. Teflon sheets, films, composites was studied [428-430].

Two different facile, low-cost methods were employed to produce self-cleaning and icephobic Teflon materials through the processes of direct replication and atmospheric-pressure plasma. Although using a plasma technique is a commonly applied method for creating superhydrophobic PTFE materials, it has always been limited to non-atmospheric low-pressure plasma, e.g. Ar, CF_4, N_2, and O_2 plasmas [164, 431]. To the best of our knowledge, neither atmospheric-pressure plasma nor direct replication has yet been used for producing icephobic and self-cleaning PTFE materials. Through our novel approach, two very different surface morphologies, i.e. microstructured rice leaf–like grooves by direct replication and hierarchical micro-nanostructured lotus leaf–like pattern by plasma treatment were obtained. Despite similar self-cleaning abilities, the structures differed in their icing behaviors.

5.3 Materials and methods

5.3.1 Fabrication of superhydrophobic Teflon surfaces

Superhydrophobic samples were produced using Teflon® (Groupe POLYALTO, QC, Canada) sheets of 30 mm × 50 mm × 2 mm. The templates for the direct replication were produced using aluminum alloy 5052 and a wet chemical etching method. The etching was carried out by submerging the template in a 10 wt.% HCl solution for various times. The etched templates were then cleaned ultrasonically using a mixture of acetone, ethanol, and distilled water to remove any residual particles from the surface. Various etching times of 10, 15, 20, 25, and 30 min were examined to produce microstructured aluminum templates. The results of WCA and CAH for Teflon surfaces replicated on the produced aluminum templates at various etching times are presented in Table 5-1. The best results in terms of superhydrophobicity of replicated Teflon surface were achieved for the etching time of 20 min.

Table 5-1. The results of WCA and CAH for Teflon surfaces replicated on the produced aluminum templates at various etching times.

Etching time of the template (min)	***WCA of the replicated Teflon surface (°)***	***CAH of the replicated Teflon surface (°)***
10	120.5 ± 2.3	29.8 ± 1.1
15	148.3 ± 1.9	16.5 ± 2.5
20	166.6 ± 1.2	4.2 ± 1.1
25	153.2 ± 1.5	13.4 ± 2.3
30	158.5 ± 2.6	10.5 ± 2.2

A press machine (Carver Inc., USA) was used for the direct replication of created patterns on the Teflon surfaces. The machine has two temperature-controllable platens, and the temperature range varies from ambient temperature to 350 °C. The platen temperatures were set at 280 °C, and the Teflon sheet was placed on the lower platen to soften. After 5 min, the aluminum template was placed carefully on the Teflon sheet and the platens were fastened using a hydraulic pump. A pressure of 170 kPa was applied for 10 min to soften the Teflon sheet and therefore replicate the aluminum template patterns faithfully. After this step, the platens were opened, and the Teflon sheet was detached from the template.

An AS400 atmospheric-pressure plasma machine (Plasmatreat GmbH, Germany) working in the pulsed mode was employed to create structures on the Teflon sheets. The compressed air was used as it is an abundant and inexpensive plasma gas. The flow rate was set at 2000 $L \cdot h^{-1}$. The speed of the movable plasma jet was 2 $m \cdot min^{-1}$. The distance between the plasma nozzle and substrate was fixed at 8 mm and set the plasma frequency at 21 kHz. As the system works in a pulsed mode, the pulsed power-cycle time was set at 100, which represents an equal time of being on and off.

5.3.2 Surface characterization and water-repellency properties

Scanning electron microscopy (SEM) (JSM-6480 LV SEM manufactured by JEOL Japan) was employed to observe the surfaces of the produced surfaces. To enhance imaging quality, the Teflon surfaces were coated with a thin layer of gold-palladium alloy prior to analysis. To better observe surface topography, a 25° angle view was used for each measurement. An optical profiler (Profil3D Filmetrics, USA) measured surface roughness. The line and area roughness values were calculated based on ASME B46.1 2D and ASME B46.1 3D standards, respectively.

WCA and CAH were determined using a Kruss™ DSA100 goniometer set at 25 ± 0.5 °C. A 4-µL deionized (DI) water droplet was deposited onto the sample surface, and the WCA was measured using the Young-Laplace approximation. The CAH was defined as the difference between the advancing and receding contact angles when the water droplet moved on the surface. WCA was measured at five points on each sample, and each measurement was repeated five times to ensure accuracy. The average value and standard deviation for each sample were reported. To evaluate whether our approaches altered the chemical composition of the Teflon surfaces, a Cary 630 Fourier transform infrared spectroscopy (FTIR) Spectrometer (Agilant, USA) in ATR (attenuated total reflection) mode was used to analyze the chemical functions of the produced surfaces.

Water-repellency was evaluated through droplet roll-off and impact tests. The behavior of water droplets rolling off surfaces inclined at 10° was assessed. Using a syringe, a water droplet was placed gently onto the surface. The droplet had no initial velocity.

Water droplet impacts were recorded using a high-speed camera (FASTCAM SA1.1 by Photron) at a framing rate of 5400 fps, and all impact experiments were conducted at a constant temperature of 22 °C. The DI water droplets had a volume of 20-µL with a diameter of ca. 3.4 mm and were released with zero initial velocity from 12 cm above the surface.

5.3.3 Icephobic and self-cleaning properties

Icephobic properties of the produced samples were determined using a homemade push-off instrument. This test measures the shear stress at which ice is detached from the surface. The selected approach is particularly useful where small samples or more complicated geometries are tested. In this test, a thin cylindrical plastic mold, 1-cm in diameter, is placed on the substrate and then filled with DI water to form an ice cylinder by remaining in a cold chamber at -10 °C for 24 h prior to the testing. The test sample is then placed on the holder and fixed by two screws (Figure 5-1). By starting the test using a remote computer-controlled interface, the motor turns the screw at a fixed rate of 0.05 $mm \cdot s^{-1}$ so that the sample holder is pushed gradually toward the force gage. The force gage measures the shear force ten times per second until the ice is detached. Therefore, the adhesion stress can be calculated by knowing the maximum force and the icing area.

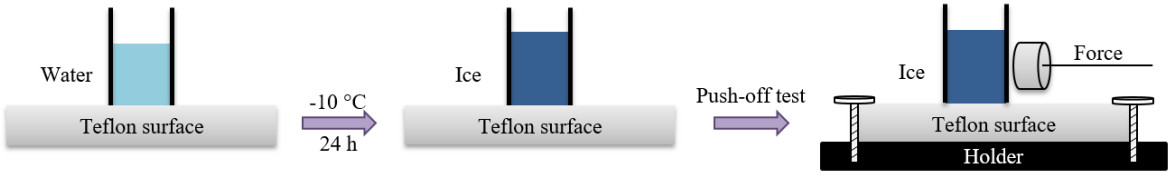

Figure 5-1. Schema of the push-off test procedure.

The freezing delay time was determined using the cold chamber of the Kruss™ DSA100 goniometer where sample stage temperature can reach -30 °C.

To assess the self-cleaning properties of the produced Teflon surfaces, kaolin powder having a chemical composition of $Al_2Si_2O_5(OH)_4$ was applied as the artificial contaminant. Equal amounts of kaolin powder were scattered homogeneously on the pristine, replicated, and plasma-treated Teflon surfaces using a 60-mesh sieve. Prior to conducting the self-cleaning test, the kaolin powder was allowed to set onto the surface for 30 min. Then a water droplet fixed to a syringe needle tip was used to sweep the kaolin powder off the Teflon surface

at a speed of 16.6 ± 0.1 $cm \cdot s^{-1}$. The images were captured by a high-quality digital camera (PowerShot SX50 HS, Canon).

The self-cleaning abilities of the produced superhydrophobic Teflon surfaces were also examined through the cleaning of a dried droplet containing a solution of several contaminants. A 24-$g \cdot L^{-1}$ dirty solution consisting of carbon black, kaolin, and salt in water was prepared for use as a contaminant. The solution was thoroughly mixed for 1 h, and before any sedimentation could occur, a droplet was placed gently onto each surface using a syringe to release ca. 3-mm-diameter droplets. The surfaces were then dried under ambient conditions for 3 h to evaporate the water and then cleaned with water droplets.

5.4 Results and discussion

5.4.1 Surface morphology

The surface morphology of the produced surfaces was examined using scanning electron microscopy. SEM images show the different surface roughness created on the Teflon surfaces by the direct replication method and plasma treatment. Compared to the pristine Teflon surface (Figure 5-2 (. SEM images of (a) pristine, (b) microstructured, and (c) micro-nanostructured surfaces.a)), the replicated Teflon surface (Figure 5-2 (b)) possesses microstructured patterns set by the aluminum template, whereas the plasma-treated Teflon surface (Figure 5-2 (c)) obtained very different patterns of surface structure.

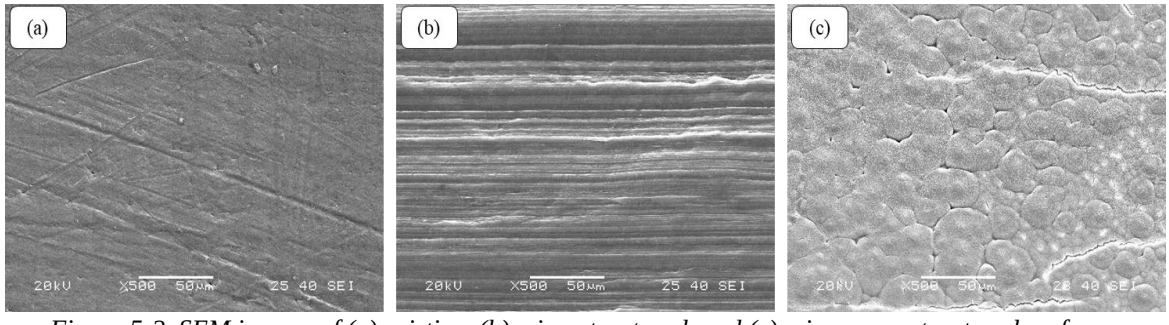

Figure 5-2. SEM images of (a) pristine, (b) microstructured, and (c) micro-nanostructured surfaces.

To better understand the precise nature of the surface roughness, SEM images at a higher magnification of the replicated Teflon surface (Figure 5-3 (a–c)) and plasma-treated Teflon surface (Figure 5-3 (d–f)) were employed. The rice leaf–like grooves created on the replicated Teflon surface ranged widely in size, from several micrometers to tens of micrometers in width. The unidirectional patterns did not lead to anisotropic wettability properties for the microstructured Teflon surface, although such unidirectional patterns, e.g. rice leaves, usually show anisotropic rolling behavior [432]. The difference between CAH of the replicated Teflon

surface in parallel and perpendicular groove direction was less than 5% showing no significant difference in CAH. This is logical as there are enough microstructures in between two adjacent grooves to establish a Cassie-Baxter wetting regime (See Figure 5-4 (b), profilometry results). In contrast, lotus leaf–like patterns were created on the plasma-treated Teflon surfaces comprised of both micro and nanostructures. The nanostructures are superimposed on each microstructure in a lotus leaf–like pattern. This hierarchical structure produces the ultra-water-repellent properties of the plasma-treated Teflon surface.

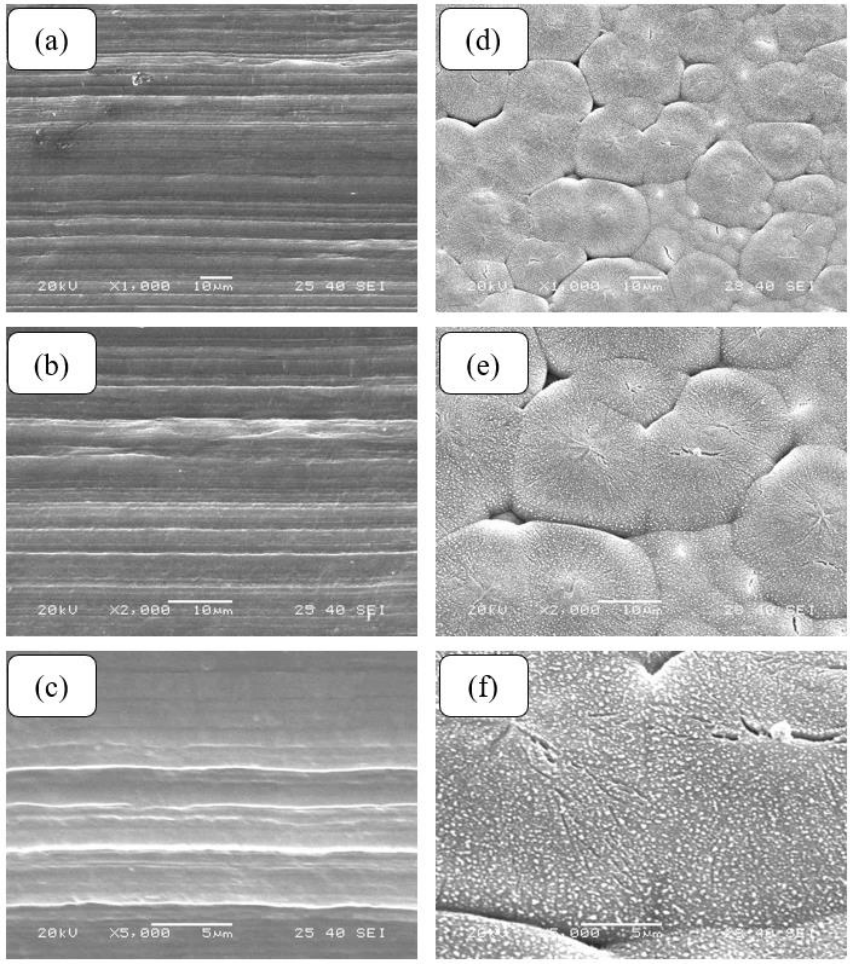

Figure 5-3. SEM images of the microstructured surface at a (a) 1000×, (b) 2000×, and (c) 5000× magnification; SEM images of the micro-nanostructured surface at (d) 1000×, (e) 2000×, and (f) 5000× magnification.

A profilometry technique was applied to evaluate the roughness of the pristine, replicated, and plasma-treated Teflon surfaces. A 400 × 400 μm^2 area of each surface was analyzed (Figure 5-4). Both 1D roughness (line roughness) and 2D roughness (area roughness) values are reported for comparison purposes (Table 5-2).

The root mean square of the replicated Teflon surface was significantly greater than that of the pristine Teflon surface (5.88× for line roughness and 1.95× for area roughness), whereas the plasma treatment led to a remarkable reduction in surface roughness (4.35× for line roughness and 9.80× for area roughness). The skewness coefficient (S_{sk}), which represents the degree of symmetry of the surface height about the mean plane [433], is lowest for the micro-nanostructured plasma-treated surface (S_{sk} = -0.15). It should be noted that zero skewness represents a fully symmetrical height distribution, positive skewness represents more peaks than valleys, and negative skewness indicates more valleys than peaks [434-436]. Consequently, via its decreased surface roughness, plasma treatment produced not only a smoother surface but also a more uniform surface where the height distribution was symmetric. This resulted in the occurrence of lotus leaf–like micro-nanostructures. On the other hand, comparing the kurtosis coefficient (S_{ku})—describing the sharpness of the probability density of the profile [435]—of the three manufactured surfaces revealed that the microstructured surface ($S_{ku} > 3$) was a jagged surface having a relatively great number of high peaks and low valleys. The pristine and micro-nanostructured surfaces had a $S_{ku} < 3$ and possessed a limited number of high peaks and low valleys. The grooves observed in the SEM images were also evident in the replicated surface of the profilometry results. These grooves are responsible for the increase in the roughness values of the replicated surface.

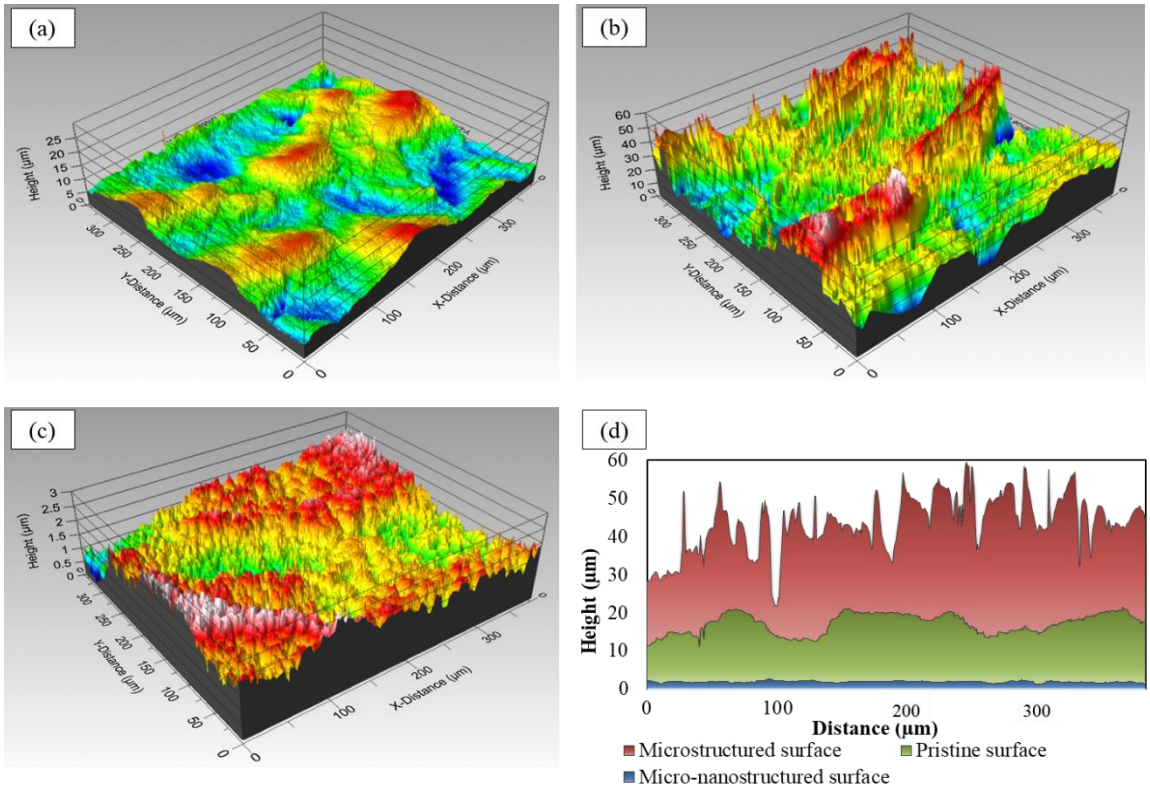

Figure 5-4. 3D surface profiles of the (a) pristine, (b) microstructured, and (c) micro-nanostructured surfaces and (d) comparison of their 2D surface profiles.

Table 5-2. Area and line roughness values obtained from profilometry analysis.

	Pristine surface	***Microstructured surface***	***Micro-nanostructured surface***
Area roughness (µm)			
Maximum peak to valley height (S_t)	44.78	59.08	3.54
Arithmetic mean height (S_a)	3.60	6.68	0.36
Root mean square height (S_q)	4.41	8.58	0.45
Skewness (S_{sk})	0.47	0.48	-0.15
Kurtosis (S_{ku})	2.57	3.31	2.86
Line roughness (µm)			
Maximum peak to valley height (R_t)	5.17	26.45	1.35
Arithmetic mean deviation (R_a)	0.60	3.39	0.13
Root mean square deviation (R_q)	0.74	4.35	0.17

5.4.2 Superhydrophobicity

Pristine Teflon is a hydrophobic material having a WCA and CAH of 108.3 ± 1.7° and 44 ± 2°, respectively. Both microstructured replicated and micro-nanostructured plasma-treated Teflon surfaces had a

WCA of >150° and a CAH of <10° representing their superhydrophobic behavior (Table 5-3). Although the microstructured surface showed a slightly higher WCA than the micro-nanostructured surface, the CAH of the microstructured surface was higher; therefore, the roll-off properties of the micro-nanostructured surfaces was slightly better than that of the replicated microstructure surfaces (See Section 5.4.4).

Table 5-3. Water contact angle (WCA) and contact angle hysteresis (CAH) of pristine, microstructured, and micro-nanostructured surfaces.

	Pristine surface	***Microstructured surface***	***Micro-nanostructured surface***
WCA (º)	108.3 ± 1.7	166.0 ± 1.2	163.2 ± 0.8
CAH (º)	44.0 ± 2.0	4.2 ± 1.1	2.3 ± 0.4

5.4.3 Fourier transform infrared spectroscopy (FTIR)

The chemical composition of the prepared superhydrophobic surfaces was assessed by means of ATR/FTIR spectroscopy. The FTIR spectra of the pristine Teflon surface was found to be identical to the produced superhydrophobic surfaces (Figure 5-5). The two broad large absorption peaks observed around 1150 and 1200 cm^{-1} can be attributed to the asymmetric and symmetric CF_2 stretching vibrations, respectively. The bands at 2349 and 1960 cm^{-1} can be assigned to a combination band associated with the CF_2 backbone and terminal double bonds in the form of $-CF=CF_2$ [431, 437]. No additional peaks were observed in the FTIR spectrum of superhydrophobic surfaces. This confirms that there were neither hydroxyl bonds due to the reaction of Teflon with oxygen in the micro-nanostructured plasma-treated surface nor a reaction between the Teflon and aluminum substrate in the microstructured replicated surface. Thus, as the chemical composition of the Teflon surfaces was not altered by the treatment processes, the creation of surface roughness was the sole cause of the superhydrophobicity of the prepared surfaces.

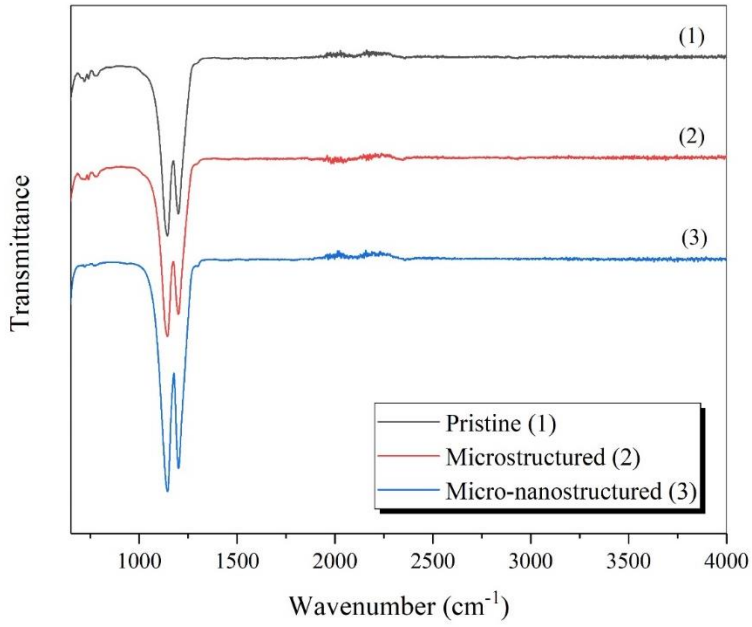

Figure 5-5. FTIR spectra of the (1) pristine, (2) microstructured, and (3) micro-nanostructured surfaces.

5.4.4 Water-repellency properties

Water droplets placed on the superhydrophobic Teflon surfaces rolled rapidly off the surface (Figure 5-6). In contrast, the pristine Teflon surface was wetted easily by the water droplet, yet no movement of the droplet on the surface was observed. The water droplet rolled off the micro-nanostructured surface more quickly (average velocity of 16.6 ± 0.1 $cm \cdot s^{-1}$) than the microstructured surface (14.9 ± 0.2 $cm \cdot s^{-1}$), a difference of 10.2%.

In sum, although microstructures replicated directly onto the Teflon surface led to a higher WCA, the microstructures also slowed water droplet movement across the surface. This pattern could also be predicted by the slightly higher CAH of the microstructure surface. The higher velocity of the water droplet on the plasma-treated Teflon surface can be related to the hierarchical structures, i.e. the presence of nanostructures superimposed on the microstructures. Although both microstructured and micro-nanostructured surfaces produced a WCA >150°, Long et al. [438] showed that the sliding angle of micro-nanostructured surfaces is lower. The sliding angle of the microstructured surfaces increased considerably more than that of the micro-nanostructured surfaces due to the stronger adhesion of microstructured surfaces to water [438]. This greater water-repellency of hierarchically structured surfaces has been observed in multiple studies [439-442].

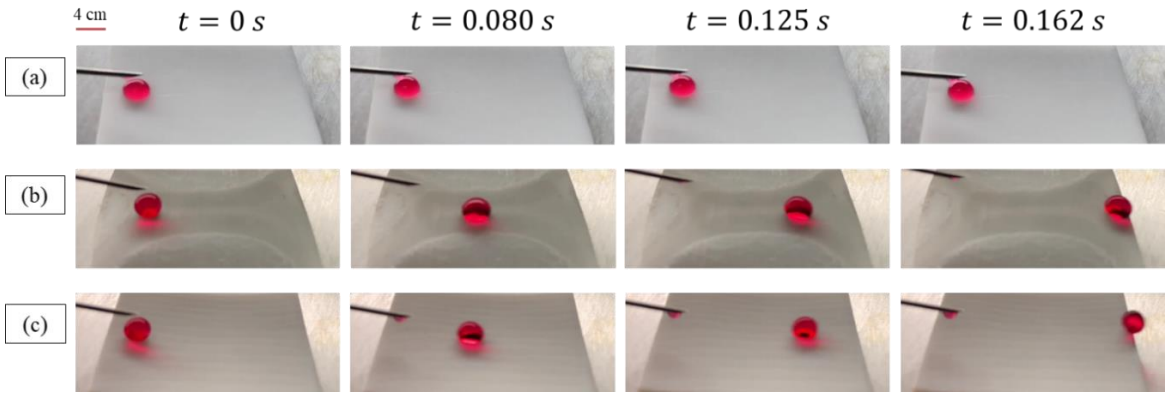

Figure 5-6. Consecutive images of dyed water droplets leaving the (a) pristine, (b) microstructured, and (c) micro-nanostructured surfaces, demonstrating the water-repellency of each surface.

5.4.5 Water droplet impact

For outdoor applications, the behavior of superhydrophobic surfaces must be assessed in relation to impact of raindrops. When a water droplet impacts a superhydrophobic surface, the spherical shape of the droplet is altered throughout four stages: contact, spreading, retraction or recoiling, and rebounding [443]. Following the initial contact, the spreading process occurs whereby energy is consumed through dissipation of the kinetic energy of the water droplet. The dissipation of kinetic energy takes place due to the impact, overcoming resistance from viscosity, and converting kinetic energy into surface energy. Therefore, the behavior of the solid surface is determined by the amount of energy dissipated, which is mostly defined by the surface properties. The portion of kinetic energy that is not dissipated during the spreading stage causes retraction and rebounding [300]. Finally, the water droplet ceases to rebound once all kinetic energy is dissipated from the droplet throughout the repeating rebounding stages, and the droplet then remains in place and does not move.

On the pristine Teflon surface, the water droplet rebounded partially off the surface (Figure 5-7 (a)). Due to its hydrophobicity and comparatively high surface adhesion, the water droplet's initial energy was dissipated, and it could not rebound fully from the surface. Once the water droplet impacted and spread fully across the microstructured surface, a wavy interface between the air and water was observed. This observation differed from that observed for the micro-nanostructured surface. This difference may be due to the high surface roughness of the microstructured surface relative to the micro-nanostructured surface [443].

On the superhydrophobic surfaces, the small amount of energy dissipation produced the retraction and rebounding stages. The retraction was observed immediately after the droplet reached its maximum spread

diameter. The droplet bounced off the surfaces without being pinned onto them. At the beginning of the rebound stage, a Worthington jet [444] (Figure 5-7 (b–c)), during which a droplet breaks up into a core droplet and some satellite droplets was observed. Both microstructured and micro-nanostructured surfaces had contact times of 17–19 ms (the time that the droplet is in contact with the surface before bouncing off [444]).

Four rebounds on the microstructured surface were observed; the maximum height of the droplet decreased steadily for each successive rebounding stage. The impacting droplet illustrated eight complete rebounds on the micro-nanostructured surface. The surface energy of microstructured and micro-nanostructured surfaces was 10.07 ± 1.80 $mJ \cdot m^{-2}$ (dispersal: 8.15 $mJ \cdot m^{-2}$, polar: 1.91 $mJ \cdot m^{-2}$) and 6.08 ± 0.90 $mJ \cdot m^{-2}$ (dispersal: 4.79 $mJ \cdot m^{-2}$, polar: 1.30 $mJ \cdot m^{-2}$) respectively, as measured by a contact angle measurement apparatus. Greater energy dissipation was expected for the microstructured surface due to its higher surface energy. The polar component of the surface energy was almost equal for both surfaces. Therefore, most of the difference between the microstructured and micro-nanostructured surfaces in terms of surface energy came from difference in their dispersal components. Apart from different surface energies of these surfaces, the different rebounding behaviors were also related to differences in surface roughness. Microstructured surfaces having deeper valleys allowed the water droplet to penetrate partially into the microstructures; thus, greater energy dissipation occurred. Hierarchical micro-nanostructures on a plasma-treated surface, however, ensured minimal contact between the droplet and the surface.

The consistency of the Cassie-Baxter regime was confirmed by observing droplets rebounding repeatedly on both superhydrophobic surfaces, and by observing that the water droplet did not become pinned to the surfaces until there was a complete dissipation of energy.

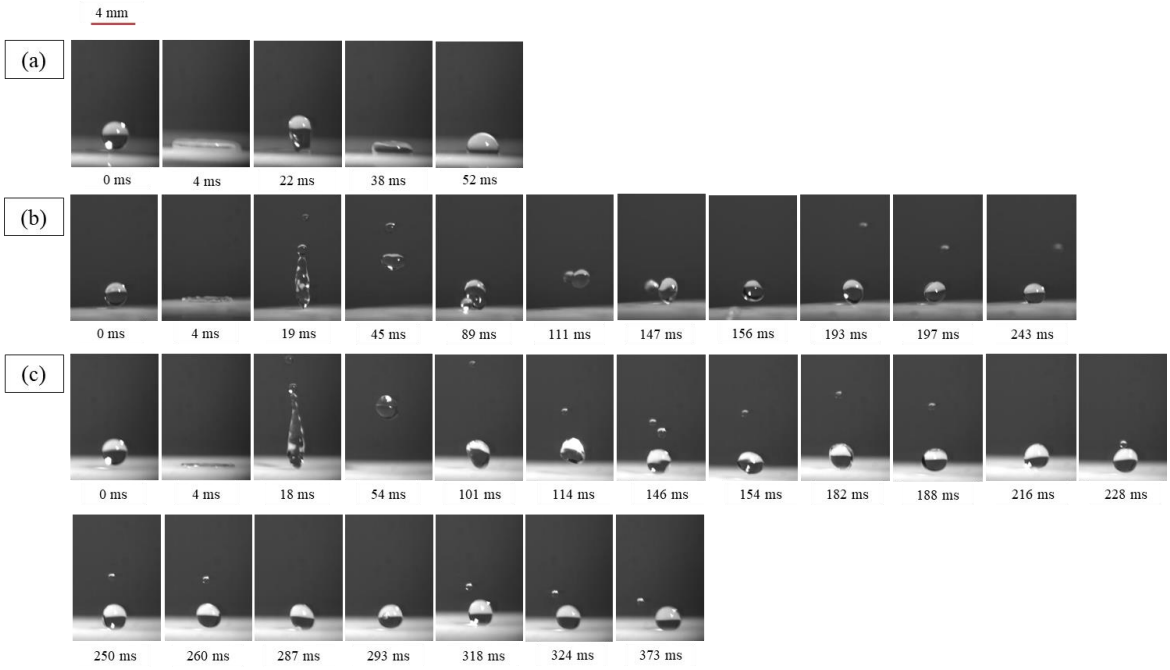

Figure 5-7. Time-lapse imagery of a water droplet impacting a (a) pristine, (b) microstructured, and (c) micro-nanostructured surface.

5.4.6 Icephobicity

The extremely low surface energy of fluorinated polymers has made them an appealing candidate for water-repellent and anti-icing applications. One of the more useful parameters for evaluating anti-icing properties is ice adhesion strength to the surface. In general, ice adhesion shear strength is measured via centrifuging an ice-covered sample [401, 426, 445-447] or applying a tensile strength [402, 447, 448] or push-off test [350, 447, 449-452]. Each approach can estimate the ice adhesion strength for a given surface [453]. The measured ice adhesion strength and ice adhesion reduction factor (ARF) of the superhydrophobic Teflon surfaces were compared to those of a pristine Teflon surface (Figure 5-8). ARF is defined as the ratio between ice adhesion strength of the pristine Teflon surface and that of the produced superhydrophobic Teflon surface. The ice adhesion strength of the pristine Teflon surface was around 50 kPa, demonstrating its low ice adhesion strength compared to that of an uncoated aluminum substrate (the ice adhesion strength on bare aluminum alloy 6061 is 800–1072 kPa [450, 453] for bulk water ice).

Whether superhydrophobicity enhances or reduces icephobicity has been a point of contention. Some studies have shown a reduction of ice adhesion strength on superhydrophobic surfaces [401, 445, 454, 455], whereas others have observed an increase [350, 453, 456, 457]. In this study, an ice adhesion strength of ca. 18 kPa for microstructured surfaces and ca. 9 kPa for micro-nanostructured surfaces was observed. These

values are respectively 2.8× and 5.6× lower than the ice adhesion strength of the pristine Teflon surface. It can be claimed that the prepared Teflon surfaces having an ice adhesion strength <20 kPa are considered as appropriate surfaces for the passive removal of ice [406]. This pattern of ice adhesion strength can be explained by the high water-repellency [453] of the surface and the presence of air pockets trapped among the micro- and nanostructures based on the Cassie-Baxter model [51, 350].

A positive correlation of CAH with ice adhesion strength was also observed as micro-nanostructured surfaces showed a lower CAH than microstructured surfaces. The correlation between CAH and ice adhesion strength on rough surfaces of similar chemistry has been observed previously [458]. The lower ARF of microstructured surfaces compared to micro-nanostructured surfaces can be attributed to the mechanical interlocking of ice with the micro-scale grooves. This mechanical interlocking increases the contact area between the ice and the microstructures thereby increasing ice adhesion [456]. The ultra-pristine and uniform surface of the micro-nanostructured Teflon caused the least contact between the ice and the surface and thus produced the lowest ice adhesion strength.

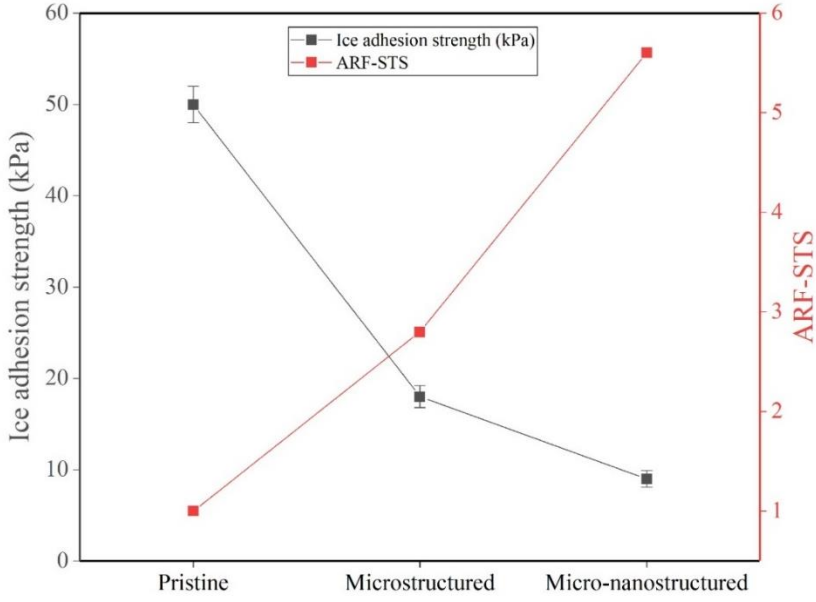

Figure 5-8. Ice adhesion strength and adhesion reduction factor (ARF) for pristine, microstructured, and micro-nanostructured surfaces.

The delay in the onset of freezing, i.e. the initiation of water droplet freezing on the surface, also provides a good assessment of the icephobic behavior of the superhydrophobic surfaces. A superhydrophobic surface having a longer freezing delay has a greater anti-icing potential, i.e. less ice accumulation over time [459]. Surface roughness also affected considerably freezing delay; interestingly, these results differed from

those obtained in the analysis of ice adhesion strength when freezing delay was assessed for the pristine, replicated, and plasma-treated Teflon surfaces at freezing temperatures of -10 °C, -15 °C, and -20 °C (Table 5-4).

The freezing delay for the pristine Teflon surface was less than that for superhydrophobic surfaces due to the high contact area between the water droplet and the pristine Teflon surface caused by the lower WCA of the pristine Teflon surface. A large contact area means a high thermal conductivity leading to a short freezing delay for the pristine Teflon surface. Among the two superhydrophobic Teflon surfaces, the microstructured surface delayed freezing the longest. At all tested temperatures, water droplets placed on the microstructured surface froze markedly later than droplets on the micro-nanostructured surface. In the freezing process of a droplet on the surface, the micro-air pockets play the most important role because they act as thermal barriers to delay droplet freezing [103, 459]. Thermodynamically speaking, the water droplet loses its energy according to [410, 460]:

$$\delta Q = \rho_w C_p (t_0 - t_s) = \Delta h.\, t$$

where δQ is the droplet's reduced energy, ρ_w is the water density, C_p is the water specific heat capacity, t_0 is the droplet's temperature at the initial point, t_s is the droplet's final temperature, Δh is heat loss of the water droplet over time, and t is time. Considering δQ as a constant value, a longer freezing time requires Δh to be as small as possible. This can be obtained through the trapping of a large amount of air that can act as thermal insulation.

Thanks to the profilometry technique, the volume of trapped air for each surface was estimated. This approach is based on the total volume of the holes and voids within the asperities of each surface. If ν is defined as the ratio between the volume of the trapped air in the produced surface to that of the pristine surface, $\nu_{microstructured}$ and $\nu_{micro\text{-}nanostructured}$ are 3.93 and 0.11, respectively. Therefore, the slower freezing process of the microstructured surface can be attributed to ~36× more trapped air pockets within the microstructured surface than within the micro-nanostructured surface. It should be noted that the uniform nanostructures on the plasma-treated Teflon surface trapped even fewer air pockets than did the pristine Teflon surface. Nevertheless, the freezing delay tests showed that the micro-nanostructured surface delayed the onset of freezing more than the pristine surface. Although the superhydrophobic, micro-nanostructured surface had fewer pockets of trapped air, the minimal contact area between the water droplet and surface delayed the onset of freezing. The pristine

hydrophobic surface having a rather larger water-surface contact area produced the quickest freezing process. Therefore, micro-air pockets have less influence on delaying freezing than water-surface contact area when comparing superhydrophobic and hydrophobic surfaces. In other words, the lower WCA of a hydrophobic surface is more important for freezing delay than a greater number of trapped air pockets.

Consequently, it was observed that the delay in the freezing of a water droplet on microstructured surfaces was ~2× longer than for micro-nanostructured surfaces and ~4× longer than for pristine surfaces at all tested temperatures (Table 5-4Table 5-4).

Table 5-4. Freezing delay in seconds of the pristine, microstructured, and micro-nanostructured surfaces at various temperatures.

Temperature (ºC)	***Freezing delay (s)***		
	Pristine surface	Microstructured surface	Micro-nanostructured surface
-10	829 ± 97	3753 ± 525	1536 ± 168
-15	395 ± 36	1632 ± 131	698 ± 90
-20	160 ± 19	338 ± 13	231 ± 28

5.4.7 Self-cleaning properties

The self-cleaning property of the produced Teflon surfaces was investigated using kaolin contaminant. A water droplet fixed to the syringe needle tip was used to sweep the powder off the Teflon surfaces. On the pristine Teflon surface, the water droplet stuck to the contaminated kaolin-covered surface upon contact (Figure 5-9 (a–c)). On both the microstructured (Figure 5-9 (d–f)) and micro-nanostructured (Figure 5-9 (g–i)) surfaces, no trace of the contaminant remained along the water droplet path following its passage across the surface. This is due to the greater adhesion of kaolin particles to the water droplet than to the superhydrophobic Teflon surfaces, benefiting from a low CAH. Therefore, kaolin particles easily adhere to the water droplet and are removed as the water droplet sweeps across the superhydrophobic surfaces.

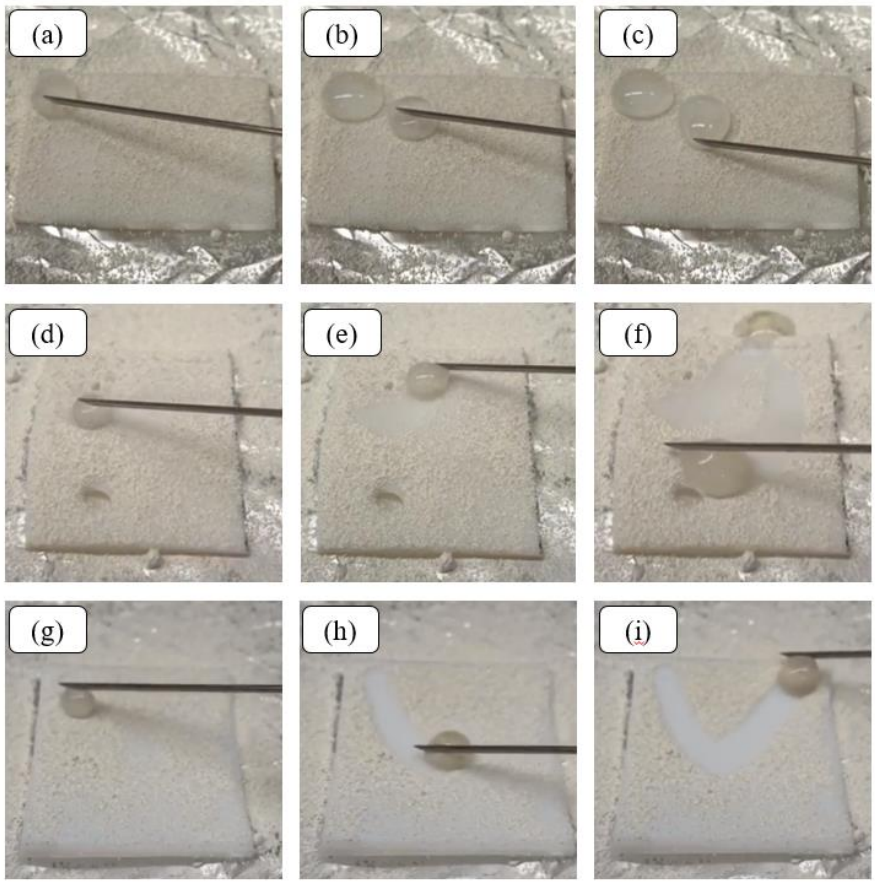

Figure 5-9. Self-cleaning properties of the (a-c) pristine, (d-f) microstructured and (g-i) micro-nanostructured surfaces examined by water droplet sweeping.

On the pristine Teflon surface, the contaminant droplet, once dried, left a completely flat deposit, whereas on the superhydrophobic Teflon surfaces, the droplet maintained its initial spherical shape (Figure 5-10 (b, f, and j)). To evaluate the self-cleaning performance of the Teflon surfaces, water droplets were then applied to remove the deposited contaminants (Figure 5-10 (c, g, and k)). A single droplet was sufficient to remove thoroughly the dried contaminant from the superhydrophobic Teflon surfaces (Figure 5-10 (h and l)) and all traces of the contaminant were removed from the superhydrophobic surfaces. However, the application of multiple water droplets could not remove the dried contaminants from the pristine Teflon surface; the contaminants were fixed onto the surface (Figure 5-10 (d)).

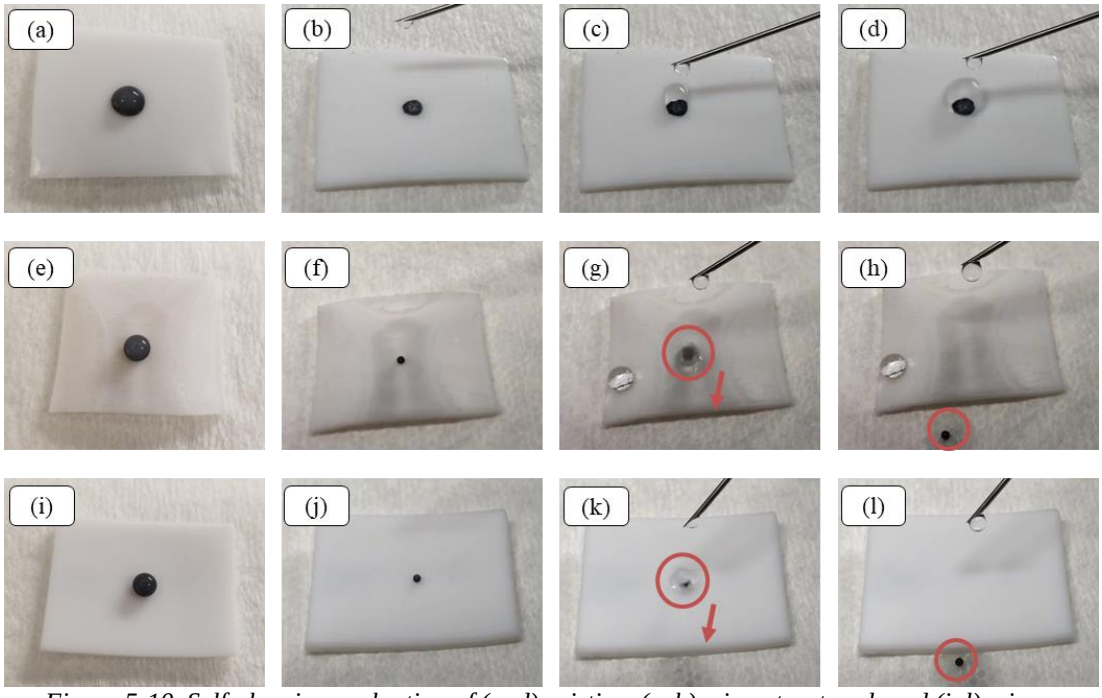

Figure 5-10. Self-cleaning evaluation of (a–d) pristine, (e–h) microstructured, and (i–l) micro-nanostructured surfaces by observing of the cleaning of a dried contaminant solution using a water droplet.

5.5 Conclusion

The effects of surface roughness on water-repellency, water droplet impact, ice adhesion strength, freezing delay, and self-cleaning properties of the superhydrophobic Teflon materials were assessed. The direct replication method resulted in microstructured rice leaf–like grooves having high peaks, whereas the atmospheric plasma treatment created hierarchical micro-nanostructured lotus leaf–like patterns. FTIR analysis showed that the produced superhydrophobic surfaces maintained spectra typical of Teflon, and thus neither method altered the chemical composition of the original Teflon surface. Although the microstructured surface had a higher WCA than the micro-nanostructured surface, the water droplets rolled off the micro-nanostructured surface slightly faster due to its lower CAH. Moreover, the observed differences in the rebounding behavior of water droplets on the surfaces were due to the difference in surface energies as well as the difference in surface roughness. It also confirmed the consistency of the Cassie-Baxter regime on superhydrophobic surfaces. There was a significant reduction in ice adhesion strength of the microstructured and micro-nanostructured surfaces by a factor of 2.8× and 5.6×, respectively. This confirmed that the microstructured surface, due to a greater contact area and mechanical interlocking, had higher ice adhesion than the micro-nanostructured surface. On the other hand, the deep grooves created on the microstructured

surface produced a large amount of micro-air pockets (~4× more than the pristine surface). This resulted in a significant water droplet freezing delay at all tested temperatures. The fabricated surfaces also showed a self-cleaning capability, able to self-clean deposits of a wet and dry contaminant.

Acknowledgments

We want to thank Mr. Pierre Camirand and Mr. Yann Girard-Lachance for their technical collaboration.

CONCLUSIONS

In the following, an overview of the important findings of this project is presented as both partial and general conclusions. As the partial conclusion, the important results obtained in the papers are separately provided in the same order as their presentation in this thesis. The general conclusions are provided afterwards.

Evaluation of Atmospheric-Pressure Plasma Parameters to Achieve Superhydrophobic and Self-cleaning HTV Silicone Rubber Surfaces via a Single-Step, Eco-Friendly Approach

- Firstly, we employed atmospheric-pressure air plasma treatment as a simple, industrially applicable, and eco-friendly approach to produce desirable micro-nanostructures on low surface energy HTV-SR surfaces. The best water-repellent superhydrophobic surface had WCA and CAH of 163.0° and 2.2° respectively.
- The effect of significant plasma parameters on the non-wettability of the plasma-treated HTV-SR surfaces was evaluated through a DoE method and the three independent factors of reference voltage, plasma jet speed and gas flow rate, each at three levels. According to the ANOVA, plasma jet speed as well as the interaction of the reference voltage and plasma jet speed were deemed the most significant factors affecting WCA and CAH results, respectively. At a constant gas flow rate, the increase in reference voltage and/or a decrease in plasma jet speed had a similar effect of increasing the WCA.
- During plasma treatment, the surface undergoes both physical and chemical modification, and both changes impact the final surface wettability. In accordance with the increase of reference voltage, the FTIR analyses highlighted the gradual elimination of hydroxyl groups due to the decomposition of ATH fillers under the high temperatures of plasma treatment.
- The formation of micro-nanostructures on the surface was confirmed via SEM and AFM analyses. SEM images illustrated the micro-scale coral-like clusters covered with nano-scale protrusions after plasma treatment. By increasing the reference voltage, the size and coalescence of clusters increased and resulted in a reduction of space between clusters and the creation of micro-roughness on the substrate.

- Based on AFM analysis, the enhanced nano-scale roughness was apparent for the plasma-treated surface that favors the entrapped air pockets within the surface roughnesss. This observation resulted in the lower adhesion of water droplets onto the surface and the increased water-repellency of the substrate.
- Furthermore, under particular plasma conditions, i.e., low reference voltage and high plasma jet speed, slippery hydrophobic surfaces having a simultaneous low WCA and low CAH were achieved. The comparatively smooth surface of slippery hydrophobic samples responsible for low CAH was also confirmed by AFM analysis.
- The prepared superhydrophobic surfaces showed considerable water-repellency as well as self-cleaning property under both wet and dry contamination scenarios.

Icephobicity and durability assessment of superhydrophobic surfaces: the role of surface roughness and the ice adhesion measurement technique

- In this article, the icephobicity and durability of the produced plasma-treated superhydrophobic surfaces were evaluated.
- The consistent Cassie-Baxter regime was observed during the evaporation of 4-µL water droplet placed on the plasma-treated surface where the water droplet preserved its initial marble-like shape even at the late stages.
- The anti-icing property was studied based on the delay in the freezing time. At -20 °C, the superhydrophobic surface having abundant nano-scale structures covered the micro-scale roughnesses and showed greater anti-icing property compared to pristine HTV-SR, i.e., ~60% reduction in freezing delay, stemmed from entrapped air pockets among the surface asperities.
- The centrifuge and push-off tests were used to evaluate the de-icing properties. The remarkable ice adhesion reduction up to 75.3% and 68.3% was attained for superhydrophobic surface in push-off and centrifuge tests, respectively. This relates to the low interlocking of ice into the surface structures which results in reduced ice adhesion strength.
- After 7 cycles of repetitive icing/de-icing, although the WCA and CAH did not show significant changes, the ice adhesion reduction decreased to 62.2% and 30.8% in push-off and

centrifuge tests, respectively. It might be resulted from the gradual elimination of nano-scale roughnesses.

- The produced superhydrophobic surfaces showed great mechanical durability against finger-press, tape-peeling, water droplet impact and sandblasting tests. Whilst mechanical abrasion and ultrasonication tests were more destructive for the plasma-treated surfaces.
- The notable chemical durability and UV resistance of the produced plasma-treated surfaces were also illustrated.

A Non-Fluorinated Mechanochemically-Robust Volumetric Superhydrophobic Nanocomposite

- Given the high demand for durable superhydrophobic materials in real-life applications, we developed an ultra-robust, non-expensive, non-fluorinated, volumetric superhydrophobic nanocomposite. The embedded micro-sized DE and nano-sized FS particles within the HTV-SR matrix were responsible for the enhanced surface and bulk water-repellency of the nanocomposite.
- Increasing the mass ratio of DE/FS had a positive effect on the surface water-repellency while decreasing of the mass ratio improved the bulk water-repellency.
- By the addition of particles, the hardness and crosslinking density of the HTV-SR nanocomposites were enhanced confirming the physical stability of the nanocomposite. The increased crosslinking density of superhydrophobic nanocomposites relative to that of pristine HTV-SR can be ascribed to the interfacial interactions between siloxane groups of DE particles and silicone rubber chains as well as the interaction among aggregated FS particles.
- With the help of profilometry and FESEM analyses, we observed the presence of particles on the surface of the nanocomposite. The specific structure of the micro-sized DE particles along with the aggregated nano-sized FS were responsible for the non-wettability of the prepared nanocomposites.
- Considering the similarity of the FTIR absorption spectra of particles and matrix, the shape and position of the absorption peaks showed negligible changes while their intensity considerably reduced.

- The mechanochemical robustness of produced superhydrophobic nanocomposites was vigorously assessed based on multiple aggressive mechanical, chemical, and UV analyses.
- Regardless of the abrasion force, i.e. 5 kPa or 25 kPa, or sandpaper grit, i.e. #160, #320 and #800, after 250 abrasion cycles the WCA of superhydrophobic nanocomposite remained almost >160° and CAH <5°. Following abrasion, the surface roughness was replaced by fresh micro-nanostructures consisting of DE and agglomerated FS particles as well as channel-like structures induced by the sandpaper.
- Knife scratching, tape peeling, water jet impact and sandblasting experiments did not affect the water-repellent properties of the prepared nanocomposite.
- Although the 2-hour ultrasonication deteriorated the superhydrophobicity of the nanocomposite, the surface water-repellency could be recovered via sanding or cutting the outermost layer. This feature provides an outstanding opportunity for real-life applications of the fabricated volumetric superhydrophobic nanocomposites. Once the water-repellency and roughness features have deteriorated, they can be endlessly regenerated by abrasion so as to preserve a super-robust superhydrophobic surface.
- The superhydrophobic nanocomposite also demonstrated outstanding chemical stability, UV resistance, and self-cleaning property as well.

A Comparative Study of the Icephobic and Self-Cleaning Properties of Teflon Materials Having Different Surface Morphologies

- As one of the well-known hydrophobic thermoplastic materials, the effect of plasma treatment on the water-repellency, water droplet impact, icephobicity and self-cleaning of the Teflon materials was assessed.
- The atmospheric-pressure plasma treatment created hierarchical micro-nanostructured lotus leaf–like patterns on Teflon surface. Whilst the FTIR analysis showed that the plasma treatment did not alter the chemical composition of the Teflon material.

- Compared to WCA, CAH had more effect on the speed of water droplet rolling off the surface. In other words, the water droplets roll off faster on the superhydrophobic surfaces having lower CAH than the surface having a higher WCA.
- Due to the low surface energy and hierarchical micro-nanostructured superhydrophobic Teflon surface, the minimal contact between the water droplet and the surface led to its outstanding behavior against water droplet impact. The impacting droplet illustrated eight complete rebounds on the produced micro-nanostructured Teflon surface.
- There was a significant reduction in ice adhesion strength of the plasma-treated micro-nanostructured surface by a factor of 5.6×. Moreover, the delay in the freezing of water droplet on the micro-nanostructured surface was ~2× longer than for pristine surface.
- The fabricated surfaces also showed a self-cleaning capability, able to self-clean deposits of a wet and dry contaminants.

General conclusions

In the current thesis, to address the catastrophic risks of the failure of high-voltage insulators due to ice and pollution accumulation on their surfaces, two different approaches are opted to effectively create artificial self-cleaning/superhydrophobic surfaces to enhance the water-repellency of the engineered silicone rubber and Teflon materials. Initially, the atmospheric-pressure air plasma treatment was used to produce self-cleaning/superhydrophobic high-temperature vulcanized silicone rubber (HTV-SR) surfaces via etching technique. To determine the effect of various plasma parameters on the non-wettability of the treated HTV-SR surfaces, we applied a design of experiment (DoE) method based on the three significant and independent factors of reference voltage, plasma jet speed and gas flow rate, each at three levels. Due to the formation of coral-like micro-nanostructures on the plasma-treated surface, a substantial enhancement in the water-repellency of HTV-SR surfaces, i.e., static water contact angle (WCA) >160° and a contact angle hysteresis (CAH) <3°, was obtained. The consistency of the Cassie-Baxter regime was confirmed by various analyses including increasing the volume of droplet, pressure test and droplet impact. The self-cleaning behavior of the superhydrophobic samples was verified based on wet and dry methods. Moreover, the notable delayed ice formation and considerable low ice adhesion strength of the plasma-treated HTV-SR surfaces illustrated their

remarkable anti-icing and de-icing capabilities. Relatively good mechanical durability and substantial chemical stability were also observed after multiple tests.

Secondly, regarding the poor mechanochemical robustness of superhydrophobic surfaces susceptible to damage, a non-fluorinated volumetric superhydrophobic nanocomposite was produced through embedding diatomaceous earth and fumed silica particles into the HTV-SR matrix. In addition to creating superhydrophobicity through each face and every layer of the nanocomposites, we enhanced the hardness and crosslinking density of the HTV-SR—confirming its physical stability—by adding micro-nanoparticles to the HTV-SR. Regarding the mechanochemical robustness of the developed nanocomposite, multiple severe mechanical and chemical tests did not considerably affect the surface water repellency. If the superhydrophobicity of the nanocomposite was deteriorated by means of any test, the water-repellency could be restored by removing the outermost layer owing to the presence of embedded low surface energy micro-nanostructures within the entire body of the nanocomposite. The superhydrophobic nanocomposite also demonstrated outstanding UV resistance and self-cleaning ability.

Thirdly, we produced plasma-treated superhydrophobic Teflon surfaces possessing ultra-water-repellent, icephobic and self-cleaning properties. Formation of the lotus leaf-like hierarchical micro-nanostructures on the plasma-treated Teflon surface was responsible for its surface water-repellency as well as remarkable low ice adhesion strength. Given the results of speed of water droplet rolling off and water droplet impact on the superhydrophobic surface, the CAH had more effect on the surface water repellency than WCA values. Moreover, the fabricated surfaces also showed a self-cleaning capability, able to self-clean deposits of a wet and dry contaminant.

RECOMMENDATIONS

In this Ph.D. thesis, superhydrophobic surfaces were produced based on two different approaches, i.e., creation of surface roughness using atmospheric-pressure plasma treatment and fabrication of damage-tolerant volumetric superhydrophobic nanocomposite. The prepared surfaces demonstrated significant superhydrophobicity, self-cleaning, icephobicity, and mechanochemical robustness. Nevertheless, there are still several suggestions worth considering for further investigations. These recommendations are presented as follows.

- A thorough investigation on the influence of all plasma operating parameters on the non-wettability as well as icephobicity of silicone rubber surfaces could be conducted. Regarding the preliminary analyses, we have selected three significant plasma operating parameters which have pronounced effect on the surface water-repellency. However, other parameters and their interactions, such as distance between nozzle and substrate, cycle time, and plasma frequency, may affect not only the superhydrophobicity but the icephobic properties of the treated surface.
- To reduce the destructive temperature of outlet plasma stream and achieve a homogenous treatment, a rotating plasma nozzle can be employed. In case of rotating jet, the forced-convection heat transfer diminishes the gas temperature. Moreover, manipulation of torch speed in rotating plasma nuzzle can alter the final plasma homogeneity and, in some point, improve it.
- To realize ordered surface structures using atmospheric-pressure plasma system, the target surface can be covered by metallic meshes having various openings which results in fabrication of structures with different dimensions. Unlike nonordered surface structures, ordered structure provide the opportunity of studying several wettability related phenomena. To achieve this goal, the enhancement of the homogeneity of the plasma jet and reducing the plasma temperature are among the main challenges. To address these problems, using the rotating plasma jet can be a promising alternative as the rotating jet has relatively more homogeneity as well as much lower plasma gas temperature rather than conventional plasma jet.

- In this project, we used air as the plasma gas because of the industrial and environmental concerns. However, the type of plasma gas and its flow rate are also of great importance in plasma treatment. Certain plasma particles react with certain atoms or certain phases on the surface which have different effect on the achieved results in terms of surface morphology and subsequent non-wettability. An interesting subject for further studies can be the investigation of the effect of various plasma gases e.g. Ar, O_2, N_2, and CF_4 on multiple properties including surface roughness, wettability, and icephobicity.
- The study of the mechanical and electrical properties of the produced superhydrophobic nanocomposites is enticing to acquire a better understanding of their functionality for high-voltage insulator application. To this end, tensile, compression and impact strength as the mechanical properties, and volume resistivity, dielectric property, tracking and erosion resistance and breakdown strength as the electrical properties can be evaluated.
- One of the appealing applications of the superhydrophobic surfaces is known as oil-water separation. Throughout this project, we observed that the produced superhydrophobic nanocomposites demonstrate the ability to selectively absorb oil from water. The oil/water separation efficiency under various conditions can be studied. In addition, it is recommended to enhance the separation efficiency by creating micro-pores within the bulk material.

APENDIX I

SUPPORTING INFORMATION FOR ARTICLE 2:

ICEPHOBICITY AND DURABILITY ASSESSEMENT OF SUPERHYDROPHOBIC SURFACES: THE ROLE OF SURFACE ROUGHNESS AND THE ICE ADHESION MEASUREMENT TECHNIQUE

K. Maghsoudi*, E. Vazirinasab, G. Momen, R. Jafari

Department of Applied Sciences, University of Quebec in Chicoutimi (UQAC)

555, boul. de l'Université, Chicoutimi, Québec, G7H 2B1, Canada

* E-mail: Khosrow.maghsoudi1@uqac.ca

This article has been accepted in:

Journal of Materials Processing Technology

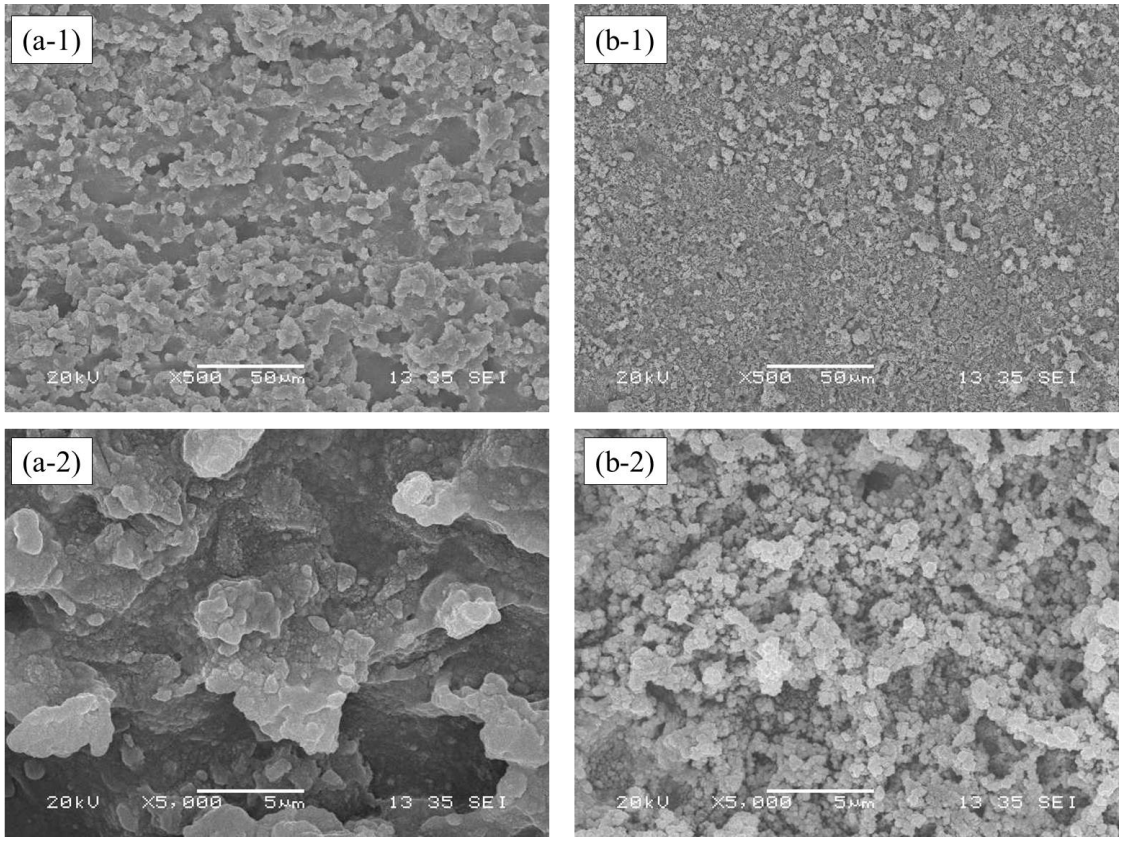

Figure AI-1. SEM images after the 7th icing/de-icing cycle in the centrifuge test at two magnifications for (a-1 & a-2) µCM and (b-1 & b-2) APP-treated surfaces.

Table AI-5. Ice adhesion reduction factor (ARF) of the µCM and APP-treated surfaces relative to the ice adhesion strength of an aluminum surface (A 6061) for push-off and centrifuge tests

Adhesion reduction factor (ARF)	**Icing/de-icing cycles**		**1**	**2**	**3**	**4**	**5**	**6**	**7**
	push-off	µCM	9.0 ± 1.3	10.1 ± 0.9	8.2 ± 1.1	9.9 ± 1.1	10.6 ± 2.2	8.7 ± 2.1	9.5 ± 0.9
		APP	25.2 ± 2.6	23.7 ± 2.1	23.2 ± 1.0	20.4 ± 2.0	18.6 ± 1.9	18.3 ± 1.8	18.0 ± 1.8
	centrifuge	µCM	8.7 ± 1.2	7.4 ± 0.8	7.8 ± 0.6	6.4 ± 0.9	7.2 ± 1.3	8.9 ± 1.4	6.4 ± 1.1
		APP	19.2 ± 2.2	16.2 ± 2.1	13.3 ± 2.6	11.8 ± 1.0	9.9 ± 0.6	9.2 ± 0.9	8.9 ± 0.9

Here, the ARF is defined as:

τ (bare aluminum)/τ (superhydrophobic silicone rubber).

It should be noted that the τ (bare aluminum) was measured as 810 ± 125 kPa.

Table AI-6. Water contact angle and contact angle hysteresis of the µCM and APP-treated surfaces before and after push-off and centrifuge tests.

	Before icing/de-icing cycles		**After 7 icing/de-icing cycles**	
	WCA (°)	CAH (°)	WCA (°)	CAH (°)
µCM	166.6 ± 1.9	0.6 ± 0.3	163.6 ± 1.0	4.7 ± 0.1
APP	165.8 ± 1.3	1.1 ± 0.6	164.0 ± 0.1	3.9 ± 0.7

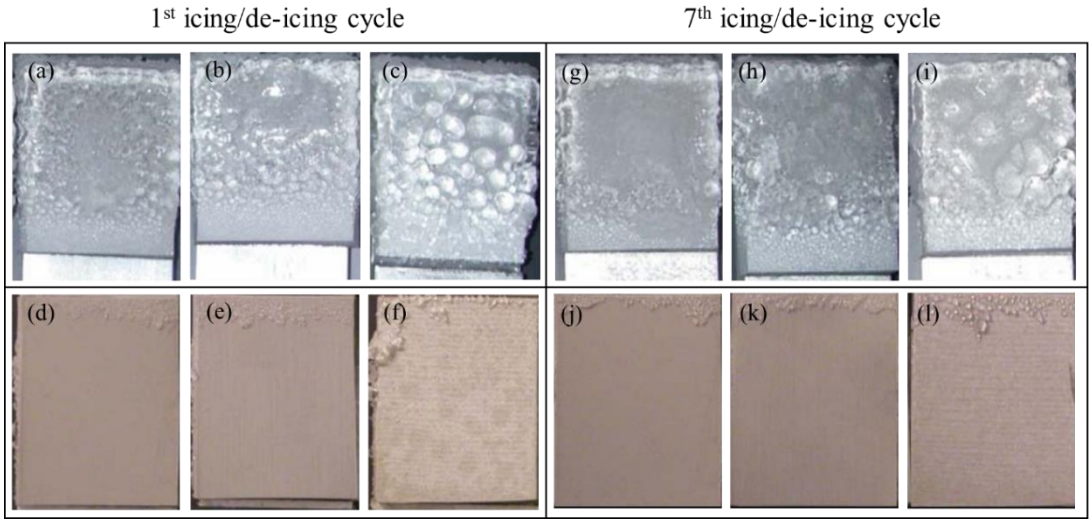

Figure AI-2. Photographs of the 1st icing/de-icing cycle of the (a, d) pristine, (b, e) μCM, and (c, f) APP-treated surfaces after ice accumulation and after ice removal in the centrifuge test. Photographs of the 7st icing/de-icing cycle of the (g, j) pristine, (h, k) μCM, and (i, l) APP-treated surfaces after ice accumulation and after ice removal in the centrifuge test.

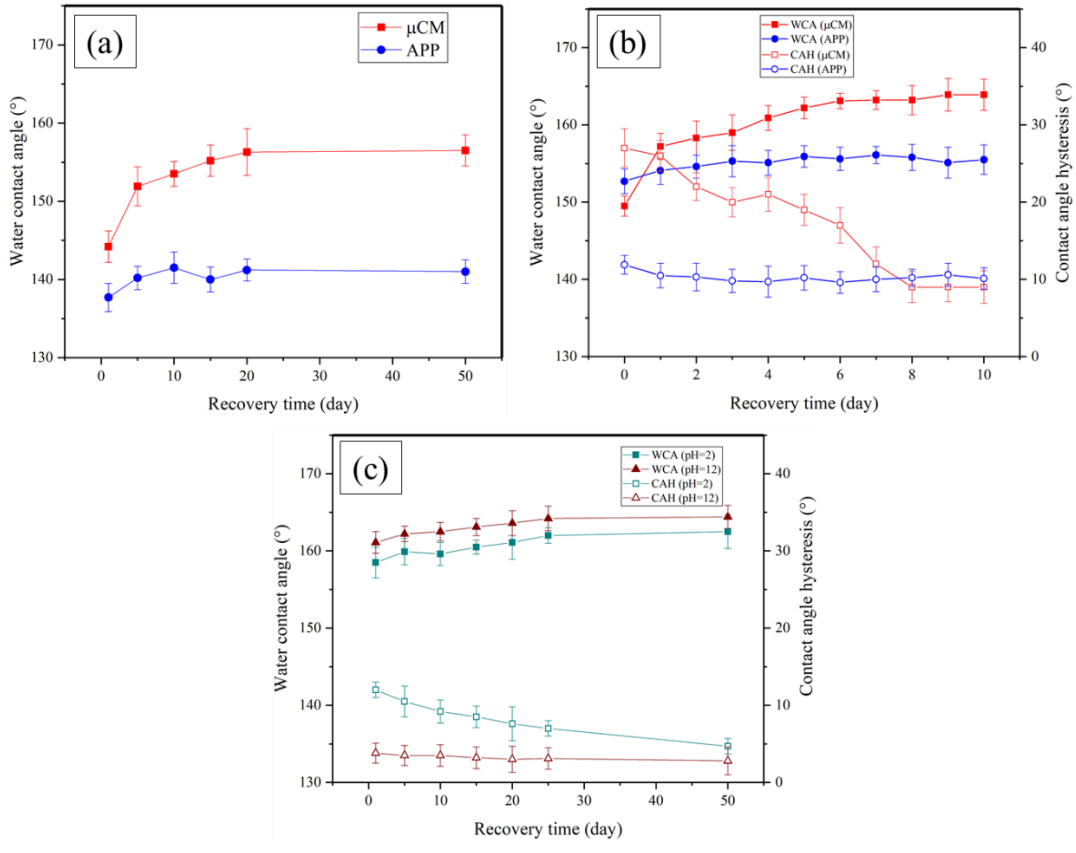

Figure AI-3. (a) Recovered WCA as a function of time for the sandpaper-abrasion test for the μCM and APP-treated surfaces abraded at 6.4 kPa; (b) recovered WCA and CAH as a function of time for the finger-press tests for the μCM and APP-treated surfaces; and (c) recovered WCA and CAH as a function of time for the μCM sample immersed in acidic and alkaline solutions.

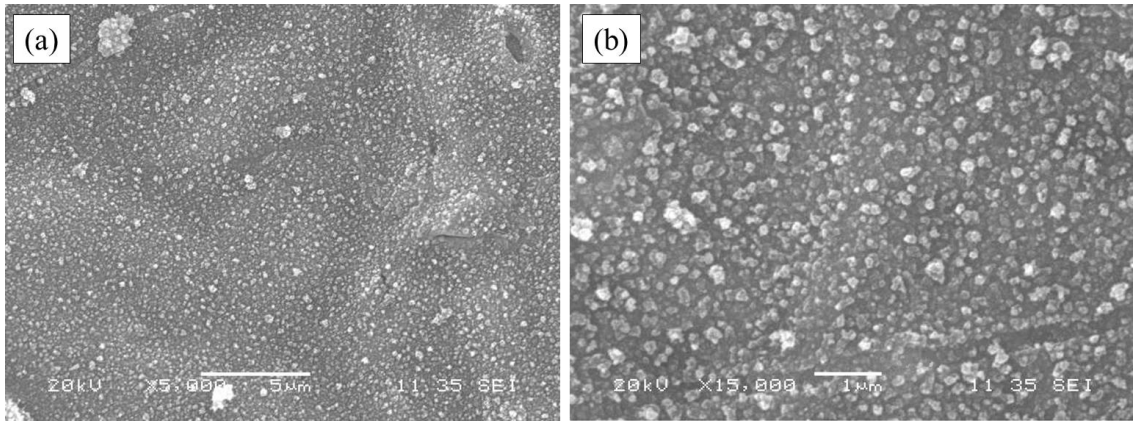

Figure AI-4. SEM images of the APP-treated surface after the ultrasonication test at a magnification of (a) ×5000 and (b) ×15000.

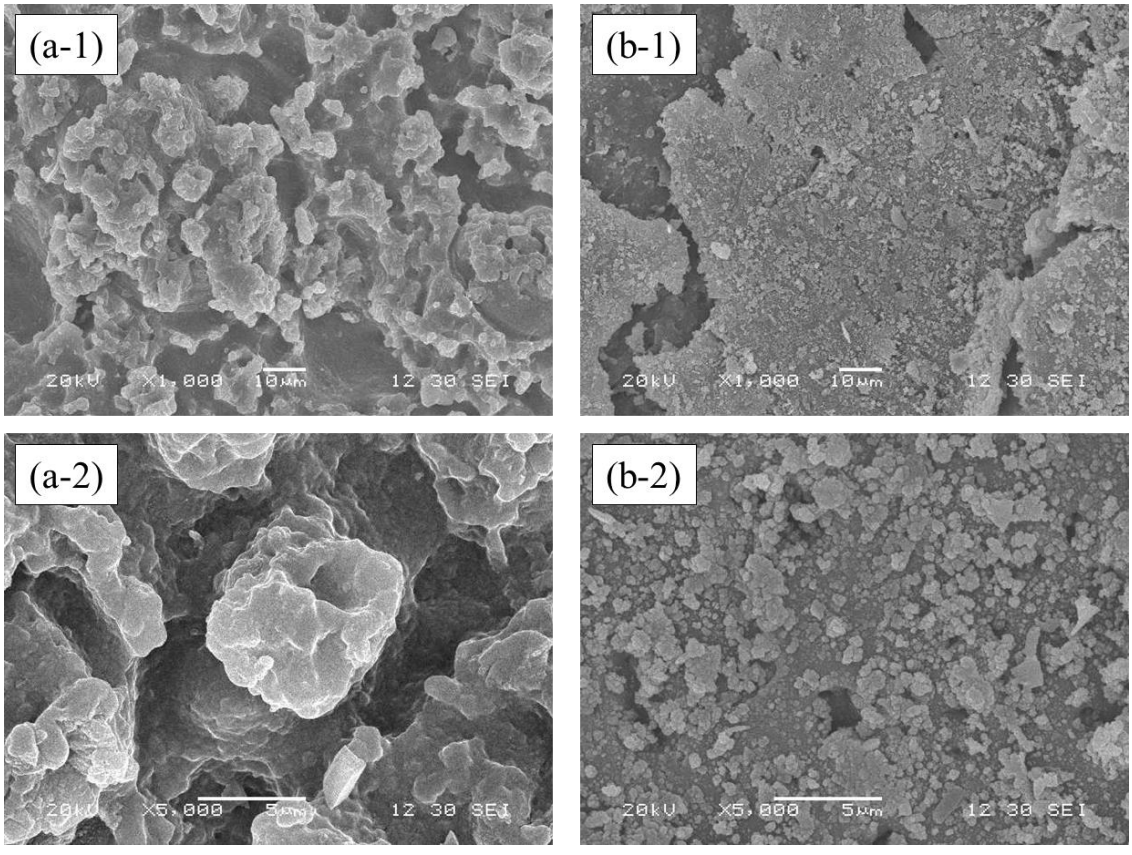

Figure AI-5. SEM images of a sandblasted (a-1 & a-2) µCM surface and (b-1 & b-2) APP-treated surface at two magnifications.

To study the durability of the produced surfaces against UV-light radiation, we selected the average annual sunlight energy in a normal direction for a site in Toronto, Ontario, reported as 8.1–13.4 $MJ.m^{-2}$ [461]. Given that only 3–6% of natural sunlight reaching the Earth's surface falls within the UV region, the annual mean of UV radiant exposure was calculated as follows:

$0.05 \times 13.4\ MJ.m^{-2} = 670{,}000\ J \cdot m^{-2}$

Therefore, to simulate the same amount of energy attaining the surfaces by UVA-340 fluorescent lamps in the QUV accelerated weathering tester, requires almost 209 h:

$Time = 670{,}000\ J.m^{-2} / 0.89\ W.m^{-2} = 209\ h$

APENDIX II

SUPPORTING INFORMATION FOR ARTICLE 3:

A NON-FLUORINATED MECHANOCHEMICALLY-ROBUST VOLUMETRIC SUPERHYDROPHOBIC NANOCOMPOSITE

E. Vazirinasab*, G. Momen, R. Jafari

Department of Applied Sciences, University of Québec in Chicoutimi (UQAC)

555, boul. de l'université, Chicoutimi, Québec, G7H 2B1 Canada

* E-mail: elham.vazirinasab1@uqac.ca

This article has been accepted in:

Journal of Materials Science and Technology

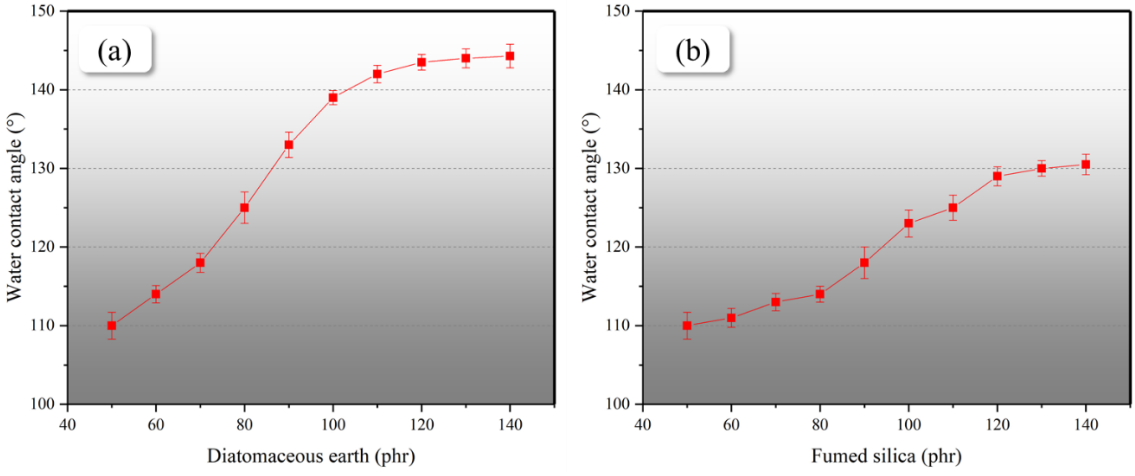

Figure AII-1. WCA of nanocomposites having different mass fractions of (a) micro-sized DE and (b) nano-sized FS.

The volumetric superhydrophobic nanocomposites were developed using both micro-sized DE and nano-sized FS particles. It was observed that the specific mass ratio of DE/FS had a great influence on the final non-wettability of the nanocomposite. Thus, the effect of particle/HTV-SR ratios on the WCA of nanocomposite was also studied as shown in Figure S1. The composites that contained only one type of particles did not exhibit any superhydrophobic properties. Increasing the DE content enhanced the WCA; the WCA attained a maximum value of 144°, a value that remained below that of the definition of superhydrophobicity. In terms of FS nano-scale particles, a maximum WCA of 130° was achieved at the

concentration >120 phr. These results confirmed that the superhydrophobic nanocomposite cannot be obtained by adding solely one type of particle. Therefore, we used a combination of micro-scale DE and nano-scale FS to develop the volumetric superhydrophobic nanocomposite.

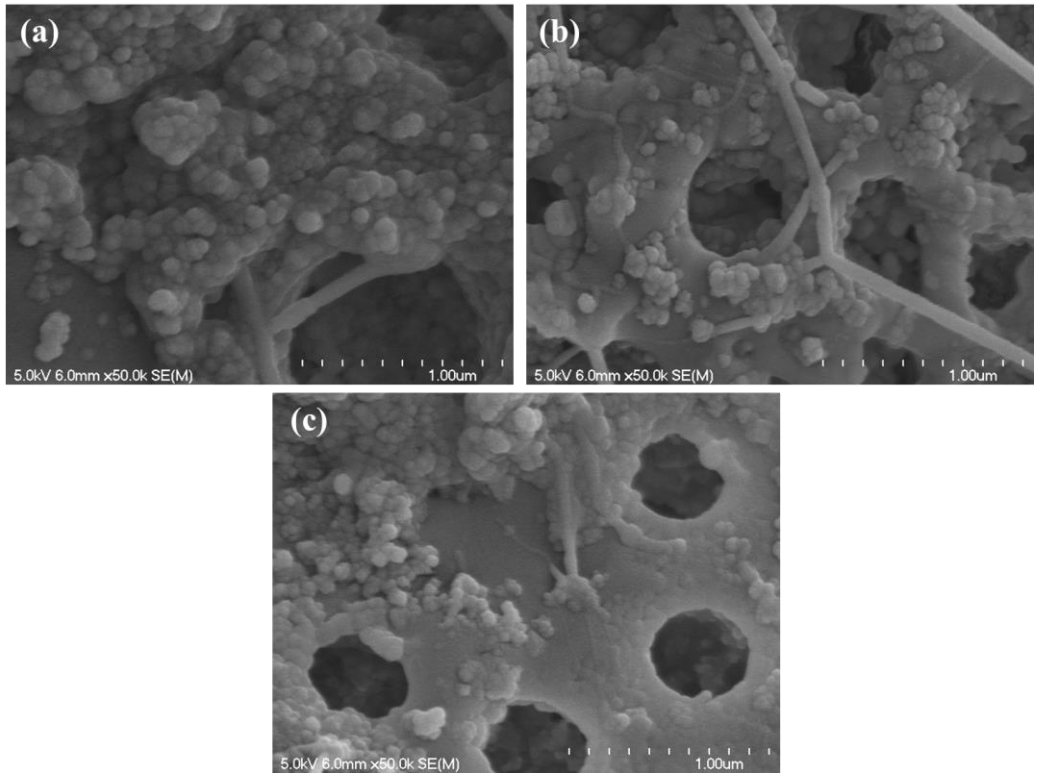

Figure AII-2. FESEM images of the surface of nanocomposites (a) D60F60, (b) D70F50, and (c) D80F40 (all images at ×50,000).

FESEM images at high magnification confirmed the presence of FS particles in the range of 100 nm on the surface of DE. The results illustrated the good compatibility of FS and DE within the HTV-SR matrix.

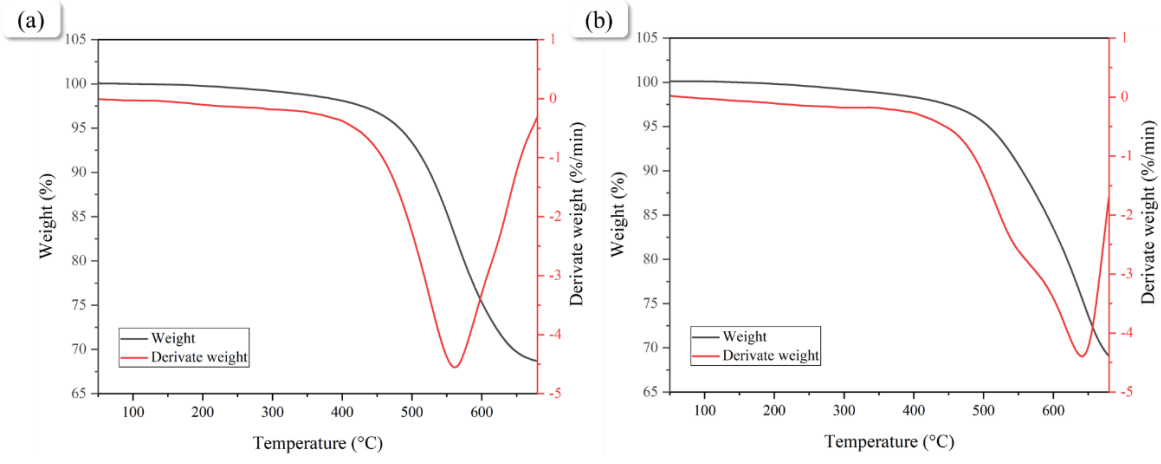

Figure AII-3. TGA and DTGA curves of the nanocomposites (a) D60F60 and (b) D80F40.

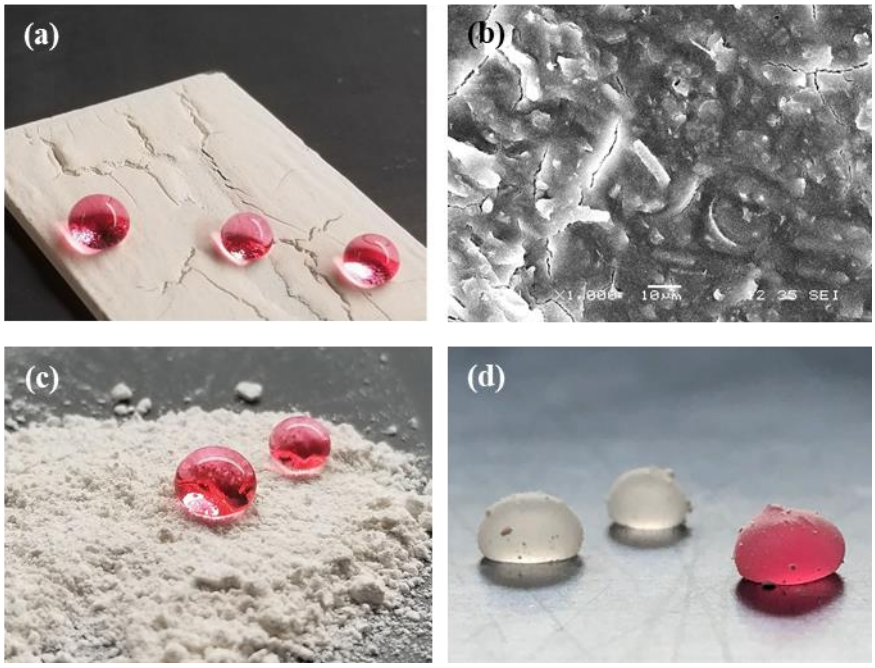

Figure AII-4. (a) Photograph and (b) SEM of a superhydrophobic coating of nanocomposite D70F50 based on dip-coating method followed by toluene evaporation at low pressure and curing at high temperature (×1000 magnification); (c) water droplets as quasi-spheres on the powdered nanocomposite D70F50 before compression molding.

Nanocomposite D70F50 was also applied as a coating on a glass slide using a dip-coating approach to examine its water-repellency and bulk durability. As shown in Figure S4a, regardless of the existence of cracks along the surface, the quasi-spherical shape of water droplets suspended on the surface established the superhydrophobicity of the coating. Moreover, the glitter of the nanocomposite beneath the water droplets stems from light reflection due to the presence of a thin air layer trapped within the interface of nanocomposite and water droplets. In terms of durability, neither abrasion nor immersion in acidic and basic solutions affected the long-term superhydrophobicity of the coating.

There is another interesting phenomenon, called liquid “marbles”, that forms due to the partially modified DE with HTV-SR. By gently moving the water droplets over the powder bed of nanocomposite D70F50 before curing, the powder was absorbed on the liquid/air interface, thereby creating these liquid marbles (Figure S4d). They are some nonwetting and nonstick droplets capable of preserving their semi-spherical shape on the solid surface.

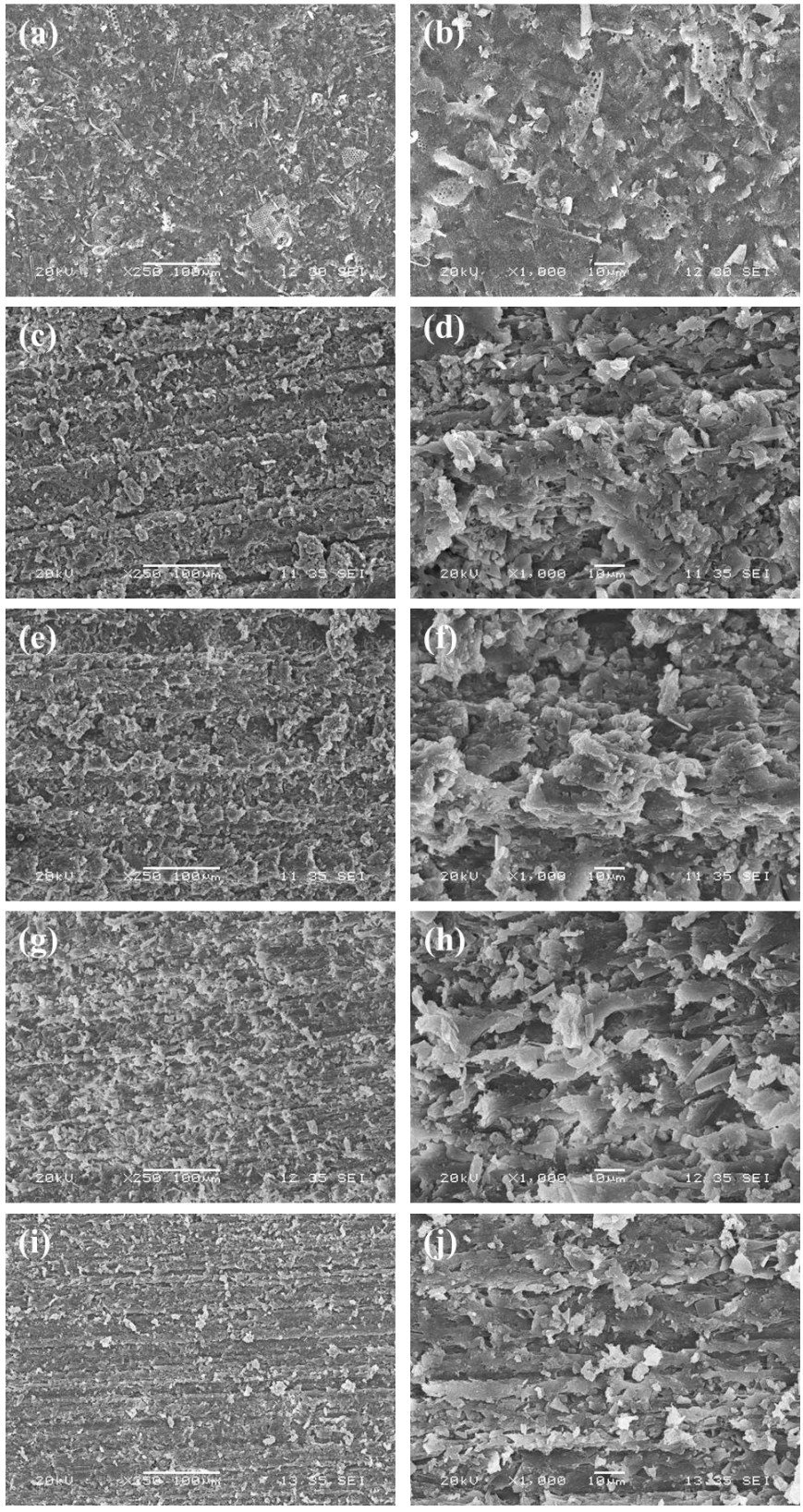

Figure AII-5. SEM images of nanocomposite N70F50 (a–b) before and after abrasion using (c–d) #180, (e–f) #320, (g–h) #800 grit sandpapers, and (i-j) #1200 grit sandpapers.

REFERENCES

[1] X. Qiao, Z. Zhang, X. Jiang, Y. He, and X. Li, "Application of grey theory in pollution prediction on insulator surface in power systems," *Engineering Failure Analysis*, vol. 106, p. 104153, 2019.

[2] M. Farzaneh, "Insulator flashover under icing conditions," *IEEE Transactions on Dielectrics Electrical Insulation*, vol. 21, no. 5, pp. 1997-2011, 2014.

[3] J. Li, Y. Zhao, J. Hu, L. Shu, and X. Shi, "Anti-icing performance of a superhydrophobic PDMS/modified nano-silica hybrid coating for insulators," *Journal of Adhesion Science Technology*, vol. 26, no. 4-5, pp. 665-679, 2012.

[4] L. Nasrat, A. Hamed, M. Hamid, and S. Mansour, "Study the flashover voltage for outdoor polymer insulators under desert climatic conditions," *Egyptian Journal of Petroleum*, vol. 22, no. 1, pp. 1-8, 2013.

[5] S. Khatoon, A. A. Khan, and S. Singh, "A review of the flashover performance of high voltage insulators constructed with modern insulating materials," *Transactions on Electrical Electronic Materials*, vol. 18, no. 5, pp. 246-249, 2017.

[6] D. L. Phillips, "Selection Considerations: Hardened Glass vs. Polymer Insulators," in *2018 IEEE/PES Transmission and Distribution Conference and Exposition (T&D)*, 2018, pp. 1-5: IEEE.

[7] G. Momen and M. J. R. A. M. S. Farzaneh, "Survey of micro/nano filler use to improve silicone rubber for outdoor insulators," vol. 27, no. 1, pp. 1-13, 2011.

[8] S. C. Shit and P. J. N. A. S. L. Shah, "A review on silicone rubber," vol. 36, no. 4, pp. 355-365, 2013.

[9] S. Li *et al.*, "Efficiently texturing hierarchical superhydrophobic fluoride-free translucent films by AACVD with excellent durability and self-cleaning ability," vol. 6, no. 36, pp. 17633-17641, 2018.

[10] S. Chen, Y. Song, F. J. A. S. C. Xu, and Engineering, "Highly transparent and hazy cellulose nanopaper simultaneously with a self-cleaning superhydrophobic surface," vol. 6, no. 4, pp. 5173-5181, 2018.

[11] Y. Xu *et al.*, "Icephobic Behaviors of Superhydrophobic Amorphous Carbon Nano-Films Synthesized from a Flame Process," 2019.

[12] S. Rajiv, S. Kumaran, and M. J. J. o. A. P. S. Sathish, "Long-term-durable anti-icing superhydrophobic composite coatings," vol. 136, no. 7, p. 47059, 2019.

[13] E. Vazirinasab, R. Jafari, and G. Momen, "Application of superhydrophobic coatings as a corrosion barrier: A review," *Surface Coatings Technology*, vol. 341, pp. 40-56, 2018.

[14] R. Jafari, S. Asadollahi, and M. Farzaneh, "Applications of plasma technology in development of superhydrophobic surfaces," *Plasma Chemistry and Plasma Processing*, vol. 33, no. 1, pp. 177-200, 2013.

[15] X. Gou and Z. J. L. Guo, "Superhydrophobic Plant Leaves: The Variation in Surface Morphologies and Wettability during the Vegetation Period," vol. 35, no. 4, pp. 1047-1053, 2019.

[16] X. Xiao, W. Xie, and Z. J. S. E. Ye, "Preparation of corrosion-resisting superhydrophobic surface on aluminium substrate," vol. 35, no. 5, pp. 411-417, 2019.

[17] W. Somrang, S. Denchitcharoen, P. Eiamchai, M. Horprathum, and C. J. M. T. P. Chananonnawathorn, "Superhydrophobic and antireflective surface of nanostructures fabricated by CF4 plasma etching," vol. 5, no. 6, pp. 13879-13885, 2018.

[18] X. Zhang, Y. Guo, H. Chen, W. Zhu, and P. Zhang, "A novel damage-tolerant superhydrophobic and superoleophilic material," *Journal of Materials Chemistry A*, vol. 2, no. 24, pp. 9002-9006, 2014.

[19] E. Wang, H. Wang, Y. Hu, Z. Liu, and Y. Zhu, "Corrosion-resistant engineering superhydrophobic and superoleophilic bulk materials with oil–water separation property," *Journal of materials science*, vol. 52, no. 12, pp. 7130-7139, 2017.

[20] Y. Li, Z. Zhang, B. Ge, X. Men, and Q. Xue, "One-pot, template-free synthesis of a robust superhydrophobic polymer monolith with an adjustable hierarchical porous structure," *Green Chemistry*, vol. 18, no. 19, pp. 5266-5272, 2016.

[21] E. Vazirinasab, R. Jafari, and G. Momen, "Evaluation of atmospheric-pressure plasma parameters to achieve superhydrophobic and self-cleaning HTV silicone rubber surfaces via a single-step, eco-friendly approach," *Surface Coatings Technology*, vol. 375, pp. 100-111, 2019.

[22] K. Maghsoudi, E. Vazirinasab, G. Momen, and R. J. J. o. M. P. T. Jafari, "Icephobicity and durability assessment of superhydrophobic surfaces: The role of surface roughness and the ice adhesion measurement technique," vol. 288, p. 116883.

[23] E. Vazirinasab, G. Momen, R. J. J. o. M. S. Jafari, and Technology, "A non-fluorinated mechanochemically robust volumetric superhydrophobic nanocomposite," 2020.
[24] E. Vazirinasab, K. Maghsoudi, R. Jafari, and G. Momen, "A comparative study of the icephobic and self-cleaning properties of Teflon materials having different surface morphologies," *Journal of Materials Processing Technology*, vol. 276, p. 116415, 2020.
[25] C. Neinhuis and W. Barthlott, "Characterization and distribution of water-repellent, self-cleaning plant surfaces," *Annals of botany*, vol. 79, no. 6, pp. 667-677, 1997.
[26] W. Barthlott and C. Neinhuis, "Purity of the sacred lotus, or escape from contamination in biological surfaces," *Planta*, vol. 202, no. 1, pp. 1-8, 1997.
[27] X. Gao and L. Jiang, "Biophysics: water-repellent legs of water striders," *Nature*, vol. 432, no. 7013, pp. 36-36, 2004.
[28] T. Sun, L. Feng, X. Gao, and L. Jiang, "Bioinspired surfaces with special wettability," *Accounts of Chemical Research*, vol. 38, no. 8, pp. 644-652, 2005.
[29] W. Lee, M.-K. Jin, W.-C. Yoo, and J.-K. Lee, "Nanostructuring of a polymeric substrate with well-defined nanometer-scale topography and tailored surface wettability," *Langmuir*, vol. 20, no. 18, pp. 7665-7669, 2004.
[30] Y. Zheng, X. Gao, and L. Jiang, "Directional adhesion of superhydrophobic butterfly wings," *Soft Matter*, vol. 3, no. 2, pp. 178-182, 2007.
[31] S. Wang *et al.*, "Icephobicity of Penguins Spheniscus Humboldti and an Artificial Replica of Penguin Feather with Air-Infused Hierarchical Rough Structures," *The Journal of Physical Chemistry C*, 2016.
[32] B. Bhushan and Y. C. Jung, "Natural and biomimetic artificial surfaces for superhydrophobicity, self-cleaning, low adhesion, and drag reduction," *Progress in Materials Science*, vol. 56, no. 1, pp. 1-108, 2011.
[33] K. Koch, B. Bhushan, and W. Barthlott, "Multifunctional surface structures of plants: an inspiration for biomimetics," *Progress in Materials science*, vol. 54, no. 2, pp. 137-178, 2009.
[34] E. Vazirinasab, R. Jafari, G. Momen, and T. Carreira, "Simple Fabrication of Superhydrophobic Surfaces Using Atmospheric-Pressure Plasma," in *Materials Science Forum*, 2018, vol. 941, pp. 1808-1814: Trans Tech Publ.
[35] E. Vazirinasab, R. Jafari, and G. Momen, "Wetting and Self-Cleaning Properties of Silicone Rubber Surfaces Treated by Atmospheric Plasma Jet," in *IEEE Conference on Electrical Insulation and Dielectric Phenomena (CEIDP)*, 2018, pp. 239-242: IEEE.
[36] W. Tong, D. Xiong, N. Wang, Z. Wu, and H. J. C. P. B. E. Zhou, "Mechanically robust superhydrophobic coating for aeronautical composite against ice accretion and ice adhesion," vol. 176, p. 107267, 2019.
[37] Y. Ye *et al.*, "One-step synthesis of superhydrophobic polyhedral oligomeric silsesquioxane-graphene oxide and its application in anti-corrosion and anti-wear fields," *Corrosion Science*, vol. 147, pp. 9-21, 2019.
[38] S. Gao *et al.*, "Rational construction of highly transparent superhydrophobic coatings based on a non-particle, fluorine-free and water-rich system for versatile oil-water separation," *Chemical Engineering Journal*, vol. 333, pp. 621-629, 2018.
[39] S. He *et al.*, "Gravity-driven and high flux super-hydrophobic/super-oleophilic poly (arylene ether nitrile) nanofibrous composite membranes for efficient water-in-oil emulsions separation in harsh environments," vol. 177, p. 107439, 2019.
[40] A. Rajappan and G. H. McKinley, "Turbulent drag reduction using biopolymers and bio-inspired superhydrophobic surfaces," *Bulletin of the American Physical Society*, 2019.
[41] X.-M. Li, D. Reinhoudt, and M. Crego-Calama, "What do we need for a superhydrophobic surface? A review on the recent progress in the preparation of superhydrophobic surfaces," *Chemical Society Reviews*, vol. 36, no. 8, pp. 1350-1368, 2007.
[42] B. Bhushan, Y. C. Jung, and K. Koch, "Self-cleaning efficiency of artificial superhydrophobic surfaces," *Langmuir*, vol. 25, no. 5, pp. 3240-3248, 2009.
[43] T. Young, "An essay on the cohesion of fluids," *Philosophical Transactions of the Royal Society of London*, vol. 95, pp. 65-87, 1805.
[44] G. Whyman, E. Bormashenko, and T. Stein, "The rigorous derivation of Young, Cassie–Baxter and Wenzel equations and the analysis of the contact angle hysteresis phenomenon," *Chemical Physics Letters*, vol. 450, no. 4, pp. 355-359, 2008.

[45] I. Sas, R. E. Gorga, J. A. Joines, and K. A. Thoney, "Literature review on superhydrophobic self-cleaning surfaces produced by electrospinning," *Journal of Polymer Science Part B: Polymer Physics*, vol. 50, no. 12, pp. 824-845, 2012.
[46] S. Gowri, L. Almeida, T. Amorim, N. Carneiro, A. Pedro Souto, and M. Fátima Esteves, "Polymer nanocomposites for multifunctional finishing of textiles-a review," *Textile Research Journal*, vol. 80, no. 13, pp. 1290-1306, 2010.
[47] R. N. Wenzel, "Resistance of solid surfaces to wetting by water," *Industrial & Engineering Chemistry*, vol. 28, no. 8, pp. 988-994, 1936.
[48] M. Callies and D. Quéré, "On water repellency," *Soft matter*, vol. 1, no. 1, pp. 55-61, 2005.
[49] D. Quéré, "Rough ideas on wetting," *Physica A: Statistical Mechanics and its Applications*, vol. 313, no. 1, pp. 32-46, 2002.
[50] D. Quéré, "Non-sticking drops," *Reports on Progress in Physics*, vol. 68, no. 11, p. 2495, 2005.
[51] A. Cassie and S. Baxter, "Wettability of porous surfaces," *Transactions of the Faraday society*, vol. 40, pp. 546-551, 1944.
[52] A. Cassie, "Contact angles," *Discussions of the Faraday Society*, vol. 3, pp. 11-16, 1948.
[53] Y. Yan, N. Gao, and W. Barthlott, "Mimicking natural superhydrophobic surfaces and grasping the wetting process: A review on recent progress in preparing superhydrophobic surfaces," *Advances in colloid and interface science*, vol. 169, no. 2, pp. 80-105, 2011.
[54] A. Marmur, "Wetting on hydrophobic rough surfaces: to be heterogeneous or not to be?," *Langmuir*, vol. 19, no. 20, pp. 8343-8348, 2003.
[55] S. Pilotek and H. K. Schmidt, "Wettability of microstructured hydrophobic sol-gel coatings," *Journal of sol-gel science and technology*, vol. 26, no. 1, pp. 789-792, 2003.
[56] R. Fillion, A. Riahi, and A. Edrisy, "A review of icing prevention in photovoltaic devices by surface engineering," *Renewable and Sustainable Energy Reviews*, vol. 32, pp. 797-809, 2014.
[57] M. Miwa, A. Nakajima, A. Fujishima, K. Hashimoto, and T. Watanabe, "Effects of the surface roughness on sliding angles of water droplets on superhydrophobic surfaces," *Langmuir*, vol. 16, no. 13, pp. 5754-5760, 2000.
[58] C. J. Long, J. F. Schumacher, and A. B. Brennan, "Potential for tunable static and dynamic contact angle anisotropy on gradient microscale patterned topographies," *Langmuir*, vol. 25, no. 22, pp. 12982-12989, 2009.
[59] X. Zhang *et al.*, "Polyelectrolyte multilayer as matrix for electrochemical deposition of gold clusters: toward super-hydrophobic surface," *Journal of the American Chemical Society*, vol. 126, no. 10, pp. 3064-3065, 2004.
[60] M. Zhou, X. Xiong, B. Jiang, and C. Weng, "Fabrication of high aspect ratio nanopillars and micro/nano combined structures with hydrophobic surface characteristics by injection molding," *Applied Surface Science*, vol. 427, pp. 854-860, 2018.
[61] S. J. Hwang *et al.*, "Dry etching of polydimethylsiloxane using microwave plasma," *Journal of Micromechanics and Microengineering*, vol. 19, no. 9, p. 095010, 2009.
[62] X. Zhao, L. Li, B. Li, J. Zhang, and A. Wang, "Durable superhydrophobic/superoleophilic PDMS sponges and their applications in selective oil absorption and in plugging oil leakages," *Journal of Materials Chemistry A*, vol. 2, no. 43, pp. 18281-18287, 2014.
[63] F. G. Fearon, *Silicon-based polymer science: a comprehensive resource*. An American Chemical Society Publication, 1990.
[64] S. C. Shit and P. Shah, "A review on silicone rubber," *National Academy Science Letters*, vol. 36, no. 4, pp. 355-365, 2013.
[65] J. Bibiao, Y. Yang, J. Xiang, Z. Rongqi, H. Jianjun, and W. Wenyun, "Preparation of hyperbranched polymers by self-condensing vinyl radical polymerization," *European polymer journal*, vol. 37, no. 10, pp. 1975-1983, 2001.
[66] Q. Wang, F. Wang, and K. Cheng, "Effect of crosslink density on some properties of electron beam-irradiated styrene–butadiene rubber," *Radiation Physics Chemistry*, vol. 78, no. 11, pp. 1001-1005, 2009.
[67] H. S. Yang and E. S. Park, "Mechanical properties and antimicrobial activity of silicone rubber compounds containing acrylated norfloxacin and its polymer," *Macromolecular Materials Engineering*, vol. 291, no. 6, pp. 621-628, 2006.

[68] E. P. Everaert, H. C. Van Der Mei, J. De Vries, and H. J. Busscher, "Hydrophobic recovery of repeatedly plasma-treated silicone rubber. Part 1. Storage in air," *Journal of adhesion science and technology,* vol. 9, no. 9, pp. 1263-1278, 1995.
[69] J. Kim, M. K. Chaudhury, and M. J. Owen, "Hydrophobic recovery of polydimethylsiloxane elastomer exposed to partial electrical discharge," *Journal of Colloid and Interface Science,* vol. 226, no. 2, pp. 231-236, 2000.
[70] R. Zhang *et al.*, "Hydrophobicity improvement of contaminated HTV silicone rubber by atmospheric plasma jet treatment," *IEEE Transactions on Dielectrics and Electrical Insulation,* vol. 23, no. 1, pp. 377-384, 2016.
[71] S. H. Gao, K. S. Zhou, M. K. Lei, and L. S. Wen, "Comparative Study of the Superhydrophobic-Modification of Silicone Rubber Surfaces by CF4 ICP and CCP," *Plasma Processes and Polymers,* vol. 6, no. 8, pp. 530-536, 2009.
[72] G. R. Artus, S. Jung, J. Zimmermann, H. P. Gautschi, K. Marquardt, and S. Seeger, "Silicone nanofilaments and their application as superhydrophobic coatings," *Advanced Materials,* vol. 18, no. 20, pp. 2758-2762, 2006.
[73] M. Ma, R. M. Hill, J. L. Lowery, S. V. Fridrikh, and G. C. Rutledge, "Electrospun poly (styrene-block-dimethylsiloxane) block copolymer fibers exhibiting superhydrophobicity," *Langmuir,* vol. 21, no. 12, pp. 5549-5554, 2005.
[74] Y. Li *et al.*, "A robust and flexible bulk superhydrophobic material from silicone rubber/silica gel prepared by thiol–ene photopolymerization," *Journal of materials chemistry A,* vol. 7, no. 12, pp. 7242-7255, 2019.
[75] P. Dimitrakellis and E. Gogolides, "Atmospheric plasma etching of polymers: A palette of applications in cleaning/ashing, pattern formation, nanotexturing and superhydrophobic surface fabrication," *Microelectronic Engineering,* vol. 194, pp. 109-115, 2018.
[76] B. J. Basu, V. D. Kumar, and C. Anandan, "Surface studies on superhydrophobic and oleophobic polydimethylsiloxane–silica nanocomposite coating system," *Applied surface science,* vol. 261, pp. 807-814, 2012.
[77] J. C. Fielding, "Fluorination of silicone rubber by plasma polymerization," University of Cincinnati, 2004.
[78] R. R. Thomas, "Material properties of fluoropolymers and perfluoroalkyl-based polymers," in *Fluoropolymers 2*: Springer, 2002, pp. 47-67.
[79] K. Aleksandrov *et al.*, "Waste incineration of Polytetrafluoroethylene (PTFE) to evaluate potential formation of per-and Poly-Fluorinated Alkyl Substances (PFAS) in flue gas," *Chemosphere,* vol. 226, pp. 898-906, 2019.
[80] J. Zhang, J. Li, and Y. Han, "Superhydrophobic PTFE surfaces by extension," *Macromolecular Rapid Communications,* vol. 25, no. 11, pp. 1105-1108, 2004.
[81] S. F. Toosi, S. Moradi, S. Kamal, and S. G. Hatzikiriakos, "Superhydrophobic laser ablated PTFE substrates," *Applied Surface Science,* vol. 349, pp. 715-723, 2015.
[82] J. Yong *et al.*, "Femtosecond laser ablated durable superhydrophobic PTFE films with micro-through-holes for oil/water separation: Separating oil from water and corrosive solutions," *Applied Surface Science,* vol. 389, pp. 1148-1155, 2016.
[83] M. Toma, G. Loget, and R. M. Corn, "Flexible teflon nanocone array surfaces with tunable superhydrophobicity for self-cleaning and aqueous droplet patterning," *ACS applied materials & interfaces,* vol. 6, no. 14, pp. 11110-11117, 2014.
[84] J. Song, Y. Li, W. Xu, H. Liu, and Y. Lu, "Inexpensive and non-fluorinated superhydrophobic concrete coating for anti-icing and anti-corrosion," *Journal of colloid and interface science,* vol. 541, pp. 86-92, 2019.
[85] J. W. Martin, D. M. Whittle, D. C. Muir, and S. A. Mabury, "Perfluoroalkyl contaminants in a food web from Lake Ontario," *Environmental Science and Technology,* vol. 38, no. 20, pp. 5379-5385, 2004.
[86] J. Seyfi *et al.*, "Antibacterial superhydrophobic polyvinyl chloride surfaces via the improved phase separation process using silver phosphate nanoparticles," *Colloids and Surfaces B: Biointerfaces,* vol. 183, p. 110438, 2019.
[87] S. Sriram and A. Kumar, "Separation of oil-water via porous PMMA/SiO2 nanoparticles superhydrophobic surface," *Colloids and Surfaces A: Physicochemical and Engineering Aspects,* vol. 563, pp. 271-279, 2019.

[88] X. Wang *et al.*, "Simple fabrication of superhydrophobic PLA with honeycomb-like structures for high-efficiency oil-water separation," *Chinese Chemical Letters*, vol. 31, no. 2, pp. 365-368, 2020.
[89] J. Lv, X. Yin, R. Li, J. Chen, Q. Lin, and L. Zhu, "Superhydrophobic PCL/PS composite nanofibrous membranes prepared through solution blow spinning with an airbrush for oil adsorption," *Polymer Engineering & Science*, vol. 59, no. S1, pp. E171-E181, 2019.
[90] S. Liu, X. Zhang, and S. Seeger, "Solvent-Free Fabrication of Flexible and Robust Superhydrophobic Composite Films with Hierarchical Micro/Nanostructures and Durable Self-Cleaning Functionality," *ACS Applied Materials & Interfaces*, vol. 11, no. 47, pp. 44691-44699, 2019.
[91] Y. Guo and Q. Wang, "Facile approach in fabricating superhydrophobic coatings from silica-based nanocomposite," *Applied surface science*, vol. 257, no. 1, pp. 33-36, 2010.
[92] R. Xing *et al.*, "Three-Dimensionally Printed Bioinspired Superhydrophobic Packings for Oil-in-Water Emulsion Separation," *Langmuir*, vol. 35, no. 39, pp. 12799-12806, 2019.
[93] X.-F. Zhang, Y.-Q. Chen, and J.-M. Hu, "Robust superhydrophobic SiO2/polydimethylsiloxane films coated on mild steel for corrosion protection," *Corrosion Science*, p. 108452, 2020.
[94] X. Zhou *et al.*, "Fabrication of superhydrophobic TiO2 quadrangular nanorod film with self-cleaning, anti-icing properties," *Ceramics International*, vol. 45, no. 9, pp. 11508-11516, 2019.
[95] M. Wang *et al.*, "Self-healing PDMS/SiO2-CaCO3 composite coating for highly efficient protection of building materials," *Materials Letters*, vol. 265, p. 127290, 2020.
[96] M. Khodaei and S. Shadmani, "Superhydrophobicity on aluminum through reactive-etching and TEOS/GPTMS/nano-Al2O3 silane-based nanocomposite coating," *Surface and Coatings Technology*, vol. 374, pp. 1078-1090, 2019.
[97] D. Upadhaya, P. Kumar, and D. D. Purkayastha, "Superhydrophobic ZnO/TiO 2 heterostructure with significantly enhanced photocatalytic activity," *Journal of Materials Science: Materials in Electronics*, vol. 30, no. 11, pp. 10399-10407, 2019.
[98] X. Zhang *et al.*, "Preparation and photocatalytic wettability conversion of TiO2-based superhydrophobic surfaces," *Langmuir*, vol. 22, no. 23, pp. 9477-9479, 2006.
[99] M. Shaban, F. Mohamed, and S. Abdallah, "Production and characterization of superhydrophobic and antibacterial coated fabrics utilizing ZnO nanocatalyst," *Scientific reports*, vol. 8, no. 1, pp. 1-15, 2018.
[100] M. Z. Khan *et al.*, "Development of UV protective, superhydrophobic and antibacterial textiles using ZnO and TiO 2 nanoparticles," *Fibers and Polymers*, vol. 19, no. 8, pp. 1647-1654, 2018.
[101] S. M. S. Shahabadi, H. Rabiee, S. M. Seyedi, A. Mokhtare, and J. A. Brant, "Superhydrophobic dual layer functionalized titanium dioxide/polyvinylidene fluoride-co-hexafluoropropylene (TiO2/PH) nanofibrous membrane for high flux membrane distillation," *Journal of Membrane Science*, vol. 537, pp. 140-150, 2017.
[102] H. Sojoudi, M. Wang, N. Boscher, G. H. McKinley, and K. K. Gleason, "Durable and scalable icephobic surfaces: similarities and distinctions from superhydrophobic surfaces," *Soft matter*, vol. 12, no. 7, pp. 1938-1963, 2016.
[103] K. Maghsoudi, G. Momen, R. Jafari, and M. Farzaneh, "Direct replication of micro-nanostructures in the fabrication of superhydrophobic silicone rubber surfaces by compression molding," *Applied Surface Science*, vol. 458, pp. 619-628, 2018.
[104] E. Gentili, L. Tabaglio, and F. Aggogeri, "Review on micromachining techniques," in *Advanced manufacturing systems and technology*: Springer, 2005, pp. 387-396.
[105] Y. Sun and Z. Guo, "Recent advances of bioinspired functional materials with specific wettability: from nature and beyond nature," *Nanoscale Horizons*, vol. 4, no. 1, pp. 52-76, 2019.
[106] K. Maghsoudi, E. Vazirinasab, R. Jafari, G. J. M. Momen, and M. Processes, "Evaluating the effect of processing parameters on the replication quality in the micro compression molding of silicone rubber," pp. 1-9, 2020.
[107] K. Yung, J. Wang, S. Huang, C. Lee, and T. Yue, "Modeling the etching rate and uniformity of plasma-aided manufacturing using statistical experimental design," *Materials and Manufacturing processes*, vol. 21, no. 8, pp. 899-906, 2006.
[108] V. M. Donnelly and A. Kornblit, "Plasma etching: Yesterday, today, and tomorrow," *Journal of Vacuum Science & Technology A: Vacuum, Surfaces, and Films*, vol. 31, no. 5, p. 050825, 2013.
[109] T. Darmanin, E. T. de Givenchy, S. Amigoni, and F. Guittard, "Superhydrophobic surfaces by electrochemical processes," *Advanced materials*, vol. 25, no. 10, pp. 1378-1394, 2013.
[110] A. Zhuang *et al.*, "Transparent superhydrophobic PTFE films via one-step aerosol assisted chemical vapor deposition," *RSC Advances*, vol. 7, no. 47, pp. 29275-29283, 2017.

[111] S. Zhou, X. Zhu, and Q. Yan, "One-step electrochemical deposition to achieve superhydrophobic cobalt incorporated amorphous carbon-based film with self-cleaning and anti-corrosion," *Surface and Interface Analysis*, vol. 50, no. 3, pp. 290-296, 2018.
[112] R. Lakshmi, P. Bera, C. Anandan, and B. J. Basu, "Effect of the size of silica nanoparticles on wettability and surface chemistry of sol–gel superhydrophobic and oleophobic nanocomposite coatings," *Applied Surface Science*, vol. 320, pp. 780-786, 2014.
[113] M. Yeganeh and N. Mohammadi, "Superhydrophobic surface of Mg alloys: a review," *Journal of magnesium alloys*, vol. 6, no. 1, pp. 59-70, 2018.
[114] P. Nguyen-Tri *et al.*, "Recent progress in the preparation, properties and applications of superhydrophobic nano-based coatings and surfaces: A review," *Progress in organic coatings*, vol. 132, pp. 235-256, 2019.
[115] D.-W. Li, H.-Y. Wang, Y. Liu, D.-S. Wei, and Z.-X. Zhao, "Large-scale fabrication of durable and robust super-hydrophobic spray coatings with excellent repairable and anti-corrosion performance," *Chemical Engineering Journal*, vol. 367, pp. 169-179, 2019.
[116] C. Qi *et al.*, "Superhydrophobic Surface Based On Assembly Of Nanoparticles For Application In Anti-icing Under Ultra-low Temperature," *ACS Applied Nano Materials*, 2020.
[117] J. Y. Park, K. O. Oh, J. C. Won, H. Han, H. M. Jung, and Y. S. Kim, "Facile fabrication of superhydrophobic coatings with polyimide particles using a reactive electrospraying process," *Journal of Materials Chemistry*, vol. 22, no. 31, pp. 16005-16010, 2012.
[118] S. Czyzyk, A. Dotan, H. Dodiuk, and S. Kenig, "Processing effects on the kinetics morphology and properties of hybrid sol-gel superhydrophobic coatings," *Progress in Organic Coatings*, vol. 140, p. 105501, 2020.
[119] E. J. Lee, J. J. Kim, and S. O. Cho, "Fabrication of porous hierarchical polymer/ceramic composites by electron irradiation of organic/inorganic polymers: route to a highly durable, large-area superhydrophobic coating," *Langmuir*, vol. 26, no. 5, pp. 3024-3030, 2010.
[120] M. Ge *et al.*, "A "PDMS-in-water" emulsion enables mechanochemically robust superhydrophobic surfaces with self-healing nature," *Nanoscale Horizons*, vol. 5, no. 1, pp. 65-73, 2020.
[121] L. T. Phan, S. M. Yoon, and M.-W. Moon, "Plasma-based nanostructuring of polymers: A review," *Polymers*, vol. 9, no. 9, p. 417, 2017.
[122] A. Schutze, J. Y. Jeong, S. E. Babayan, J. Park, G. S. Selwyn, and R. F. Hicks, "The atmospheric-pressure plasma jet: a review and comparison to other plasma sources," *IEEE transactions on plasma science*, vol. 26, no. 6, pp. 1685-1694, 1998.
[123] K. Samanta, M. Jassal, and A. K. Agrawal, "Atmospheric pressure glow discharge plasma and its applications in textile," 2006.
[124] I. Junkar, "Interaction of Cells and Platelets with Biomaterial Surfaces Treated with Gaseous Plasma," in *Advances in Biomembranes and Lipid Self-Assembly*, vol. 23: Elsevier, 2016, pp. 25-59.
[125] G. Allan, A. Fotheringham, and P. Weedall, "The use of plasma and neural modelling to optimise the application of a repellent coating to disposable surgical garments," *AUTEX Research Journal*, vol. 2, no. 2, pp. 64-68, 2002.
[126] N. Ulbin-Figlewicz, A. Zimoch-Korzycka, and A. Jarmoluk, "Antibacterial activity and physical properties of edible chitosan films exposed to low-pressure plasma," *Food and Bioprocess Technology*, vol. 7, no. 12, pp. 3646-3654, 2014.
[127] J. Pulpytel, V. Kumar, P. Peng, V. Micheli, N. Laidani, and F. Arefi-Khonsari, "Deposition of Organosilicon Coatings by a Non-Equilibrium Atmospheric Pressure Plasma Jet: Design, Analysis and Macroscopic Scaling Law of the Process," *Plasma Processes and Polymers*, vol. 8, no. 7, pp. 664-675, 2011.
[128] U. Lommatzsch and J. Ihde, "Plasma Polymerization of HMDSO with an Atmospheric Pressure Plasma Jet for Corrosion Protection of Aluminum and Low-Adhesion Surfaces," *Plasma Processes and Polymers*, vol. 6, no. 10, pp. 642-648, 2009.
[129] J. A. Jofre-Reche, J. Pulpytel, F. Arefi-Khonsari, and J. M. Martín-Martínez, "Increased adhesion of polydimethylsiloxane (PDMS) to acrylic adhesive tape for medical use by surface treatment with an atmospheric pressure rotating plasma jet," *Journal of Physics D: Applied Physics*, vol. 49, no. 33, p. 334001, 2016.
[130] K. N. Pandiyaraj *et al.*, "Low-pressure plasma enhanced immobilization of chitosan on low-density polyethylene for bio-medical applications," *Applied Surface Science*, vol. 328, pp. 1-12, 2015.

[131] F. Rezaei, M. D. Dickey, M. Bourham, and P. J. Hauser, "Surface modification of PET film via a large area atmospheric pressure plasma: An optical analysis of the plasma and surface characterization of the polymer film," *Surface and Coatings Technology,* vol. 309, pp. 371-381, 2017.
[132] F. Palumbo, R. Di Mundo, D. Cappelluti, and R. d'Agostino, "SuperHydrophobic and SuperHydrophilic Polycarbonate by Tailoring Chemistry and Nano-texture with Plasma Processing," *Plasma Processes and Polymers,* vol. 8, no. 2, pp. 118-126, 2011.
[133] Z. Fang, Y. Liu, K. Liu, T. Shao, and C. Zhang, "Surface modifications of polymethylmetacrylate films using atmospheric pressure air dielectric barrier discharge plasma," *Vacuum,* vol. 86, no. 9, pp. 1305-1312, 2012.
[134] M. E. Vlachopoulou, G. Kokkoris, C. Cardinaud, E. Gogolides, and A. Tserepi, "Plasma etching of poly (dimethylsiloxane): Roughness formation, mechanism, control, and application in the fabrication of microfluidic structures," *Plasma Processes and Polymers,* vol. 10, no. 1, pp. 29-40, 2013.
[135] F. Leroux, C. Campagne, A. Perwuelz, and L. Gengembre, "Polypropylene film chemical and physical modifications by dielectric barrier discharge plasma treatment at atmospheric pressure," *Journal of colloid and interface science,* vol. 328, no. 2, pp. 412-420, 2008.
[136] A. Van Deynse, P. Cools, C. Leys, N. De Geyter, and R. Morent, "Surface activation of polyethylene with an argon atmospheric pressure plasma jet: Influence of applied power and flow rate," *Applied Surface Science,* vol. 328, pp. 269-278, 2015.
[137] H. Yasuda and C. Wang, "Plasma polymerization investigated by the substrate temperature dependence," *Journal of Polymer Science Part A: Polymer Chemistry,* vol. 23, no. 1, pp. 87-106, 1985.
[138] T. Homola, L. Y. Wu, and M. Černák, "Atmospheric plasma surface activation of poly (ethylene terephthalate) film for roll-to-roll application of transparent conductive coating," *The Journal of Adhesion,* vol. 90, no. 4, pp. 296-309, 2014.
[139] S. Chen *et al.*, "Surface modification of epoxy resin using He/CF4 atmospheric pressure plasma jet for flashover withstanding characteristics improvement in vacuum," *Applied Surface Science,* vol. 414, pp. 107-113, 2017.
[140] A. Kuzminova *et al.*, "Treatment of poly (ethylene terephthalate) foils by atmospheric pressure air dielectric barrier discharge and its influence on cell growth," *Applied Surface Science,* vol. 357, pp. 689-695, 2015.
[141] J. P. Youngblood and T. J. McCarthy, "Ultrahydrophobic polymer surfaces prepared by simultaneous ablation of polypropylene and sputtering of poly (tetrafluoroethylene) using radio frequency plasma," *Macromolecules,* vol. 32, no. 20, pp. 6800-6806, 1999.
[142] D. Ben Salem, J. Pulpytel, F. Pillier, A. Pailleret, and F. Arefi-Khonsari, "Amorphization and Polymorphism Modification of Polyamide-6 Films via Open-Air Non-Equilibrium Atmospheric Pressure Plasma Jet Treatment," *Plasma Processes and Polymers,* vol. 11, no. 10, pp. 961-973, 2014.
[143] J. Jeong *et al.*, "Etching materials with an atmospheric-pressure plasma jet," *Plasma Sources Science and Technology,* vol. 7, no. 3, p. 282, 1998.
[144] B. N. Chapman, *Glow discharge processes: sputtering and plasma etching*. Wiley, 1980.
[145] R. A. Siliprandi, S. Zanini, E. Grimoldi, F. S. Fumagalli, R. Barni, and C. Riccardi, "Atmospheric pressure plasma discharge for polysiloxane thin films deposition and comparison with low pressure process," *Plasma Chemistry and Plasma Processing,* vol. 31, no. 2, pp. 353-372, 2011.
[146] N. Inagaki, K. Narushim, N. Tuchida, and K. Miyazaki, "Surface characterization of plasma-modified poly (ethylene terephthalate) film surfaces," *Journal of Polymer Science Part B: Polymer Physics,* vol. 42, no. 20, pp. 3727-3740, 2004.
[147] E. Carbone, N. Boucher, M. Sferrazza, and F. Reniers, "How to increase the hydrophobicity of PTFE surfaces using an rf atmospheric-pressure plasma torch," *Surface and interface analysis,* vol. 42, no. 6-7, pp. 1014-1018, 2010.
[148] R. Wang, Y. Shen, C. Zhang, P. Yan, and T. Shao, "Comparison between helium and argon plasma jets on improving the hydrophilic property of PMMA surface," *Applied Surface Science,* vol. 367, pp. 401-406, 2016.
[149] J. Juárez-Moreno, L. Brito-Argáez, A. Ávila-Ortega, A. Oliva, F. Avilés, and J. Cauich-Rodríguez, "Effect of the type of plasma on the polydimethylsiloxane/collagen composites adhesive properties," *International Journal of Adhesion and Adhesives,* vol. 77, pp. 85-95, 2017.
[150] I. D. Huner and H. A. Gulec, "Fouling behavior of poly (ether) sulfone ultrafiltration membrane during concentration of whey proteins: Effect of hydrophilic modification using atmospheric pressure argon jet plasma," *Colloids and Surfaces B: Biointerfaces,* vol. 160, pp. 510-519, 2017.

[151] R. Wang, C. Zhang, X. Liu, Q. Xie, P. Yan, and T. Shao, "Microsecond pulse driven Ar/CF4 plasma jet for polymethylmethacrylate surface modification at atmospheric pressure," *Applied surface science*, vol. 328, pp. 509-515, 2015.
[152] S. H. Lee *et al.*, "One-step production of superhydrophobic coatings on flat substrates via atmospheric rf plasma process using non-fluorinated hydrocarbons," *ACS applied materials & interfaces*, vol. 3, no. 2, pp. 476-481, 2011.
[153] T. Kewitz, M. Fröhlich, J. von Frieling, and H. Kersten, "Investigation of a commercial atmospheric pressure plasma jet by a newly designed calorimetric probe," *IEEE Transactions on Plasma Science*, vol. 43, no. 5, pp. 1769-1773, 2015.
[154] T. Homola, J. Matoušek, B. Hergelová, M. Kormunda, L. Y. Wu, and M. Černák, "Activation of poly (ethylene terephthalate) surfaces by atmospheric pressure plasma," *Polymer degradation and stability*, vol. 97, no. 11, pp. 2249-2254, 2012.
[155] U. Little *et al.*, "Surface modification of poly (ε-caprolactone) using a dielectric barrier discharge in atmospheric pressure glow discharge mode," *Acta biomaterialia*, vol. 5, no. 6, pp. 2025-2032, 2009.
[156] K. Kostov, T. Nishime, L. Hein, and A. Toth, "Study of polypropylene surface modification by air dielectric barrier discharge operated at two different frequencies," *Surface and Coatings Technology*, vol. 234, pp. 60-66, 2013.
[157] K. Gotoh, Y. Kobayashi, A. Yasukawa, and Y. Ishigami, "Surface modification of PET films by atmospheric pressure plasma exposure with three reactive gas sources," *Colloid and Polymer Science*, vol. 290, no. 11, pp. 1005-1014, 2012.
[158] U. Lommatzsch, D. Pasedag, A. Baalmann, G. Ellinghorst, and H. E. Wagner, "Atmospheric pressure plasma jet treatment of polyethylene surfaces for adhesion improvement," *Plasma Processes and Polymers*, vol. 4, no. S1, 2007.
[159] P. K. Chu, J. Chen, L. Wang, and N. Huang, "Plasma-surface modification of biomaterials," *Materials Science and Engineering: R: Reports*, vol. 36, no. 5-6, pp. 143-206, 2002.
[160] A. Van Deynse, P. Cools, C. Leys, R. Morent, and N. De Geyter, "Surface modification of polyethylene in an argon atmospheric pressure plasma jet," *Surface and Coatings Technology*, vol. 276, pp. 384-390, 2015.
[161] H. C. Barshilia and N. Gupta, "Superhydrophobic polytetrafluoroethylene surfaces with leaf-like micro-protrusions through Ar+ O2 plasma etching process," *Vacuum*, vol. 99, pp. 42-48, 2014.
[162] J. Ryu *et al.*, "Nearly perfect durable superhydrophobic surfaces fabricated by a simple one-step plasma treatment," *Scientific reports*, vol. 7, no. 1, p. 1981, 2017.
[163] A. O. Lobo, S. C. Ramos, E. F. Antunes, F. R. Marciano, V. J. Trava-Airoldi, and E. J. Corat, "Fast functionalization of vertically aligned multiwalled carbon nanotubes using oxygen plasma," *Materials Letters*, vol. 70, pp. 89-93, 2012.
[164] T. Takahashi *et al.*, "Change in surface morphology of polytetrafluoroethylene by reactive ion etching," *Radiation Physics and Chemistry*, vol. 80, no. 2, pp. 253-256, 2011.
[165] I. Woodward, W. Schofield, V. Roucoules, and J. Badyal, "Super-hydrophobic surfaces produced by plasma fluorination of polybutadiene films," *Langmuir*, vol. 19, no. 8, pp. 3432-3438, 2003.
[166] C. Yang *et al.*, "CF4 plasma-modified superhydrophobic PVDF membranes for direct contact membrane distillation," *Journal of Membrane Science*, vol. 456, pp. 155-161, 2014.
[167] S.-H. Gao, K.-S. Zhou, M.-K. Lei, and L.-S. Wen, "Surface modification of silicone rubber by CF 4 radio frequency plasma immersion," *Plasma Chemistry and Plasma Processing*, vol. 28, no. 6, pp. 715-728, 2008.
[168] S. H. Kim, J.-H. Kim, B.-K. Kang, and H. S. Uhm, "Superhydrophobic CF x Coating via In-Line Atmospheric RF Plasma of He− CF4− H2," *Langmuir*, vol. 21, no. 26, pp. 12213-12217, 2005.
[169] R. Morent, N. De Geyter, T. Desmet, P. Dubruel, and C. Leys, "Plasma surface modification of biodegradable polymers: a review," *Plasma Processes and Polymers*, vol. 8, no. 3, pp. 171-190, 2011.
[170] P. Dimitrakellis, A. Travlos, V. P. Psycharis, and E. Gogolides, "Superhydrophobic paper by facile and fast atmospheric pressure plasma etching," *Plasma Processes and Polymers*, vol. 14, no. 3, 2017.
[171] E. Her *et al.*, "Superhydrophobic transparent surface of nanostructured poly (methyl methacrylate) enhanced by a hydrolysis reaction," *Plasma Processes and Polymers*, vol. 10, no. 5, pp. 481-488, 2013.
[172] D. Kontziampasis, G. Boulousis, A. Smyrnakis, K. Ellinas, A. Tserepi, and E. Gogolides, "Biomimetic, antireflective, superhydrophobic and oleophobic PMMA and PMMA-coated glass surfaces fabricated by plasma processing," *Microelectronic Engineering*, vol. 121, pp. 33-38, 2014.

[173] D. J. Marchand *et al.*, "Atmospheric rf plasma deposition of superhydrophobic coatings using tetramethylsilane precursor," *Surface and Coatings Technology,* vol. 234, pp. 14-20, 2013.
[174] C. Huang, H.-H. Lin, and C. Li, "Atmospheric Pressure Plasma Polymerization of Super-Hydrophobic Nano-films Using Hexamethyldisilazane Monomer," *Plasma Chemistry and Plasma Processing,* vol. 35, no. 6, pp. 1015-1028, 2015.
[175] F. N. Ahmad, M. Jaafar, S. Palaniandy, and K. A. M. Azizli, "Effect of particle shape of silica mineral on the properties of epoxy composites," *Composites Science Technology,* vol. 68, no. 2, pp. 346-353, 2008.
[176] S. J. Blott and K. Pye, "Particle shape: a review and new methods of characterization and classification," *Sedimentology,* vol. 55, no. 1, pp. 31-63, 2008.
[177] I. Pleşa, P. V. Noţingher, S. Schlögl, C. Sumereder, and M. Muhr, "Properties of polymer composites used in high-voltage applications," *Polymers,* vol. 8, no. 5, p. 173, 2016.
[178] A. Aqel, K. M. A. El-Nour, R. A. Ammar, and A. Al-Warthan, "Carbon nanotubes, science and technology part (I) structure, synthesis and characterisation," *Arabian Journal of Chemistry,* vol. 5, no. 1, pp. 1-23, 2012.
[179] Y. Qi, N.-X. Hu, Q. Zhang, G. Sisler, and B. McAneney, "Nanotube reinforced fluorine-containing composites," ed: Google Patents, 2016.
[180] J. Šubrt, V. Štengl, S. Bakardjieva, and L. Szatmary, "Synthesis of spherical metal oxide particles using homogeneous precipitation of aqueous solutions of metal sulfates with urea," *Powder technology,* vol. 169, no. 1, pp. 33-40, 2006.
[181] W. Tuntanatewin, K. Tani, K. Ishikura, H. Zhang, and Y. Okamura, "One-pot fabrication of polymer micro/nano-discs via phase separation and a roll-to-roll coating process," *Colloids Surfaces A: Physicochemical Engineering Aspects,* vol. 586, p. 124274, 2020.
[182] S.-N. Ding, C.-L. Zheng, N. Wan, and S. Cosnier, "Graphene/clay composite electrode formed by exfoliating graphite with Laponite for simultaneous determination of ascorbic acid, dopamine, and uric acid," *Monatshefte für Chemie-Chemical Monthly,* vol. 145, no. 9, pp. 1389-1394, 2014.
[183] A. A. Moud, M. Arjmand, J. Liu, Y. Yang, A. Sanati-Nezhad, and S. H. Hejazi, "Cellulose nanocrystal structure in the presence of salts," *Cellulose,* vol. 26, no. 18, pp. 9387-9401, 2019.
[184] F. Zhang *et al.*, "Superhydrophobic carbon nanotubes/epoxy nanocomposite coating by facile one-step spraying," *Surface Coatings Technology,* vol. 341, pp. 15-23, 2018.
[185] A. Asthana, T. Maitra, R. Büchel, M. K. Tiwari, and D. Poulikakos, "Multifunctional superhydrophobic polymer/carbon nanocomposites: graphene, carbon nanotubes, or carbon black?," *ACS applied materials interfaces,* vol. 6, no. 11, pp. 8859-8867, 2014.
[186] Y. Feng *et al.*, "Superhydrophobic nanocomposite coatings with photoinitiated three-dimensional networks based on reactive graphene nanosheet-induced self-wrinkling patterned surfaces," *Journal of colloid interface science,* vol. 536, pp. 149-159, 2019.
[187] A. C. Ribeiro, J. G. Furtado, L. A. Silva, and B. G. Soares, "Superhydrophobic nanostructured coatings for electrical insulators," *Polymer Composites*.
[188] W. Huang *et al.*, "Super-hydrophobic polyaniline-TiO2 hierarchical nanocomposite as anticorrosion coating," *Materials Letters,* vol. 258, p. 126822, 2020.
[189] P. Cully, F. Karasu, L. Müller, T. Jauzein, and Y. Leterrier, "Self-cleaning and wear-resistant polymer nanocomposite surfaces," *Surface Coatings Technology,* vol. 348, pp. 111-120, 2018.
[190] T. Ren, M. Yang, K. Wang, Y. Zhang, and J. He, "CuO nanoparticles-containing highly transparent and superhydrophobic coatings with extremely low bacterial adhesion and excellent bactericidal property," *ACS applied materials & interfaces,* vol. 10, no. 30, pp. 25717-25725, 2018.
[191] Q. F. Xu, Y. Liu, F.-J. Lin, B. Mondal, and A. M. Lyons, "Superhydrophobic TiO2–polymer nanocomposite surface with UV-induced reversible wettability and self-cleaning properties," *ACS applied materials interfaces,* vol. 5, no. 18, pp. 8915-8924, 2013.
[192] B. Ding, D. Zhi, H. Chen, and X. Zhang, "Facile Fabrication of Superhydrophobic and Superoleophilic Bulk Materials with Excellent Durability."
[193] C.-H. Xue, X.-J. Guo, J.-Z. Ma, and S.-T. Jia, "Fabrication of robust and antifouling superhydrophobic surfaces via surface-initiated atom transfer radical polymerization," *ACS applied materials & interfaces,* vol. 7, no. 15, pp. 8251-8259, 2015.
[194] M. W. Lee, S. An, S. S. Latthe, C. Lee, S. Hong, and S. S. Yoon, "Electrospun polystyrene nanofiber membrane with superhydrophobicity and superoleophilicity for selective separation of water and low viscous oil," *ACS applied materials & interfaces,* vol. 5, no. 21, pp. 10597-10604, 2013.

[195] T. Verho, C. Bower, P. Andrew, S. Franssila, O. Ikkala, and R. H. Ras, "Mechanically durable superhydrophobic surfaces," *Advanced materials,* vol. 23, no. 5, pp. 673-678, 2011.
[196] A. Milionis, E. Loth, and I. S. Bayer, "Recent advances in the mechanical durability of superhydrophobic materials," *Advances in colloid interface science,* vol. 229, pp. 57-79, 2016.
[197] N. Puretskiy, G. Stoychev, A. Synytska, and L. Ionov, "Surfaces with self-repairable ultrahydrophobicity based on self-organizing freely floating colloidal particles," *Langmuir,* vol. 28, no. 8, pp. 3679-3682, 2012.
[198] K. Chen, S. Zhou, and L. Wu, "Facile fabrication of self-repairing superhydrophobic coatings," *Chemical Communications,* vol. 50, no. 80, pp. 11891-11894, 2014.
[199] M. Lewin and Y. Tang, "Nanocomposites and their surfaces," ed: Google Patents, 2010.
[200] X. Huang, X. Kong, Y. Cui, X. Ye, X. Wang, and B. Shi, "Durable superhydrophobic materials enabled by abrasion-triggered roughness regeneration," *Chemical Engineering Journal,* 2017.
[201] T. Lv, Z. Cheng, E. Zhang, H. Kang, Y. Liu, and L. Jiang, "Self-Restoration of Superhydrophobicity on Shape Memory Polymer Arrays with Both Crushed Microstructure and Damaged Surface Chemistry," *Small,* vol. 13, no. 4, p. 1503402, 2017.
[202] Y. Xiu, Y. Liu, D. W. Hess, and C. Wong, "Mechanically robust superhydrophobicity on hierarchically structured Si surfaces," *Nanotechnology,* vol. 21, no. 15, p. 155705, 2010.
[203] Y. Li, L. Li, and J. Sun, "Bioinspired Self-Healing Superhydrophobic Coatings," *Angewandte Chemie,* vol. 122, no. 35, pp. 6265-6269, 2010.
[204] X. Wang, X. Liu, F. Zhou, and W. Liu, "Self-healing superamphiphobicity," *Chemical Communications,* vol. 47, no. 8, pp. 2324-2326, 2011.
[205] Y. Li, L. Li, and J. Sun, "Bioinspired self-healing superhydrophobic coatings," *Angewandte Chemie International Edition,* vol. 49, no. 35, pp. 6129-6133, 2010.
[206] K. Golovin, M. Boban, J. M. Mabry, and A. Tuteja, "Designing self-healing superhydrophobic surfaces with exceptional mechanical durability," *ACS applied materials & interfaces,* vol. 9, no. 12, pp. 11212-11223, 2017.
[207] Z. Yan, X. Liang, Y. Gao, and Y. Liu, "Aging and self-healing properties of superhydrophobic silicone rubber," *IEEE Transactions on Dielectrics and Electrical Insulation,* vol. 23, no. 6, pp. 3531-3538, 2016.
[208] K. Tu, X. Wang, L. Kong, and H. Guan, "Facile preparation of mechanically durable, self-healing and multifunctional superhydrophobic surfaces on solid wood," *Materials Design,* vol. 140, pp. 30-36, 2018.
[209] X. Zhu *et al.*, "A novel superhydrophobic bulk material," *Journal of Materials Chemistry,* vol. 22, no. 38, pp. 20146-20148, 2012.
[210] B. Ge, Z. Zhang, X. Zhu, G. Ren, X. Men, and X. Zhou, "A magnetically superhydrophobic bulk material for oil removal," *Colloids and Surfaces A: Physicochemical and Engineering Aspects* vol. 429, pp. 129-133, 2013.
[211] O. C. Aktas *et al.*, "Superhydrophobic 3D Porous PTFE/TiO2 Hybrid Structures," *Advanced Materials Interfaces,* vol. 6, no. 4, p. 1801967, 2019.
[212] S. Ramakrishna, K. S. Kumar, D. Mathew, and C. R. Nair, "A robust, melting class bulk superhydrophobic material with heat-healing and self-cleaning properties," *Scientific reports,* vol. 5, p. 18510, 2015.
[213] Z. Cai, L. Shen, X. Wang, and Q. Guo, "Fabrication of a bulk superhydrophobic conductive material by mechanical abrasion," *Composites Science Technology,* vol. 164, pp. 238-247, 2018.
[214] X. Zhang *et al.*, "Super-durable, non-fluorinated superhydrophobic free-standing items," *Journal of Materials Chemistry A,* vol. 6, no. 2, pp. 357-362, 2018.
[215] K. Maghsoudi, G. Momen, R. Jafari, and M. Farzaneh, "Rigorous testing to assess the self-cleaning properties of an ultra-water-repellent silicone rubber surface," *Surface and Coatings Technology,* vol. 374, pp. 557-568, 2019.
[216] X. Zhang, L. Wang, and E. Levänen, "Superhydrophobic surfaces for the reduction of bacterial adhesion," *RSC Advances,* vol. 3, no. 30, pp. 12003-12020, 2013.
[217] V. A. Ganesh, H. K. Raut, A. S. Nair, and S. Ramakrishna, "A review on self-cleaning coatings," *Journal of Materials Chemistry,* vol. 21, no. 41, pp. 16304-16322, 2011.
[218] S. Das, S. Kumar, S. K. Samal, S. Mohanty, and S. K. Nayak, "A review on superhydrophobic polymer nanocoatings: recent development and applications," *Industrial Engineering Chemistry Research,* vol. 57, no. 8, pp. 2727-2745, 2018.

[219] X. Liu, K. Wang, W. Zhang, J. Zhang, and J. Li, "Robust, self-cleaning, anti-fouling, superamphiphobic soy protein isolate composite films using spray-coating technique with fluorinated HNTs/SiO2," *Composites Part B: Engineering*, vol. 174, p. 107002, 2019.
[220] T. Heckenthaler, S. Sadhujan, Y. Morgenstern, P. Natarajan, M. Bashouti, and Y. Kaufman, "Self-Cleaning Mechanism: Why Nanotexture and Hydrophobicity Matter," *Langmuir*, vol. 35, no. 48, pp. 15526-15534, 2019.
[221] M. Yu, S. Chen, B. Zhang, D. Qiu, and S. Cui, "Why a lotus-like superhydrophobic surface is self-cleaning? An explanation from surface force measurements and analysis," *Langmuir*, vol. 30, no. 45, pp. 13615-13621, 2014.
[222] R. Fürstner, W. Barthlott, C. Neinhuis, and P. Walzel, "Wetting and self-cleaning properties of artificial superhydrophobic surfaces," *Langmuir*, vol. 21, no. 3, pp. 956-961, 2005.
[223] M. Nosonovsky and B. Bhushan, "Multiscale friction mechanisms and hierarchical surfaces in nano- and bio-tribology," *Materials Science Engineering: R: Reports*, vol. 58, no. 3-5, pp. 162-193, 2007.
[224] M. Nosonovsky and B. Bhushan, "Do hierarchical mechanisms of superhydrophobicity lead to self-organized criticality?," *Scripta Materialia*, vol. 59, no. 9, pp. 941-944, 2008.
[225] F. Geyer *et al.*, "When and how self-cleaning of superhydrophobic surfaces works," *Science Advances*, vol. 6, no. 3, p. eaaw9727, 2020.
[226] Y. T. Cheng, D. Rodak, C. Wong, and C. Hayden, "Effects of micro-and nano-structures on the self-cleaning behaviour of lotus leaves," *Nanotechnology*, vol. 17, no. 5, p. 1359, 2006.
[227] X. Huang *et al.*, "A survey of icephobic coatings and their potential use in a hybrid coating/active ice protection system for aerospace applications," *Progress in Aerospace Sciences*, vol. 105, pp. 74-97, 2019.
[228] X. Qiao, Z. Zhang, X. Jiang, Y. He, and X. J. E. F. A. Li, "Application of grey theory in pollution prediction on insulator surface in power systems," p. 104153, 2019.
[229] Y. Shen, X. Wu, J. Tao, C. Zhu, Y. Lai, and Z. Chen, "Icephobic materials: Fundamentals, performance evaluation, and applications," *Progress in Materials Science*, 2019.
[230] V. Hejazi, K. Sobolev, and M. Nosonovsky, "From superhydrophobicity to icephobicity: forces and interaction analysis," *Scientific reports*, vol. 3, p. 2194, 2013.
[231] W. Cui, Y. Jiang, K. Mielonen, and T. A. Pakkanen, "The verification of icephobic performance on biomimetic superhydrophobic surfaces and the effect of wettability and surface energy," *Applied Surface Science*, vol. 466, pp. 503-514, 2019.
[232] Y. Xu *et al.*, "Icephobic behaviors of superhydrophobic amorphous carbon nano-films synthesized from a flame process," *Journal of colloid and interface science*, vol. 552, pp. 613-621, 2019.
[233] T. Yu, S. Lu, W. Xu, and R. Boukherroub, "Preparation of superhydrophobic/superoleophilic copper coated titanium mesh with excellent ice-phobic and water-oil separation performance," *Applied Surface Science*, vol. 476, pp. 353-362, 2019.
[234] G. Momen, R. Jafari, and M. Farzaneh, "Ice repellency behaviour of superhydrophobic surfaces: Effects of atmospheric icing conditions and surface roughness," *Applied Surface Science*, vol. 349, pp. 211-218, 2015.
[235] X. Wu, S. Zheng, D. A. Bellido-Aguilar, V. V. Silberschmidt, and Z. Chen, "Transparent icephobic coatings using bio-based epoxy resin," *Materials & Design*, vol. 140, pp. 516-523, 2018.
[236] X. Wu, V. V. Silberschmidt, Z.-T. Hu, and Z. Chen, "When superhydrophobic coatings are icephobic: Role of surface topology," *Surface and Coatings Technology*, vol. 358, pp. 207-214, 2019.
[237] Y. Shen *et al.*, "Anti-icing performance of superhydrophobic texture surfaces depending on reference environments," *Advanced Materials Interfaces*, vol. 4, no. 22, p. 1700836, 2017.
[238] Y. He, C. Jiang, X. Cao, J. Chen, W. Tian, and W. Yuan, "Reducing ice adhesion by hierarchical micro-nano-pillars," *Applied surface science*, vol. 305, pp. 589-595, 2014.
[239] M. Montemor, "Functional and smart coatings for corrosion protection: a review of recent advances," *Surface and Coatings Technology*, vol. 258, pp. 17-37, 2014.
[240] G. Schmitt, "Global needs for knowledge dissemination, research, and development in materials deterioration and corrosion control," *World Corrosion Organization*, pp. 3-8, 2009.
[241] T. Zhang and D. Tang, "Current research status of corrosion resistant coatings," *Rec. Pat. Corros. Sci*, vol. 1, pp. 1-5, 2009.
[242] P. B. Raja and M. G. Sethuraman, "Natural products as corrosion inhibitor for metals in corrosive media—a review," *Materials Letters*, vol. 62, no. 1, pp. 113-116, 2008.

[243] Y.-L. Zhang, H. Xia, E. Kim, and H.-B. Sun, "Recent developments in superhydrophobic surfaces with unique structural and functional properties," *Soft Matter,* vol. 8, no. 44, pp. 11217-11231, 2012.
[244] D. Zhang, L. Wang, H. Qian, and X. Li, "Superhydrophobic surfaces for corrosion protection: a review of recent progresses and future directions," *Journal of Coatings Technology and Research,* vol. 13, no. 1, pp. 11-29, 2016.
[245] Y. Huang, *Protection of metal and alloy surfaces using corrosion resistance nanostructured superhydrophobic coatings*. Université du Québec à Chicoutimi, 2012.
[246] K. Ellinas, A. Tserepi, and E. Gogolides, "Durable superhydrophobic and superamphiphobic polymeric surfaces and their applications: A review," *Advances in colloid and interface science,* vol. 250, pp. 132-157, 2017.
[247] G. B. Darband, M. Aliofkhazraei, S. Khorsand, S. Sokhanvar, and A. Kaboli, "Science and engineering of superhydrophobic surfaces: review of corrosion resistance, chemical and mechanical stability," *Arabian Journal of Chemistry,* vol. 13, no. 1, pp. 1763-1802, 2020.
[248] S. P. Dalawai *et al.*, "Recent Advances in durability of superhydrophobic self-cleaning technology: A critical review," *Progress in Organic Coatings,* vol. 138, p. 105381, 2020.
[249] C.-F. Wang, W.-N. Wang, C.-H. Lin, K.-J. Lee, C.-C. Hu, and J.-Y. Lai, "Facile Fabrication of Durable Superhydrophobic Films from Carbon Nanotube/Main-Chain Type Polybenzoxazine Composites," *Polymers,* vol. 11, no. 7, p. 1183, 2019.
[250] A. Milionis, R. Ruffilli, and I. S. Bayer, "Superhydrophobic nanocomposites from biodegradable thermoplastic starch composites (Mater-Bi®), hydrophobic nano-silica and lycopodium spores," *RSC Advances,* vol. 4, no. 65, pp. 34395-34404, 2014.
[251] M. Long *et al.*, "A robust superhydrophobic PDMS@ ZnSn (OH) 6 coating with under-oil self-cleaning and flame retardancy," *Journal of Materials Chemistry A,* vol. 5, no. 43, pp. 22761-22771, 2017.
[252] F. Wang, S. Yu, J. Ou, M. Xue, and W. Li, "Mechanically durable superhydrophobic surfaces prepared by abrading," *Journal of Applied Physics,* vol. 114, no. 12, p. 124902, 2013.
[253] A. Milionis, E. Loth, and I. S. Bayer, "Recent advances in the mechanical durability of superhydrophobic materials," *Advances in Colloid and Interface Science,* vol. 229, pp. 57-79, 2016.
[254] X. Deng *et al.*, "Transparent, thermally stable and mechanically robust superhydrophobic surfaces made from porous silica capsules," *Advanced materials,* vol. 23, no. 26, pp. 2962-2965, 2011.
[255] A. Steele, I. Bayer, and E. Loth, "Adhesion strength and superhydrophobicity of polyurethane/organoclay nanocomposite coatings," *Journal of Applied Polymer Science,* vol. 125, no. S1, pp. E445-E452, 2012.
[256] L. Boinovich and A. Emelyanenko, "The behaviour of fluoro-and hydrocarbon surfactants used for fabrication of superhydrophobic coatings at solid/water interface," *Colloids and Surfaces A: Physicochemical and Engineering Aspects,* vol. 481, pp. 167-175, 2015.
[257] Y. Wang, Y. Liu, L. Zhang, M. Zhang, G. He, and Z. Sun, "Facile fabrication of a low adhesion, stable and superhydrophobic filter paper modified with ZnO microclusters," *Applied Surface Science,* vol. 496, p. 143743, 2019.
[258] S. Xu, Q. Wang, N. Wang, and X. Zheng, "Fabrication of superhydrophobic green surfaces with good self-cleaning, chemical stability and anti-corrosion properties," *Journal of Materials Science,* vol. 54, no. 19, pp. 13006-13016, 2019.
[259] S. K. Pandit, B. K. Tudu, I. M. Mishra, and A. Kumar, "Development of stain resistant, superhydrophobic and self-cleaning coating on wood surface," *Progress in Organic Coatings,* vol. 139, p. 105453, 2020.
[260] S. Jia *et al.*, "One-step approach to prepare superhydrophobic wood with enhanced mechanical and chemical durability: Driving of alkali," *Applied Surface Science,* vol. 455, pp. 115-122, 2018.
[261] G. Gong *et al.*, "A highly durable silica/polyimide superhydrophobic nanocomposite film with excellent thermal stability and abrasion-resistant performance," *Journal of Materials Chemistry A,* vol. 3, no. 2, pp. 713-718, 2015.
[262] K. Maghsoudi, R. Jafari, G. Momen, and M. Farzaneh, "Micro-nanostructured polymer surfaces using injection molding: A review," *Materials today communications,* vol. 13, pp. 126-143, 2017.
[263] W.-T. Cao, Y.-J. Liu, M.-G. Ma, and J.-F. Zhu, "Facile preparation of robust and superhydrophobic materials for self-cleaning and oil/water separation," *Colloids and Surfaces A: Physicochemical and Engineering Aspects,* vol. 529, pp. 18-25, 2017.

[264] Y. Tuo, W. Chen, H. Zhang, P. Li, and X. Liu, "One-step hydrothermal method to fabricate drag reduction superhydrophobic surface on aluminum foil," *Applied Surface Science*, vol. 446, pp. 230-235, 2018.
[265] R. Jafari, G. Momen, and E. Eslami, "Fabrication of icephobic aluminium surfaces by atmospheric plasma jet polymerisation," *Surface Engineering*, pp. 1-6, 2018.
[266] L. F. Mobarakeh, R. Jafari, and M. Farzaneh, "Robust icephobic, and anticorrosive plasma polymer coating," *Cold Regions Science and Technology*, vol. 151, pp. 89-93, 2018.
[267] Y. Zhao, C. Xing, Z. Zhang, and L. Yu, "Superhydrophobic polyaniline/polystyrene micro/nanostructures as anticorrosion coatings," *Reactive Functional Polymers*, vol. 119, pp. 95-104, 2017.
[268] T. Ning, G. Yang, W. Zhao, and X. Liu, "One-pot solvothermal synthesis of robust ambient-dried polyimide aerogels with morphology-enhanced superhydrophobicity for highly efficient continuous oil/water separation," *Reactive Functional Polymers*, vol. 116, pp. 17-23, 2017.
[269] S. Wang *et al.*, "Icephobicity of penguins spheniscus humboldti and an artificial replica of penguin feather with air-infused hierarchical rough structures," *The Journal of Physical Chemistry C*, vol. 120, no. 29, pp. 15923-15929, 2016.
[270] T. Young, "III. An essay on the cohesion of fluids," *Philosophical transactions of the royal society of London*, vol. 95, pp. 65-87, 1805.
[271] A. Eifert, D. Paulssen, S. N. Varanakkottu, T. Baier, and S. Hardt, "Simple fabrication of robust water-repellent surfaces with low contact-angle hysteresis based on impregnation," *Advanced Materials Interfaces*, vol. 1, no. 3, p. 1300138, 2014.
[272] A. Kumar *et al.*, "Development of macroporous silicone rubber for acoustic applications," *Industrial & Engineering Chemistry Research*, vol. 55, no. 32, pp. 8751-8760, 2016.
[273] N. Gupta, S. Sasikala, and H. C. Barshilia, "Corrosion study of superhydrophobic magnesium alloy AZ31 surfaces prepared by wet chemical etching process," *Nanoscience and Nanotechnology letters*, vol. 4, no. 8, pp. 757-765, 2012.
[274] X. Xiao, W. Xie, and Z. Ye, "Preparation of corrosion-resisting superhydrophobic surface on aluminium substrate," *Surface Engineering*, pp. 1-7, 2018.
[275] K. Maghsoudi, G. Momen, R. Jafari, M. Farzaneh, and T. Carreira, "Micro-Nanostructured Silicone Rubber Surfaces Using Compression Molding," in *Materials Science Forum*, 2018, vol. 941, pp. 1802-1807: Trans Tech Publ.
[276] R. Jafari, G. Momen, and M. Farzaneh, "Durability enhancement of icephobic fluoropolymer film," *Journal of Coatings Technology Research*, vol. 13, no. 3, pp. 405-412, 2016.
[277] H. S. Salapare III, B. A. T. Suarez, H. S. O. Cosiñero, M. Y. Bacaoco, and H. J. Ramos, "Irradiation of poly (tetrafluoroethylene) surfaces by CF4 plasma to achieve robust superhydrophobic and enhanced oleophilic properties for biological applications," *Materials Science and Engineering: C*, vol. 46, pp. 270-275, 2015.
[278] W. Somrang, S. Denchitcharoen, P. Eiamchai, M. Horprathum, and C. Chananonnawathorn, "Superhydrophobic and antireflective surface of nanostructures fabricated by CF 4 plasma etching," *Materials Today: Proceedings*, vol. 5, no. 6, pp. 13879-13885, 2018.
[279] L. Feng, H. Zhang, Z. Wang, and Y. Liu, "Superhydrophobic aluminum alloy surface: fabrication, structure, and corrosion resistance," *Colloids and Surfaces A: Physicochemical and Engineering Aspects*, vol. 441, pp. 319-325, 2014.
[280] L. Liu, F. Xu, and L. Ma, "Facile fabrication of a superhydrophobic Cu surface via a selective etching of high-energy facets," *The Journal of Physical Chemistry C*, vol. 116, no. 35, pp. 18722-18727, 2012.
[281] M. I. Kayes, A. J. Galante, N. A. Stella, S. Haghanifar, R. M. Shanks, and P. W. Leu, "Stable lotus leaf-inspired hierarchical, fluorinated polypropylene surfaces for reduced bacterial adhesion," *Reactive Functional Polymers*, vol. 128, pp. 40-46, 2018.
[282] B. K. Lee *et al.*, "Fabrication of a Large-Area Hierarchical Structure Array by Combining Replica Molding and Atmospheric Pressure Plasma Etching," *Advanced Materials Interfaces*, vol. 2, no. 11, p. 1500141, 2015.
[283] P. Dimitrakellis and E. Gogolides, "Hydrophobic and superhydrophobic surfaces fabricated using atmospheric pressure cold plasma technology: A review," *Advances in colloid and interface science*, 2018.

[284] H. S. Salapare III, F. Guittard, X. Noblin, E. T. de Givenchy, F. Celestini, and H. J. Ramos, "Stability of the hydrophilic and superhydrophobic properties of oxygen plasma-treated poly (tetrafluoroethylene) surfaces," *Journal of colloid interface science,* vol. 396, pp. 287-292, 2013.
[285] S.-H. Gao, M.-K. Lei, Y. Liu, and L.-S. Wen, "CF4 radio frequency plasma surface modification of silicone rubber for use as outdoor insulations," *Applied Surface Science,* vol. 255, no. 11, pp. 6017-6023, 2009.
[286] Z. Vaseghi, O. Tavakoli, and A. Nematollahzadeh, "Rapid biosynthesis of novel Cu/Cr/Ni trimetallic oxide nanoparticles with antimicrobial activity," *Journal of Environmental Chemical Engineering,* vol. 6, no. 2, pp. 1898-1911, 2018.
[287] S. B. Patel and J. V. Gohel, "Enhanced solar cell performance by optimization of spray coated CZTS thin film using Taguchi and response surface method," *Journal of Materials Science: Materials in Electronics,* vol. 29, no. 7, pp. 5613-5623, 2018.
[288] L. Chen, Z. Liu, P. Sun, and W. Huo, "Formulation of a fuel spray SMD model at atmospheric pressure using Design of Experiments (DoE)," *Fuel,* vol. 153, pp. 355-360, 2015.
[289] D. Mei, Y. L. He, S. Liu, J. Yan, and X. Tu, "Optimization of CO2 conversion in a cylindrical dielectric barrier discharge reactor using design of experiments," *Plasma Processes and Polymers,* vol. 13, no. 5, pp. 544-556, 2016.
[290] P. Chen, *Molecular interfacial phenomena of polymers and biopolymers*. Taylor & Francis US, 2005.
[291] K. Grundke *et al.*, "Experimental studies of contact angle hysteresis phenomena on polymer surfaces—Toward the understanding and control of wettability for different applications," *Advances in colloid and interface science,* vol. 222, pp. 350-376, 2015.
[292] J. Zhang, B. Li, B. Wang, and S. Dong, "Analysis on formation mechanism of ultra-smooth surfaces in atmospheric pressure plasma polishing," *The International Journal of Advanced Manufacturing Technology,* vol. 65, no. 9-12, pp. 1239-1245, 2013.
[293] K. Nojiri, "Mechanism of dry etching," in *Dry Etching Technology for Semiconductors*: Springer, 2015, pp. 11-30.
[294] A. del Campo, A. Nogales, T. A. Ezquerra, and J. Rodríguez-Hernández, "Modification of poly (dimethylsiloxane) as a basis for surface wrinkle formation: Chemical and mechanical characterization," *Polymer,* vol. 98, pp. 327-335, 2016.
[295] N. Encinas, R. Dillingham, B. Oakley, J. Abenojar, M. Martínez, and M. Pantoja, "Atmospheric pressure plasma hydrophilic modification of a silicone surface," *The Journal of Adhesion,* vol. 88, no. 4-6, pp. 321-336, 2012.
[296] M. T. Nazir, B. Phung, and M. Hoffman, "Performance of silicone rubber composites with SiO 2 micro/nano-filler under AC corona discharge," *IEEE Transactions on Dielectrics and Electrical Insulation,* vol. 23, no. 5, pp. 2804-2815, 2016.
[297] L. Chen *et al.*, "High-Performance Triphase Bio-Photoelectrochemical Assay System Based on Superhydrophobic Substrate-Supported TiO2 Nanowire Arrays," *Advanced Functional Materials,* p. 1801483, 2018.
[298] X. J. Huang, J. H. Lee, J. W. Lee, J. B. Yoon, and Y. K. Choi, "A One-Step Route to a Perfectly Ordered Wafer-Scale Microbowl Array for Size-Dependent Superhydrophobicity," *Small,* vol. 4, no. 2, pp. 211-216, 2008.
[299] S. Peng, D. Tian, X. Miao, X. Yang, and W. Deng, "Designing robust alumina nanowires-on-nanopores structures: Superhydrophobic surfaces with slippery or sticky water adhesion," *Journal of colloid interface science,* vol. 409, pp. 18-24, 2013.
[300] Y. Wang, J. Xue, Q. Wang, Q. Chen, and J. Ding, "Verification of icephobic/anti-icing properties of a superhydrophobic surface," *ACS applied materials interfaces,* vol. 5, no. 8, pp. 3370-3381, 2013.
[301] P. B. Weisensee, J. Tian, N. Miljkovic, and W. P. King, "Water droplet impact on elastic superhydrophobic surfaces," *Scientific reports,* vol. 6, p. 30328, 2016.
[302] B. Ding, H. Wang, X. Zhu, R. Chen, and Q. Liao, "How supercooled superhydrophobic surfaces affect dynamic behaviors of impacting water droplets?," *International Journal of Heat Mass Transfer,* vol. 124, pp. 1025-1032, 2018.
[303] C. Guo, D. Zhao, Y. Sun, M. Wang, and Y. Liu, "Droplet Impact on Anisotropic Superhydrophobic Surfaces," *Langmuir,* vol. 34, no. 11, pp. 3533-3540, 2018.
[304] S. Li *et al.*, "Efficiently texturing hierarchical superhydrophobic fluoride-free translucent films by AACVD with excellent durability and self-cleaning ability," *Journal of Materials Chemistry A,* vol. 6, no. 36, pp. 17633-17641, 2018.

[305] S. Nishimoto and B. Bhushan, "Bioinspired self-cleaning surfaces with superhydrophobicity, superoleophobicity, and superhydrophilicity," *Rsc Advances*, vol. 3, no. 3, pp. 671-690, 2013.
[306] K. Maghsoudi, G. Momen, R. Jafari, and M. Farzaneh, "Rigorous testing to assess the self-cleaning properties of an ultra-water-repellent silicone rubber surface," *Surf. Coat. Tech.*, vol. 374, pp. 557-568, 2019.
[307] K. Maghsoudi, E. Vazirinasab, G. Momen, and R. Jafari, "Advances in the fabrication of superhydrophobic polymeric surfaces by polymer molding processes," *Ind. Eng. Chem. Res.*, 2020.
[308] E. Vazirinasab, R. Jafari, and G. Momen, "Evaluation of atmospheric-pressure plasma parameters to achieve superhydrophobic and self-cleaning HTV silicone rubber surfaces via a single-step, eco-friendly approach," *Surf. Coat. Tech.*, vol. 375, pp. 100-111, 2019.
[309] E. Vazirinasab, R. Jafari, and G. Momen, "Application of superhydrophobic coatings as a corrosion barrier: A review," *Surf. Coat. Tech.*, vol. 341, pp. 40-56, 2018.
[310] L. Huang, L. Zhang, J. Song, X. Wang, and H. Liu, "Superhydrophobic Nickel-Electroplated Carbon Fibers for Versatile Oil/Water Separation with Excellent Reusability and High Environmental Stability," *ACS Appl. Mater. Inter.*, vol. 12, no. 21, pp. 24390-24402, 2020.
[311] D. Yuan, T. Zhang, Q. Guo, F. Qiu, D. Yang, and Z. Ou, "Recyclable biomass carbon@ SiO2@ MnO2 aerogel with hierarchical structures for fast and selective oil-water separation," *Chem. Eng. J.*, vol. 351, pp. 622-630, 2018.
[312] J. Li *et al.*, "Rectification of mobile Leidenfrost droplets by planar ratchets," *Small*, vol. 16, no. 9, p. 1901751, 2020.
[313] A. Alizadeh *et al.*, "Dynamics of ice nucleation on water repellent surfaces," *Langmuir*, vol. 28, no. 6, pp. 3180-3186, 2012.
[314] G. Momen and M. Farzaneh, "Facile approach in the development of icephobic hierarchically textured coatings as corrosion barrier," *Applied Surface Science*, vol. 299, pp. 41-46, 2014.
[315] A. A. Yancheshme, G. Momen, and R. J. Aminabadi, "Mechanisms of ice formation and propagation on superhydrophobic surfaces: A review," *Adv. Colloid Interface Sci.*, p. 102155, 2020.
[316] Y. Shen, H. Tao, S. Chen, L. Zhu, T. Wang, and J. Tao, "Icephobic/anti-icing potential of superhydrophobic Ti6Al4V surfaces with hierarchical textures," *RSC Adv.*, vol. 5, no. 3, pp. 1666-1672, 2015.
[317] P. Eberle, M. K. Tiwari, T. Maitra, and D. Poulikakos, "Rational nanostructuring of surfaces for extraordinary icephobicity," *Nanoscale*, vol. 6, no. 9, pp. 4874-4881, 2014.
[318] Y. Yao, C. Li, H. Zhang, and R. Yang, "Modelling the impact, spreading and freezing of a water droplet on horizontal and inclined superhydrophobic cooled surfaces," *Appl. Surf. Sci.*, vol. 419, pp. 52-62, 2017.
[319] E. J. Y. Ling, V. Uong, J.-S. b. Renault-Crispo, A.-M. Kietzig, and P. Servio, "Reducing ice adhesion on nonsmooth metallic surfaces: wettability and topography effects," *ACS Appl. Mater. Interfaces*, vol. 8, no. 13, pp. 8789-8800, 2016.
[320] C. E. Cansoy, H. Y. Erbil, O. Akar, and T. Akin, "Effect of pattern size and geometry on the use of Cassie–Baxter equation for superhydrophobic surfaces," *Colloids Surf., A*, vol. 386, no. 1-3, pp. 116-124, 2011.
[321] Q. Li and Z. Guo, "Fundamentals of icing and common strategies for designing biomimetic anti-icing surfaces," *J. Mater. Chem. A*, vol. 6, no. 28, pp. 13549-13581, 2018.
[322] Y. He, C. Jiang, X. Cao, J. Chen, W. Tian, and W. Yuan, "Reducing ice adhesion by hierarchical micro-nano-pillars," *Appl. Surf. Sci.*, vol. 305, pp. 589-595, 2014.
[323] C. C. Ryerson, "Ice protection of offshore platforms," *Cold Reg. Sci. Technol.*, vol. 65, no. 1, pp. 97-110, 2011.
[324] C. Stenroos, "Properties of icephobic surfaces in different icing conditions," 2015.
[325] Y. Liu *et al.*, "Study of the effect of ice adhesion on electrical power transmission insulator," *J. Adhes. Sci. Technol.*, vol. 26, no. 4-5, pp. 593-602, 2012.
[326] G. Fortin and J. Perron, "Ice adhesion models to predict shear stress at shedding," *J. Adhes. Sci. Technol.*, vol. 26, no. 4-5, pp. 523-553, 2012.
[327] A. Work and Y. Lian, "A critical review of the measurement of ice adhesion to solid substrates," *Prog. Aerosp. Sci.*, vol. 98, pp. 1-26, 2018.
[328] S. Rønneberg, J. He, and Z. Zhang, "The need for standards in low ice adhesion surface research: a critical review," *J. Adhes. Sci. Technol.*, vol. 34, no. 3, pp. 319-347, 2020.

[329] K. Golovin, M. Boban, J. M. Mabry, and A. Tuteja, "Designing Self-Healing Superhydrophobic Surfaces with Exceptional Mechanical Durability," *ACS Appl. Mater. Interfaces,* vol. 9, no. 12, pp. 11212-11223, 2017.
[330] A. Milionis, E. Loth, and I. S. Bayer, "Recent advances in the mechanical durability of superhydrophobic materials," *Adv. Colloid Interface Sci.,* vol. 229, pp. 57-79, 2016.
[331] R. Jafari, G. Momen, and M. Farzaneh, "Durability enhancement of icephobic fluoropolymer film," *J. Coat. Technol. Res.,* vol. 13, no. 3, pp. 405-412, 2016.
[332] G. Momen, R. Jafari, and M. Farzaneh, "Ice repellency behaviour of superhydrophobic surfaces: Effects of atmospheric icing conditions and surface roughness," *Appl. Surf. Sci.,* vol. 349, pp. 211-218, 2015.
[333] L. F. Mobarakeh, R. Jafari, and M. Farzaneh, "Robust icephobic, and anticorrosive plasma polymer coating," *Cold Reg. Sci. Technol.,* vol. 151, pp. 89-93, 2018.
[334] Z. Ghalmi and M. Farzaneh, "Experimental investigation to evaluate the effect of PTFE nanostructured roughness on ice adhesion strength," *Cold Reg. Sci. Technol.,* vol. 115, pp. 42-47, 2015.
[335] A. Lazauskas *et al.*, "Water droplet behavior on superhydrophobic SiO2 nanocomposite films during icing/deicing cycles," *Mater. Charact.,* vol. 82, pp. 9-16, 2013.
[336] Z. Yan, X. Liang, C. Wu, W. Bao, S. Li, and Y. Liu, "Aging and recovery of superhydrophobic silicone rubber under electrical and non-electrical stresses," in *IEEE Conference on Electrical Insulation and Dielectric Phenomena (CEIDP)*, 2015, pp. 189-192: IEEE.
[337] H. Hillborg, M. Sandelin, and U. W. Gedde, "Hydrophobic recovery of polydimethylsiloxane after exposure to partial discharges as a function of crosslink density," *Polymer,* vol. 42, no. 17, pp. 7349-7362, 2001.
[338] H. Liu, G. A. Cash, R. D. Sovar, G. A. George, and D. Birtwhistle, "Studies of the diffusion of low molecular weight silicone fluids on polluted hv silicone insulators. I. use of diffuse reflectance FTIR," *IEEE Transactions on Dielectrics Electrical Insulation,* vol. 13, no. 4, pp. 877-884, 2006.
[339] C. Sansom, P. Comley, P. King, H. Almond, C. Atkinson, and E. Endaya, "Predicting the effects of sand erosion on collector surfaces in CSP plants," *Energy Procedia,* vol. 69, pp. 198-207, 2015.
[340] M. Qiang, F. Chen, A. Zhou, S. Xiao, J. Zhang, and Z. Wang, "Impacts of wind velocity on sand and dust deposition during dust storm as inferred from a series of observations in the northeastern Qinghai–Tibetan Plateau, China," *Powder Technology,* vol. 175, no. 2, pp. 82-89, 2007.
[341] E. Vazirinasab, K. Maghsoudi, R. Jafari, and G. Momen, "A comparative study of the icephobic and self-cleaning properties of Teflon materials having different surface morphologies," *J. Mater. Process. Technol.,* vol. 276, p. 116415, 2020.
[342] H. Zhang, Y. Tu, Y. Lu, Z. Xu, C. Chen, and L. Xie, "Study on aging characteristics of silicone rubber insulator sheds using FTIR," in *2012 IEEE International Symposium on Electrical Insulation*, 2012, pp. 83-86: IEEE.
[343] K. R. Khedir *et al.*, "Advanced studies of water evaporation kinetics over teflon-coated tungsten nanorod surfaces with variable hydrophobicity and morphology," *The Journal of Physical Chemistry C,* vol. 115, no. 28, pp. 13804-13812, 2011.
[344] D. Chu, A. Nemoto, and H. Ito, "Enhancement of dynamic wetting properties by direct fabrication on robust micro–micro hierarchical polymer surfaces," *Applied Surface Science,* vol. 300, pp. 117-123, 2014.
[345] S. Dash and S. V. Garimella, "Droplet evaporation dynamics on a superhydrophobic surface with negligible hysteresis," *Langmuir,* vol. 29, no. 34, pp. 10785-10795, 2013.
[346] X. Huang *et al.*, "A survey of icephobic coatings and their potential use in a hybrid coating/active ice protection system for aerospace applications," *Progress in Aerospace Sciences,* 2019.
[347] M. Rahimi, A. Afshari, and E. Thormann, "Effect of aluminum substrate surface modification on wettability and freezing delay of water droplet at subzero temperatures," *ACS Applied Materials & Interfaces,* vol. 8, no. 17, pp. 11147-11153, 2016.
[348] F. Behroozi and P. Behroozi, "Determination of surface tension from the measurement of internal pressure of mini soap bubbles," *American Journal of Physics,* vol. 79, no. 11, pp. 1089-1093, 2011.
[349] G. Heydari, E. Thormann, M. Järn, E. Tyrode, and P. M. Claesson, "Hydrophobic surfaces: topography effects on wetting by supercooled water and freezing delay," *The Journal of Physical Chemistry C,* vol. 117, no. 42, pp. 21752-21762, 2013.

[350] M. Zou, S. Beckford, R. Wei, C. Ellis, G. Hatton, and M. Miller, "Effects of surface roughness and energy on ice adhesion strength," *Applied Surface Science,* vol. 257, no. 8, pp. 3786-3792, 2011.
[351] A. Davis, Y. H. Yeong, A. Steele, I. S. Bayer, and E. Loth, "Superhydrophobic nanocomposite surface topography and ice adhesion," *ACS Applied Materials & Interfaces,* vol. 6, no. 12, pp. 9272-9279, 2014.
[352] J. Guo, H. Qian, P. Liu, and J. Ma, "Fabrication of durability superhydrophobic LDH coating on zinc sheet surface via NH4F-assisted in-situ growth and post-modification for enhancing anti-corrosion and anti-icing," *Applied Clay Science,* vol. 180, p. 105182, 2019.
[353] J.-H. Zhi, L.-Z. Zhang, Y. Yan, and J. Zhu, "Mechanical durability of superhydrophobic surfaces: The role of surface modification technologies," *Applied Surface Science,* vol. 392, pp. 286-296, 2017.
[354] G. Ren *et al.*, "A simple way to an ultra-robust superhydrophobic fabric with mechanical stability, UV durability, and UV shielding property," *Journal of Colloid and Interface Science,* vol. 522, pp. 57-62, 2018.
[355] N. Wang, D. Xiong, Y. Deng, Y. Shi, and K. Wang, "Mechanically robust superhydrophobic steel surface with anti-icing, UV-durability, and corrosion resistance properties," *ACS Applied Materials & Interfaces,* vol. 7, no. 11, pp. 6260-6272, 2015.
[356] J. H. van Boxel, "Numerical model for the fall speed of rain drops in a rain fall simulator," in *Workshop on wind and water erosion*, 1997, pp. 77-85.
[357] P. Papadopoulos, B.-E. Pinchasik, M. Tress, D. Vollmer, M. Kappl, and H.-J. J. Butt, "Wetting of soft superhydrophobic micropillar arrays," *Soft Matter,* vol. 14, no. 36, pp. 7429-7434, 2018.
[358] Z. Wang *et al.*, "Effect of aluminum hydroxide on low-molecular-weight siloxane distribution and microstructure of high-temperature vulcanized silicone rubber," *Journal of Applied Polymer Science,* vol. 135, no. 6, p. 45803, 2018.
[359] H. Kim and S. H. Kim, "Nonwettable hierarchical structure effect on droplet impact and spreading dynamics," *Langmuir,* vol. 34, no. 19, pp. 5480-5486, 2018.
[360] E. Vazirinasab, R. Jafari, and G. Momen, "Wetting and Self-Cleaning Properties of Silicone Rubber Surfaces Treated by Atmospheric Plasma Jet," in *2018 IEEE Conference on Electrical Insulation and Dielectric Phenomena (CEIDP)*, 2018, pp. 239-242: IEEE.
[361] W. Tong, D. Xiong, N. Wang, Z. Wu, and H. Zhou, "Mechanically robust superhydrophobic coating for aeronautical composite against ice accretion and ice adhesion," *Composites Part B: Engineering,* vol. 176, p. 107267, 2019.
[362] E. Vazirinasab, R. Jafari, and G. Momen, "Application of superhydrophobic coatings as a corrosion barrier: A review," *Surface and Coatings Technology,* vol. 341, pp. 40-56, 2018.
[363] S. He *et al.*, "Gravity-driven and high flux super-hydrophobic/super-oleophilic poly (arylene ether nitrile) nanofibrous composite membranes for efficient water-in-oil emulsions separation in harsh environments," *Composites Part B: Engineering,* vol. 177, p. 107439, 2019.
[364] Y. Liu *et al.*, "Design and preparation of biomimetic polydimethylsiloxane (PDMS) films with superhydrophobic, self-healing and drag reduction properties via replication of shark skin and SI-ATRP," *Chemical Engineering Journal,* vol. 356, pp. 318-328, 2019.
[365] J. Dong, X. Ouyang, J. Han, W. Qiu, and W. Gao, "Superhydrophobic surface of TiO2 hierarchical nanostructures fabricated by Ti anodization," *Journal of colloid and interface science,* vol. 420, pp. 97-100, 2014.
[366] Y. Li *et al.*, "Fast preparation of mechanically stable superhydrophobic surface by UV cross-linking of coating onto oxygen-inhibited layer of substrate," *Chemical Engineering Journal,* vol. 338, pp. 440-449, 2018.
[367] E. Vazirinasab, R. Jafari, and G. Momen, "Evaluation of atmospheric-pressure plasma parameters to achieve superhydrophobic and self-cleaning HTV silicone rubber surfaces via a single-step, eco-friendly approach," *Surface and Coatings Technology,* 2019.
[368] H. Alamri *et al.*, "Self-cleaning superhydrophobic epoxy coating based on fibrous silica-coated iron oxide magnetic nanoparticles," *Journal of colloid interface science,* vol. 513, pp. 349-356, 2018.
[369] R. Jafari, C. Cloutier, A. Allahdini, and G. Momen, "Recent progress and challenges with 3D printing of patterned hydrophobic and superhydrophobic surfaces," *The International Journal of Advanced Manufacturing Technology,* pp. 1-14, 2019.
[370] K. Maghsoudi, G. Momen, R. Jafari, M. Farzaneh, and T. Carreira, "Micro-Nanostructured Silicone Surfaces for Highvoltage Application," in *2018 IEEE Conference on Electrical Insulation and Dielectric Phenomena (CEIDP)*, 2018, pp. 179-182: IEEE.

[371] H. Zhou, H. Wang, H. Niu, A. Gestos, X. Wang, and T. Lin, "Fluoroalkyl silane modified silicone rubber/nanoparticle composite: a super durable, robust superhydrophobic fabric coating," *Advanced materials*, vol. 24, no. 18, pp. 2409-2412, 2012.
[372] A. Bezdomnikov, A. Emel'yanenko, K. Emel'yanenko, and L. Boinovich, "Delay in the Freezing of Supercooled Water Drops on Superhydrophobic Surfaces of Silicone Rubber at Negative Temperatures," *Russian Journal of Physical Chemistry A*, vol. 92, no. 1, pp. 178-184, 2018.
[373] H. Ye *et al.*, "Robust and Durable Self-Healing Superhydrophobic Polymer-Coated MWCNT Film for Highly Efficient Emulsion Separation," *Environmental Science: Nano*, 2019.
[374] M. Yu, Z. Cui, F. Ge, C. Man, L. Lei, and X. Wang, "Fabrication of durable and roughness-regeneration superhydrophobic composite materials by hot pressing," *Composites Part B: Engineering*, vol. 179, p. 107431, 2019.
[375] A. Ijaz, A. Miko, and A. Demirel, "Anti-icing agent releasing diatomaceous earth/SBS composites," *New Journal of Chemistry*, vol. 42, no. 11, pp. 8544-8552, 2018.
[376] H. J. Perera, H. Mortazavian, and F. D. Blum, "Surface Properties of Silane-Treated Diatomaceous Earth Coatings: Effect of Alkyl Chain Length," *Langmuir*, vol. 33, no. 11, pp. 2799-2809, 2017.
[377] M. J. Nine, M. A. Cole, L. Johnson, D. N. Tran, and D. Losic, "Robust superhydrophobic graphene-based composite coatings with self-cleaning and corrosion barrier properties," *ACS applied materials and interfaces*, vol. 7, no. 51, pp. 28482-28493, 2015.
[378] G. Polizos *et al.*, "Scalable superhydrophobic coatings based on fluorinated diatomaceous earth: Abrasion resistance versus particle geometry," *Applied Surface Science*, vol. 292, pp. 563-569, 2014.
[379] H. J. Perera, B. K. Khatiwada, A. Paul, H. Mortazavian, and F. D. Blum, "Superhydrophobic surfaces with silane-treated diatomaceous earth/resin systems," *Journal of Applied Polymer Science*, vol. 133, no. 41, 2016.
[380] H. Zhang, H. Yang, B. Shentu, S. Chen, and M. Chen, "Effect of titanium dioxide on the UV-C ageing behavior of silicone rubber," *Journal of Applied Polymer Science*, vol. 135, no. 14, 2018.
[381] P. J. Flory and J. Rehner Jr, "Statistical mechanics of cross-linked polymer networks I. Rubberlike elasticity," *The journal of chemical physics*, vol. 11, no. 11, pp. 512-520, 1943.
[382] V. Silva, M. Paschoalino, M. Gonçalves, M. Felisberti, W. Jardim, and I. Yoshida, "Silicone rubbers filled with TiO2: Characterization and photocatalytic activity," *Materials Chemistry and Physics*, vol. 113, no. 1, pp. 395-400, 2009.
[383] S. Diao, K. Jin, Z. Yang, H. Lu, S. Feng, and C. Zhang, "The effect of phenyl modified fumed silica on radiation resistance of silicone rubber," *Materials Chemistry and Physics*, vol. 129, no. 1-2, pp. 202-208, 2011.
[384] O. Zabihi, M. Aghaie, and K. Zare, "Study on a novel thermoset nanocomposite form DGEBA–cycloaliphatic diamine and metal nanoparticles," *Journal of thermal analysis and calorimetry*, vol. 111, no. 1, pp. 703-710, 2013.
[385] A. Olad, H. Zebhi, D. Salari, A. Mirmohseni, and A. Reyhanitabar, "Synthesis, characterization, and swelling kinetic study of porous superabsorbent hydrogel nanocomposite based on sulfonated carboxymethylcellulose and silica nanoparticles," *Journal of Porous Materials*, vol. 25, no. 5, pp. 1325-1335, 2018.
[386] N. D. Bansod and C. Das, "Studies on mechanical, rheological, thermal and morphological properties of in situ silica-filled butadiene rubber composites," *Plastics, Rubber and Composites*, vol. 47, no. 8, pp. 345-351, 2018.
[387] Y. Tong *et al.*, "Effect of surface chemistry and morphology of silica on the thermal and mechanical properties of silicone elastomers," *Journal of Applied Polymer Science*, vol. 135, no. 35, p. 46646, 2018.
[388] Y. Lin, L. Wang, F. Yin, M. Farzaneh, Y. Liu, and S. Gao, "Comparison of four commonly used high temperature vulcanized silicone rubber formulas for outdoor insulator and their regional adaptability," *Journal of Applied Polymer Science*, p. 47477, 2019.
[389] H. Dodiuk and S. H. Goodman, *Handbook of thermoset plastics*. William Andrew, 2013.
[390] Y. Lin, L. Wang, F. Yin, M. Farzaneh, Y. Liu, and S. Gao, "Comparison of four commonly used high temperature vulcanized silicone rubber formulas for outdoor insulator and their regional adaptability," *Journal of Applied Polymer Science*, vol. 136, no. 19, p. 47477, 2019.
[391] A. Milionis, K. Dang, M. Prato, E. Loth, and I. Bayer, "Liquid repellent nanocomposites obtained from one-step water-based spray," *Journal of Materials Chemistry A*, vol. 3, no. 24, pp. 12880-12889, 2015.

[392] W.-Z. Yuan and L.-Z. Zhang, "Lattice Boltzmann simulation of droplets impacting on superhydrophobic surfaces with randomly distributed rough structures," *Langmuir,* vol. 33, no. 3, pp. 820-829, 2017.
[393] M. Amin, A. Khattak, and M. Ali, "Accelerated aging investigation of silicone rubber/silica composites for coating of high-voltage insulators," *Electrical Engineering,* vol. 100, no. 1, pp. 217-230, 2018.
[394] Z. Chen, G. Li, L. Wang, Y. Lin, and W. Zhou, "A strategy for constructing superhydrophobic multilayer coatings with self-cleaning properties and mechanical durability based on the anchoring effect of organopolysilazane," *Materials and Design,* vol. 141, pp. 37-47, 2018.
[395] N. Wang, D. Xiong, Y. Deng, Y. Shi, and K. Wang, "Mechanically robust superhydrophobic steel surface with anti-icing, UV-durability, and corrosion resistance properties," *ACS applied materials and interfaces,* vol. 7, no. 11, pp. 6260-6272, 2015.
[396] W. Tong, D. Xiong, N. Wang, Z. Wu, and H. Zhou, "Mechanically robust superhydrophobic coating for aeronautical composite against ice accretion and ice adhesion," *Composites Part B: Engineering,* p. 107267, 2019.
[397] E. Bormashenko, G. Chaniel, and R. Grynyov, "Towards understanding hydrophobic recovery of plasma treated polymers: Storing in high polarity liquids suppresses hydrophobic recovery," *Applied Surface Science,* vol. 273, pp. 549-553, 2013.
[398] N. R. Canada, "Photovoltaic and solar resource maps," 2017.
[399] B.-H. Youn and C.-S. Huh, "Surface degradation of HTV silicone rubber and EPDM used for outdoor insulators under accelerated ultraviolet weathering condition," *IEEE Transactions on Dielectrics and Electrical Insulation,* vol. 12, no. 5, pp. 1015-1024, 2005.
[400] Z. Wang, Z. Jia, M. Fang, and Z. Guan, "Absorption and permeation of water and aqueous solutions of high-temperature vulcanized silicone rubber," *IEEE Transactions on Dielectrics and Electrical Insulation,* vol. 22, no. 6, pp. 3357-3365, 2015.
[401] R. Menini, Z. Ghalmi, and M. Farzaneh, "Highly resistant icephobic coatings on aluminum alloys," *Cold Regions Science Technology,* vol. 65, no. 1, pp. 65-69, 2011.
[402] M. Susoff, K. Siegmann, C. Pfaffenroth, and M. Hirayama, "Evaluation of icephobic coatings—Screening of different coatings and influence of roughness," *Applied Surface Science,* vol. 282, pp. 870-879, 2013.
[403] F. Wang, W. Ding, J. He, and Z. Zhang, "Phase transition enabled durable anti-icing surfaces and its DIY design," *Chemical Engineering Journal,* vol. 360, pp. 243-249, 2019.
[404] D. Chen, M. D. Gelenter, M. Hong, R. E. Cohen, and G. H. McKinley, "Icephobic surfaces induced by interfacial nonfrozen water," *ACS applied materials interfaces,* vol. 9, no. 4, pp. 4202-4214, 2017.
[405] Z. A. Janjua *et al.*, "Performance and durability tests of smart icephobic coatings to reduce ice adhesion," *Applied Surface Science,* vol. 407, pp. 555-564, 2017.
[406] K. Golovin, S. P. Kobaku, D. H. Lee, E. T. DiLoreto, J. M. Mabry, and A. Tuteja, "Designing durable icephobic surfaces," *Science Advances,* vol. 2, no. 3, p. e1501496, 2016.
[407] R. Menini and M. Farzaneh, "Advanced icephobic coatings," *Journal of adhesion science technology,* vol. 25, no. 9, pp. 971-992, 2011.
[408] Y. Y. Yan, N. Gao, and W. Barthlott, "Mimicking natural superhydrophobic surfaces and grasping the wetting process: A review on recent progress in preparing superhydrophobic surfaces," *Advances in colloid interface science,* vol. 169, no. 2, pp. 80-105, 2011.
[409] P. Guo, Y. Zheng, M. Wen, C. Song, Y. Lin, and L. Jiang, "Icephobic/anti-icing properties of micro/nanostructured surfaces," *Advanced Materials,* vol. 24, no. 19, pp. 2642-2648, 2012.
[410] Y. Shen, H. Tao, S. Chen, L. Zhu, T. Wang, and J. Tao, "Icephobic/anti-icing potential of superhydrophobic Ti6Al4V surfaces with hierarchical textures," *RSC Advances,* vol. 5, no. 3, pp. 1666-1672, 2015.
[411] C. Wei, B. Jin, Q. Zhang, X. Zhan, and F. Chen, "Anti-icing performance of super-wetting surfaces from icing-resistance to ice-phobic aspects: Robust hydrophobic or slippery surfaces," *Journal of Alloys Compounds,* vol. 765, pp. 721-730, 2018.
[412] E. J. Y. Ling, V. Uong, J.-S. b. Renault-Crispo, A.-M. Kietzig, and P. Servio, "Reducing ice adhesion on nonsmooth metallic surfaces: wettability and topography effects," *ACS Applied Materials Interfaces,* vol. 8, no. 13, pp. 8789-8800, 2016.
[413] P. Hao, C. Lv, and X. Zhang, "Freezing of sessile water droplets on surfaces with various roughness and wettability," *Applied physics letters,* vol. 104, no. 16, p. 161609, 2014.

[414] Y. Rahmawan, L. Xu, and S. Yang, "Self-assembly of nanostructures towards transparent, superhydrophobic surfaces," *Journal of Materials Chemistry A*, vol. 1, no. 9, pp. 2955-2969, 2013.
[415] M. Gong, X. Xu, Z. Yang, Y. Liu, H. Lv, and L. Lv, "A reticulate superhydrophobic self-assembly structure prepared by ZnO nanowires," *Nanotechnology*, vol. 20, no. 16, p. 165602, 2009.
[416] J. Wu *et al.*, "Rinse-resistant superhydrophobic block copolymer fabrics by electrospinning, electrospraying and thermally-induced self-assembly," *Applied Surface Science*, vol. 422, pp. 769-777, 2017.
[417] P. S. Brown and B. Bhushan, "Bioinspired, roughness-induced, water and oil super-philic and super-phobic coatings prepared by adaptable layer-by-layer technique," *Scientific reports*, vol. 5, p. 14030, 2015.
[418] D. Lopez-Torres, C. Elosua, M. Hernaez, J. Goicoechea, and F. Arregui, "From superhydrophilic to superhydrophobic surfaces by means of polymeric layer-by-layer films," *Applied Surface Science*, vol. 351, pp. 1081-1086, 2015.
[419] K. Feng, G.-Y. Hung, J. Liu, M. Li, C. Zhou, and M. Liu, "Fabrication of high performance superhydrophobic coatings by spray-coating of polysiloxane modified halloysite nanotubes," *Chemical Engineering Journal*, vol. 331, pp. 744-754, 2018.
[420] R. Tan *et al.*, "A new approach to fabricate superhydrophobic and antibacterial low density isotropic pyrocarbon by using catalyst free chemical vapor deposition," *Carbon*, 2019.
[421] Y. Tang, Q. Zhang, X. Zhan, and F. Chen, "Superhydrophobic and anti-icing properties at overcooled temperature of a fluorinated hybrid surface prepared via a sol–gel process," *Soft Matter*, vol. 11, no. 22, pp. 4540-4550, 2015.
[422] Q. Li, Y. Yan, M. Yu, B. Song, S. Shi, and Y. Gong, "Synthesis of polymeric fluorinated sol–gel precursor for fabrication of superhydrophobic coating," *Applied Surface Science*, vol. 367, pp. 101-108, 2016.
[423] J. Li, R. Wu, Z. Jing, L. Yan, F. Zha, and Z. Lei, "One-step spray-coating process for the fabrication of colorful superhydrophobic coatings with excellent corrosion resistance," *Langmuir*, vol. 31, no. 39, pp. 10702-10707, 2015.
[424] K. Maghsoudi, G. Momen, R. Jafari, M. Farzaneh, and T. Carreira, "Micro-Nanostructured Silicone Surfaces for Highvoltage Application," in *IEEE Conference on Electrical Insulation and Dielectric Phenomena (CEIDP)*, 2018, pp. 179-182: IEEE.
[425] Q. Zhao, Y. Liu, and S. Wang, "Surface modification of water treatment equipment for reducing CaSO4 scale formation," *Desalination*, vol. 180, no. 1-3, pp. 133-138, 2005.
[426] R. Jafari, R. Menini, and M. Farzaneh, "Superhydrophobic and icephobic surfaces prepared by RF-sputtered polytetrafluoroethylene coatings," *Applied Surface Science*, vol. 257, no. 5, pp. 1540-1543, 2010.
[427] R. Jafari and M. Farzaneh, "Fabrication of superhydrophobic nanostructured surface on aluminum alloy," *Applied Physics A*, vol. 102, no. 1, pp. 195-199, 2011.
[428] D. Jucius *et al.*, "Hot embossing of PTFE: towards superhydrophobic surfaces," *Applied Surface Science*, vol. 257, no. 6, pp. 2353-2360, 2011.
[429] Y. Zhan *et al.*, "Fabrication of anisotropic PTFE superhydrophobic surfaces using laser microprocessing and their self-cleaning and anti-icing behavior," *Colloids Surfaces A: Physicochemical Engineering Aspects*, vol. 535, pp. 8-15, 2017.
[430] Y. Zhu *et al.*, "Preparation of large-scale, durable, superhydrophobic PTFE films using rough glass templates," *Surface Interface Analysis*, vol. 49, no. 13, pp. 1422-1430, 2017.
[431] S. Zanini, R. Bami, R. Della Pergola, and C. Riccardi, "Development of super-hydrophobic PTFE and PET surfaces by means of plasma processes," in *Journal of Physics: Conference Series*, 2014, vol. 550, no. 1, p. 012029: IOP Publishing.
[432] S. G. Lee, H. S. Lim, D. Y. Lee, D. Kwak, and K. Cho, "Tunable anisotropic wettability of rice leaf-like wavy surfaces," *Advanced Functional Materials*, vol. 23, no. 5, pp. 547-553, 2013.
[433] M. Merola, A. Ruggiero, J. S. De Mattia, and S. Affatato, "On the tribological behavior of retrieved hip femoral heads affected by metallic debris. A comparative investigation by stylus and optical profilometer for a new roughness measurement protocol," *Measurement*, vol. 90, pp. 365-371, 2016.
[434] A. Canabarro, F. Figueiredo, S. Paciornik, and G. De-Deus, "Two-and three-dimensional profilometer assessments to determine titanium roughness," *Scanning: The Journal of Scanning Microscopies*, vol. 31, no. 4, pp. 174-179, 2009.

[435] E. Gadelmawla, M. Koura, T. Maksoud, I. Elewa, and H. Soliman, "Roughness parameters," *Journal of materials processing Technology,* vol. 123, no. 1, pp. 133-145, 2002.
[436] M. Sedlaček, B. Podgornik, and J. Vižintin, "Correlation between standard roughness parameters skewness and kurtosis and tribological behaviour of contact surfaces," *Tribology international,* vol. 48, pp. 102-112, 2012.
[437] A. Galante, O. Galante, and L. Campos, "Study on application of PTFE, FEP and PFA fluoropolymers on radiation dosimetry," *Nuclear Instruments, Methods in Physics Research Section A: Accelerators, Spectrometers, Detectors Associated Equipment,* vol. 619, no. 1-3, pp. 177-180, 2010.
[438] J. Long *et al.*, "Cassie-state stability of metallic superhydrophobic surfaces with various micro/nanostructures produced by a femtosecond laser," *Langmuir,* vol. 32, no. 4, pp. 1065-1072, 2016.
[439] B. Bhushan, Y. C. Jung, and K. Koch, "Micro-, nano-and hierarchical structures for superhydrophobicity, self-cleaning and low adhesion," *Philosophical Transactions of the Royal Society of London A: Mathematical, Physical and Engineering Sciences,* vol. 367, no. 1894, pp. 1631-1672, 2009.
[440] Y. Shen *et al.*, "Water repellency of hierarchical superhydrophobic Ti6Al4V surfaces improved by secondary nanostructures," *Applied Surface Science,* vol. 321, pp. 469-474, 2014.
[441] D. Wu *et al.*, "Facile creation of hierarchical PDMS microstructures with extreme underwater superoleophobicity for anti-oil application in microfluidic channels," *Lab on a Chip,* vol. 11, no. 22, pp. 3873-3879, 2011.
[442] K. Mielonen, M. Suvanto, and T. Pakkanen, "Curved hierarchically micro–micro structured polypropylene surfaces by injection molding," *Journal of Micromechanics and Microengineering,* vol. 27, no. 1, p. 015025, 2016.
[443] P. Hao, C. Lv, F. Niu, and Y. Yu, "Water droplet impact on superhydrophobic surfaces with microstructures and hierarchical roughness," *Science China Physics, Mechanics Astronomy,* vol. 57, no. 7, pp. 1376-1381, 2014.
[444] L. Chen, Z. Xiao, P. C. Chan, and Y.-K. Lee, "Static and dynamic characterization of robust superhydrophobic surfaces built from nano-flowers on silicon micro-post arrays," *Journal of micromechanics microengineering,* vol. 20, no. 10, p. 105001, 2010.
[445] S. Kulinich and M. Farzaneh, "Ice adhesion on super-hydrophobic surfaces," *Applied Surface Science,* vol. 255, no. 18, pp. 8153-8157, 2009.
[446] H. Niemelä-Anttonen *et al.*, "Icephobicity of Slippery Liquid Infused Porous Surfaces under Multiple Freeze–Thaw and Ice Accretion–Detachment Cycles," *Advanced Materials Interfaces,* vol. 5, no. 20, p. 1800828, 2018.
[447] A. Work and Y. Lian, "A critical review of the measurement of ice adhesion to solid substrates," *Progress in Aerospace Sciences,* 2018.
[448] S. Yang, Q. Xia, L. Zhu, J. Xue, Q. Wang, and Q.-m. Chen, "Research on the icephobic properties of fluoropolymer-based materials," *Applied Surface Science,* vol. 257, no. 11, pp. 4956-4962, 2011.
[449] X. Li, Y. Zhao, H. Li, and X. Yuan, "Preparation and icephobic properties of polymethyltrifluoropropylsiloxane–polyacrylate block copolymers," *Applied Surface Science,* vol. 316, pp. 222-231, 2014.
[450] R. Dou *et al.*, "Anti-icing coating with an aqueous lubricating layer," *ACS applied materials & interfaces,* vol. 6, no. 10, pp. 6998-7003, 2014.
[451] C. Wang, W. Zhang, A. Siva, D. Tiea, and K. J. Wynne, "Laboratory test for ice adhesion strength using commercial instrumentation," *Langmuir,* vol. 30, no. 2, pp. 540-547, 2014.
[452] X. Wu, X. Zhao, J. W. C. Ho, and Z. Chen, "Design and durability study of environmental-friendly room-temperature processable icephobic coatings," *Chemical Engineering Journal,* vol. 355, pp. 901-909, 2019.
[453] T. Bharathidasan, S. V. Kumar, M. Bobji, R. Chakradhar, and B. J. Basu, "Effect of wettability and surface roughness on ice-adhesion strength of hydrophilic, hydrophobic and superhydrophobic surfaces," *Applied Surface Science,* vol. 314, pp. 241-250, 2014.
[454] R. Menini and M. Farzaneh, "Elaboration of Al2O3/PTFE icephobic coatings for protecting aluminum surfaces," *Surface and Coatings Technology,* vol. 203, no. 14, pp. 1941-1946, 2009.
[455] G. Momen, M. Farzaneh, and R. Jafari, "Wettability behaviour of RTV silicone rubber coated on nanostructured aluminium surface," *Applied Surface Science,* vol. 257, no. 15, pp. 6489-6493, 2011.

[456] K. K. Varanasi, T. Deng, J. D. Smith, M. Hsu, and N. Bhate, "Frost formation and ice adhesion on superhydrophobic surfaces," *Applied Physics Letters*, vol. 97, no. 23, p. 234102, 2010.
[457] J. Chen *et al.*, "Superhydrophobic surfaces cannot reduce ice adhesion," *Applied Physics Letters*, vol. 101, no. 11, p. 111603, 2012.
[458] S. Kulinich and M. Farzaneh, "How wetting hysteresis influences ice adhesion strength on superhydrophobic surfaces," *Langmuir*, vol. 25, no. 16, pp. 8854-8856, 2009.
[459] Q. Yang *et al.*, "Air cushion convection inhibiting icing of self-cleaning surfaces," *ACS applied materials interfaces*, vol. 8, no. 42, pp. 29169-29178, 2016.
[460] J. Yang and W. Li, "Preparation of superhydrophobic surfaces on Al substrates and the anti-icing behavior," *Journal of Alloys Compounds*, vol. 576, pp. 215-219, 2013.
[461] N. R. Canada. (2017). *Photovoltaic and solar resource maps*. Available: https://www.nrcan.gc.ca/18366

PUBLICATIONS

Journal Articles

1- **"Icephobicity and durability assessment of superhydrophobic surfaces: the role of surface roughness and the ice adhesion measurement technique"**, K. Maghsoudi, E. Vazirinasab, G. Momen, R. Jafari, *Materials Processing Technology*, 288, 116883, 2020.

2- **"A Non-Fluorinated Mechanochemically-Robust Volumetric Superhydrophobic Nanocomposite"**, E. Vazirinasab, G. Momen, R. Jafari, *Materials Sience and Technology*, 2020.

3- **"Evaluating the effect of processing parameters on the replication quality in a micro molding process"**, K. Maghsoudi, E. Vazirinasab, R. Jafari, G. Momen, *Materials and Manufacturing Processes*, 35, 1567-1575, 2020.

4- **"Advances in the fabrication of superhydrophobic polymeric surfaces by polymer molding processes"**, K. Maghsoudi, E. Vazirinasab, G. Momen, R. Jafari, *ACS I&EC Research*,59, 9343-9363, 2020.

5- **"A comparative study of the icephobic and self-Cleaning properties of Teflon materials having different surface morphologies"**, E. Vazirinasab, K. Maghsoudi, R. Jafari, G. Momen, *Materials Processing Technology*, 276, 116415, 2020.

6- **"Evaluation of atmospheric-pressure plasma parameters to achieve superhydrophobic and self-cleaning HTV silicone rubber surfaces via a single-step, eco-friendly approach"**, E. Vazirinasab, R. Jafari, G. Momen, *Surface and Coatings Technology*, 375, 100-111, 2019.

7- **"Application of superhydrophobic coatings as a corrosion barrier: A review**", E. Vazirinasab, R. Jafari, G. Momen, *Surface and Coatings Technology*, 341, 40-56, 2018.

8- **"Simple fabrication of superhydrophobic surfaces using atmospheric-pressure plasma"**, E. Vazirinasab, R. Jafari, G. Momen, T. Carreira, *Materials Science Forum*, 941, 1808-1814, 2018.

Conferences

1- **"Volumetric Superhydrophobic Nanocomposite using Diatomaceous Earth",** E. Vazirinasab, G. Momen, R. Jafari, *QCAM Symposium*, University of Montreal, Montreal, Quebec, Canada, Nov. 2019.
2- **"Wetting and Self-Cleaning Properties of Silicone Rubber Surfaces Treated by Atmospheric Plasma Jet",** E. Vazirinasab, R. Jafari, G. Momen, *IEEE Conference on Electrical Insulation and Dielectric Phenomena (CEIDP)*, Cancun, Mexico, Oct. 2018.
3- **"Développement de surfaces superhydrophobes utilisant un jet de plasma à pression atmosphérique",** E. Vazirinasab, R. Jafari, G. Momen, *86^{e} congrès de l'ACFAS*, UQAC, Chicoutimi, Quebec, Canada, May 2018.
4- **"Superhydrophobic Silicone Rubber Using Atmospheric Pressure Plasma Jet",** E. Vazirinasab, R. Jafari, G. Momen, *1st Annual QCAM Symposium*, University of Sherbrooke, Canada, Oct. 2017.